RESPONSIVE AND STRUCTURED SILICA-POLYPEPTIDE COMPOSITE PARTICLES AND THEIR COMPONENTS

A Dissertation
Presented to
The Academic Faculty

by

Alyssa M. Blake

In Partial Fulfillment
of the Requirements for the Degree
Doctorate in Philosophy in the
School of Chemistry and Biochemistry

Georgia Institute of Technology
August 2020

RESPONSIVE AND STRUCTURED SILICA-POLYPEPTIDE COMPOSITE PARTICLES AND THEIR COMPONENTS

Approved by:

Dr. Paul S. Russo, Advisor
School of Materials Science and Engineering
Georgia Institute of Technology

Dr. Jiri (Art) Janata
School of Chemistry and Biochemistry
Georgia Institute of Technology

Dr. M.G Finn
School of Chemistry and Biochemistry
Georgia Institute of Technology

Dr. Valeria Milam
School of Materials Science and Engineering
Georgia Institute of Technology

Dr. Ronghu Wu
School of Chemistry and Biochemistry
Georgia Institute of Technology

Date Approved: May 19, 2020

ACKNOWLEDGEMENTS

I would like to thank my advisor. Dr. Paul Russo, for his support during my time in the Russo lab. I would also like to thank my committee members – Dr. M.G Finn, Dr. Jiri (Art) Janata, Dr. Valeria Milam, and Dr. Ronghu Wu – for all of their help and support throughout my graduate school tenure. Without my advisor and committee members input, guidance and support it would not be possible to complete this work.

This work would not have been possible without the help, advice, and feedback from my colleagues in the Russo group, Georgia Tech staff members, and other graduate students across multiple disciplines at Georgia Tech. Without the collaborative community that Georgia Tech fosters, I would not have been able to troubleshoot my projects and complete my work. A special thanks to the teaching community at Georgia Tech, especially my teaching assistant boss and mentor throughout my tenure – Dr. Christy O'Mahony – without whose guidance, continued support, and advice I would not have furthered my teaching abilities.

I would especially like to thank my friends and family, without whose guidance and continued support I would not be where I am today. In particular, I would like to thank my mother, father, and siblings for their constant encouragement and advice throughout this process. Finally, I would like to thank my late grandfather for his unwavering support and positivity during a lot of challenging times.

TABLE OF CONTENTS

LIST OF TABLES

LIST OF FIGURES

LIST OF SYMBOLS AND ABBREVIATIONS

AEAPTMS	Aminoethyl-aminopropyl timethyl silane
APS	3-aminopropyl triethoxysilane
BLG	γ-benzyl-α,L-glutamate
BTY	o-benzyl-L-tyrosine
CBL	ε-carbobenzyloxy-L-lysine
$Đ$	Polydispersity Index
DLS	Dynamic Light Scattering
DMF	N'N-Dimethyl formamide
EtOH	Ethanol
FITC	Fluorescein isothiocyanate
FPR	Fluorescence Photobleaching Recovery
FTIR	Fourier transform infrared spectroscopy
GPC	Gel permeation chromatography
MALS	Multi-angle light scattering
MTMS	Methyltrimethoxysilane
M_w	Weight-average molecular weight
NCA	*N*-carboxyanhydrides
NMR	Nuclear Magnetic Resonance
OR	Optical rotation
ORD	Optical rotatory dispersion
PBLG	Poly(γ-benzyl- α,L-glutamate)
PBTY	Poly(o-benzyl-L-tyrosine)

PCBL	Poly(ε-carbobenzyloxy-L-lysine)
PCP	Polypeptide Composite Particles
PICUP	Photo-induced cross-linking of unmodified proteins
PTYR	Poly(L-tyrosine)
RITC	Rhodamine B isothiocyanate
ROP	Ring-opening polymerization
SEM	Scanning Electron Microscopy
TEOS	Tetraethyl orthosilicate
TEM	Transmission electron microscopy
TGA	Thermogravimetric Analysis
THF	Tetrahydrofuran
TYR	Tyrosine
XPS	X-ray photoelectron spectroscopy

SUMMARY

Nature produces spectacular multifunctional particles by joining different components together. Living cells consist of multifaceted compartments that house DNA, RNA, ribosomes, vesicles, and surface signaling molecules. Virus particles store important viral information enclosed in a capsid decorated with a corona of responsive proteins. Not only can nature seamlessly combine a variety of molecules and components into a single system, but nature's particles know how to assemble to achieve long-range function, including muscle movement. No synthetic particle or collection of particles has approached this elegant combination of function. This dissertation discusses the beginning of building functional and structured particles. It describes a system that combines colloidal silica, known for its ability to assume different and stable shapes, and polypeptides, known for their ability to change shape, assume different chemical features such as charge and hydrophobicity, and for their chirality. Throughout, the goal is to produce silica-polypeptide composite particles (PCPs) that can illuminate a path to multiple function. The focus is on creating these multi-functional particles and understanding their physical properties and behaviors. For the moment, success consists of particles that can change their size and, perhaps, some other property such as magnetic susceptibility.

When combining multiple materials and components into a single system, it is necessary to understand each component individually and what characteristics they will bring to the new material. The dissertation consists of four projects. The first (Chapter 2) considers degradation of the polypeptides by ultrasonic energy, which is important because, like nature, the long-range goal is to build particles that last and survive the

assembly process. Future workers may also wish to disassemble the particle's outer polypeptide layer. For the first time, ultrasonic degradation of untethered PCBL was studied. It is believed that PCBL forms a more flexible helix than its PBLG counterpart which provides increased freedom in the chain that may slow degradation. Also due to its ability to undergo long range ordering by forming liquid crystals, it was hypothesized that increasing the concentration of PCBL and thus decreasing its mobility would further protect the polypeptide from degradation. Understanding the degradation of the polypeptide via ultrasonication gives insight into how the polypeptide will degrade during materials processing which provides information about the best way to work with and handle polymeric materials for industrial scale up applications.

The second project (Chapter 3) continues the study of polypeptides as individual components. Sound is again applied, but this time much weaker amplitude in order to test the hypothesis that simple, modern instrumentation can detect polypeptide conformational transitions (e.g., helix-to-coil) even when spectroscopic and optical methods become difficult. These spectroscopic and optical methods can be blinded by scattering that will occur when the polypeptides are attached to colloidal silica, especially silica with magnetic inclusions, which is part of the intended multifunctional package. For the first time, it was learned that a modestly priced, commercially available instrument for industrial labs and operated by technicians can perform a job that is normally reserved for expensive machinery requiring PhD staff. Sound velocity measurements provide comparable results to the conventional methods, but allow for optically active solvents and strongly scattering or even turbid samples to be more easily measured. The combination of sound velocity and

optical methods provides a new way to understand polypeptide transitions in complex environments and real-world formulations.

After studying and understanding the individual components, the silica and polypeptides can be combined to create multifunctional PCPs. The third project (Chapter 5) walks through the synthesis and characterization of magnetic and thermoresponsive PCPs. Combining multiple response mechanisms into a single material is needed to mimic the extraordinary functions of bioparticles and biology. Examples of these extraordinary functions would be the expansion and contraction mechanism of muscle fibers. Aligning of the composite particles via an applied magnetic field provides a technique to create long crosslinked fibers to produce a synthetic muscle fiber. The superparamagnetic properties of the magnetic inclusion were retained in the composite particles and the PCBL shell was still able to undergo its conformational transition. Even after several years, the PCPs retained their magnetic and responsive properties. Even more remarkable, the helix-coil transition altered the magnetic susceptibility of the cobalt nougat buried at the particle center. This discovery opens the way for particles whose magnetic character is sensitive to such environmental parameters as salt, temperature or pH. Even without this remarkable and surprising feature, PCPs constitute an easily manipulated composite material containing a reversibly thermoresponsive, biologically relevant molecule attached to the surface.

The fourth and final project (Chapter 6) works to add to the types of multifunctional particles that can be created by focusing on synthesizing and characterizing polypeptide-coated Janus particles. The silica-polypeptide composite Janus particles are unique because they combine a stimuli-responsive PCBL shell with an inorganic colloidal silica core, half

of which is coated by a metal. Ideally gold would be the metal of choice due to its biocompatibility but for ease of synthesis, chromium was used to determine the ability to create large, Janus composite particles. Creation of these cores used an inexpensive substrate, Scotch-tape, to protect half the silica particle. Successful half-coating of the silica with chromium and removal from the tape was followed by the polymerization of a polypeptide shell onto the Janus core particle. The use of these materials was altered once it was determined that the polypeptide was grafted to the entire particle surface. These polypeptide coated Janus cores could be used to create hollow vesicle structures. The silica core can be removed via etching with HF to leave a polypeptide vesicle with a small chromium side. Secondary conformational transition studies can be conducted on the polypeptide chains to determine if a hollow structure affects the transition. These materials can also be used to create micromotors for self-propelling particles through manipulation of the chromium coating and the polypeptide-shell conformational transition.

CHAPTER 1. INTRODUCTION AND LITERATURE REVIEW

1.1 Colloidal Silica

1.1.1 Metal Alkoxide and Colloids Introduction

Metal alkoxides (metal-organic compounds that have an organic alkoxy ligand attached to a metal atom) are a popular precursor to synthesizing colloidal suspensions because they readily react with water to undergo a hydrolysis reaction.[1] A colloid is a two-phase system in which one of the phases is microscopic in size and dispersed within the other phase.[2] The size of the dispersed phase ranges from approximately one nanometer to more than one micrometer.[3-4] In this size range, the dispersed phase exhibits Brownian motion (random walk of dispersed phase driven by the momentum from collisions with molecules of the suspending phase), gravitational forces are negligible, and the dominating interactions are from short-range forces (i.e. Van der Waals and surface charges).[3] When talking about colloids a few different terms might arise such as sol, sol-gel, emulsion, and aerosol. For the course of this work, the focus will be on sols (a liquid with solid particles dispersed throughout to create a colloidal suspension) with some mention of emulsions (a colloidal suspension containing liquid droplets dispersed in a liquid).[3] Figure 1 shows a general image of the two colloidal suspensions, sol and emulsion.

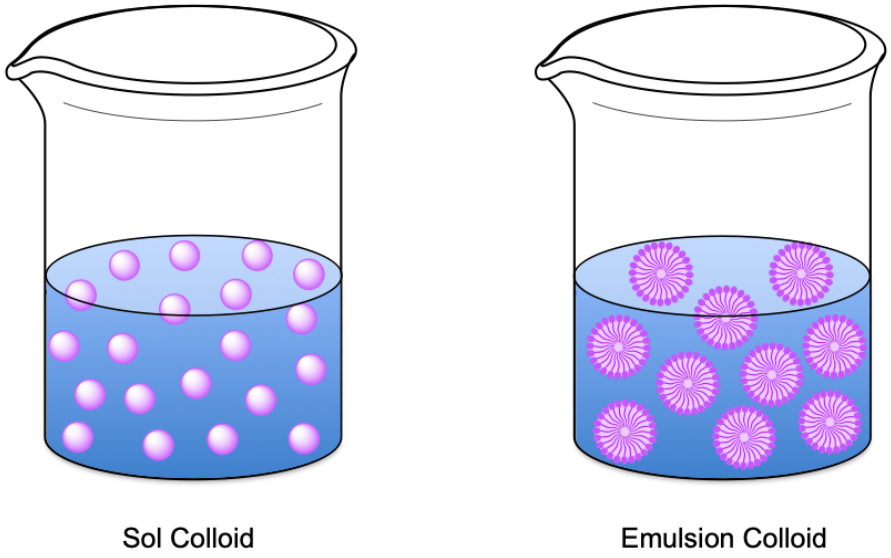

Figure 1. General illustration of a sol and emulsion colloidal suspensions.

Colloids can be used to produce polymers and particles that make ceramic materials.[1] Starting in the 1850s, colloidal suspensions made from metal oxides that could gel, were used in various applications, such as preparation of oxide films, phase equilibrium studies, and formation of radioactive oxides for use in nuclear reactor fuel cells.[3] Many types of metal oxides were used to create these colloidal suspensions, for example titanium oxide, aluminum oxide, silicon oxide, etc. The most thoroughly studied metal alkoxide is silica tetraethoxide (also known as tetraethyl orthosilicate, TEOS) used to make colloidal silica suspensions.

A detailed analysis of colloidal silica came in the late 1950s when Iler wrote his book about the colloid chemistry of silica and other silicates.[2] A large effort was placed on understanding the mechanism behind creating a stable silica colloidal suspension. A development during this time found that to obtain a concentrated and stable sol, the silica particles have to be in an optimum size range. Along with the size, the particles must have

some ionic charge associated with them so that the mutual repulsion will help minimize the collisions and aggregation of the particles. By the 1970s, stable sol suspensions were readily developed, progressing research pertaining to the chemistry and interactions of colloidal suspensions.[1-2] Due to their simple production and scale-up, silica-colloidal particles have been used across many platforms for use in separations, drug delivery, scaffolding, etc.[5-6]

1.1.2 Synthesis of Silica Colloidal Particles

Polysilicate gels and particles are formed through silicate hydrolysis and condensation.[2] Natural silica prepared via this process can be found in a variety of applications from flint to the development of mammals.[1] The most common example of this process in nature is the formation of opal.[2] To produce this precious gem, repeated hydrolysis and condensation steps involving soluble silica lead to the formation of polysilicate species. Under appropriate conditions, these evolve into spherical silica particles of SiO_2.[2] The procedures for making synthetic silicate gels and particles follow the hydrolysis and condensation reactions found for centuries in nature.

Silicate gels are usually synthesized by hydrolyzing a monomer (in most cases it is a tetra-functional alkoxide) using an acid or a base as catalyst for the reaction.[2] Figure 2 illustrates the reactions occurring to produce silica sol-gels. Previous literature explains the difference in particle growth between the base-catalyzed and acid-catalyzed approaches.[1] Under acidic conditions, the primary particles tend to remain smaller, then aggregate and form chains. In contrast, basic conditions are conducive to the formation of larger primary particles decreasing the overall number of particles in solution. The acidic conditions favor

gel production due to the lack of surface charge on the particles, resulting in flocculation or connectivity between particles. Basic conditions create a negative surface charge on the particles, which stabilizes the suspensions.[7] This work centers around creating stable colloidal suspensions of spherical particles, thus base-catalyzed was chosen for the production of the silica colloidal particles.

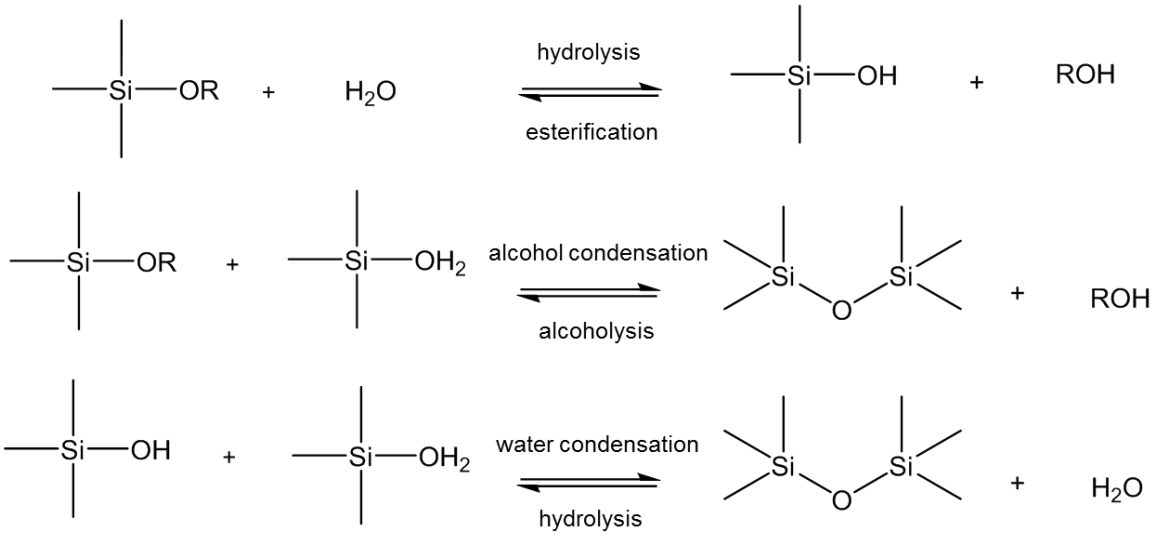

Figure 2. Reaction schemes illustrating the hydrolysis and condensation of alkoxides to form silicates. Adapted from Brinker and Scherer.[1]

The most common procedure for making monodisperse silica spheres is the Stöber method.[8] Shown in Figure 3, a silicon alkoxide (TEOS) undergoes hydrolysis/condensation into a crosslinked silicate network whose nucleation and growth result in amorphous silica particles.[8] It has been shown previously that a variety of particle sizes can be obtained by altering reaction conditions, such as temperature, rate of stirring, and reactant concentration.[9-10] The Stöber method relies on an ammonium base-catalyzed hydrolysis at a pH of 9–10. The overall reaction parameters are shown in Figure 3. Upon reaction completion, the silica particles are negatively charged due to the presence of the hydroxyl

groups (OH) on the surface. Repulsion between the particles helps reduce aggregation and creates a stable dispersion of particles throughout the solution.[9]

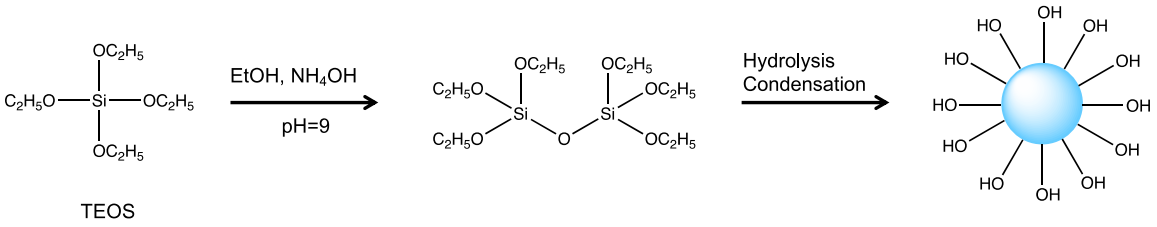

Figure 3. Reaction schematic showing the Stöber (base-catalyzed) silica synthesis. The reagents used are TEOS, ethanol, ammonium hydroxide, and water.

The Stöber method was able to produce relatively low size distributions of silica spheres but relied on distillation of the TEOS before use. Variations of the Stöber method are prevalent in the literature focusing on increasing the monodispersity of the spherical silica particles. Bogush, Tracy and Zukowski expanded on the work Stöber reported to create silica spheres with narrow size distributions.[11] A larger concentration range for the reactants (ammonium hydroxide, water, ethanol, and TEOS) was studied along with a different reaction temperatures (9–55 ºC). Their main goal was to provide a range over which monodispersity can be achieved and develop a way to predict final particle size given specific reactant concentrations. From their studies, the seeded growth method was developed which could produce particles with larger size and mass fraction. Previously synthesized silica particles, typically following the Stöber procedure, would be used as nucleation points (or seeds) for continued reaction of freshly added TEOS. The seeded growth method did not require the TEOS to be distilled prior to use but creation of the seed particles still required freshly distilled TEOS.[11] More recently, Zhang *et al*. reproducibly synthesize spherical silica particles from undistilled, reagent grade TEOS by implementing

the dilution of TEOS into their synthesis.[12] They found that by diluting TEOS with 4× volume of ethanol before addition to the reaction eliminated the time-consuming distillation of TEOS before use while producing silica with low polydispersity. A decrease in the reaction time for the seeded growth technique was also developed by diluting TEOS with 4× volume of ethanol and adding it dropwise to the seed suspension.

Another common synthetic technique for creating smaller, less densely cross-linked colloidal silica particles is by a reverse microemulsion reaction. Osseo-Asare and Arriagada prepared monodisperse silica particles ranging in size from 50–70 nm by creating a reverse micellar system.[13] The ratio of water to surfactant was varied and showed that increasing this ratio results in a smaller and more uniform particle. Other scientists continue to use the reverse microemulsion system to create small and monodisperse colloidal silica particles that were hard to obtain via traditional hydrolysis and condensation methods such as the Stöber method.[14] With increased size control and the ability to use more readily available chemicals without preprocessing, colloidal silica particles have found many uses in biomedical, chemical, optical, and physical applications.[6]

1.1.3 Applications of Colloidal Silica Particles

Silica particles find uses in many different applications such as drug delivery vesicles, Janus particles, colloidal crystals, optical lenses, and imaging agents.[5-6, 15-16] Lui *et al*. reported an increase in the contrast of ultrasound images of mice liver when using 100 nm silica particles.[17] More recent applications of silica particles require surface modification or alteration of the structure and morphology of the silica particles so they can perform correctly. Figure 4 illustrates various synthetic pathways available for creating

different particle morphologies and structures with silica. How new surface functionalization, dye molecules, or polymers will attach to silica particles can result in either isotropic or anisotropic particles. A discussion of isotropic particles, their synthesis and applications, will be provided first, then followed by a short discussion of anisotropic particles.

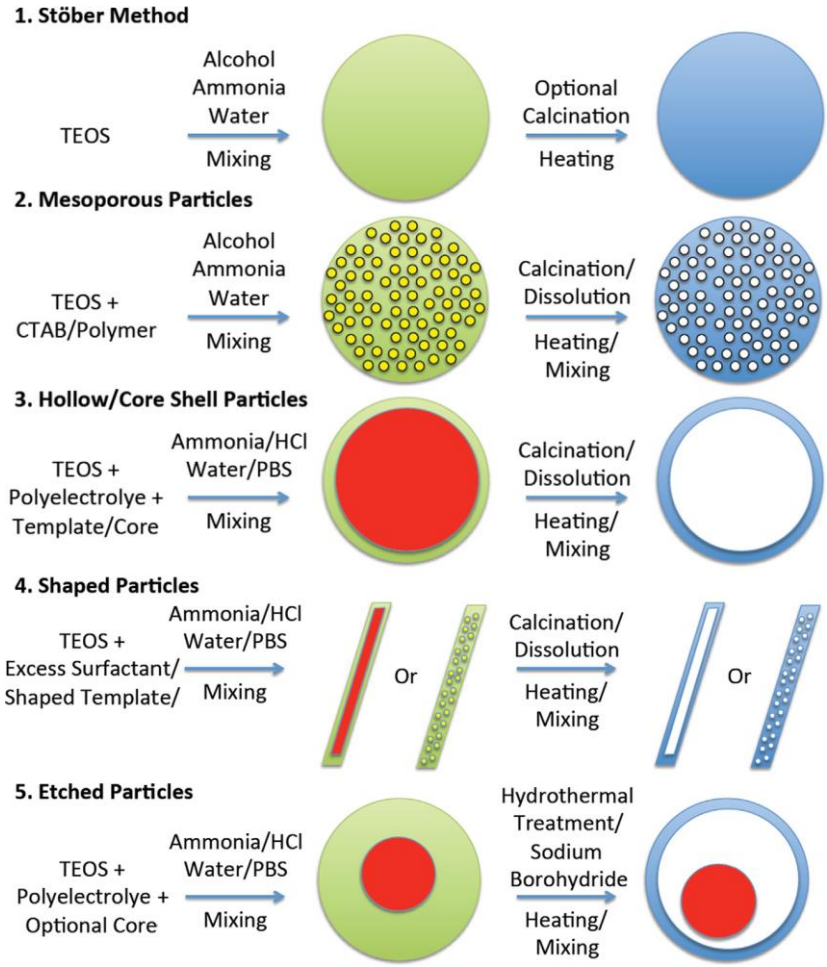

Figure 4. Common synthetic procedures for creating silica particles with different morphologies. Reprinted with permission from Liberman *et al.*[6]

A focus of many researchers is altering the chemistry of the functional groups on the surface of the silica particles. This surface modification provides a way to alter or tune

inter-particles interactions.[18] Changing the functional groups on the silica surface can allow attachment of other polymers, particles, or chemical molecules.[19] Soto-Cantu *et al*. attached amino functional groups to the silica spheres. They controled the number of amino groups that coated the particle surface.[20] These amino groups were then used as initiating sites for different polymerization reactions and attachment of other molecules.[19] Alternatively, dye molecules can be added to the silica particles for increased visualization. The dye can be attached to the surface or incorporated into the crosslinking of the particle. When the dye is incased and incorporated inside of the particle versus on the surface, the particles can be used for bio-imaging of cancer cells or blockages in the body.[21-22] For example, Bagwe *et al*. doped silica particles with Tris (2,2‘-bipyridyl) dichlororuthenium (II) dye using the reverse microemulsion method.[23] Fuller *et al*. fluorescently label silica particles using the Stöber method to illustrate their ability to be used in intracellular imaging and delivery due to increased cellular uptake.[24] Adding a fluorescent label to the particles typically results in increased resolution and contrast of the particles at lower concentrations.

Advantages of using silica particles compared to other polymers and liposomes is their *in vivo* stability.[6, 25] This is one of the reasons silica particles have been used as a material for drug delivery systems, and various studies evaluate the controlled release of different payloads stored within the particles.[6, 15, 26-27] Hollowing the center of silica particles provides another type of silica particle for bio-imaging. Inside the hollow silica particle, fluorophores, in the form of bound chemical species or gas, can be placed to allow fluorescence imaging of different parts of the body. Creating a mesoporous structure can lead to applications in drug delivery and release studies.[15, 26-28] Giri *et al*. synthesized functionalized mesoporous silica that allowed the loading of drugs into the interior of the

silica core. The functional groups blocked the pores and prevented the drug from being released until they were cleaved by intracellular reducing agents inside the body.[15] Other researchers have synthesized particles that have gates on the pores that can be triggered to release drugs and other pay loads when they encounter certain enzymes.[27]

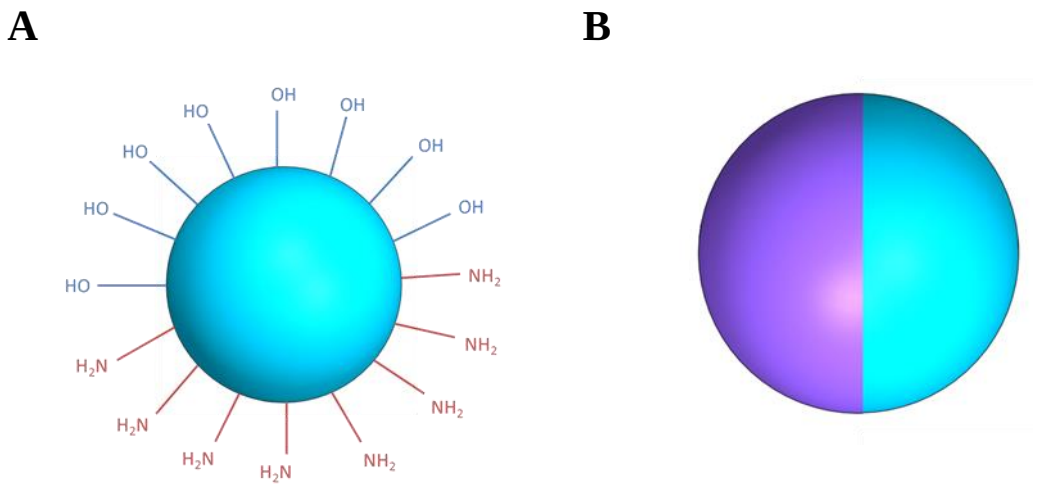

Figure 5. An illustration of two different Janus particles. (A) shows a Janus particle that is made of a single material but each half is functionalized differently, whereas (B) is a Janus particle where half of the particle (shown in purple) is one type of material while the other half of the particle (shown in blue) is a different type of material.

Along with altering the morphology of the silica particles, the shape of the particle can be varied to yield interesting anisotropic materials for liquid crystalline and phase studies.[29-31] Kuijk, van Blaaderen, and Imhof produced rod shaped colloidal silica particles with tunable length and aspect ratio.[29] Due to their large size, these particles are useful as model systems for studying liquid crystal phases and rod-like systems. Yang *et al.* developed a route to synthesize bent rigid silica rods using an emulsion-templated growth method.[32] The particles resemble banana-shaped molecules and can self-assemble to form

liquid crystals. They have the potential to be used in nonconventional photonic crystals or as a templating material for fabricating other structures.

Creation of anisotropic particles, such as Janus particles, is of interest due to their inherent dual-face properties and their ability to be stable at different interfaces.[33-35] Figure 5 shows an example of a Janus particle that can be synthesized from a silica colloidal particle. Janus particles can be created using a variety of different methods involving solution-based chemistry or physical vapor desorption methods. Many researchers created Janus particles made of silica coated with metals such as gold, nickel, platinum, etc.[34, 36] When these particles rotate in solution, the metallic part of the particles can be used as an optical mirror.[37-38] Janus particles can be used to create reconfigurable materials and are useful in studying self-assembly dynamics.

Magnetic inclusions have also been added to the silica particles to create stimuli-responsive colloidal particles. A variety of magnetically active molecules have been used such as cobalt, ferromagnetite, and gold.[39-42] These additions to the silica particles allow the particles to be aligned via a magnetic field and provide a way to control the movement and location of the particles in solution.[39, 41, 43-44] Kobayashi *et al*. synthesized silica coated cobalt particles with different sized cobalt cores and silica shells.[42] Figure 6 shows a schematic of a silica-coated cobalt particle and the respective TEM and EDX analysis of particle synthesized in our lab using the Kobayashi procedure. Kobayashi *et al*. show that the cobalt inclusion was still magnetically susceptible, which opens a huge array of applications from separation techniques to drug delivery materials.

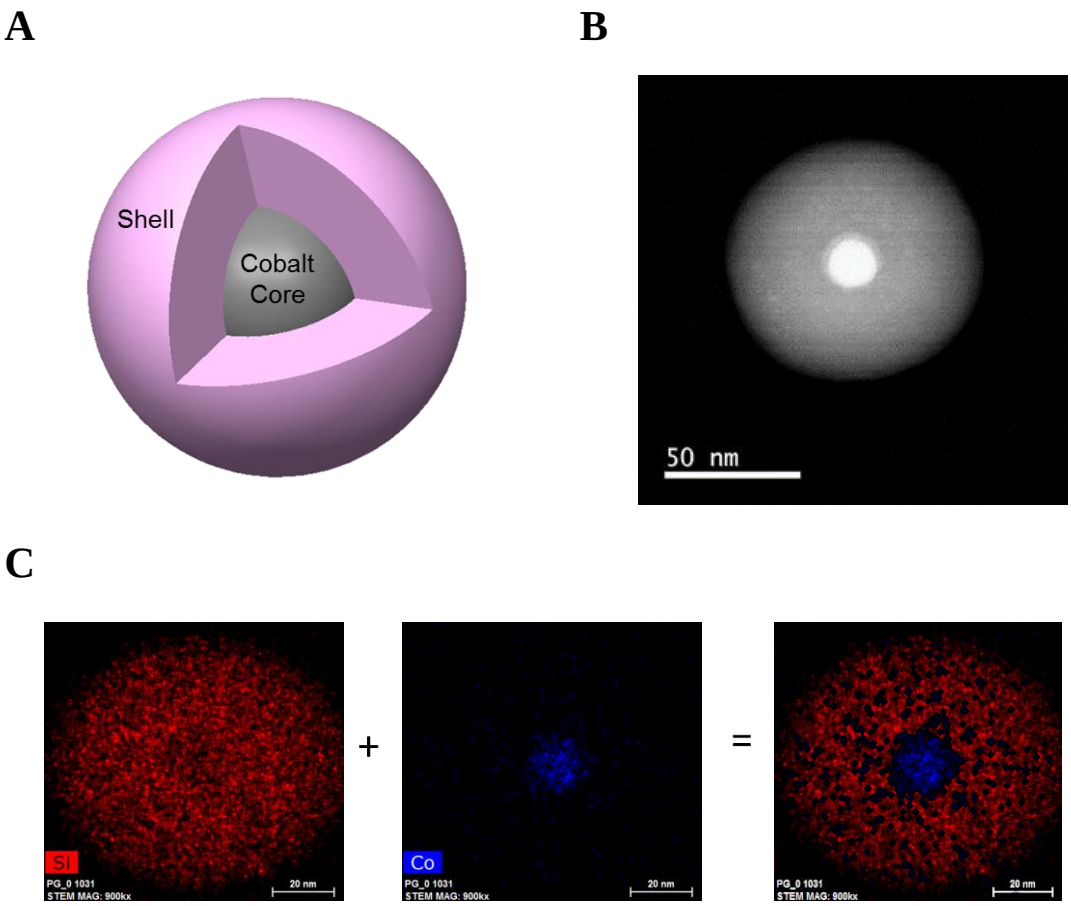

Figure 6. An illustration of a magnetic colloidal particle where the magnetic material is cobalt that is surrounded by silica (A). TEM image of a magnetic silica particle with a cobalt inclusion (B). EDX was used to map the silica shell and cobalt inclusion (C).

There are seemingly endless possibilities for the uses of silica particles in many disciplines of science and technology. The field started by creating stable suspensions of silica particles. Moved toward controlling the size and growth of the particles in solution and then progressed to changing the surface functional groups to alter particle interactions and allow for further surface chemistry to be performed. From there stemmed this interest in more complex external and internal structure and morphology of the silica. Recently, research has focused on attaching various polymers and biological molecules to the silica

particles. For this work, the main material used is a core-shell composite particle, consisting of a silica core particle that is coated with a polypeptide shell.

1.2 Polypeptides

1.2.1 General Background of Polypeptides

Polymers can be referred to as macromolecules and are molecules that are made up of many parts, via assembly of repeating units of many small molecules called monomers.[45] In the case of polypeptides, the monomers are amino acids that are linked together through peptide (amide) bonds.[46] They are naturally occurring biological molecules that form complex structures such as proteins. These structures play important roles in biological functions, which make polypeptide synthesis and application a major area of focus for scientists.

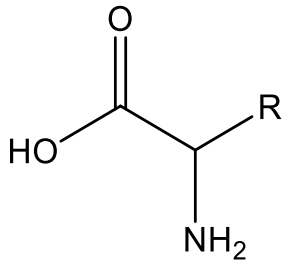

Figure 7. A generalized amino acid structure. The R group refers to the side chain unique to each amino acid residue.

Amino acids are biological organic compounds that consist of an amine and carboxylic acid functional group and a side chain.[46] The side chain is specific to each amino acid and there are a total of twenty naturally occurring amino acids. A generalized structure of an amino acid is shown in Figure 7. The amino groups are located on the α-carbon of

the molecule and are therefore called α-amino acids. To form long polypeptide chains, the amino acids are linked covalently through peptide bonds. A condensation reaction can take place between the carboxyl group of one amino acid residue and the α-amino group of a second amino acid residue to form the peptide bond as shown in Figure 8. Once formed the peptide chain has different active groups at its end. The free α-amino group is called the N-terminal and the free carboxyl group is called the C-terminal. These active ends can undergo more reactions in order to form longer peptide chains to create polypeptides.

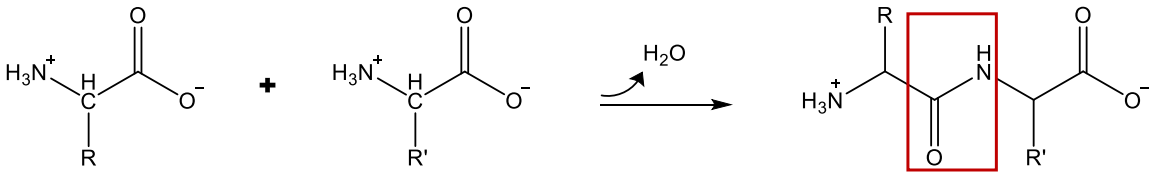

Figure 8. The formation of a peptide bond (red square) through a condensation reaction.

These long polypeptide chains can form proteins, which can take on four different structures: primary, secondary, tertiary, or quaternary.[47] The secondary structure of a protein is controlled and based on the hydrogen bonding between the amine and carboxyl group of the peptide backbone. Three secondary structure configurations most commonly observed are the α-helix, beta sheet, and random coil (Figure 9).

The most common configuration is the α-helix. It uses hydrogen bonding within one polypeptide chain to create a tight helix formation. Hydrogen bonding occurs between each backbone amine group and the backbone carbonyl group that is four residues earlier in the polypeptide chain. The α-helix is a right-handed helix, which means if someone's line of sight were along the helix's axis then the helix would move away from the person when going in a clockwise screwing motion.[48] A right-handed helix consists of 3.6 residues

per turn with a pitch of 5.4 Å. In this formation, the amino acid side chains will project outward and downward from the helix. This allows the amino acid residues to avoid steric interference with each other and the polypeptide backbone.[46, 48]

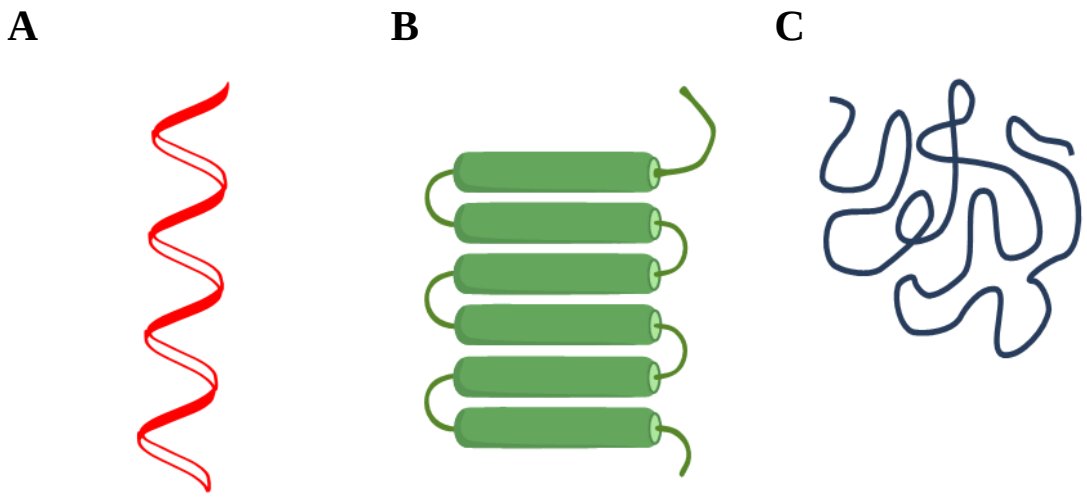

Figure 9. Three common secondary structure configurations: (a) α-helix, (b) beta sheet, (c) random coil.

The beta sheet structure has a configuration that resembles a pleated sheet or folded chain. This structure arises when extended polypeptide chains form hydrogen bonds between neighboring polypeptide chains.[46] A beta sheet can take on either a parallel or an anti-parallel orientation. In a parallel beta sheet formation, all the polypeptide chains run in the same direction; in the anti-parallel formation, the neighboring chains run in opposite directions.[48] In this secondary structure, the amino acid residues project outward to opposite sides of the beta sheet.

The third secondary structure, random coil, is a disordered and rapidly fluctuating polymer chain configuration.[46] Proteins that have been denatured in solution usually assume this conformation. Denaturation of a protein occurs when certain solvents or

temperature changes disrupt hydrogen bonding. The effect of specific types of solvents and/or temperature changes varies from polypeptide to polypeptide. A couple of solvents that have been known to denature polypeptides are trifluoroacetic acid (TFA) and dichloroacetic acid (DCA).[49]

1.2.2 Background and Synthesis of Synthetic Polypeptides

Polypeptides are naturally occurring molecules, but they can also be produced synthetically. Naturally occurring polypeptides usually feature a distinct sequence of amino acids that give rise to its specific complex secondary and tertiary structures in proteins.[46] The appeal of synthetic polypeptides is their simplicity when compared to natural polypeptides. Many synthetic polypeptides are known as homopolypeptides, meaning they are comprised of only one type of amino acid residue. This greatly reduces the complexity of the overall polypeptide chain for further studies. The main polypeptide used in this work is poly(ε-carbobenzyloxy-L-lysine), PCBL. A general structure of PCBL is shown in Figure 10. It is a well-studied polypeptide, less extensively studied than a similar homopolypeptide poly(γ-benzyl-α, L-glutamate), PBLG. They both exhibit similar properties but the working temperature range and solvent systems for PCBL are easier than PBLG. Accordingly, it makes a good choice for the development of new architectures or superstructures such as our hybrid composite of polypeptide tethered to a silica particle.

Among the poly(α-amino acids), PCBL is one of the commonly used synthetic polypeptides, behind the most widely studied PBLG.[49] PCBL has two main secondary conformations it can reside in, the α-helix or random coil conformation. In certain solvents, known as helicogenic solvents, the PCBL will remain in the α-helix conformation. These

solvents are organic solvents such as DMF, chloroform, THF, and pyridine.[49] Fasman, Idelson, and Blout determined that PCBL underwent a sharp conformational transition from its random coil to helical state in a mixed solvent system of DCA and chloroform.[50] Karasz, O'Reilly, and Bair found that in that same mixed solvent system (DCA and chloroform), PCBL could undergo a secondary conformational transition as a function of temperature, from its ordered, α-helical state to its disordered, random coil state.[51] By varying the concentration of DCA in the mixed solvent system, the temperature at which this transition occurs shifts to higher temperatures.[52] Matsuoka *et al*. conducted more conformational transition studies of PCBL and determined that this transition from α-helix to random coil could also take place in a single solvent system of *m*-cresol.[53]

Over the years, many research groups have studied the synthesis, characterization, and inherent properties of poly(α-amino acids).[52, 54-58] This work uses the polypeptides PBLG, PCBL, and PTBY, which share similar synthetic routes with PCBL. The basic structure for these three polypeptides is shown in Figure 10.

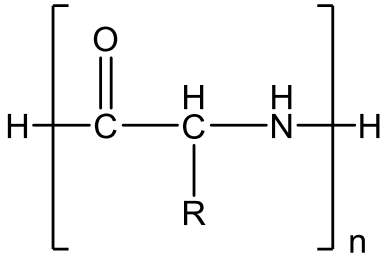

Figure 10. General structure of a poly(α-amino acid). The R group can be either $(CH_2)_2CO_2CH_2C_6H_5$, $(CH_2)_4NHCO_2CH_2C_6H_5$, or $CH_2OCH_2C_6H_4OCH_2C_6H_5$ to obtain PBLG, PCBL, or PTBY respectively.

The most common method for obtaining these synthetic polypeptides is the ring-opening polymerization of the N-carboxyanhydride derivatives of the corresponding α-amino acid (α-amino acid NCA).[49-50, 55] These α-amino acid NCA monomers have to be synthesized from the amino acid precursor molecule. The first synthesis of an α-amino acid NCA compound was by Leuchs in 1906 where he reacted thionyl chloride with N-carbomethoxyl-C-phenol-amino-acetic acid.[59] In 1922, Fuchs developed a different method for preparing the α-amino acid NCA molecule. He performed a ring closing reaction between phosgene, the reaction initiator, and the amino acid backbone.[60] This method and some modified versions are widely used for polypeptide synthesis.[9] Disadvantages of the phosgenation of the α-amino acid are the amount of hydrochloric acid (HCl) created as a by-product and the high toxicity of phosgene. The NCA molecule is also moisture-sensitive; thus, removal of the by-products through recrystallization requires an inert atmosphere and anhydrous solvents.[9]

The method for synthesizing and purifying the NCA compound proposed by Poché and Daly in 1988 is the technique used in the Russo group.[61] This procedure involves substituting triphosgene for phosgene because it is slightly safer to handle and the amount required for the ring closing reaction is one third that of phosgene (Figure 11). The α-amino acid NCA synthesis initiated by triphosgene, also found support due to the decrease in the amount of by-products, including HCl and phosgene .[9] Later, Poché *et al.* determined that cold water can be used to purify the α-amino acid NCA from its by-products; this method allows a decrease in number of recrystallizations.[62]

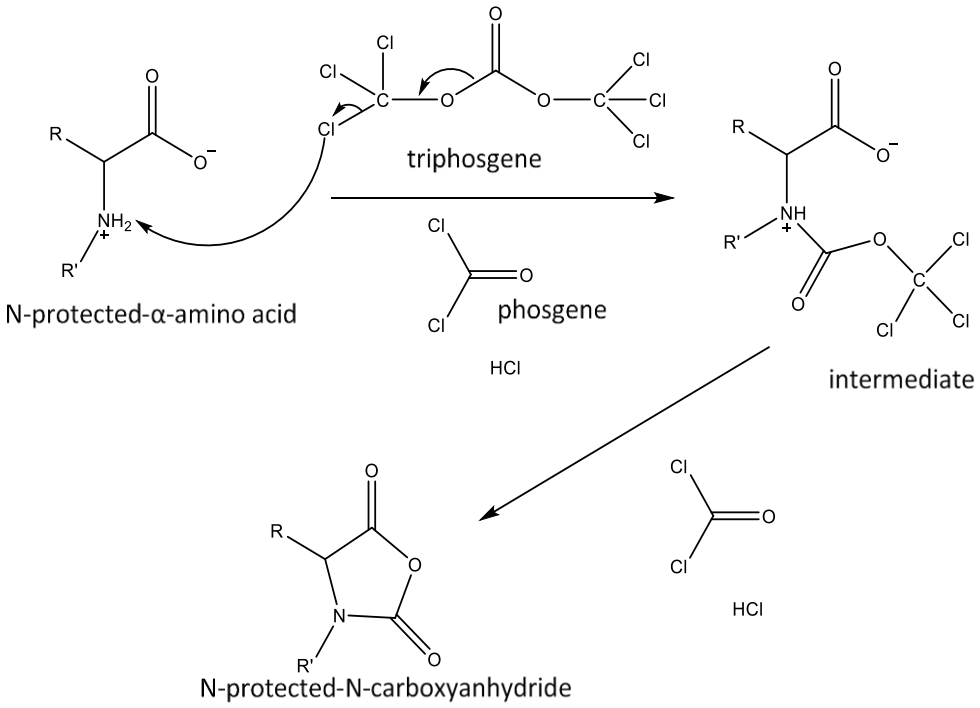

Figure 11. The NCA reaction that is used to create the polypeptide precursors before they are attached to the silica particles.

The need for anhydrous and moisture-free environments makes synthesizing the NCA monomer a tedious task. More recently, researchers have gone back to using phosgene as an initiator for the NCA synthesis. It is argued that phosgene results in a faster reaction of amino acid to NCA and produces a purer NCA compound. Cheng *et al*., from the University of Illinois Urbana-Champaign, show that high molecular weight polypeptides could be synthesized using non-purified NCA.[63] Their reaction involved initiating the NCA ring closure with phosgene and then removing the solvent and phosgene under vacuum. According to their study, the non-purified NCA created higher molecular weight polypeptides with comparable polydispersity to the purified NCA monomer. Regardless of the route taken to achieve the NCA monomer, limiting the amount of initial moisture in the reaction, glassware, and reagents is still needed.

Once the NCA monomer is synthesized the polypeptide can be polymerized via a ring-opening polymerization (ROP). PBLG and PCBL have been synthesized and characterized since the early 1940s. Many types of ring-opening initiators have been studied including amines (primary, secondary, and tertiary) salts of weak acids, and alkoxide ions.[55, 64] Blout *et al*. showed that polypeptides with intermediate molecular weights (50,000 or less) could be synthesized with primary amines but to get very high molecular weights (100,000 or more); a secondary or tertiary amine or a strong base was needed.[65] Upon further testing, Blout determined that a strong base should be the preferred method for yielding very high molecular weight with a relatively narrow molecular weight distribution.[55] For the polypeptides of focus in this work, the most common solvent systems for polymerization are anhydrous THF or 1,4-dioxane. Even with the various initiators and solvents that can be used for polymerization of the polypeptides, high molecular weights with narrow molecular weight distributions are relatively attainable.

1.2.3 Applications of Synthetic Polypeptides

Synthetic poly-α-glutamates have been of interest since the 1950s, with an increase in interest once it was determined that the polypeptides can undergo secondary conformational transitions when external stimuli are applied.[49, 66] Figure 12 illustrated some of the external stimuli that can be used to produce these conformational changes in polypeptides. They have been used as model systems for studying the physical-chemical properties of proteins due to their simplicity and relative ease of creating various molecular weights.[47, 66-67] These synthetic polypeptides create a bridge between natural and synthetic polymeric materials by combining a naturally occurring building block (i.e. amino acids)

with the flexibility and control of synthetic techniques to achieve specific properties in biomaterials.[68]

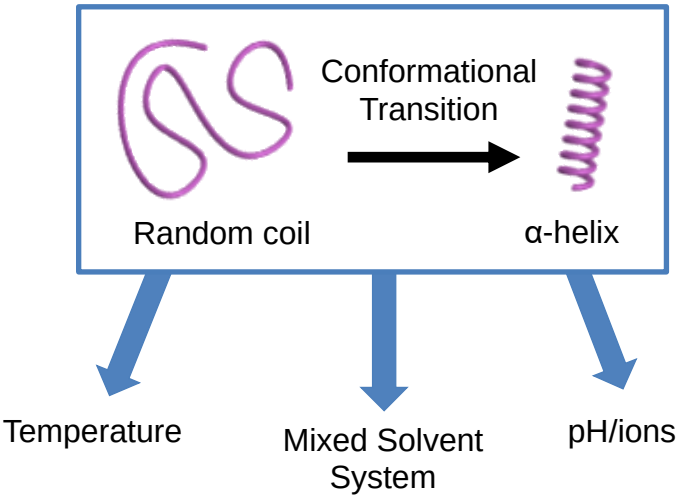

Figure 12. A schematic depicting some of the external stimuli that can induce a conformational transition in synthetic polypeptides.

From early studies of synthetic polypeptides, it was determined that these materials could be used quite readily for biological studies. The initial use of poly-α-glutamates was to help protein chemists elucidate the correlation between structure and function of biological products such as polypeptides and proteins.[69] An alternative approach to using natural polypeptides and proteins was to use synthetic polypeptides. The use of these synthetic polypeptides as a model compound and system aided in understanding and determining the roles of different amino acid residues and sequences in biological properties. Pauling and Corey elucidated the different conformational states of polypeptides with the use of synthetic polypeptides.[70] Furthermore, creation of synthetic poly(amino-acids) aided in understanding protein folding.

Inspiration from nature has pushed science in the direction of developing biological mimics, such as protein mimics, to produce synthetic higher ordered structures and materials for use in biomedical applications.[63] Polypeptides tend to be some of the most widely studied materials for this mimicry because of their peptide backbone, biocompatibility, and biodegradation.[63] When compared with other common polymeric materials, polypeptides can produce highly diverse chemistries on their sidechains, which can incorporate charged, stimuli-responsive, or highly reactive moieties into the polypeptide materials. Formation of secondary structures inherent to polypeptides enables their use and study in conformational-specific assemblies and bioactivity.[68] Rodríguez-Hernández and Lecommandoux created self-assembling polymeric vesicles using polypeptide materials comprised of glutamic acid and lysine. At different biological pH, the two polypeptides will have differing charges on their side chains, allowing them to self-assembly into a vesicle structures for use in drug delivery applications.[71] A successful example of polypeptides being used in biomedical applications is Glatiramer Acetate. It is a commercially available drug used to treat multiple sclerosis made up of glutamic acid, lysine, tyrosine, and alanine units randomly polymerized via NCAs.[72]

Because ROP of the polypeptides can be initiated with a variety of different chemicals, these polypeptides can easily be polymerized from substrate surfaces, which broaden their applicability for various studies.[73-75] Interest in tethering polypeptides and other biological molecules to surfaces and particles started in the 1990's. Some of the first studies with polypeptide attached to a surface were conducted by Worley, Linton, and Samulski.[76] They self-assembled disulfide-capped PBLG on a gold substrate and determine how application of different voltages altered the assembly of the polypeptide on the gold.

Wang and Cheng attached PCBL to a flat surface and then deprotected the side chain to create poly(L-lysine) which is soluble in aqueous conditions.[73] They illustrated that the polypeptide can still undergo its secondary conformational transition under external stimuli when tethered to a flat surface placed in an aqueous solution. More recently, studies have migrated toward tethering and polymerizing synthetic polypeptides from the surface of colloidal particles to produce a hybridized material with control over specific properties and their subsequent enhancement.[44, 75]

1.3 Polypeptide Composite Particles

1.3.1 Background of Core-shell Particles

Core-shell materials are a broad class of materials that have a range of applications in the literature due to their ability to have superior synergistic properties that are not individually associated with the core and shell material.[77] In general, a core-shell material consists of at least two different components, one being incased or surrounded by the other. Figure 13 shows two general examples of core-shell materials. One of the first investigations of a core-shell material was in 1961 when Hughes and Brown studied the physical properties and morphology of core-shell polymers.[78] Combining two components allows for the addition of smart or responsive properties to these materials which find many uses in biomedicine, specifically as drug delivery systems and materials.[77]

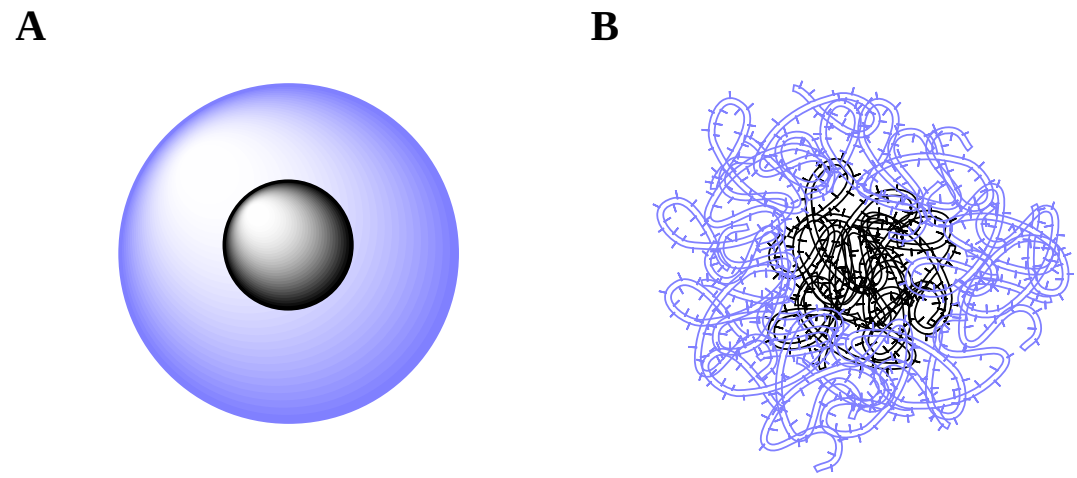

Figure 13. An illustration of two types of core-shell particles, the core material (black) is surrounded by a different shell material (purple). The examples show a colloidal core-shell particle (A) and a polymeric core-shell particle (B).

The use of an organic-inorganic nanocomposite material has grown in the core-shell field over the past few decades. These types of materials have an inorganic core particle that is surrounded by an organic shell of polymers or biological materials.[77]. Some literature refers to these particles as organic-inorganic composite while other literature refers to them as hairy particles. Interest in these types of materials stems from studies pertaining to soft condensed matter physics.[79] The ultimate goal is to design materials with properties tuned for specific applications. The well-studied classes of materials are "soft" linear flexible polymers and "hard" colloidal spheres. These are two extreme spatial organizational cases, however, when it comes to these types of materials.[79] By combining materials from the soft regime and hard regime, a hybrid material can be produced and the properties can be altered to obtain a desired overall hardness/softness. These hairy particle structures, as shown in Figure 14, also bear a resemblance to structures found in many biological organisms. In biology and nature, these structures aid in sensing, antifouling, preventing surface wetting, and dynamic attachment.[80-81]

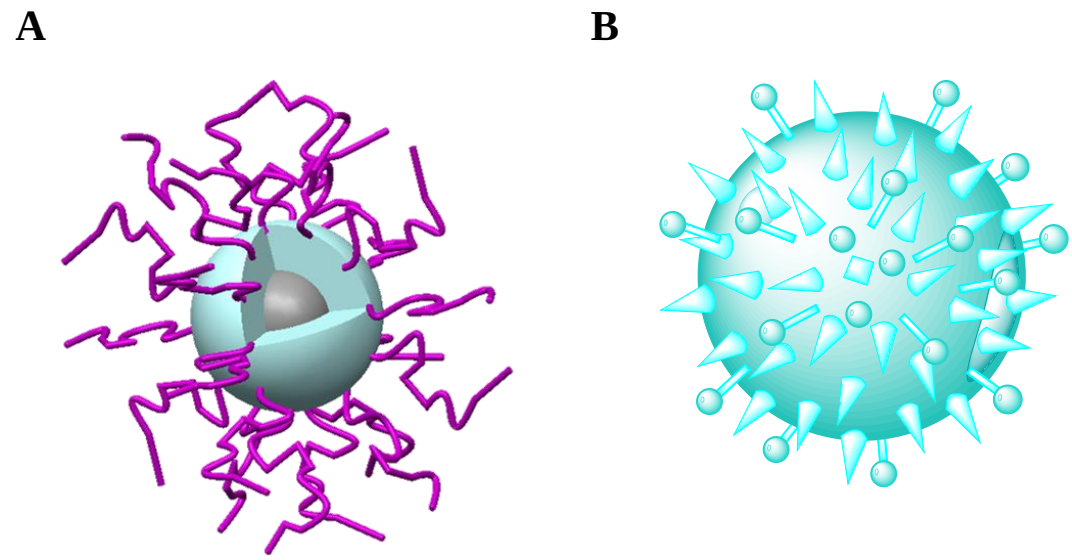

Figure 14. A general illustration of a hairy particle consisting of an inorganic core and an organic polymeric shell (A). Different applications can require multiple polymers or materials to be attached to the core particle (illustrated by the two shapes attached to the core particle in B).

Researchers have synthesized a variety of hairy particles, using SiO_2, magnetite, poly(N-isopropylacrylamide) (P-NIPAM), etc. as the core material and polymerized various organic polymers such as PMMA, P-NIPAM, polystyrene, etc. to form the shell.[77, 81] Wan *et al.* produced magnetic hair particles that are able to trap and uptake pollen in polluted water samples.[80] They removed the pollutant from the water by separating the particle via an applied magnetic field. Lv *et al.* created bioinspired hairy particles that produced a robust superhydrophobic coating that enhanced self-cleaning and anticorrosive properties of the particles by increasing water-repulsion.[82] Various biomedical applications such as drug delivery, imaging, and tumor/cell targeting use hairy particle materials. Zhang, Kholer, and Zhang modified the surfaces of superparamagnetic nanoparticles with polyethylene glycol (PEG) and folic acid to help improve cell targeting and uptake.[41] The most common reason for producing hybrid polymer-inorganic composite particles is to

achieve improved mechanical, optical, mechanical, and thermal properties.[81] Membranes and separation techniques, smart coatings, catalysts, drug carriers, tissue engineering, and sensors are just a few of the applications that use organic-inorganic nanocomposite materials.[39, 41, 81, 83]

This work focuses on using a responsive organic-inorganic nanocomposite material referred to as polypeptide composite particles. The material consists of an inorganic silica colloidal core particle and an organic polypeptide shell. The hybridization of a silica particle and synthetic polypeptides are useful for responsive material and biological applications. The Russo group started working with PCPs in the 1990s when they synthesized PBLG-coated silica particles. Since then, the group has successfully synthesized more PBLG-PCPs along with PCBL-PCPs, PSLG-PCPs, and PTYR-PCPs. Interest in these particles stems from their simplicity when compared to other biological materials and their increased complexity versus normal macromolecular particles. The homopolypeptide shells add a responsive nature that cannot be obtained from a silica core alone but makes for a less complex model system when conducting bio-oriented research and provides a more in-depth understanding of inter- and intra-particle interactions.

1.3.2 Synthesis of PCPs

PCPs can be synthesized by a variety of techniques, the three main categories being *grafting to, grafting from,* and *grafting through*.[9] The two techniques that are used most commonly in the Russo group are the *grafting to* and *grafting from* techniques. These syntheses allow for the addition of the polypeptide shell onto the silica core particle. Each technique requires the surface of the silica to be functionalized differently.[9] Both

techniques require a ROP of the corresponding polypeptide precursor, the NCA monomer, using a primary amine either in solution or attached to a particle surface.

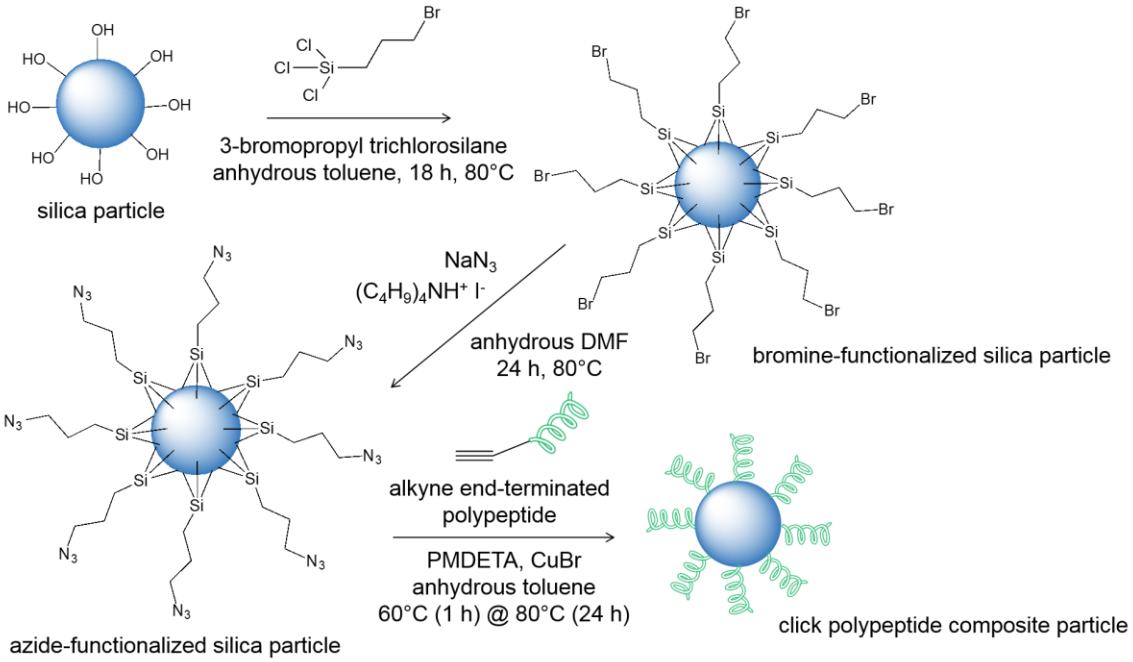

Figure 15. A schematic of the *grafting to* method for making polypeptide shell on the silica particles.

The *grafting to* method uses the selectivity of click chemistry to bind the silica and polypeptide together by matching specific functional groups, as shown in Figure 15. This technique requires the polypeptide to be polymerized in solution prior to that attachment of the chains to the core particle. Commonly, an alkyne terminated primary amine is used to initiate the ROP of the polypeptide. Once the polypeptide polymerization is complete, the polypeptide can be attached to the silica particle, which has been functionalized with an azide functional group. These two groups, the alkyne and azide, will undergo a Huisgen 1,3-dipolar cycloaddition that will attach the polypeptide chains to the silica core particle.[84] Speed and chemoselectivity are two important features of the *grafting to* method, but the

main advantage is that this method produces a uniform shell composed of a well-characterized polypeptide. A disadvantage of the *grafting to* method is that it requires many steps.[9]

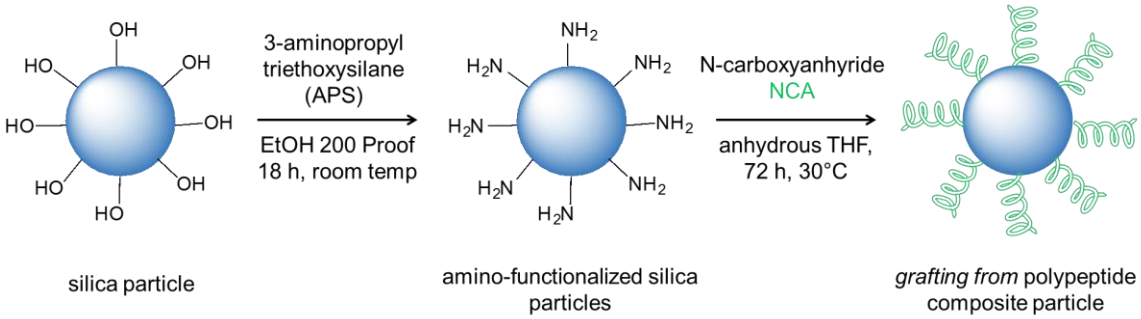

Figure 16. A schematic of the *grafting from* method used to make silica polypeptide composite particles.

The *grafting from* method uses amine-functionalized silica cores for the ROP of the polypeptide. The amine groups on the silica exert a nucleophilic attack on the NCA ring, causing it to open.[9, 19, 85-86] Propagation of the polypeptide shell is continued by the amine end functional group on the nascent polypeptide chain attacking and ring opening another NCA molecule in solution. Figure 16 illustrates a simplified version of the *grafting from* approach. An advantage of this method is that there are fewer and less synthetically taxing steps to create the final composite particles when compared to the *grafting to* method. In addition, the polypeptide loading on the silica particles can be much higher than the *grafting to* method. Some disadvantages of the *grafting from* approach are reduced control over the polypeptide grafting density and difficulty assessing the molecular weight of the polypeptide shell.[9]. The *grafting from* method was the primary technique used for the work presented in this document.

1.3.3 Applications of PCPs

Polypeptide composite particles are a unique set of materials that, by combining an inorganic colloidal core particle and an organic polypeptide shell, have found many applications in the physical, biological, and material disciplines. Because of the amount of alteration and tailoring one can do with these hybrid materials, they can find uses in applications such as artificial muscle fibers, model systems for virus-like particles, and pollutant removal.[26, 87-89] Adding multiple pathways for responsiveness or particle manipulation also increases the potential use of these particles in separation processes.[90] In polymer physics, having control over the softness or hardness of the shell material allows these PCPs to be used as model systems for phase transition studies and particle-particle interactions.[79, 87, 91]

A large area of research for PCPs is the biological and biomedical fields. The Sen Gupta group uses polypeptide-coated silica particles to make macroporous structures for potential use in tissue engineering applications.[92] The same group is also interested in grafting other polypeptide chains onto the mesoporous silica particles to be used for DNA delivery and controlled drug release.[26] Thornton and Heise have used silica particles coated with a polypeptide shell for enzyme-mediated release of macromolecules.[27] Borase, Iancono, Ali, *et al*. used poly(glutamic acid) coated silica particles to selectively release dye from the particles due to a change in pH illustrating the use of these hybrid materials as drug or payload delivery materials.[93] Similarly, Yu, Gentle, and Lu used coated mesoporous silica particles with polypeptides that could release enzymes from the biocompatible microcapsules when external stimuli, such as change in pH or salt concentration, were applied to the system.[25]

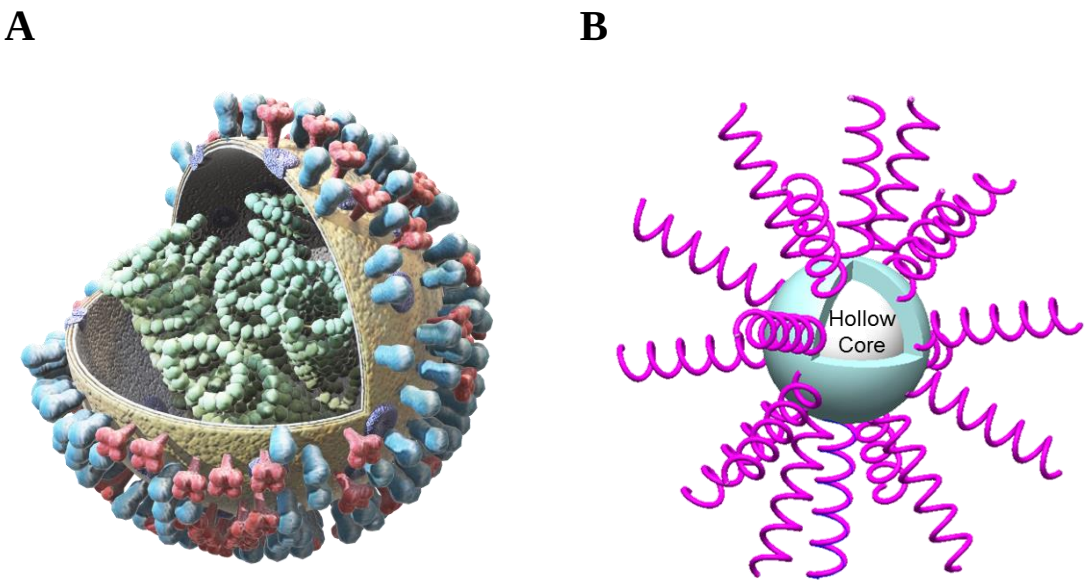

Figure 17. A general virus-like structure, illustrating the proteins that make up its corona and the RNA material encased in the virus vesicle (A). The structure in A is compared to the general schematic of a hollowed-out polypeptide composite particle, showing the similarities between these synthetic vesicles and virus particles (B). Virus particle (A) was obtained from Microsoft Creative Commons.

Our group mainly focuses on the fundamental studies of these particles. With these complex PCPs, previous group members have used different polypeptide chains (PCBL, PSLG, PBLG), varied the grafting density of the polypeptide shells, and created colloidal crystals consisting of many domains.[19, 84-85, 94-95] This work focuses primarily on the polypeptide PCBL, both tethered and untethered from silica surfaces. Many of the projects center on fundamental studies of these polypeptides and particles as model systems for physical and biological applications.

The responsive nature of polypeptides has been known and studied for many years and for that reason it can be used as a model system. The simplicity of the system stems from the chain consisting of a single amino acid repeat unit. This makes the transition easier to probe when compared to naturally occurring polypeptides that consist of many different

amino acid residues, in various different sequences. Having this added complexity to the polypeptide chain makes it harder to discern the underlying physical properties and interactions between neighboring polypeptide chains, and between the polypeptide and other compounds in solution. Working with a polypeptide that undergoes a transition in a single organic solvent with a change in temperature, most complexities are removed and allows the probing of specific interactions such as van der Waals forces, hydrophobic interactions, and hydrogen bonding in the polypeptide backbone. Compared to working in aqueous solvents which typically use salts and different pH solutions to induce a conformational transition, organic solvents alleviate additional outside forces that might interact with the polypeptide chain. By limiting the number of interfering variables (such as counter ions, competing species, etc.) that need to be taken into account, less approximations have to be made resulting in a more direct probing of the polypeptide transition.

The addition of the polypeptide to the silica particle surface resulting in a polypeptide composite particle creates an interesting model system for studying particle-particle interactions for both biological and physical studies. The structure and responsive nature of the composite particles resemble interesting biological systems such as virus particles, influenza virus being one of the most commonly studied. Figure 17A shows a general schematic of a virus particle, consisting of a spherical core structure, housing its genetic material, surrounded by a protein corona. The protein corona undergoes a similar "popping open" mechanism to the polypeptide particles, allowing these materials to be used as simple model systems for mimicking virus particles. Silica core size, shape, and crosslinking density is easily controlled, which aids in producing a large size range of

particles. Control over the size of the core particles allows more variety in the techniques that can be used to study and characterize these particles. Because the size ranges from ~100 nm-10 μm, both microscope and macroscopic techniques can be used. Altering the size of the core particles also aids in manipulation of the composite particles. Smaller particles are harder to control and manipulate in experimental set up whereas the larger particles provide more ease. Combining the homopolypeptide with the easily synthesized silica particle provides one of the simplest composite systems to study.

Studying the physical characteristics of the polypeptides, both attached to surfaces and free in solution, allow for a better understanding of their interactions with their surroundings for potential use as drug delivery vesicles, chiral separation substrates, and responsive materials. Their overall structure and responsiveness of polypeptides to external stimuli resemble many important biological molecules such as viruses including influenza and other coronaviruses. These properties make the polypeptide-coated silica particles a useful and simplistic model system to aid in understanding particle-particle and particle-environment interactions.

CHAPTER 2. ULTRASONIC DEGRADATION OF THE POLYPEPTIDE POLY(CARBOBENZYLOXY-L-LYSINE)

2.1 Introduction

Ultrasonic degradation of polymers and macromolecules has been used to help decipher degradation mechanisms and flexibility levels of polymers.[96-97] It provides a way to study the degradation of different polymers and macromolecules in elongational flows.[98] In different industries, some applications and processing methods subject polymeric materials to various types of stresses. Often, these stresses are elongational in nature. Sometimes this ultrasonic degradation is useful because it creates a reduction in intrinsic viscosity, which can lead to more stable products such as slurries.[99] On the other hand, these elongational stresses can cause degradation of the material in way that alters the physical properties of the polymers.[98, 100-101] When determining the types of polymeric materials to use to create a specific product, understanding the way they can mechanically degrade from various processing techniques will help decipher the best materials to use in production. Using ultrasonication to investigate the effects of elongational stresses on polymers is ideal because it is relatively easy to conduct these experiments. The types of stresses that are caused by the cavitation bubbles collapsing are shown to be experimentally similar to stresses encountered during processing and end-use applications.[98, 101]

Studies on the ultrasonic degradation of polymeric materials has been explored for recycling and potential upcycling of polymers.[102-103] Ultrasonication has been a useful method for the depolymerization of macromolecules because it reduces the molecular

weight of the polymer. Grönroos *et al.* used ultrasonic energy to study the degradation of polyvinyl alcohol.[104] The recycling of polyurethane foams focuses on a variety of degradation techniques, one main technique being ultrasonic degradation of the polymer.[102] The use of plastics and the amount of plastic waste has increased over the last 20 years, bringing with it a need to develop ways to reuse or upcycle these materials. Due to its ability to depolymerize and uncrosslink polymers, ultrasonication degradation is being considered as a potential technique for polymeric recycling.[105]

Biologically compatible materials and polymers have gained interest for applications such as drug delivery and the creation of materials for biological imaging [63, 67] Sleiman *et al.* are using DNA to create nanostructures, cages, and assembled materials for use at the biological interface.[106-109] In the medical field, ultrasonics are predominately used for sterilization purposes due to its ability to breakdown microbes and biological molecules. More recently, ultrasonic degradation has migrated towards biologically relevant materials and molecules such as polypeptides and DNA.[110-111]

Striegel and Ostlund looked at ultrasonic degradation of poly(benzyl-L-glutamate), PBLG, a similar polypeptide to PCBL.[96] They concluded that PBLG degrades as sonication time is increased but even with increased degradation the polypeptide retains its helical structure. Price and Smith studied the ultrasonic degradation of polystyrene by varying the solution temperature, polymer molecular weight, ultrasonic energy, and the amount of dissolved gases in the samples.[99] Their findings illustrated a dependence of molecular weight on the degradation of the polymer chains. Based on the previous literature, different molecular weights of PCBL and temperature conditions were tested to determine their effect on the degradation of the polypeptide in conjunction with increased chain flexibility.

Another interest was determining whether increasing the concentration of PCBL and thus limiting its mobility in solution, would protect the polypeptide from degradation. It has been shown that cavitation results in scission of linear polymers until it reaches a limiting molar mass in which degradation is no longer possible. Because ultrasonication is a means of processing materials in industry and is also used in some medical technologies and devices, it is important to understand how these stresses degrade materials which can lead to their change in physical properties.[96, 98-101]

Ultrasonic degradation of polypeptides is not well studied in the literature. Conventional polymers such as polystyrene are used in these studies despite polypeptides having a long length and the ability to stabilize multiple secondary structures due to hydrogen bonding. PCBL differs from PBLG in the rigidity of its helical from and its predisposition to branching.[50, 65] Increased flexibility and chain mobility coupled with having a highly monodisperse polymer that is potentially highly branched creates new avenues to explore in polypeptide degradation. This project focuses on determining whether an increase in chain flexibility alters the degradation of the polypeptide chains. Based on the previous literature, different molecular weights of PCBL and temperature conditions were tested to determine their effect on the degradation of the polypeptide in conjunction with increased chain flexibility. Another interest was determining whether increasing the concentration of PCBL and thus limiting its mobility in solution, would protect the polypeptide from degradation. Ultrasonic degradation of polypeptides will help to understand how the degradation of the polypeptide chains alters their inherent physical properties.

2.2 Materials

Carbobenzyloxy-L-lysine (CBL), anhydrous hexane, anhydrous tetrahydrofuran (THF), anhydrous dioxane, sodium carbonate ($NaHCO_3$, anhydrous powder), triphosgene, magnesium sulfate ($MgSO_4$), N,N-dimethylformamide (DMF, ACS reagent grade) and sodium methoxide solution (ACS reagent, 0.5 M CH3ONa in methanol) were purchased from Sigma-Aldrich and used as received. Anhydrous ethyl acetate was purchased from VWR. Ethanol (200 proof) was obtained from Koptec. Water (18.1 MΩ · cm) was withdrawn from a Millipore Synergy UV-R instrument with a BioPak polisher.

2.3 Methods

2.3.1 Synthesis of N-carboxyanhydride (NCA) monomer

The ring-closing of the α-amino acid precursor was conducted similarly to the procedure outlined by Poché and Daly.[61] In a medium glove bag (38 in × 51.5 in, deflated dimensions) under a nitrogen atmosphere, 160 mL of anhydrous ethyl acetate and ~5.12 g of amino acid (dried at least 8 hours in vacuo) were added to a 500 mL three-neck round bottom flask. A stir bar was placed into the round bottom flask and the flask was capped with three rubber septa. The flask was removed from the glove bag, connected to a condenser capped with a rubber septum, and placed into an aluminum bead bath that was heated. Argon gas was bubbled through the reaction slurry to ensure an inert atmosphere and the mixture was brought to reflux. In a small glove bag under a nitrogen atmosphere, ~2.52 g of triphosgene ([M]:[I] of ~3:1 with a slight excess added) was weighed out into an oven-dried scintillation vial. The triphosgene was quickly added to the refluxing mixture and the reaction was allowed to proceed until the solution became clear. Once the solution

cleared, the reaction solution was cooled and placed into a -20 °C freezer to rest overnight. Removal of unreacted amino acid precursor and side products was performed by washing the NCA according the procedure developed by Poché et.al[62]. The NCA solution was placed into a 500 mL separatory funnel with 100 mL of icy water, swirled to mix, and the organic phase of interest was retained. A 0.5% solution of $NaHCO_3$, 100 mL, was added to the separatory funnel, swirled to mix, and the organic phase of interest was decanted into a clean 250 mL round bottom flask. This vessel was then placed into the medium glove bag under an inert atmosphere where $MgSO_4$ was added quickly until no more clumping occurred in the flask, indicating that all water was removed from the NCA solution. The clear NCA solution was filtered by suction through Whatman 90 mm filter paper in a clean, dry vacuum flask to remove the $MgSO_4$. The filtrate was placed into a new, clean, dry 250 mL round bottom flask and the volume was reduced to 1/3 using a rotatory evaporator. Inside a medium glove bag, under a nitrogen atmosphere, approximately 100 mL of cold anhydrous hexane was poured slowly into the NCA solution. White crystals of NCA started to form and the flask was capped and placed into the freezer to allow precipitation to occur. The precipitated NCA was collected on Whatman 90 mm filter paper using vacuum filtration to pull through the liquid and dry the precipitate. This suction dried NCA was placed into a new clean, dry 250 mL round bottom flask and dissolved in 15 mL of dry THF. Cold anhydrous hexane was poured slowly into the flask while it was being swirled until white crystals began to form. The flask was capped and placed inside the freezer overnight for crystallization to complete.

2.3.2 Synthesis of Poly(ε-carbobenzyloxy-L-lysine)

Inside a nitrogen-filled glove bag, a magnetic stir bar and ~2.31 g of CBL-NCA were added to a 100 mL flame-dried round bottom flask. Anhydrous THF, ~51 mL, was added to the flask and the flask was capped with a rubber septum. The flask was placed into an aluminum bead bath and allowed to stir. A volume totaling 0.2 mL of sodium methoxide solution was subsequently injected into the stirring solution. In order to release CO_2 gas produced during the reaction, a bubbler containing silicon oil was connected to the flask via tubing with a needle at the end. The reaction was heated to 35 °C and stirred until bubbles stopped forming in the oil in the connected bubbler (usually 48 hours). A rotatory evaporator was used to reduce the reaction volume to 1/3 to obtain a viscous solution that was then slowly poured into a beaker with water, causing the polypeptide to precipitate out of solution. The polypeptide was suction filtered using a Whatman 90 mm filter paper and allowed to dry completely.

2.3.3 Sonication of PCBL

Each polypeptide sonication sample was made in a 20 mL PTFE-capped vial to create a 15 mL solution with a concentration of 2 mg/mL (unless otherwise stated). The samples were suspended the tank of a Branson MH Series ultrasonic bath (Model 2800, M2800H) with a mechanical timer and heater. Suspension was achieved using small squares of foam, which were cut so the vials could be inserted into the foam and then placed into the sonicator bath tank. Aliquots of the PCBL samples were taken at the same time points and placed into a 4 mL PTFE-capped vial for further characterization.

The temperature of the system was measured using a Vernier LabQuest Mini outfitted with a stainless-steel temperature probe. LoggerLite Software (provided with the Vernier LabQuest Mini) was used to record the temperature of the bath liquid for the entire sonication experiment. To stabilize the temperature of the water in the bath sonicator, a water circulator bath was connected to a copper tube (bent into a coil) with Tygon tubing and the circulating bath temperature was sent to 16 ℃.

2.3.4 Gel Permeation Chromatography (GPC)

Gel permeation chromatography with multi-angle light scattering, GPC-MALS, was used to measure the molecular weight of the synthesized PCBL. The instrument includes a Wyatt Dawn EOS multi-angle-light scattering detector connected to a Tosoh EcoSEC HLC-8320GPC. A TSK SuperH-H (4.6mm ID × 3.5 cm L) guard column was placed before two TSKgel SuperHM-H (mixed-bed) analytical columns (6.0 mm ID × 15 cm L) for the sample flow. A TSKgel SuperH-RC column (6.0 mm ID × 15 cm L) was used as the reference column for the dual flow type refractive index detector. A Tosoh EcoSEC HLC-8320GPC control module was used to operate the GPC, and data acquisition and analysis were controlled using Wyatt Astra 5.0 software. The mobile phase was N,N-Dimethylformamide with 0.1M LiBr flowing at 0.35 mL/min, and the instrument temperature was set to 60 ℃. Polymer samples of concentration 2–3 mg/mL were dissolved overnight (at least 12 h) prior to measurements to ensure homogeneity. Solutions were then filtered through Whatman PTFE 0.45 μm syringe filters into Agilent 2 mL GPC vials. In order to obtain the absolute molecular weight of the polypeptide a dn/dc value of 0.123 mL/g was used for the data analysis. To establish reproducibility, multiple injections (20 μL) were performed for each sample measured by GPC/MALS.

2.4 Results and Discussion

2.4.1 Characterization of Synthesized PCBL and Effect of Molecular Weight on its Ultrasonic Degradation

The four synthesized PCBL samples were characterized using GPC-MALS to determine molecular weight and polydispersity. Figure 18 shows the GPC chromatograms, overlayed with the molar mass trace for each of the polypeptide samples before sonication. The molecular weights of the polypeptide samples were determined to be 250 kDa, 91 kDa, 81 kDa, and 55 kDa with dispersity $Đ$ = 1.18, 1.09, 1.11, and 1.15 respectively. These samples were used for the different sonication experiments conducted with the main sample being PCBL-250.

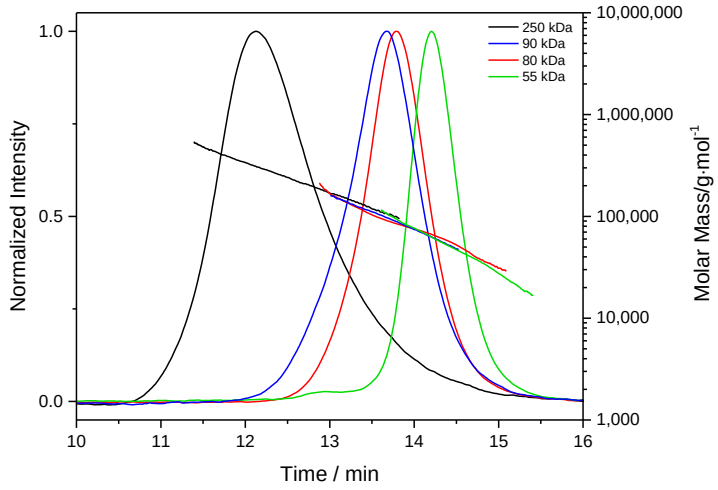

Figure 18. GPC-MALS data for the four PCBL polypeptide samples used in the ultrasonic degradation studies. The molecular weights of the polypeptide samples were 250 kDa, 90 kDa, 80kDa and 55 kDa with dispersity factors of 1.07, 1.23, and 1.04 respectively

Sonication experiments were performed on all four of the PCBL samples, summarized in Table 1 and shown in Figure 18, to determine if molecular weight has an effect on the degradation of the polypeptide. The experiments were conducted on different days due to the size of the bath sonicator and the aliquot time points. Table 2 shows a summary of the results for the four molecular weights. Samples PCBL-250, PCBL-90, and PCBL-80 show differing degrees of degradation over a period of time whereas PCBL-55 does not seem to show any signs of degradation over a period of six hours. The two main parameters taken into account when determining degradation of the polypeptide chains were molecular weight and polydispersity (shown using dispersity factor).

Table 1. Summary of Characterization Results for PCBL Polypeptide Samples

Sample Name	Molecular Weight/M_w	Polydispersity/ Đ	Notebook Code
PCBL-250	246,600 Da	1.18	AB.4.177A-redispersed
PCBL-90	90,600 Da	1.09	Sonication-PCBL
PCBL-80	81,000 Da	1.11	AB.4.164A
PCBL-55	54,500 Da	1.15	AB.4.177C

The molecular weight and polydispersity were calculated for each sonication time point to determine the ultrasonic degradation of the samples. PCBL-55 does not seem to undergo any degradation as indicated by the consistent molecular weight and dispersity factor over a six-hour sonication experiment. The samples PCBL-90 and PCBL-80 show some amount of degradation. They both show a decrease in molecular weight as the sonication time was increased. Additionally, the dispersity factor for the two samples increases slightly with increasing sonication time indicating a decrease in monodispersity, which can be related to the breaking apart of the polypeptide from the applied ultrasonic energy.

Table 2. Ultrasonic Degradation Results for the PCBL Polypeptide Samples with Varying Molecular Weights

Sample Name	Sonication Time/hrs	Molecular Weight/M_w	Polydispersity/ Đ
PCBL-250	0	246.60	1.18
	0.5	253.97	1.16
	1	223.90	1.17
	2	196.97	1.19
	3	190.63	1.18
	4	164.00	1.18
	5	146.37	1.20
	6	141.23	1.19
	7	133.17	1.17
	8	135.45	1.15
	9	114.10	1.17
	10	111.77	1.18
	Overnight (24 hrs)	83.60	1.12
PCBL-90	0	90.67	1.09
	0.5	88.77	1.10
	1	90.30	1.10
	2	86.83	1.11
	3	82.90	1.10
	4	81.37	1.11
	5	79.23	1.12
	6	76.37	1.11
	7	75.60	1.12
	8	75.07	1.11
	9	72.20	1.13
	10	71.17	1.13
PCBL-80	0	81.07	1.11
	0.5	81.10	1.10
	1	76.20	1.11
	2	73.93	1.10
	3	66.93	1.11
	4	64.10	1.10
	5	54.17	1.12
	6	52.63	1.12
	Overnight (17 hrs)	52.20	1.12

Table 2 Continued. Ultrasonic Degradation Results for the PCBL Polypeptide Samples with Varying Molecular Weights

Sample Name	Sonication Time/hrs	Molecular Weight/M_w	Polydispersity/ Đ
PCBL-55	0	54.50	1.15
	0.5	55.00	1.13
	1	54.90	1.14
	2	55.07	1.14
	3	55.47	1.14
	4	55.07	1.15
	5	55.63	1.13
	6	55.90	1.11

PCBL-250 was the sample that showed the most degradation of the polypeptide chains. There is a large change in molecular weight as the sonication time is increased. A steady decrease in molecular weight is apparent from the initial time point (0 hours) to the 10-hour time point as shown in Table 2. The molecular weight starts at 245 kDa and decreases to 111 kDa. Unlike in PCBL-90 and 80, PCBL-250 does not show any trend indicating an increase in dispersity factor as a function of sonication time. The sample seems to become more monodisperse after sonication continued overnight for a total of 24 hours of sonication. This could be correlated to the higher molecular weight polypeptide chains degrading and breaking apart to reach a sort of equilibrium chain length.

2.4.2 Temperature Effects on Degradation of PCBL via Sonication

After determining that molecular weight seems to have an effect on the ultrasonic degradation of the polypeptide, temperature was considered as another factor that would alter the polypeptide degradation. Due to the larger degradation of the PCBL-250 sample, the temperature studies (at a low temperature and high temperature) were conducted using that sample. The sonicator bath temperature was controlled in the low temperature study

by having cold water circulate through the system to reduce heating of the sonicator bath water over time. The high temperature study did not use the water-circulating bath to control the sonicator bath temperature but instead allowed the water in the bath reservoir to heat due to the ultrasonic energy being applied during the experiment.

Table 3. Results for the Ultrasonic Degradation of a 250 kDa PCBL Polypeptide Sample at Low and Controlled Water Bath Temperature.

Sample Name	Sonication Time/hrs	Molecular Weight/M_w	Polydispersity/ Đ
PCBL-250 Low Temperature	0	246.60	1.18
	0.5	253.97	1.16
	1	223.90	1.17
	2	196.97	1.19
	3	190.63	1.18
	4	164.00	1.18
	5	146.37	1.20
	6	141.23	1.19
	7	133.17	1.17
	8	135.45	1.15
	9	114.10	1.17
	10	111.77	1.18
	Overnight (24 hrs)	83.60	1.12

The results obtained from the low temperature sonication experiment are outlined in Table 3. Sonication time was altered from 0 hours to overnight, which was approximately 24 hours. Molecular weight and polydispersity of each time point aliquot were calculated from the GPC data. There is a clear trend for the molecular weight of the polypeptide as a function of sonication time, the molecular weight decreases with increasing sonication time. For the dispersity factor of the aliquots, there does not seem to be an apparent trend. As sonication time is increased, the dispersity factor seems to fluctuate between 1.18–1.20 until you reach the overnight time point. The last row in Table

3 shows the data for the overnight sonication time point, which shows a drop in the dispersity factor from 1.18 at 10 hours to 1.12.

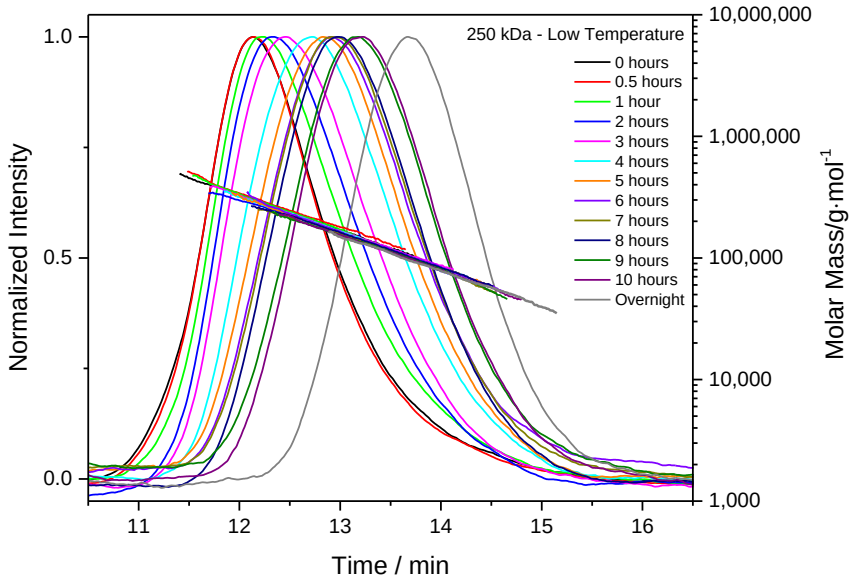

Figure 19. GPC-MALS data for PCBL-250 polypeptide sample used in the ultrasonic degradation studies at low temperature. The molecular weight decreased consistently from 250 kDa to 84 kDa as the sonication time increased from 0 hours (black line) to overnight (~24 hours, gray line).

Figure 19 shows the GPC-MALS traces for each of the time point aliquots to help illustrate the change in the molecular weight as a function of sonication time. The sonication time is increased from left to right in the figure, indicating a change in molecular weight of the polypeptide chains. The initial time point is shown in black and the last time point, taken ~24 hours later, is shown in grey. The molar mass for each sample is also overlayed on the graph in Figure 19, but it is much easier to visualize the decrease in molecular weight from the chromatogram traces.

Table 4. Results for the Ultrasonic Degradation of a 250 kDa PCBL Polypeptide Sample at Elevated Water Bath Temperature.

Sample Name	Sonication Time/hrs	Molecular Weight/M_w	Polydispersity/ Đ
PCBL-250 High Temperature	0	239.30	1.23
	0.5	231.50	1.20
	1	220.20	1.20
	2	193.17	1.20
	3	176.37	1.21
	4	161.87	1.18
	5	155.33	1.19
	6	138.27	1.17
	7	132.53	1.15
	8	118.40	1.14
	9	100.47	1.14
	10	95.57	1.12
	Overnight (24 hrs)	57.20	1.10

The results obtained from the high temperature sonication experiment are presented in Table 4. For comparison, the sonication time points were the same as in the low temperature experiment, ranging from 0 hours to overnight (~24 hours). Similar to the low temperature experiment, the molecular weight and polydispersity of each time point aliquot were calculated from the GPC data for the high temperature experiment. There is a clear trend for the molecular weight of the polypeptide as a function of sonication time, the molecular weight decreases with increasing sonication time. Unlike in the low temperature data, this data shows an apparent trend in the values calculated for the dispersity factor. As sonication time is increased, the dispersity factor decreases from a value of 1.23 to 1.10. Interestingly, the high temperature polypeptide sample after ~24 hours of sonication had a molecular weight similar to the PCBL-55, which did not show degradation from ultrasonic energy.

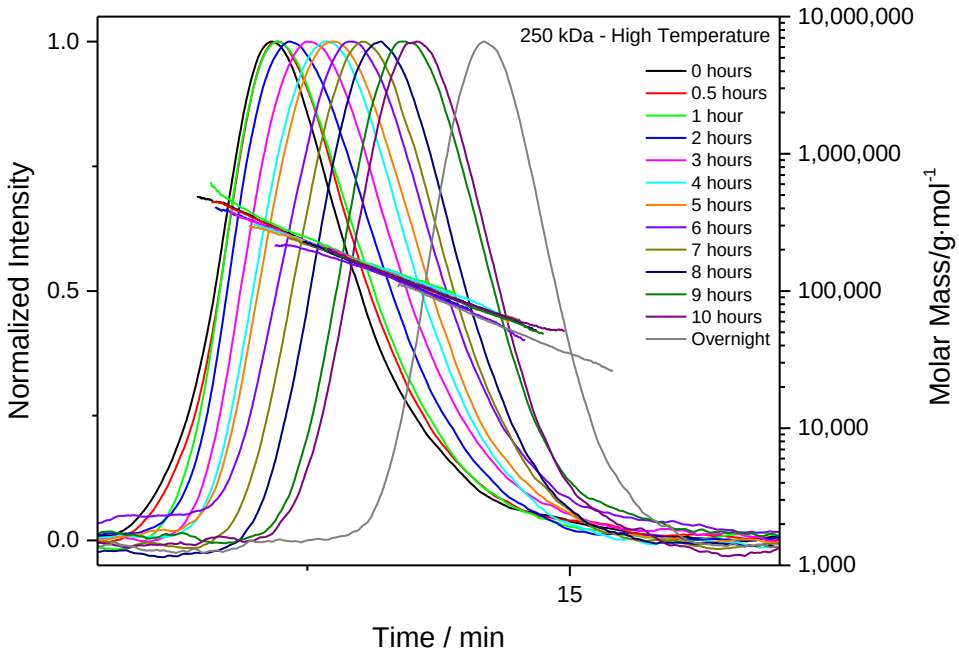

Figure 20. GPC-MALS data for PCBL-250 polypeptide sample used in the ultrasonic degradation studies at high temperature. The molecular weight decreased consistently from 250 kDa to 57 kDa as the sonication time increased from 0 hours (black line) to overnight (~24 hours, gray l line).

Figure 20 shows the GPC-MALS traces for each of the time point aliquots to help illustrate the change in the molecular weight as a function of sonication time. The change in molecular weight of the polypeptide is apparent because the retention time of the sample increases with increasing sonication time indicating the degradation of the chains into smaller fragments. The initial time point is shown in black and the last time point, taken ~24 hours later, is shown in grey. The molar mass for each sample is also overlayed on the graph in Figure 20, but it is easier to visualize the decrease in molecular weight from the chromatogram traces. The polypeptide chains degrade more and faster with an increase in temperature as seen in Table 4 and Figure 20 compared to lower temperatures, data shown

in **Error! Reference source not found.** and Figure 19. Higher temperatures resulted in a polypeptide chain with a weight average molecular weight of 57 kDa after ~24 hours of sonication whereas the lower temperature sample had a molecular weight of 84 kDa after the same time period.

2.4.3 Concentration Effects on the Degradation of PCBL via Sonication

An inherent property of the polypeptide (PCBL) is its ability to form a liquid crystal at high concentrations. This phase transition, due to increased alignment of the polypeptide chains, is hypothesized to provide protection against ultrasonic degradation because of the decrease in chain mobility. In order to determine if concentration of the polypeptide solution effects the overall degradation of the sample, a total of five polypeptide concentrations were tested. All of the experiments were conducted at low sonicator bath temperatures controlled with an external water-circulating bath. The other sonication experiments (temperature and molecular weight studies) were conducted at the normal 2 mg/mL concentration, which can be seen as a control for the concentration studies. The five polypeptide concentrations tested range from 2–112 mg/mL. The results of these studies are shown in Table 5 and the GPC chromatograms (all concentrations except 2 mg/mL, shown in Figure 19) are shown in Figure 21.

Table 5. Ultrasonic Degradation Results for a 250 kDa PCBL Polypeptide Sample at Increasing Concentrations. Samples were Diluted after Aliquot Collection for Injection into GPC-MALS Instrument.

Concentration	Sonication Time/hrs	Molecular Weight/M_w	Polydispersity/ Đ
2 mg/mL	0	246.60	1.18
	0.5	253.97	1.16
	1	223.90	1.17
	2	196.97	1.19
	3	190.63	1.18
	4	164.00	1.18
	5	146.37	1.20
	6	141.23	1.19
	7	133.17	1.17
	8	135.45	1.15
	9	114.10	1.17
	10	111.77	1.18
	Overnight (24 hrs)	83.60	1.12
30 mg/mL	0	246.60	1.18
	0.5	255.43	1.17
	1	245.40	1.19
	2	251.20	1.23
	3	233.90	1.23
	4	236.47	1.22
	5	235.97	1.22
	6	243.60	1.23
	7	227.55	1.32
	8	230.60	1.27
	9	235.63	1.26
	10	253.17	1.18

Table 5 Continued. Ultrasonic Degradation Results for a 250 kDa PCBL Polypeptide Sample at Increasing Concentrations. Samples were Diluted after Aliquot Collection for Injection into GPC-MALS Instrument.

Concentration	Sonication Time/hrs	Molecular Weight/M_w	Polydispersity/ Đ
60 mg/mL	0	246.60	1.18
	0.5	226.17	1.31
	1	243.93	1.31
	2	244.37	1.27
	3	237.53	1.27
	4	246.07	1.28
	5	243.10	1.30
	6	252.67	1.26
	7	246.23	1.36
	8	249.47	1.31
	9	256.20	1.29
	10	252.10	1.38
	Overnight (24 hrs)	255.00	1.31
80 mg/mL	0	246.60	1.18
	0.5	235.40	1.34
	1	235.50	1.32
	2	245.80	1.32
	3	245.10	1.29
	4	261.03	1.32
	5	246.20	1.34
	6	243.53	1.35
	7	256.20	1.30
	8	246.90	1.37
	9	251.40	1.34
	10	254.70	1.31
	Overnight (24 hrs)	251.63	1.25
112 mg/mL	0	246.60	1.18
	0.5	243.90	1.28
	1	270.00	1.35
	2	269.50	1.36
	3	264.17	1.36

PCBL samples with concentrations falling between the isotropic and liquid crystalline regime were studied to determine if the ultrasonic degradation was prevented once a specific concentration was reached. The 2mg/mL sample is the same data previously presented as the low temperature PCBL-250 sample (Table 3 and Figure 19). For a review, the 2 mg/mL sample did show signs of degradation indicated by the molecular weight decreasing as the sonication time increased. The second concentration tested was 30 mg/mL and the data are outlined in Table 5 and shown in Figure 21. There seems to be no apparent change in the molecular weight as a function of sonication time. The dispersity factor does increase with increasing sonication time until the last time point at 10 hours where the dispersity factor drops back to the original value of 1.18.

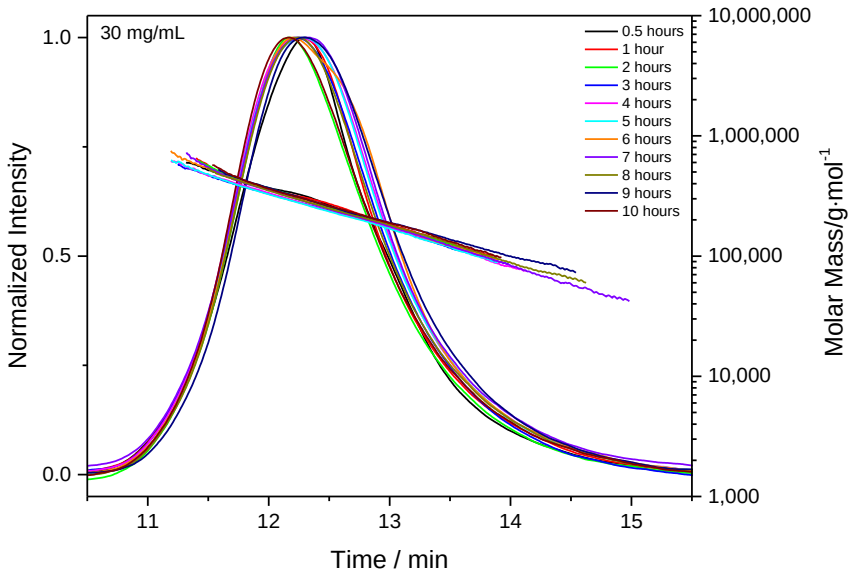

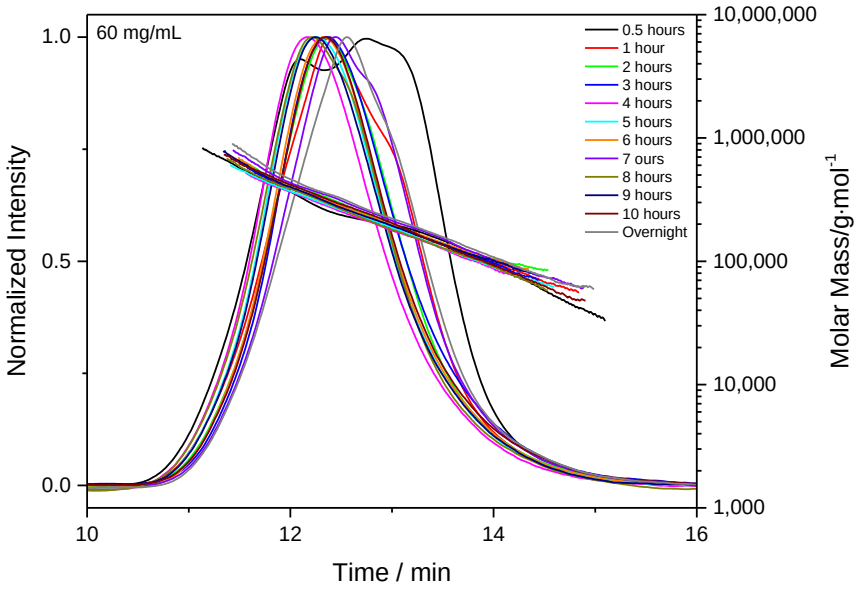
60 mg/mL
0.5 hours
1 hour
2 hours
3 hours
4 hours
5 hours
6 hours
7 ours
8 hours
9 hours
10 hours
Overnight
Normalized Intensity
Molar Mass/g·mol-1
Time / min
1.0
0.5
0.0
10,000,000
1,000,000
100,000
10,000
1,000
10
12
14
16

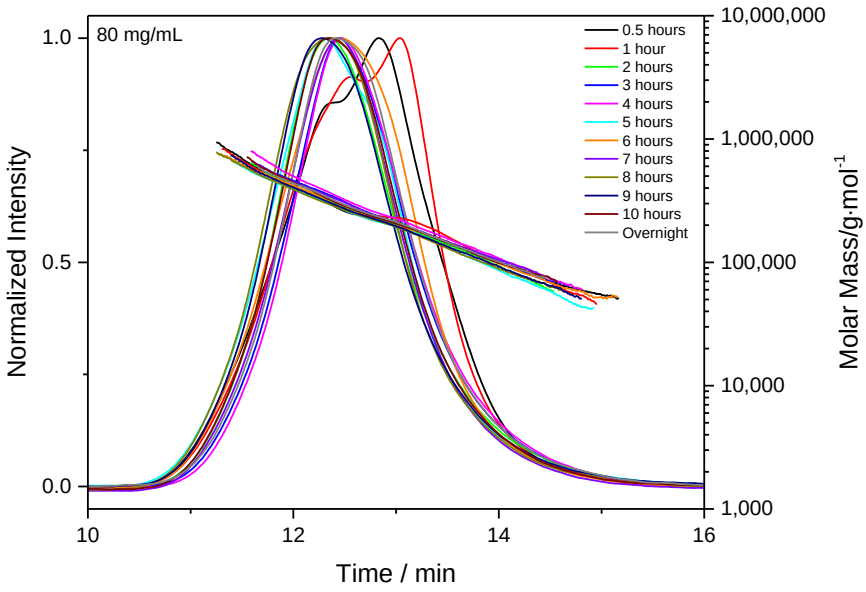
80 mg/mL
0.5 hours
1 hour
2 hours
3 hours
4 hours
5 hours
6 hours
7 hours
8 hours
9 hours
10 hours
Overnight
Normalized Intensity
Molar Mass/g·mol-1
Time / min
1.0
0.5
0.0
10,000,000
1,000,000
100,000
10,000
1,000
10
12
14
16

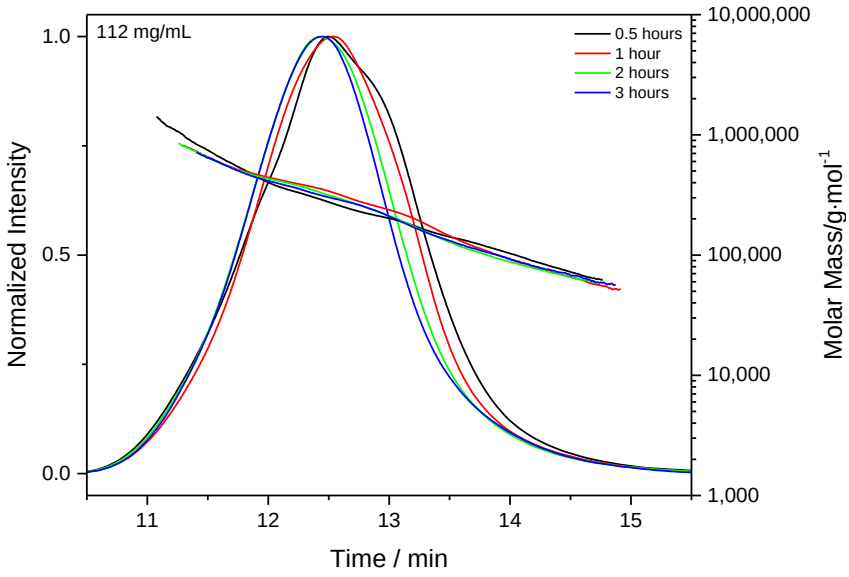

Figure 21. GPC-MALS data for different concentrations of the PCBL-250 polypeptide sample used in the ultrasonic degradation studies. The samples are shown in increasing concentration and illustrate a lack of degradation as sonication time is increased (longest time point is overnight, ~24 hours, and is shown in gray).

The other three concentrations, 60 mg/mL, 80 mg/mL, and 112 mg/mL behaved similarly. As the sonication time was increased the molecular weight did change very much, there was a slight increase in the calculated molecular weight, but all of the values are within error of each other. An interesting observation was that the dispersity factor increased with increasing sonication time. This trend is expected if ultrasonic degradation is occurring because the polypeptide chains are degrading and breaking apart. In this concentration study, the data does not suggest that the polypeptide chains are breaking apart with application of ultrasonic energy. It seems counterintuitive that the molecular weight would remain the same (or have a slight increase) over time while the polydispersity of the system increases. This trend of increasing molecular weight and polydispersity is more apparent in the sample at the highest concentration, even with the few aliquots that

were obtained. There is a slight increase in molecular weight from 247 kDa to 270 kDa but quite a large increase in the polydispersity from 1.18 to 1.36. An explanation of this phenomenon could be that at higher concentrations the polypeptide chains are stacking or interdigitating with each other.

2.5 Conclusions

Ultrasonication was used as a means to degrade the polypeptide, PCBL, by elongational flow stresses. Temperature, molecular weight, and concentration were varied to determine their effect on polypeptide degradation. Molecular weight did have an effect on the overall degradation of the polypeptide chains. As the molecular weight increased, the amount of degradation also increased. These results agree with previous reports that the cavitation process breaks apart linear polymers until it reaches a limiting molar mass. It is believed that the lower molecular weight samples did not degrade as much as the high molecular weight samples because they were closer to this limiting molar mass for PCBL. A similar trend was apparent in the temperature studies as well. Low and controlled temperature degraded the sample, but the higher temperature resulted in a faster degradation of the polypeptide chains. It can be seen in the temperature data, the polypeptide (after ~24 hours) reached a similar molar mass to the low molecular weight sample that did not show any degradation as a function of sonication time.

Concentration of the polypeptide was also varied to determine its effect on ultrasonic degradation as a function of time. It was believed that because PCBL can form a liquid crystal at high concentrations, this ability to align and interdigitate could help prevent the degradation of the polypeptide chains. The data showed that as the

concentration of PCBL was increased, the degradation of the polypeptide decreased. Ultrasonication was allowed to proceed overnight for a total of 24 hours. Even after prolonged sonication times, the higher concentration samples did not degrade, their molecular weight actually increased slightly along with their polydispersity. The thought is that the polypeptide chains interacting with one another and their decrease in mobility resulted in the prevention of degradation as a function of ultrasonication time.

CHAPTER 3. DETECTION OF POLYPEPTIDE CONFORMATIONAL TRANSITIONS VIA SOUND VELOCITY

3.1 Introduction

Synthetic polypeptides have long been appealing choices for chiral separations, biocompatible and responsive materials, and drug delivery systems.[44, 75, 112] Studies of synthetic polypeptide structure go back at least to the 1950s when Blout, Karlson, Doty, and others were able to synthesize different homopolypeptides and stimulate a secondary conformational transition from coil to helix in these polymer chains.[50, 56, 113-114] In aqueous systems, such transitions are followed conveniently by circular dichroism, CD, but this method is limited in UV-opaque solvents. In typical organic solvents for synthetic polypeptides, optical rotatory dispersion, ORD, the Kramers-Kronig counterpart to CD, has been used instead.[115-117] By combining ORD and the simpler experiment of optical rotation at a single wavelength, OR, Fasman, Idelson, and Blout revealed that poly(ε-carbobenzyloxy-L-lysine), PCBL, underwent a sharp conformational transition from random coil to helix when the composition of the solvent was varied for a mixed solvent system of dichloroacetic acid and chloroform.[50] Karasz, O'Reilly, and Bair found that PCBL underwent an inverse coil-to-helix transition as a function of temperature when in the same mixed solvent system.[51, 116] The advantage of simplicity accrues to measurements

made in a single solvent, so it was convenient that Matsuoka et al. discovered that PCBL underwent an inverse coil-to-helix transition as a function of temperature in pure *m*-cresol. The nominal temperature of the PCBL/*m*-cresol transition was about 27 °C, depending somewhat on polypeptide molecular weight.[53] Other polypeptide systems also undergo temperature transitions in single solvents, but not at convenient temperatures.[116]

More recently, synthetic polypeptides have been attached to flat surfaces and colloidal particles to create stimuli-responsive materials.[74, 118-120] Yang, Wang, and Chang studied homopolymer and block copolymer films consisting of responsive, synthetic polypeptides for their use in chemical sensing applications.[121] Liu et.al prepared magnetic silica cores with polypeptide grafted to the surface for use in chiral separations.[44] Yan et al. created a biocompatible nanogel by crosslinking the polypeptide shell and etching away the silica core particle, yielding a responsive vesicle for drug delivery.[75] Applications for such materials rely on the secondary conformational transition in response to external stimuli such as temperature, pH, and chemical environment.

Accordingly, many techniques have been devised to follow conformational transitions. In addition to CD and ORD, NMR and other spectroscopic techniques have been used.[122-129] Each has inherent strengths and drawbacks. NMR requires (or often benefits from) deuterated solvents, which can be expensive. Reliance on NMR also limits the design of materials because magnetic components that can provide added functionality and/or ease of manipulation cannot be evaluated.[44] Infrared and Raman spectroscopy probe the secondary structure of polypeptides and proteins.[128] Accurate assignment of helix or random coil structures using these vibrational spectroscopies requires careful inspection of the environmentally sensitive amide stretching bands.[128] Hillenbrand et al. were able to

identify secondary structures using IR nanospectroscopy, but the small amounts of analyte being measured can result in undersampling.[125] For these reasons, CD, ORD and OR remain the most heavily used tools to study polymer conformation. Complications arise, though, when the polypeptides are attached to surfaces (limited signal) or particles (limited signal plus turbidity). This laboratory recently reported a PCBL-coated silica particle with a superparamagnetic cobalt nougat.[130] This system provides an opportunity to study virus-like expansion and contraction of tethered polypeptides without strong polyelectrolyte effects. Surprisingly, the magnetic properties responded to the helix-coil transition, which proved difficult to study by optical means due to scattering from the particles and impossible to study by NMR due to the magnetic character. The present investigation is devoted to testing a method to study such troublesome yet promising systems.

We consider sound velocity (SV) as a method to detect conformational transitions of polypeptides in solution. We are not the first to use SV to probe polypeptide conformational transitions. Long ago, Noguchi and Yang built and applied a custom instrument to follow the α-β transition of poly-L-lysine and the coil-to-helix transition of poly-L-glutamic acid using volume and sound velocity changes.[131] Other studies from the same era targeted changes in volume and adiabatic compressibility (via sound velocity) associated with conformational transitions.[132-133] Today, SV measurements can be performed alongside density measurements in a single high-precision, automated instrument commonly used in the fuels industry and in food chemistry laboratories.[134-140] Perhaps due to economies of scale, the instrumentation is modestly priced compared to the above-mentioned alternatives. In the present work, we follow the temperature-induced conformational transition of PCBL dissolved in *m*-cresol. A comparison to optical rotation

measurements reveals that sound velocity is a viable way to follow polypeptide transitions. With the assumption that sound velocity changes are linearly related to helical content, the method returns sensible parameters for the classic Zimm-Bragg/Schellman theory of cooperative helix-coil transitions.

3.2 Materials

Carbobenzyloxy-L-lysine (CBL), anhydrous hexane, anhydrous tetrahydrofuran (THF), sodium carbonate ($NaHCO_3$, anhydrous powder), triphosgene, magnesium sulfate ($MgSO_4$), N,N-dimethylformamide (DMF, ACS reagent grade) and sodium methoxide solution (ACS reagent, 0.5 M CH_3ONa in methanol) were purchased from Sigma-Aldrich and used as received. A bottle of 99% m-cresol was obtained from Sigma-Aldrich but was freshly distilled (under small vacuum at 180 °C) to remove any impurities and discoloration. Anhydrous ethyl acetate was purchased from VWR. Ethanol (200 proof) was obtained from Koptec. Water (18.1 MΩ · cm) was withdrawn from a Millipore Synergy UV-R instrument with a BioPak polisher.

3.3 Methods

3.3.1 Synthesis of N-carboxyanhydride (NCA) monomer

The ring-closing of the α-amino acid precursor was conducted similarly to the procedure outlined by Poché and Daly.[61] In a medium glove bag (38 in × 51.5 in, deflated dimensions) under a nitrogen atmosphere, 150 mL of anhydrous ethyl acetate and ~5 g of amino acid (dried at least 8 hours in vacuo) were added to a 500 mL three-neck round bottom flask. A stir bar was placed into the round bottom flask and the flask was capped

with three rubber septa. The flask was removed from the glove bag, connected to a condenser capped with a rubber septum, and placed into an aluminum bead bath that was heated. Argon gas was bubbled through the reaction slurry to ensure an inert atmosphere and the mixture was brought to reflux. In a small glove bag under a nitrogen atmosphere, ~2.15 g of triphosgene ([M]:[I] of ~3:1 with a slight excess added) was weighed out into an oven-dried scintillation vial. The triphosgene was quickly added to the refluxing mixture and the reaction was allowed to proceed until the solution became clear. Once the solution cleared, the reaction solution was cooled and placed into a -20 °C freezer to rest overnight. Removal of unreacted amino acid precursor and side products was performed by washing the NCA according the procedure developed by Poché et.al[62]. The NCA solution was placed into a 500 mL separatory funnel with 100 mL of icy water, swirled to mix, and the organic phase of interest was retained. A 0.5% solution of $NaHCO_3$, 100 mL, was added to the separatory funnel, swirled to mix, and the organic phase of interest was decanted into a clean 250 mL round bottom flask. This vessel was then placed into the medium glove bag under an inert atmosphere where $MgSO_4$ was added quickly until no more clumping occurred in the flask, indicating that all water was removed from the NCA solution. The clear NCA solution was filtered by suction through Whatman 90 mm filter paper in a clean, dry vacuum flask to remove the $MgSO_4$. The filtrate was placed into a new, clean, dry 250 mL round bottom flask and the volume was reduced to 1/3 using a rotatory evaporator. Inside a medium glove bag, under a nitrogen atmosphere, approximately 100 mL of cold anhydrous hexane was poured slowly into the NCA solution. White crystals of NCA started to form and the flask was capped and placed into the freezer to allow precipitation to occur. The precipitated NCA was collected on Whatman 90 mm filter paper using vacuum

filtration to pull through the liquid and dry the precipitate. This suction-dried NCA was placed into a new clean, dry 250 mL round bottom flask and dissolved in 15 mL of dry THF. Again cold anhydrous hexane was poured slowly into the flask while it was being swirled until white crystals began to form. The flask was capped and placed inside the freezer overnight for crystallization to complete.

3.3.2 Synthesis of Poly(ε-carbobenzyloxy-L-lysine)

Inside a nitrogen-filled glove bag, a magnetic stir bar and ~2.08 g of CBL-NCA were added to a 100 mL flame-dried round bottom flask. Approximately ~50 mL of anhydrous THF was added to the flask and the flask was capped with a rubber septum. The flask was placed into an aluminum bead bath and allowed to stir. A volume totaling 0.2 mL of sodium methoxide solution was subsequently injected into the stirring solution. In order to release CO_2 gas produced during the reaction, a bubbler containing silicon oil was connected to the flask via tubing with a needle at the end. The reaction was heated to 35 °C and stirred until bubbles stopped forming in the oil in the connected bubbler (usually 48 hours). A rotatory evaporator was used to reduce the reaction volume to 1/3 to obtain a viscous solution that was then slowly poured into a beaker with water, causing the polypeptide to precipitate out of solution. The polypeptide was suction filtered using a Whatman 90 mm filter paper and allowed to dry completely.

3.3.3 Fourier-Transform Infrared Spectroscopy (FTIR)

Spectra of PCBL were obtained with a Thermo Scientific Nicolet iS50 FT-IR Spectrometer equipped with a Smart-iTR (ATR) accessory. Thermo Scientific Omnic 9 software was used to control the instrument and for data acquisition and analysis. Each

sample was dried in the oven overnight (at least 12h) prior to measurements. A total of 64 scans were taken for each sample with a resolution of 1 cm^{-1} and a data spacing of 0.121 cm^{-1}. The final data format was transmittance and an ATR correction was applied to the data. To ensure reproducibility a background scan was collect before every sample consisting of 16 scans.

3.3.4 Gel Permeation Chromatography (GPC)

Gel permeation chromatography with multi-angle light scattering, GPC-MALS, was used to measure the molecular weight of the synthesized PCBL. The instrument includes a Wyatt Dawn EOS multi-angle-light scattering detector connected to a Tosoh EcoSEC HLC-8320GPC. A TSK SuperH-H (4.6mm ID × 3.5 cm L) guard column was placed before two TSKgel SuperHM-H (mixed-bed) analytical columns (6.0 mm ID × 15 cm L) for the sample flow. A TSKgel SuperH-RC column (6.0 mm ID × 15 cm L) was used as the reference column for the dual flow type refractive index detector. A Tosoh EcoSEC HLC-8320GPC control module was used to operate the GPC, and data acquisition and analysis were controlled using Wyatt Astra 5.0 software. The mobile phase was N,N-Dimethylformamide with 0.1M LiBr flowing at 0.35 mL/min, and the instrument temperature was set to 60 °C. Polymer samples of concentration 2–3 mg/mL were dissolved overnight (at least 12 h) prior to measurements to ensure homogeneity. Solutions were then filtered through Whatman PTFE 0.45 μm syringe filters into Agilent 2 mL GPC vials. In order to obtain the absolute molecular weight of the polypeptide a dn/dc value of 0.123 mL/g was used for the data analysis. To establish reproducibility, multiple injections (20 μL) were performed for each sample measured by GPC/MALS.

3.3.5 Optical Rotatory Measurements (OR)

The optical rotation of the polypeptide samples was measured with a JASCO-J815 instrument equipped with an ORD-M detector. The Jasco Spectra Manager Version 2 software was used to operate the instrument and for data acquisition via the temperature interval measurement experiment. The temperature measurements were conducted from 10–45 °C with a data pitch of 1 °C and a temperature gradient of 1 °C/min. The temperature was controlled at the sample holder, which had to remain within 0.1 °C for 10 seconds to trigger a 180 second delay time to ensure temperature stabilization before the measurement scans were acquired. The three channels monitored for each measurement were ORD-M, HT (voltage), and Abs (absorption). The Digital Integration Time, DIT, parameter in the Jasco software was set for 1 second and the bandwidth was 1.00 nm. At each temperature, three accumulations were obtained at the wavelength 436 nm. An ORD-M Zero Clear was performed, with the shutter open and the sample holder empty, before running each sample to ensure there was no signal drift in the detector between the runs. A fluorescence cuvette with a path length of 1 mm was used for all the sample measurements. The Jasco Spectra Manager Version 2 software was used for analysis of the temperature runs using the interval data analysis program. The polypeptide samples were prepared by dissolving the polypeptide in *m*-cresol overnight (at least 12h) prior to measurements to ensure complete dissolution. Any blanks or corrections were subtracted manually from each acquisition during data analysis.

3.3.6 Sound Velocity Measurements (SV)

The sound velocity was measured with an Anton-Paar DSA 5000M Density and Sound Velocity Meter. Polypeptide samples were prepared by dissolving the sample in *m*-cresol overnight (at least 12h) prior to measurements to ensure homogeneity. A total of six temperature runs, three heating runs, where the temperature was increased during the measurements, and three cooling runs, where the temperature was decreased during the measurements, were acquired for all of the samples. The temperature range measured for each sample was 13–30 °C at 1 °C intervals (temperature stability was ± 0.001 °C).

3.3.7 MATLAB code

MATLAB Version: R2017b

- **Purpose:** imports one dataset already converted to f_H vs. T (centigrade) by associating the low-*T* part of an OR or SV curve with 0% helix and the high-*T* part with 100% helix, permits adjustment of ΔH, ΔS, σ, scaling and offset of the curves.

- **Speed:** About 1 s (Laptop, Windows 10 64-bit, Intel i7 @ 2.9 GHz, 16 Gb RAM)

3.4 Results and Discussion

3.4.1 Characterization of PCBL

FTIR was performed on the NCA monomers and PCBL samples. The main spectral lines to identify in the polypeptide samples are the amide A band (N-H stretch), amide I band (backbone C=O stretch), amide II band (N-H bending), and the amide I C=O

vibration.[49-50, 87] Similarly, the NCA monomer has strong spectral signals due to the anhydride and the amide in the sidechain.[87]

Table 6. Summary of Characterization Results for PCBL Polypeptide Samples

Sample Name	Molecular Weight/M_w	Polydispersity/ Đ	Notebook Code
PCBL-155	155,000 Da	1.07	AB.4.177A
PCBL-79	78,800 Da	1.23	PCBL-Untethered
PCBL-55	54,500 Da	1.04	AB.4.177C

Figure 22 shows the FTIR spectra for as-synthesized CBL-NCA monomer and a PCBL sample. The CBL-NCA monomer, shown in Figure 22A, was identified by the characteristic carbonyl bands from the anhydride functional group in the ring system as well as from the carbonyl group in the monomer side chain. These peaks are present at 1847 cm^{-1} and 1772 cm^{-1}. Another characteristic peak is found at 3338 cm^{-1} from the amide N-H stretching in the monomer ring system and side chain which produced a sharp spectral signal. Figure 22B shows the FTIR spectrum for a synthesized polypeptide sample. The N-H amide stretch, shown at 3290 cm^{-1} for the polypeptide, is shifted slightly and more broad compared to the monomer signal indicative of the ring-opening of of the monomer units. There are two strong spectral signals in the polypeptide spectrum at 1648 cm^{-1} and 1526 cm^{-1} showing the amide I band and the amide II band respectively. The final peak that is highlighted in the polypeptide sample is the strong spectral signal at 1688 cm^{-1} which indicates a carbonyl stretch (C=O) from the ester and the amide functional groups in the polypeptide backbone and sidechain.

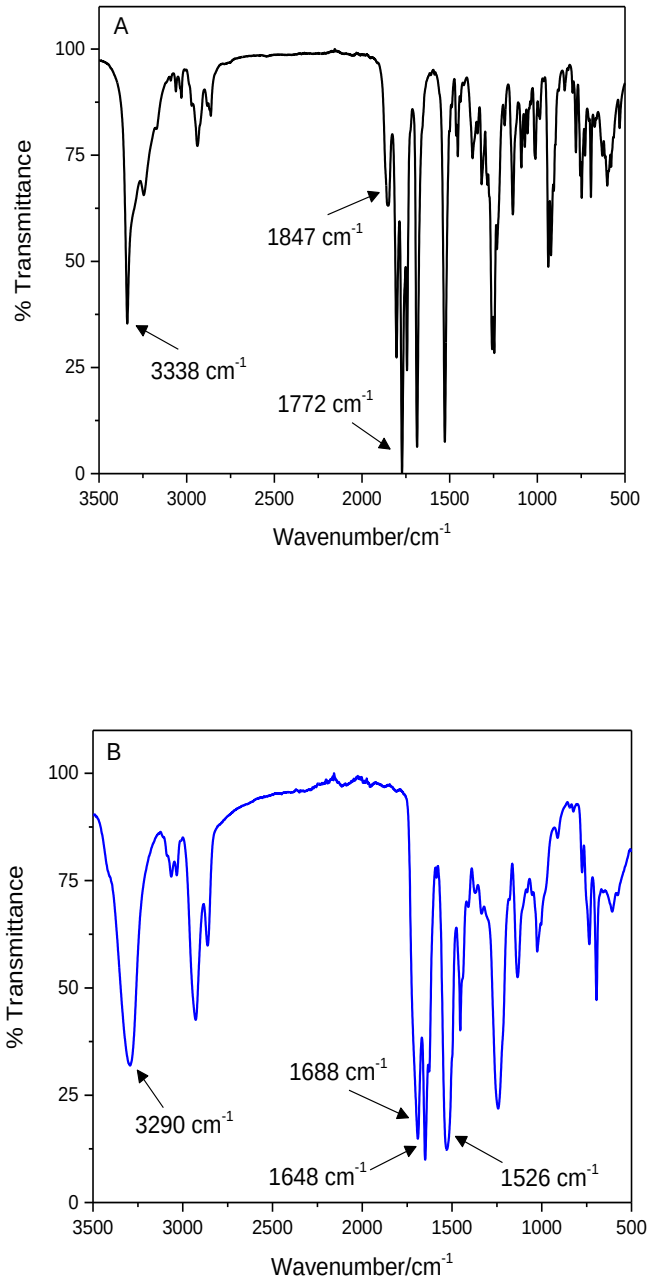

Figure 22. FTIR spectra for a CBL-NCA monomer (A) and a PCBL polypeptide sample (B). The arrows highlight the important and specific spectral lines that were used to identify and characterize each of the compounds; see Text.

After FTIR confirmed that PCBL was successfully synthsized, GPC-MALS was used to determine the molecular weight and polydispersity. In order to obtain a range of

molecular weights, three PCBL polypeptide samples were measured (Table 6). Figure 23 shows the corresponding chromatograms overlayed with the molar mass trace for each sample. The molecular weights of the polypeptide samples were determined to be 155 kDa, 79 kDa, and 55 kDa with dispersities $Đ$ = 1.07, 1.23, and 1.04 respectively. The range of molecular weights and uniformity suggested these polypeptides could be used to assess whether the sound velocity and optical rotation experiments agree on the shift in conformational transition temperature with molar mass.

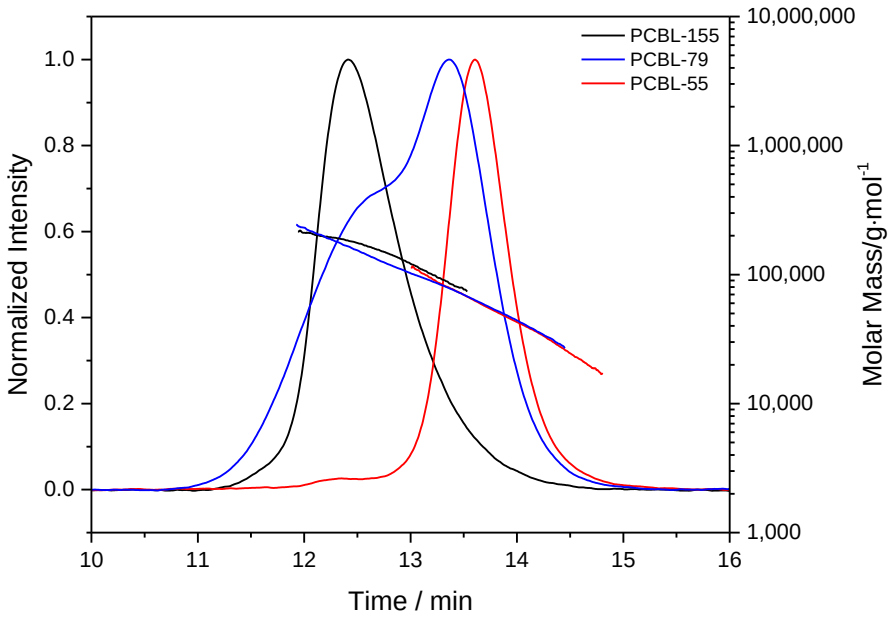

Figure 23. GPC-MALS traces showing normalized light scattering intensity at θ = 90° and molecular weight profiles for the three PCBL polypeptide samples used to conduct the optical rotation and sound velocity measurements. The molecular weights of the polypeptide samples were 155 kDa, 79 kDa, and 55 kDa. Each sample had a low dispersity factor of $Đ$ = 1.07, 1.23, and 1.04 respectively.

3.4.2 Optical Rotation.

3.4.2.1 Understanding Optical Rotation and Experiment Design

The random coil conformation for PCBL has a more negative specific optical rotation than the α-helix conformation.[50] In *m*-cresol, Matsuoka *et al*. reported an optical rotation of -87° for the random coil conformation and -22° for the α-helix conformation under the conditions of their measurements.[53] Figure 24 illustrates the expected optical rotation behavior as a function of temperature for PCBL. As the temperature is increased from 10–30 °C, the polypeptide will undergo its coil-to-helix transition.

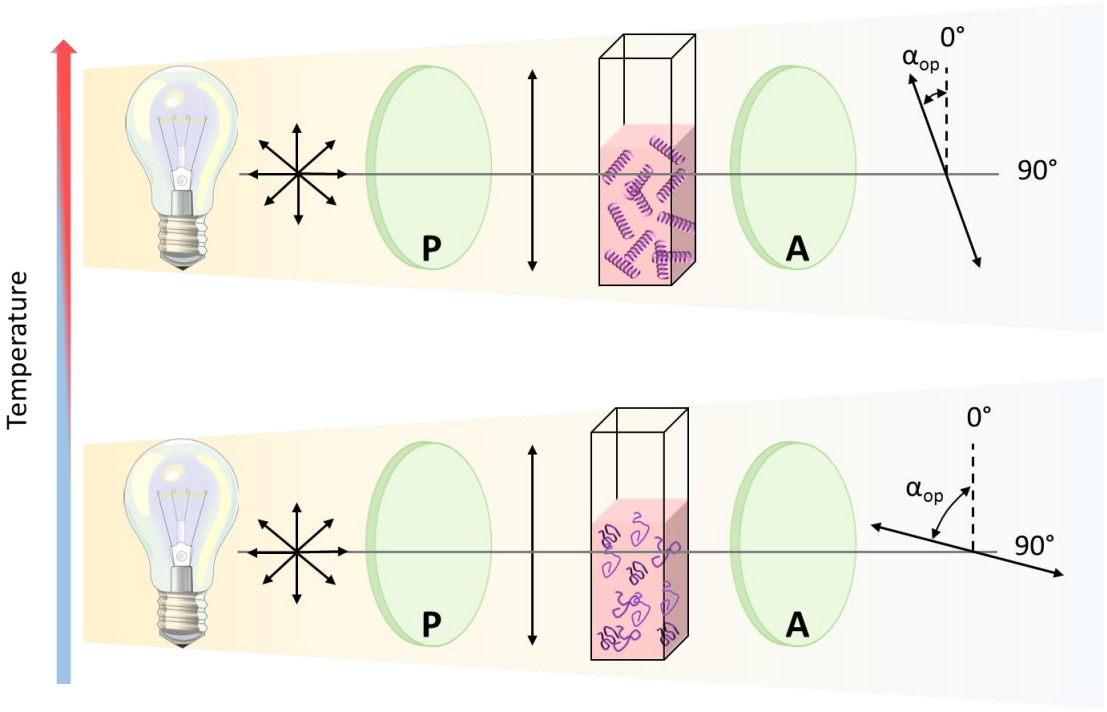

Figure 24. In optical rotation, a light source is placed in front of a polarizer (labeled P) to obtained linearly polarized light which is cast through the sample. The chirality of the sample rotates the polarization of the light and the deviation from 0° is measured with an analyzer (labeled A). This figure illustrates the conformational coil-to-helix transition of PCBL as a function of temperature in *m*-cresol measured by optical rotation. The polypeptide undergoes its conformational transition from

random coil to α-helix as the solution is heated, resulting in a positive change in optical rotation.

OR data were collected at 1 °C intervals for the experimental temperature range, 10–40 °C. Following the protocol outlined in the methods section, readings at different temperatures were separated by about 4 min. Figure 25 shows that the instrument temperature stabilizes within this time frame, even for the extreme case of a large temperature jump at >15 °C/min, and that the polypeptide conformation as reported by OR keeps pace. In order to account for the concentration of the polypeptide in each of the samples, the specific optical rotation was calculated using the equation,

$$\alpha_{sp} = \frac{100 \cdot \alpha_{op}}{l \cdot c} \quad (1)$$

where α_{sp} is the specific optical rotation, α_{op} is the optical rotation, l is the length of the cuvette in dm, and c is the polypeptide concentration in g/100 mL.

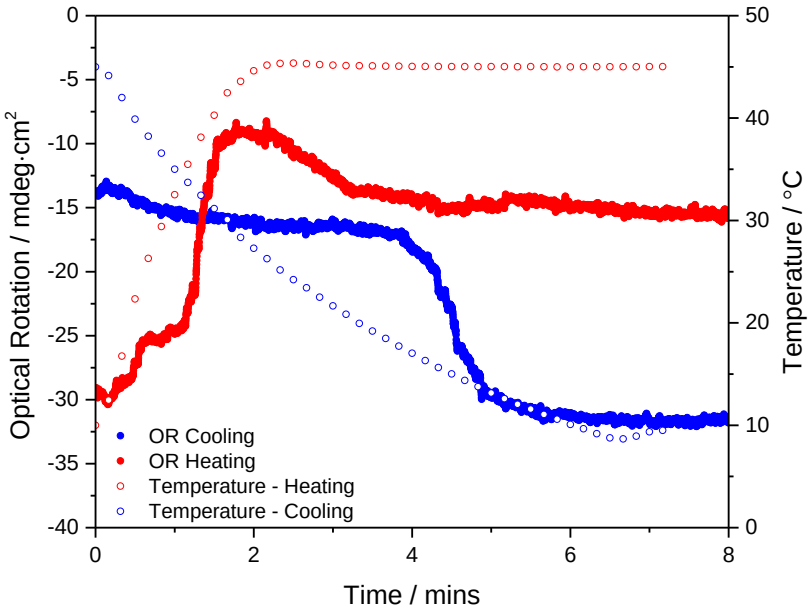

Figure 25. Temperature jump control experiment using PCBL-79 in *m*-cresol. A heating and cooling experiment was conducted to determine how quickly the conformational transition occurs to determine the hold time for the optical rotation experiments.

3.4.2.2 Optical Rotation of PCBL with Varying Molecular Weights

The specific optical rotation results, Figure 26, show the transition from random coil to α-helix when the sample is heated and vice versa when the sample is cooled. Matsuoka *et al*. showed previoulsy that PCBL has a transition at ~27 °C but the transition shifts and broadens depending on the molecular weight of the polypeptide.[53] Our results confirm this finding. The procedure used to identify the transition temperature is described in the Data Analysis of Optical Rotation Measurements section, but simple visual inspection to locate the inflection points in Figure 26 gives almost the same transition points. The transition temperature as a function of molecular weight is shown in Figure 26. Also appearing are somewhat higher transition temperatures identified by the Zimm-Bragg

model.[141] (These temperatures are defined differently, as will be discussed after all results based on the empirical fitting procedure are presented.) Decreasing transition temperatures of 24 °C, 22 °C and 19 °C for PCBL-55, PCBL-79, and PCBL-155 respectively, show dependence between molecular weight and transition temperature.

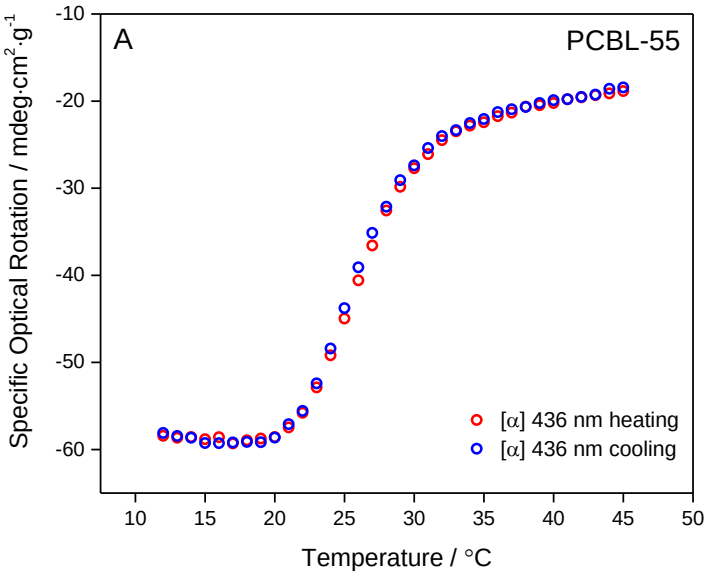

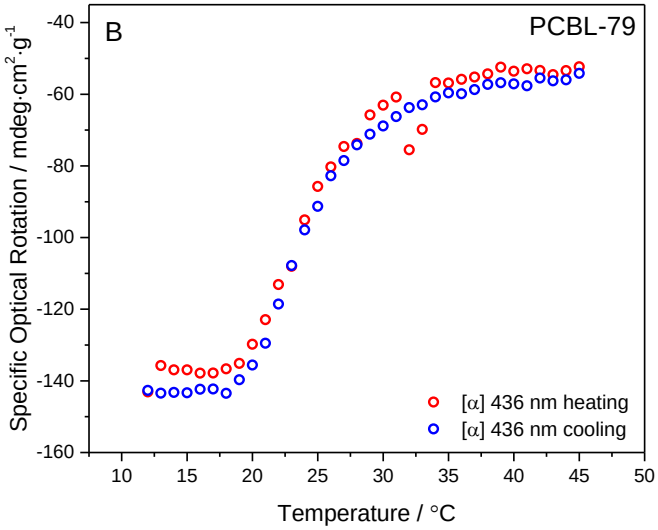

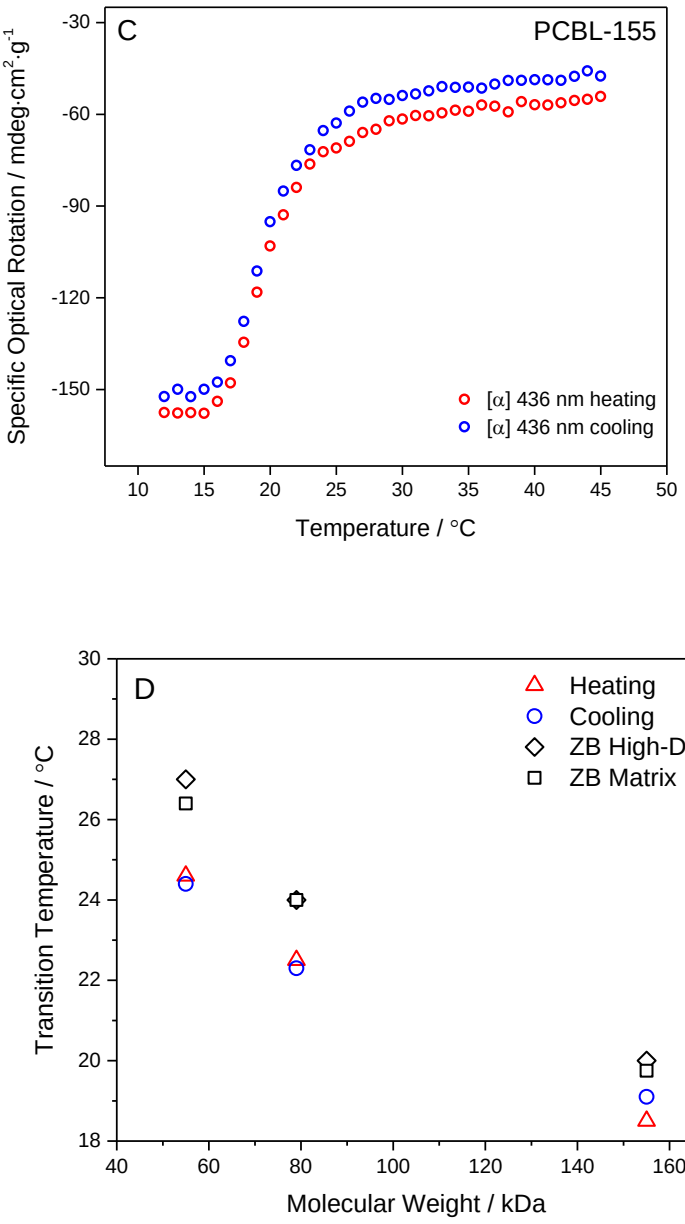

Figure 26. Optical rotation curves for three different PCBL polypeptide samples, PCBL-55 (A), PCBL-79 (B), and PCBL-155 (C), at concentrations 49.9, 50.1, and 50.2 mg/mL respectively. As the temperature is increased, the polypeptide undergoes its conformational transition from random coil to α-helix and vice versa when the temperature is decreased. This is evident from the positive change in optical rotation at higher temperatures and a more negative change in optical rotation at lower temperatures. Transition temperature as a function of molecular weight (D) illustrates the effect of polypeptide molecular weight on the conformational transition

temperature, as determined by empirical and Zimm-Bragg methods, in both the high-DP limit and by matrix calculation.

3.4.3 Sound Velocity

3.4.3.1 Understanding Sound Velocity

The same polypeptide solutions measured by optical rotation were used in the sound velocity measurements. The samples were measured for three heating and cooling cycles to probe the reversibility of the conformational transition. Early workers studied the coil-to-helix transition and the α-helix to β-sheet transition for poly(L-glutamic acid) and poly(L-lysine) using sound velocity and adiabatic compressibility.[131] Based on their findings, Figure 27 illustrates the expected results and behavior of our PCBL as a function of temperature for the sound velocity measurements.

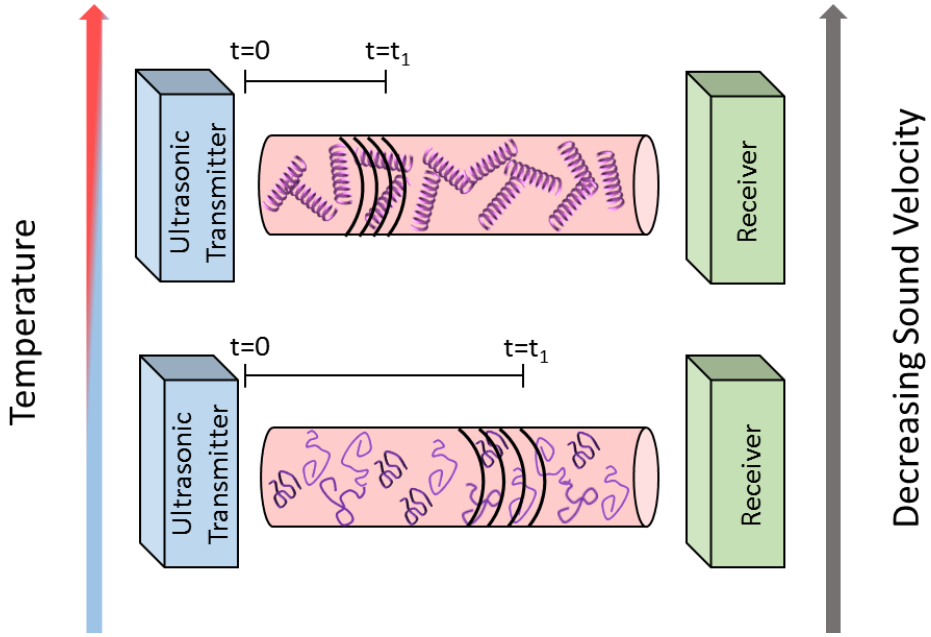

Figure 27. Illustration of the conformational coil-to-helix transition of PCBL as a function of temperature in *m*-cresol measured by sound velocity. As the temperature

increases, the PCBL conformation changes to α-helix and the sound velocity decreases.

Figure 28A shows that sound velocity decreases with temperature, as expected in organic solvents.[131] Although the decrease seems nearly linear, the residuals plot reveals correlated errors of fit; a line does not fit the data to within the very small (<0.015%) uncertainties. Confirming this impression, the derivative plot, Figure 28B, shows a significant deflection at a temperature close (within 1 °C) to that observed by OR.

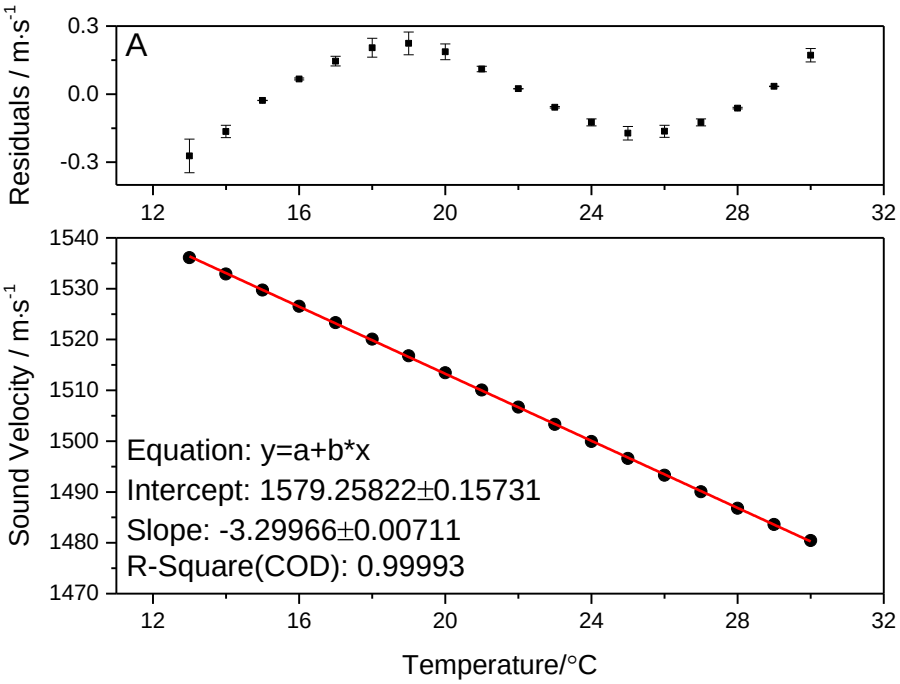

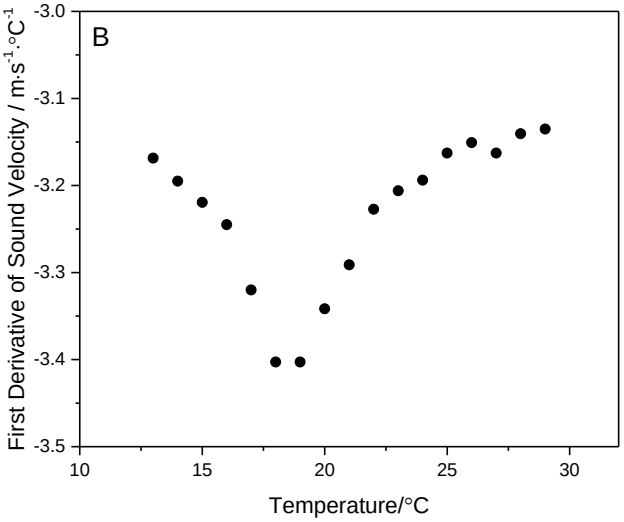

Figure 28. (A) Raw data of a sound velocity measurement showing sound velocity as a function of temperature for PCBL-155/*m*-cresol at *c* = 5.0 g/dL; uncertainties are much smaller than data points, about 0.015%. The residuals plot shows strongly correlated errors of a linear fit, well beyond the error bars for, reflecting the inadequacy of a linear model. (B) The derivative of the sound velocity as a function of temperature, showing a deviation in the seemingly perfectly linear raw data set.

3.4.3.2 Sound Velocity of PCBL with Varying Molecular Weights

The details of extracting the transition temperature from plots such as Figure 28A appear in the Data Analysis of Sound Velocity Measurements section. Briefly, a linear regime in the SV vs *T* plot is identified away from the transition. A straight line is drawn through that regime, and the difference between the measured SV and the extrapolated line values, SV_{calc}, is computed. When plotted against temperature, this difference exhibits a sigmoidal appearance, similar to the OR vs *T* plots, as shown in Figure 29. The results confirm the viability of sound velocity as a technique for following the polypeptide conformational transitions. The three polypeptide samples are shown in Figure 29A–C in order of descending molecular weight. PCBL-79 and PCBL-55 exhibit an abnormal

heating curve on the first heating, which is believed to be due to degassing of the sample. Apart from this abnormality, the sound velocity measurements agree with the measurements taken via optical rotation and show reversibility of the polypeptide transition. Figure 29D shows transition temperature as a function of molecular weight indicating a dependence between these two parameters similar to optical rotation.

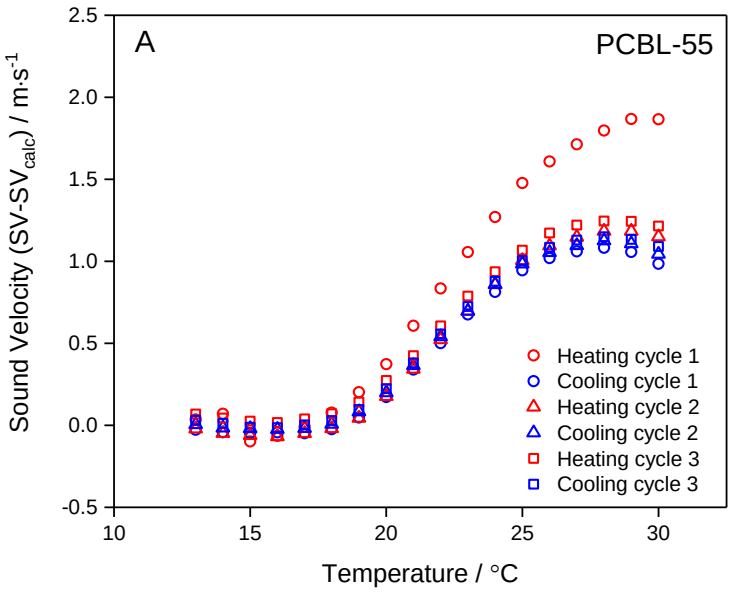

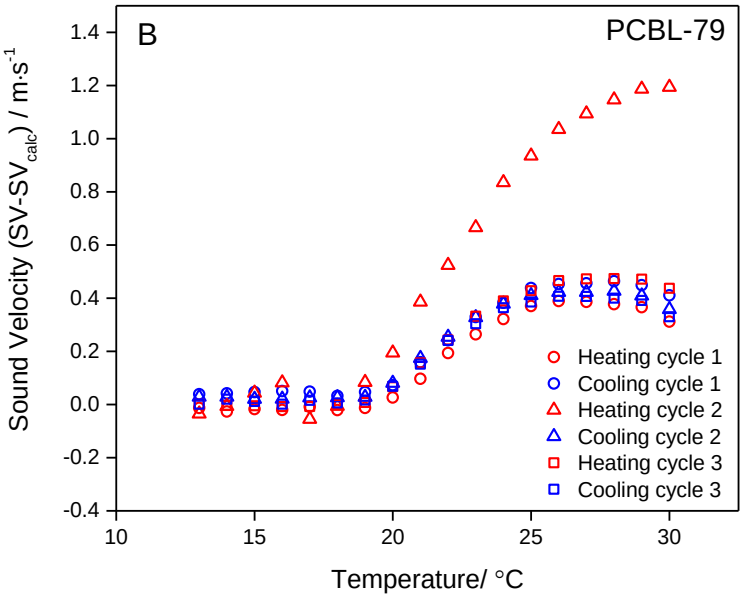
B
PCBL-79
Sound Velocity (SV-SV$_{calc}$) / m·s^{-1}
Temperature/ °C
Heating cycle 1
Cooling cycle 1
Heating cycle 2
Cooling cycle 2
Heating cycle 3
Cooling cycle 3

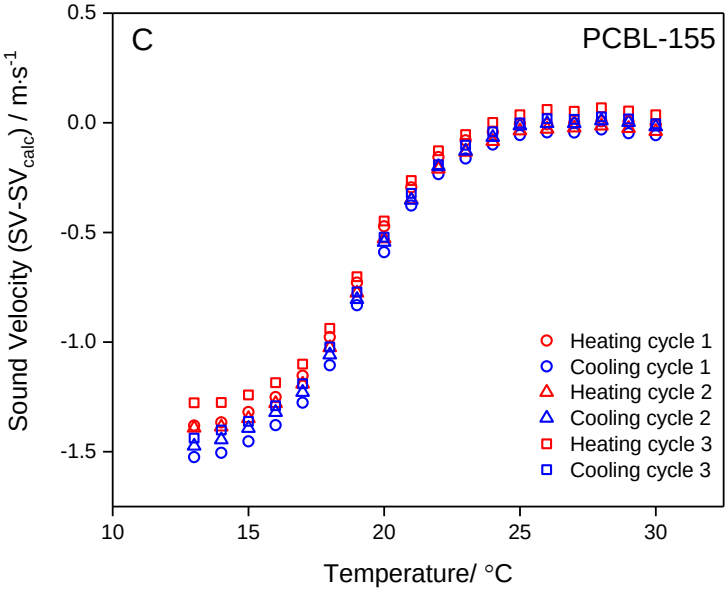
C
PCBL-155
Sound Velocity (SV-SV$_{calc}$) / m·s^{-1}
Temperature/ °C
Heating cycle 1
Cooling cycle 1
Heating cycle 2
Cooling cycle 2
Heating cycle 3
Cooling cycle 3

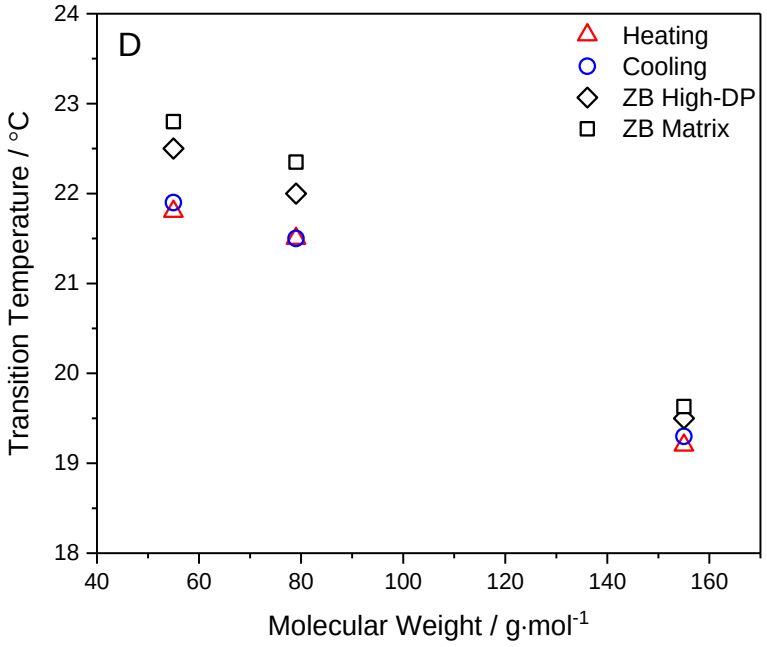

Figure 29. Sound velocity curves for three different PCBL samples, PCBL-55 (A), PCBL-79 (B), and PCBL-155 kDa (C). Transition temperature as a function of molecular weight (D) illustrates the conformational transition dependence on polypeptide molecular weight, as determined by empirical and Zimm-Bragg methods in both its high-DP limit and matrix forms.

3.4.4 Effect of Concentration on PCBL Conformational Transition

Because the transition temperature changes as a function of molecular weight, and given the low concentrations at which rodlike polymers enter the semidilute regime, which also depends on molecular weight, the effect of concentration on the polypeptide transition was examined.[142]

Solutions of PCBL-155 with concentrations ranging from 50–15 mg/mL were analyzed using optical rotation. The measurements were conducted from 10–45 °C at 1 °C increments. Figure 30A shows the OR curves for four different concentration solutions of

PCBL-155. A vertical dotted line was added to the plot at 27 °C, which is the nominal literature value of the transition temperature of PCBL.[53] As seen in Figure 30B, there is a slight shift in the transition temperature to lower temperatures as the concentration of the polypeptide solution increases. Remembering that helices form on the high-temperature side of the transition in PCBL/*m*-cresol, this result suggests that neighboring molecules assist in the formation of helices, an effect predicted long ago by Pincus and deGennes and investigated in the context of liquid crystal formation coupled to conformational transitions by Lin *et al*[143-144].

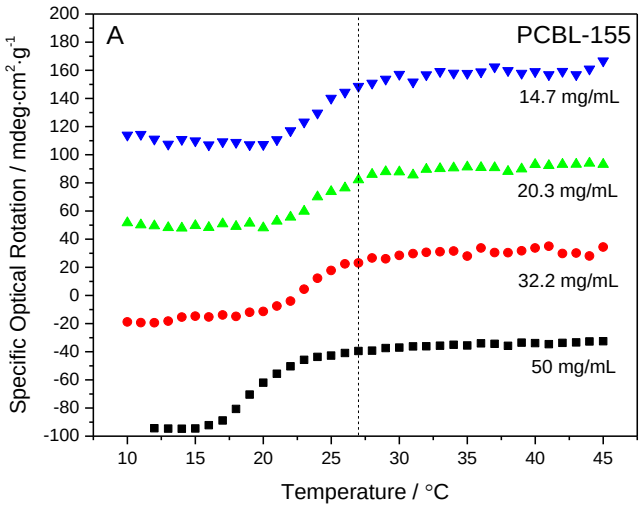

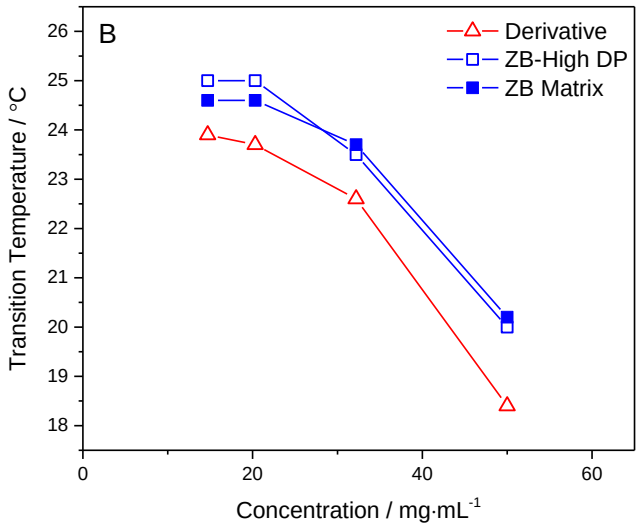

Figure 30. Optical rotation curves (A) for PCBL polypeptide sample PCBL-155 at varying concentrations. Data have been shifted vertically for clarity. The concentrations are shown from lowest (blue line) to highest (black line). The dotted line highlights the reported transition temperature of 27 °C. The transition temperature as a function of concentration (B) was plotted to illustrate the change in transition temperature for high concentrations of polypeptide; also included are results from Zimm-Bragg analysis by high-DP approximation and matrix calculations.

As a companion to the OR concentration study, the same PCBL-155 was analyzed using sound velocity at three different concentrations ranging from 50–12 mg/mL. The temperature was varied from 13–30 °C with a data point collected at 1 °C intervals. Figure 31A shows an overlay plot of the sound velocity data for the three different concentrations of PCBL-155. The transition temperatures were obtained as explained in the Data Analysis of Sound Velocity Measurements section. Concentration as a function of transition temperature is shown in Figure 31B. A slight shift in transition temperature is evident as the concentration of the polypeptide is varied; again, higher concentrations correspond to

lower transition temperatures. Also appearing in this figure are the transition temperatures from Zimm-Bragg analysis, which are defined differently.

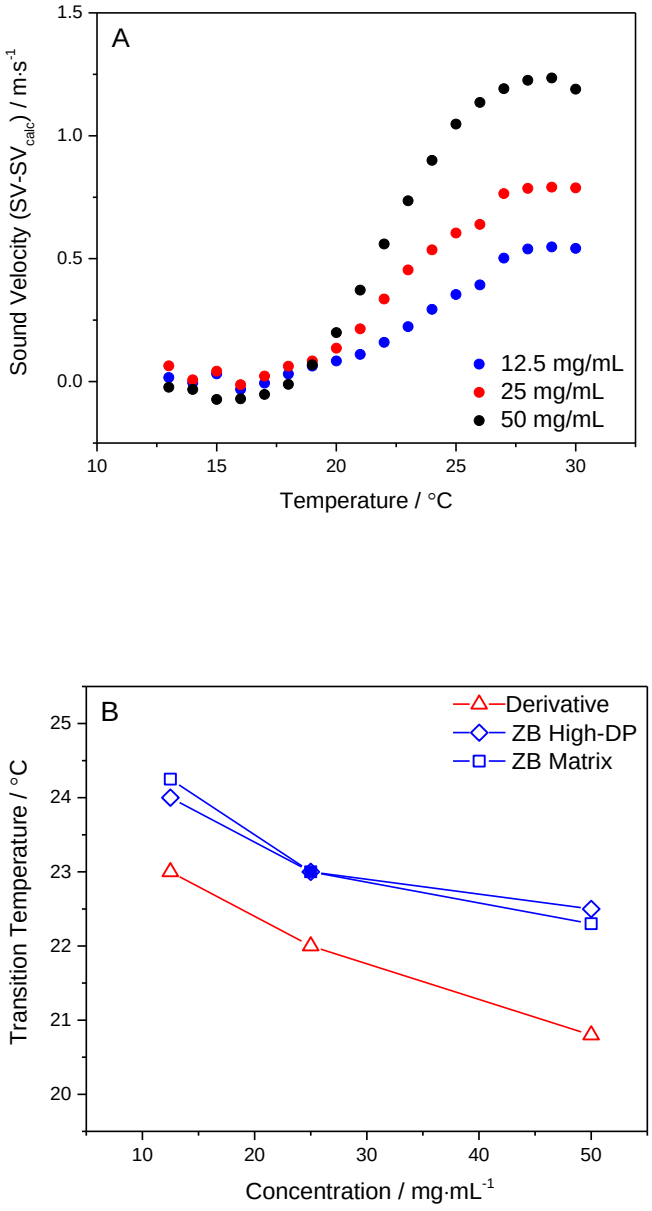

Figure 31. Sound velocity curves (A) for PCBL-155 at varying concentrations. The concentrations are shown from highest (black line) to lowest (blue line). Transition temperature as a function of concentration (B) shows a slight shift to lower transition

temperatures as the concentration increases, whether by empirical or Zimm-Bragg analysis.

3.4.5 Data Analysis of Optical Rotation Measurements

To aid in identification of the transition temperature, a derivative of the speific optical rotation was calculated and is shown in Figure 32. From the derivative curve, it is clear that the transition occurs around ~19 °C with agreement between the heating and cooling measurments. The reversibility and reproducbility of the conformational transition is clear when comparing the two temperature cycles.

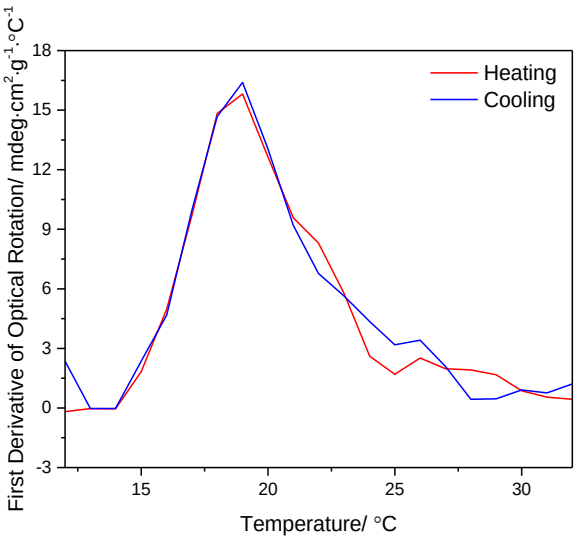

Figure 32. A first-order derivative of the heating and cooling data for PCBL-155 to determine the transition temperature from optical rotation. A transition temperature of ~19 °C was obtained for PCBL-155.

A problem arises once the concentration is reduced for the PCBL samples. The derivative curves have more noise in their baselines. Due to this increase in noise, a Logistic 5 sigmoidal fit (Origin Pro 2016) can be applied to the optical rotation data (e.g., Figure 26A–C) to help smooth the data as shown in Figure 33A. The first-order derivative

is taken of this fit to help elucidate the transition temperature for each sample. Logistic regression model is commonly used to analyze/model a system made up of a binary response.[145-147] The probability of the polypeptide system to exist as one of two classes/events (random coil or α-helix), makes it suitable to be analyzed by a logistic sigmoidal fit.[145-147] The derivative curves obtained from the logistic fit for PCBL-155 are shown in Figure 33B, illustrating a transition temperature around 19 °C. Matsuoka et.al reported a transition temperature of ~26 °C for a PCBL sample with a similar molecular weight.[53] The disagreement between the values previously reported and the values in this work could arise from differences in insturmental equipment, sample preparation, polypeptide concentration, dispersity, and solvent purity.[53]

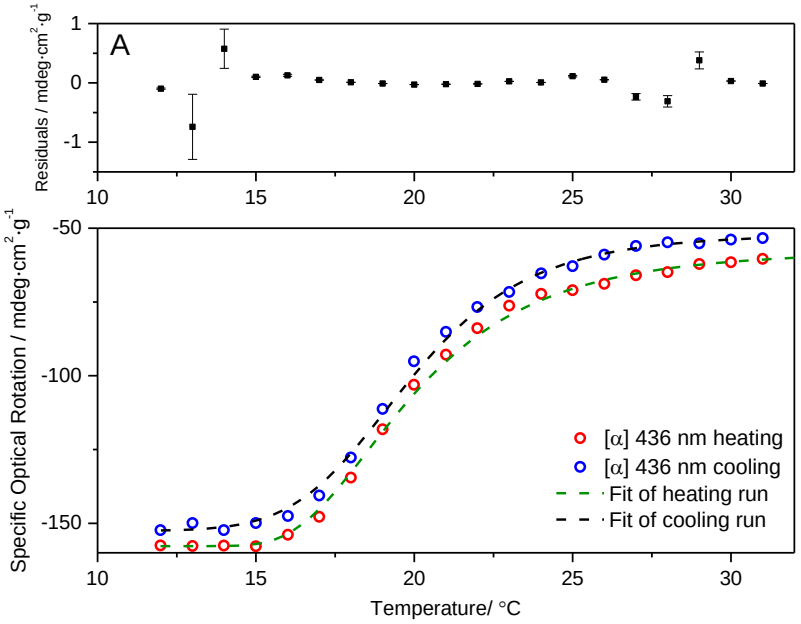

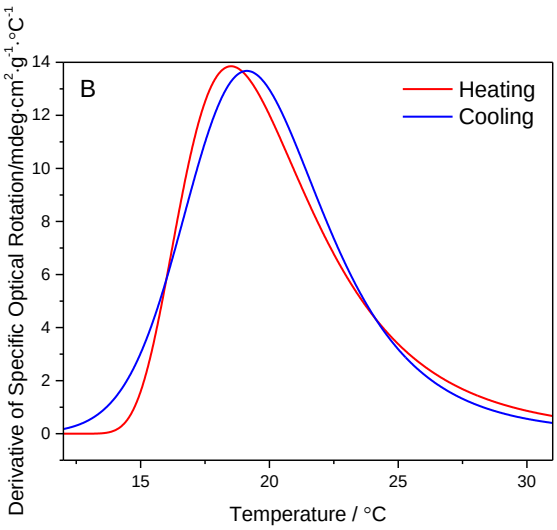

Figure 33. (A) Logistic 5 sigmoidal fit applied to the specific optical rotation data for PCBL-155. The fit helps to smooth the curve and reduce the noise of the data. (B) A first-order derivative was taken of the Logistic 5 sigmoidal fit for PCBL-155 to determine the transition temperature for the optical rotation data. A transition temperature of ~19 °C was obtained for PCBL-155.

3.4.6 Data Analysis of Sound Velocity Measurements

Similar to optical rotation, sound velocity measurements require post-measurement data processing and analysis. A plot of sound velocity against temperature is almost linear, as shown in Figure 28A. Close inspection reveals a barely perceptible deviation from linearity near the polypeptide transition temperature according to OR measurements. The derivative was taken of the raw sound velocity data to illustrate this minute deviation from linearity, resulting in Figure 28B, which indicates a change in the sample at ~18 °C. The high precision (5 significant digits) of the sound velocity measurements enables the subtle change to be detected. The difference of fit can be calculated for each temperature run by determining a baseline from the derivative. Figure 28B shows the derivative for PCBL-155. At higher tempearatures, above 24 °C, the sound velocity levels off showing no

significant change. For this reason, the baseline was chosen to be 25–30 °C. These five data points were plotted and a linear trendline was generated to calculate the difference of fit for the entire temperature run from 13–30 °C.

Although identifying the existence of a transition point by taking a derivative was effective, a different procedure was used to display the transition as a continuous change. An example for calcluating the difference of fit for the sound velocity of PCBL-155 follows. Using the equation,

$$y = a + bx \tag{2}$$

where *b* is the slope and *a* is the *y*-intercept obtained from the linear fit equation generated from a five-data point baseline, the extrapolated sound velocity can be calculated for each tempearture between 13–30 °C. This will be denoted as the sound velocity fit data (SV_{calc}). Next, the difference between the SV_{calc} data and the experimental sound velocity data can be calculated ($SV\text{-}SV_{calc}$). The difference is then plotted as a function of temperature producing the sound velocity ($SV\text{-}SV_{calc}$) transition curve.

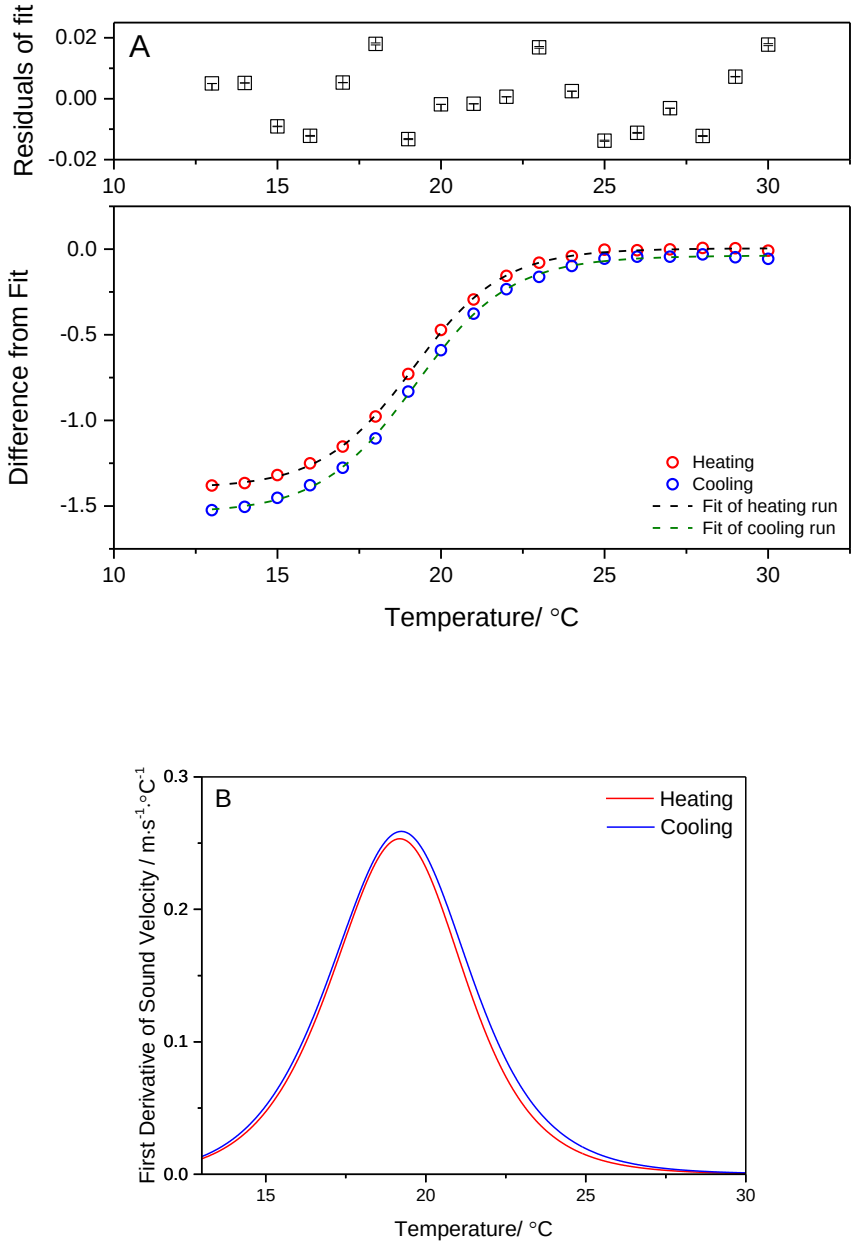

Figure 34. (A) Logistic 5 sigmoidal fit applied to both heating and cooling sound velocity data for PCBL-155. Smoothing of the data helps to reduce the noise that can interfere with obtaining a transition temperature. (B) A first-order derivative was taken of the fit to determine the transition temperature for the sound velocity data and was determined to be ~19 °C.

Similar to the OR, once the concentration of PCBL is decreased, the sound velocity data and its respective derivative become noisy. To counteract this increase in noise level,

the Logistic 5 fit was applied to the sound velocity data in the same way it was applied to the OR data. Once the fit was obtained, the first-order derivative was taken to determine the transition temperature. Figure 34 shows the SV data with the Logistic fit applied and then the derivative obtained from the fit.

3.4.7 PBLG Control Experiment

To demonstrate that the change in conformation of PCBL was being probed, a control study using poly-γ-benzyl-L-glutamate, PBLG, was performed. Figure 35 shows the results of the control study for both sound velocity and optical rotation. In both experiments, PBLG shows a flat, unchanging line indicating the polypeptide is not undergoing a conformational structure change, unlike the PCBL-155 results overlaid onto the same plot. This is expected because in the chosen temperature range, PBLG should remain in its helical conformation.

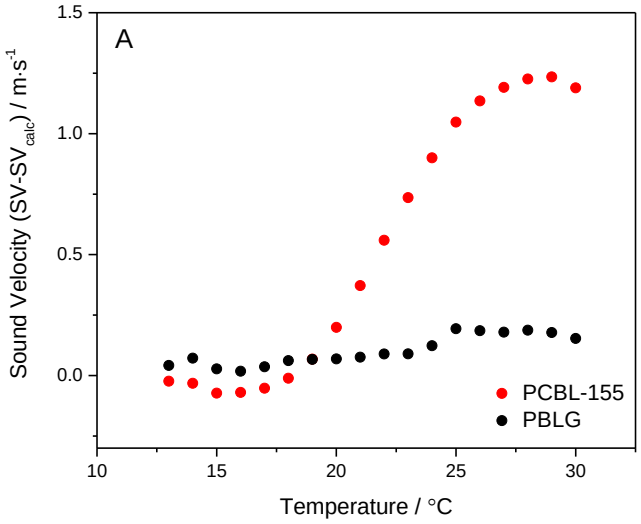

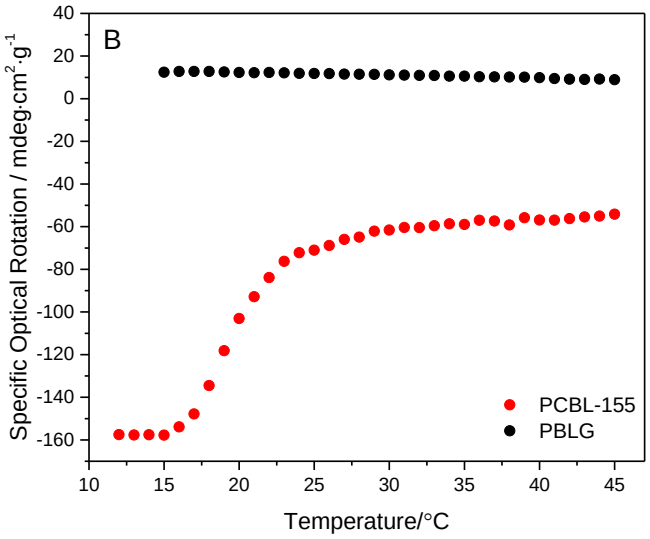

Figure 35. Sound velocity (A) and optical rotation (B) as a function of temperature for PCBL-155 and PBLG-control samples, both in *m*-cresol. The PCBL-155 sample undergoes its secondary conformational transition in the tested temperature range while the PBLG control group shows no change in secondary conformation.

3.4.8 Comparison of Optical Rotation and Sound Velocity

To assess the correlation between the SV and OR results, Figure 36 shows the polypeptide molecular weight as a function of transition temperature for both methods. For PCBL-155 and PCBL-79, the two methods agree within 1 °C. Once the molecular weight decreases to less than 79 kDa, the sound velocity result no longer tracks the optical rotation result closely. Comparing the two methods, it is apparent that molecular weight does affect the transition temperature, but the effect is more noticeable in optical rotation than it is using sound velocity. These results are independent of the method used to find the transition temperature, as shown in Figure 37. Again, the Zimm-Bragg results appear on this plot, to be discussed below.

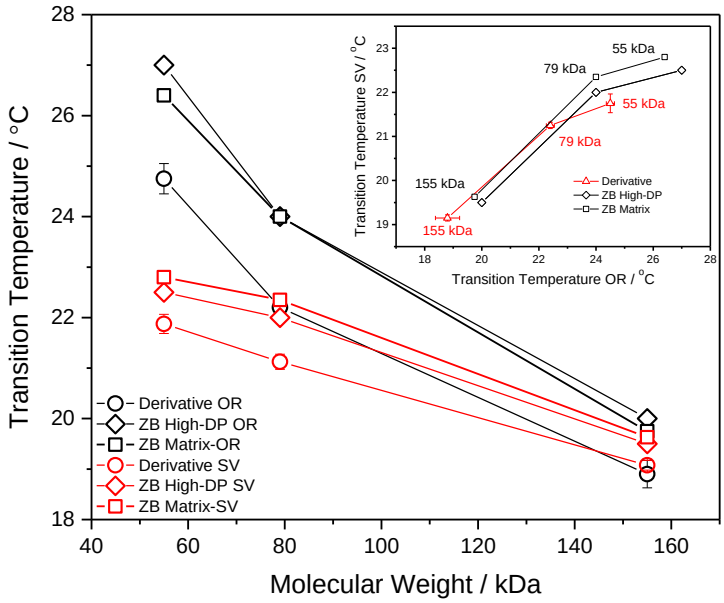

Figure 36. Comparison of the sound velocity (red) and optical rotation data (black) showing the dependence of the conformational transition temperature on the polypeptide molecular weight. The transition temperatures shown in the main figure are the averages obtained for each molecular weight for one heating and one cooling run. The inset shows the correlation of transition temperatures determined by sound velocity with those from the optical rotation method.

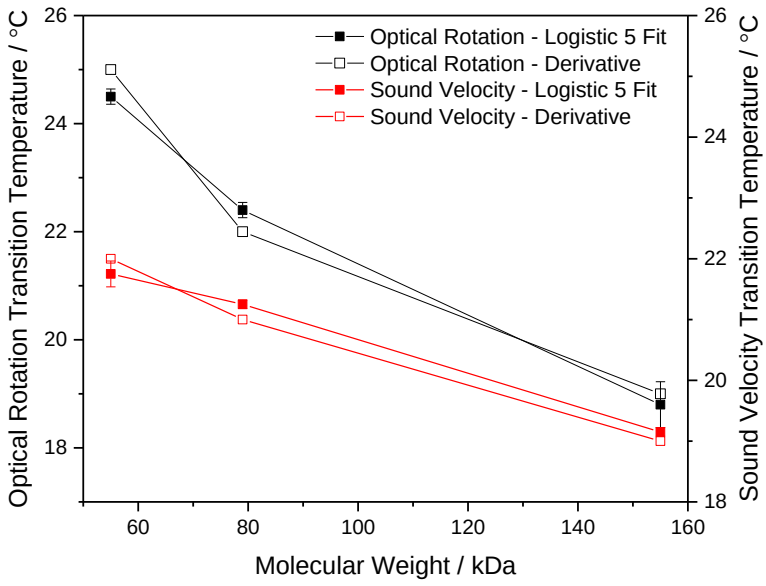

Figure 37. Deviation in transition temperature for each molecular weight obtained by the two analysis methods: first order derivative of the data (open squares) vs smoothing the data with a Logistic 5 function (filled squares)

3.4.9 Absolute Sound Velocity Trends

The present study, which is focused on finding transitions, has little to say about absolute sound velocity, or its dependence on concentration or mass. At any measured temperature, SV decreases with solution concentration, Figure 38, suggesting that the polymer dissipates some of the sound wave rather than acting as a rigid solid. At a given concentration (50 mg/mL) the highest sound velocities were observed for the shortest polymer, Figure 39.

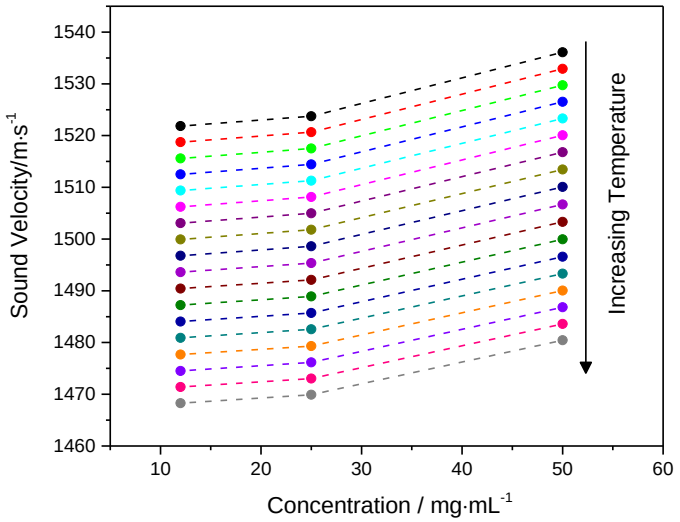

Figure 38. Sound velocity decreases with concentration at any temperature measured.

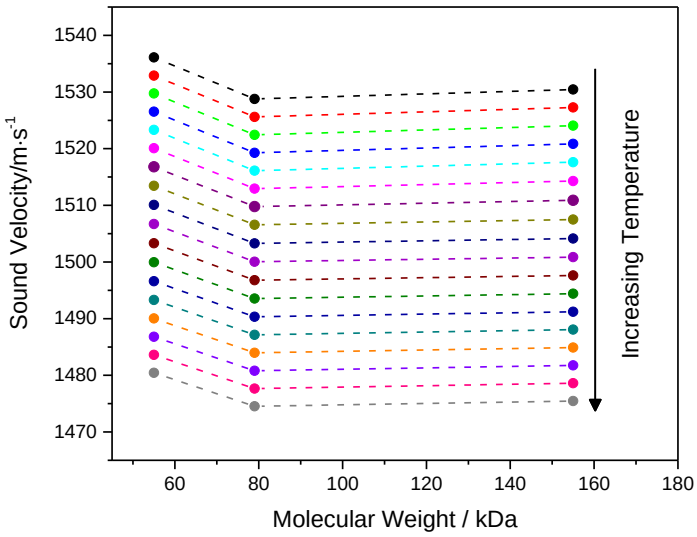

Figure 39. Sound velocity increases moderately with molar mass at any temperature measured.

3.4.10 Physical Insights from the Zimm-Bragg Schellan Model

An investigation was launched to re-introduce the old idea of sound velocity as an analytical method to follow conformational transitions in systems that prove difficult to study by spectroscopy. To identify transition temperatures, the data have been fit to empirical functional forms lacking physical meaning. Although the agreement between OR and SV transition temperatures is usually good, this does not establish a relationship between sound velocity and helical content. Encouraged by helpful reviewers, we now ask whether standard treatments of cooperative transitions can fit the data as well as the empirical approach, while providing physical insight.

The necessary theoretical underpinnings were provided long ago by Zimm and Bragg (ZB).[141, 148] These authors extended the Schellman model[149-152] and reduced some of its limitations by using a powerful and convenient matrix formalism to calculate various parameters, including the average fraction of subunits in the helical state, f_{H}. The model uses two Boltzmann statistical weights, a cooperativity parameter, $\sigma = e^{-\Delta G_{\mathrm{i}}/RT}$, where ΔG_{i} is the Gibbs free energy required to interrupt a helical segment (creating thereby two helix-coil interfaces), and an extension parameter, $s = e^{-\Delta G/RT}$, where ΔG is the Gibbs free energy for extending an existing helical segment by one additional unit. As usual, R is the gas constant and T the Kelvin temperature. In a simple version of the theory, the fraction of helical units is given by

$$f_{\mathrm{H}} = \frac{1}{nz}(1000)\begin{pmatrix} U & U_s \\ 0 & U \end{pmatrix}^n \begin{pmatrix} 0 \\ 0 \\ 1 \\ 1 \end{pmatrix} \tag{3}$$

where

$$U = \begin{pmatrix} 1 & \sigma s \\ 1 & s \end{pmatrix} \tag{4}$$

$$U_s = \frac{dU}{d(\ln s)} = \begin{pmatrix} 0 & \sigma s \\ 0 & s \end{pmatrix} \tag{5}$$

$$z = (1, \sigma s) \begin{pmatrix} 1 & \sigma s \\ 1 & s \end{pmatrix}^n \begin{pmatrix} 1 \\ 1 \end{pmatrix} \tag{6}$$

In these equations, *n* is the number of assignable bonds (the difference between *n* and DP is negligible in our case). These matrix formulae reduce to simple algebraic expressions in the limit of long polymers with high degrees of polymerization.[152] In this high-DP limit, the fraction of subunits in the helical conformation is given by

$$f_{\mathrm{H}} \approx \frac{s}{\lambda} \frac{d\lambda}{ds} \tag{7}$$

where

$$\lambda = \frac{s+1+\sqrt{(s-1)^2+4\sigma s}}{2} \tag{8}$$

If the Zimm-Bragg theory can fit both OR and SV data using the same or similar parameters, confidence in the ability of SV to follow helix-coil transitions would be bolstered. The process of fitting either Equation 3 or Equation 7 to experimental variables relies on the conversion of the OR and SV signals to f_H. In both cases, the sigmoidal signal is assumed to represent the sum of coil and helix contributions. Such a relationship has been suggested for SV[153] and is widely accepted for OR. The conversion of measured data to f_H was facilitated by a graphical interface in Excel software. To set the span of the transition, the low-temperature "floor" of an OR vs T or SV vs T dataset was associated with $f_H = 0$, and the high-temperature "shelf" was associated with $f_H = 1$. We were guided by Matsuoka et al., who estimated $f_H = 0.9$ at 30°C for PCBL in *m*-cresol.[53] Small values of σ are required to capture the sharp increase of f_H with T in PCBL/*m*-cresol, which Matsuoka et al. painstakingly showed to be much more cooperative than most other polypeptide systems. Using the high-DP approximation with appropriate values of σ, the resulting curves tended to overshoot the experimental data, which rose more gradually towards $f_H = 1$ than predicted by Equation 7, as shown in Figure 40A.

The full matrix calculation, Equation 3, matches the data better. This observation calls into question the validity of the high-DP approximation for such a highly cooperative transition, even though all samples are reasonably large (589, 300 and 209 monomer subunits). Figure 40B shows calculations performed using MATLAB (see Supporting Information) for these chain lengths and for higher and lower extremes (2000 and 30

subunits, corresponding to $M_{PCBL} \approx 1.6 \times 10^6$ and $\approx 2.4 \times 10^4$ respectively). The limiting high-DP behavior is not approached, even at our highest molecular weight. Above the transition midpoint, the "climb" is much gentler than it is when using the high-DP approximation.

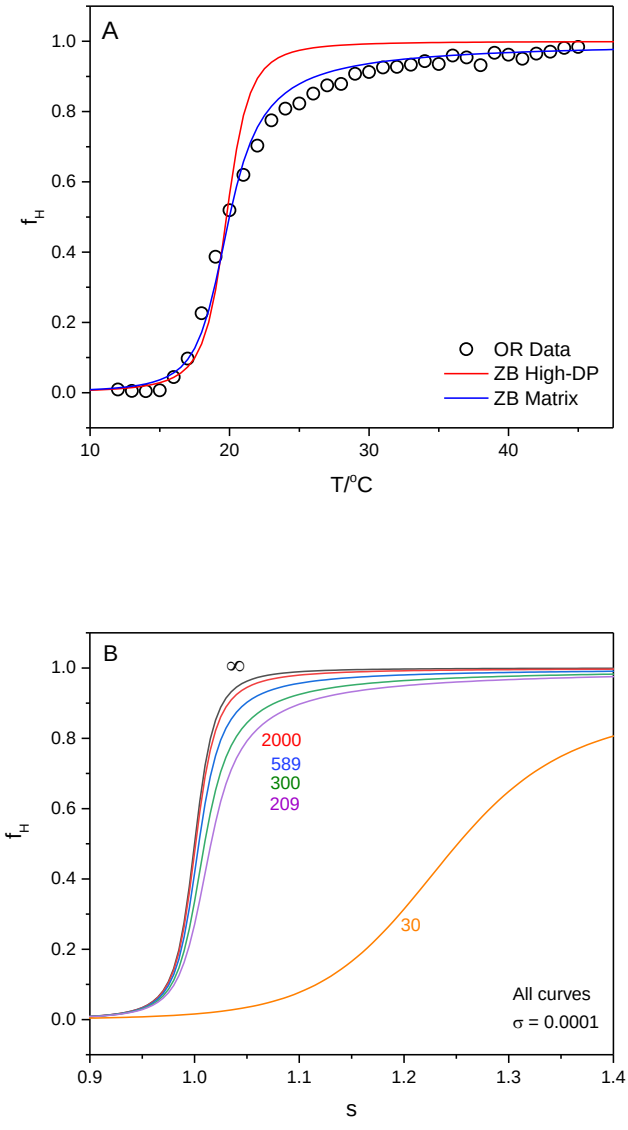

Figure 40. (A) Optical rotation data (PCBL-155,000/m-cresol, 50 mg/mL) was converted to fraction of helical units, fH, as described in the text and overlaid with curves from the Zimm-Bragg theory in its accurate matrix form (blue curve,

Equation 2) and approximation, Equation 3, at various DP values indicated. The calculation was performed for $\sigma = 0.0001$.

Matrix fits to other SV and OR experiments are shown in Figure 41 and Figure 42. The conversion of SV data to f_H was delicate because the temperature range of these experiments was limited, but the transition temperatures were still consistent with those derived from the OR data. The molecular weight and concentration trends for the transition temperatures were the same as those determined using the empirical models. The transition temperatures seem higher for the Zimm-Bragg fits than for the empirical method because we chose the temperature at which $f_H = ½$ as the transition point instead of seeking the peak of a derivative plot (corresponding to the inflection point in the sigmoidal trace itself).

Although the high-DP approximation and full matrix method agreed on the transition temperatures, precise determinations of σ, ΔH and ΔS was challenging by either approach. The same Excel code that facilitated conversion of OR and SV data to f_H was outfitted with a Solver routine to optimize the fit of Equation 7 for ΔH, ΔS and σ. The results were not in satisfactory agreement with those of Matsuoka et al, nor were they good starting points for MATLAB calculations designed to fit the data. The matrix calculations are extraordinarily sensitive to ΔH, ΔS and σ. We began with $\Delta H \approx 0.93$ kcal/mol, as suggested by Matsuoka et al. We chose $\Delta S \approx \Delta H/300\text{K}$ which is sensible for transitions occurring near room temperature. For the cooperativity parameter, we began with the extraordinarily small value determined by Matsuoka at 26.2 °C, $\sigma = 6.25 \times 10^{-6}$. Subsequent adjustments to these parameters are described in the Supporting Information. Our calculations confirm that the PCBL/*m*-cresol system indeed demonstrates high cooperativity. Similar parameters work for almost all the experiments, whether OR or SV,

giving us confidence in the SV method. The intriguing exception was the difficult-to-fit case of OR measurements for the longest polymer at the highest concentration. Here alone, substantially larger ΔH and ΔS values were observed (~1.4 kcal/mol and 0.0049 kcal/mol·K, respectively). This behavior is not understood.

An important addition to the long history of helix-coil transitions was made by Ren et al. who reopened the investigation of the ZB theory, taking advantage of the improved uniformity of polypeptides synthesized using high-vacuum methods.[154] They chose to study PBLG. The stable helices of this polymer in helicogenic solvents necessitated addition of an acid to bring the helix-coil transition temperature within an easily accessible range, which introduces pH and polyelectrolyte effects. The latter will be expected to exacerbate intermolecular interactions and perhaps couple to the helix-coil transition to keep intramolecular charges distant. Preferential solvation is also possible in mixed-solvent systems. It might seem that PCBL/*m*-cresol would be the simpler system to study, but its possible advantage over PBLG/mixed solvents is tempered by complications due to its very high cooperativity. Computationally, the extra steps to implement the matrix calculation to avoid the overshoot phenomenon are no longer a concern. A more significant problem for PCBL might be the possibility of branching during synthesis, due to initiation by any unprotected lysine sidechains.

3.4.11 Zimm-Bragg Simulations and Fitting

Figure 41 and Figure 42 overlay output from the MATLAB code, representing Equation 7, onto data converted to f_H from sound velocity or optical rotation signals. In a typical manual fitting session, we began with $\Delta H = 0.93$ kcal/mol, $\sigma = 6.25 \times 10^{-6}$, and ΔS

= (1/300) kcal·mol^{-1}·K^{-1}. Small adjustments were sometimes made to increase or decrease the span of the SV or OR signals, up to 5% (program variable smush). Only in one case was subtraction a linear offset deemed necessary (about 2%) to ensure a zero signal at low temperatures (program variable offset). Adjustments to match the theory to the data were made, as follows:

- Increase ΔH: flattens low-T part of curve; pushes transition to higher temperatures.
- Decrease σ: sharpens the upturn near the critical temperature and steepens the rapidly rising part of the curve.
- Decrease parameter "smush" (default value = 1). This parameter was used to scale the input data to $f_H \approx 0.9$ at 30°C, as suggested by Matsuoka et al.[1]

The transition temperature was taken as the value when $f_H = ½$. Due to the asymmetry of the sigmoidal curves, which reflects the high cooperativity of the transition, this slightly exceeds the inflection point identified by the empirical method

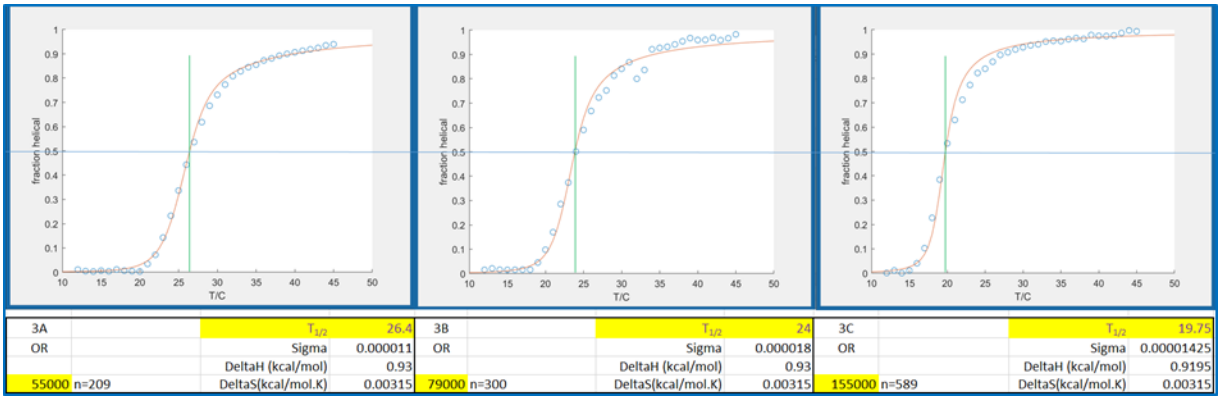

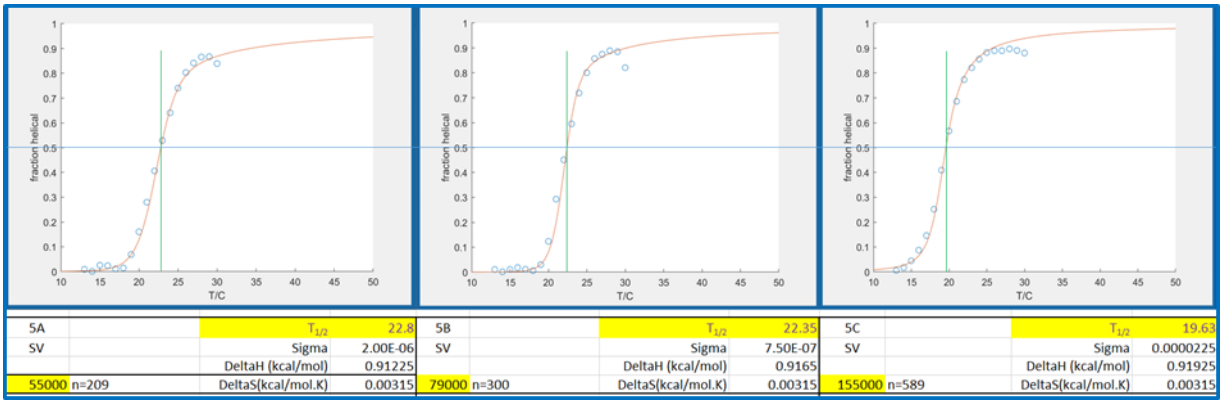

Figure 41. MATLAB-simulated helix vs. temperature curves using Equation 2 of the main text are overlaid on data measured different molecular weights, both for optical rotation (top) and sound velocity (bottom) experiments. Parameters used are shown in tables.

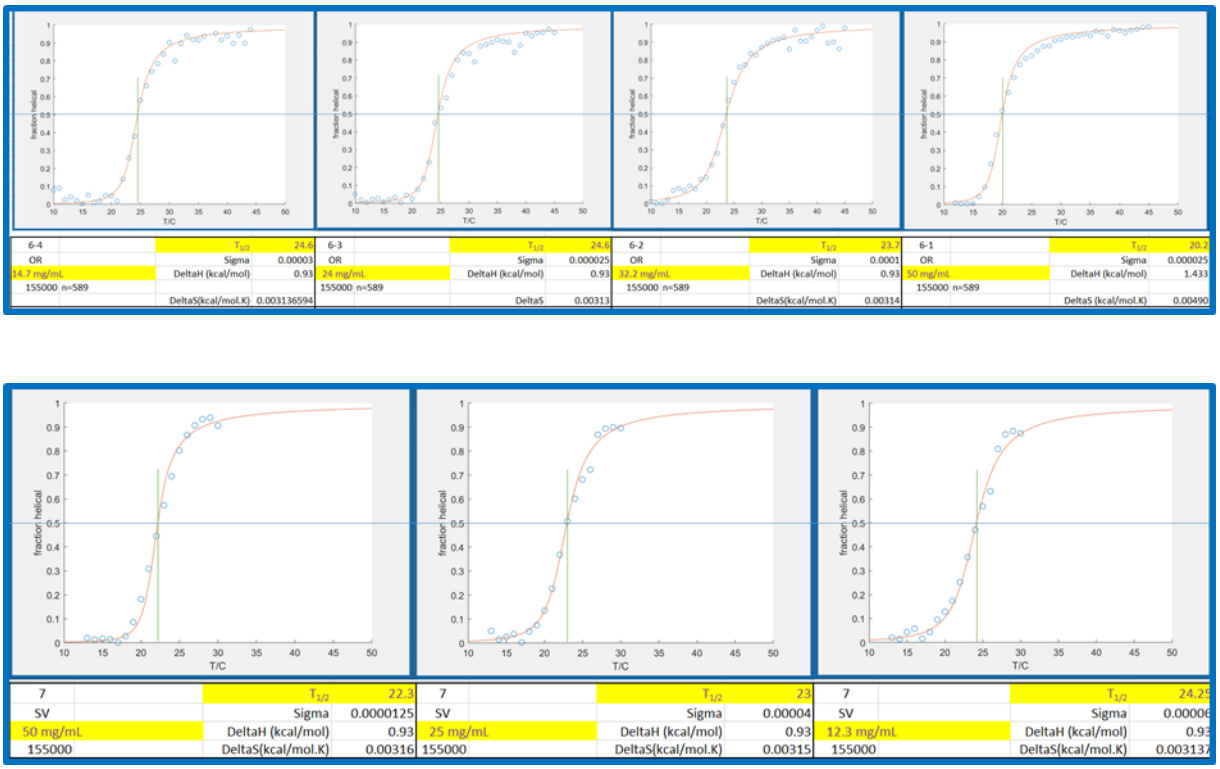

Figure 42. MATLAB-simulated helix vs. temperature curves using Equation 2 of the main text are overlaid on data measured different concentrations for PCBL-155, both for optical rotation (top) and sound velocity (bottom) experiments. Parameters used

in the manual simulation are shown in tables. The sample at 32.2 mg/mL was not measured by SV.

3.5 Conclusion

In the particular case of PCBL/*m*-cresol, trends with concentration and molecular weight were clearly identified, even though the helix-coil transition only slightly alters the temperature dependence of the sound velocity. The difference between sound velocity and optical rotation estimates of the transition temperature is moderate at high molecular weights, but increases at lower ones, suggesting that smaller molecules may be more difficult to detect using the present instrumentation. The more conventional 50% helix transition temperature determined by the Zimm-Bragg method revealed the same trends. The Zimm-Bragg analysis is best performed using its full matrix formalism, especially for strongly cooperative systems. The infinite chain approximation was nevertheless adequate for locating transition temperatures. Regarding studies of other polypeptides in UV-opaque solvents, there is a good chance that sound velocity can follow the transitions almost as well as optical rotation does. The required instrumentation is commercially available, simple, automated, precise, inexpensive, and most of all not defeated by solvent absorption or sample turbidity. It may be anticipated that polypeptide transitions are measurable, even in the presence of particles or other components found in practical formulations. Most of these will be aqueous in nature, and the present study does not guarantee success in that richer environment. The study of polypeptides bound to particles beckons, as does behavior at high concentrations. Finally, although the focus here has been on the detection of transitions using simple instrumentation, sound propagation can reveal even more. For example, Brillouin scattering experiments can return structural details in the colloidal size

regime, which is comparable to that usually associated with large polymers such as the ones studied here.[155]

CHAPTER 4. ORGANOPHILIC, SUPERPARAMAGNETIC AND REVERSIBLY THERMORESPONSIVE SILICA POLYPEPTIDE CORE SHELL PARTICLES

Adapted with permission from Turksen-Selcuk, S.; Rosu, C.; Blake, A.; Soto-Cantu, E.; Qiu, J.; Wu, Y.; DiTusa, J.F.; Steffens, A.; Russo, P. S., Organophilic, Superparamagnetic and Reversibly Thermoresponsive Silica-Polypeptide Core-Shell Particles. *Langmuir* 2019, 35, 44, 14248-14257.

*Contributed to the following sections: Methods - 4.3.1, 4.3.2, 4.3.3, 4.3.5, 4.3.7, 4.3.8, 4.3.9, 4.3.11 and Results – Particle Visualization, GPC Particle Characteristics, and Optical Rotation Evidence of Conformational Transition

4.1 Introduction

Interest in stimulus-responsive core-shell particles with tailored structure and surface properties is driven by the demand for such materials in biomedical, electronic, purification and sensory applications.[5, 28, 156] The applied stimulus can be magnetic, electrical, pH, thermal, or photonic, but usually it is just one of these. Multifunctional particles that combine responses are needed to mimic the extraordinary functions of bioparticles. For example, influenza viruses carry information in the form of a nucleic acid "blueprint" for reproduction, along with a shell that expands and contracts in response to pH, helping the particles gain access to the host cell.[157] Such sophistication is lacking in synthetic particle technology, and this is particularly true for organosoluble particles that can be investigated in the absence of strong salt- or pH-induced effects.

It will be some time before the elegance of bioparticles can be duplicated in the laboratory. Here, a simple approach was followed to combine thermal and magnetic response, along with other features such as chirality and optical activity, by attaching synthetic polypeptides to silica cores to yield polypeptide-composite particles. With only minor variations, silica-polypeptide chemistry can lead to particles that function in aqueous media or typical organic solvents. Polypeptides can exhibit a coil⇔helix transition, even in organic solvents or their mixtures with strong organic acids.[158-160] This transition tends to be cooperative and sharp.[161-162] Most of what is known about conformational transitions of covalently bound homopolypeptides has been determined by attaching them to flat surfaces,[163-168] but polypeptides can be grown one monomer at a time on spherical silica particles, or even attached to them after polymerization. This field has been reviewed,[169-170] as has recent progress in polypeptide synthesis[171] and responsiveness.[68] In addition to drug delivery or protein enrichment,[172] potential applications include colloidal crystals that self-anneal, taking advantage of thermal transitions to grow larger domains for improved performance, or poly(colloids) created by magnetic chaining that expand or contract in response to thermal stimulus. After deprotection of the benzyl sidechain and dispersion in an aqueous medium, such poly(colloid) fibrils can be expected to expand and contract in response to pH or salt. Long ago, Pauling and Corey considered the coil⇔helix transition as the motive force underlying muscle action.[173] Today it is known that is not how muscles work, but Pauling and Corey's calculation of the energetics shows that it is not unreasonable to dream of muscle-like actuators built by assembling polypeptide composite particles.

To start along a path leading to such futuristic materials, an investigation of the reversible coil⇔helix conformational transition of PCBL (poly(ε-carbobenzyloxy-L-lysine)) covalently attached to a Co@SiO_2 core in response to thermal and magnetic stimuli. Unlike the more commonly studied PBLG (poly(γ-benzyl-L-glutamate)), which has been attached to Fe_3O_4-containing magnetic silica particles,[90] untethered PCBL polymer exhibits an inverse (coil to helix) transition as the temperature rises above 27°C in *m*-cresol.[158] The transition is fully reversible. From the standpoint of fundamental science, the existence of a well-behaved conformational change in a pure organic solvent is especially attractive because transitions can be studied without interference from strong electrostatic forces. It was known at the outset of this study that particles with a very high grafting density and therefore a crowded surface fail to exhibit a coil⇔helix transition.[174] The shell cannot be too sparsely populated with PCBL, though, because then its transitions will be difficult to follow. To achieve a response that can be detected, the particles presently under discussion were made using partially functionalized/partially passivated silica cores as described previously.[175] A variety of techniques confirm the coil⇔helix transition for the PCBL polymer when tethered to the Co@SiO_2 particle. The PCBL polymer, analyzed after detachment from the Co@SiO_2 core, exhibits a remarkably broad molecular weight dispersity. The possibility that the PCBL shell, which greatly outweighs the cobalt inclusion, could modulate the overall particle magnetic response is considered. Portions of this work have appeared in preliminary form.[176-178]

4.2 Materials

The overall preparation of the particles is shown in Scheme 1. Unless otherwise noted, all synthetic procedures were carried out in a dry, inert nitrogen atmosphere. Chemicals and solvents were obtained from Sigma-Aldrich, Pharmco-AAPER, or Acros Organics with the highest purity available, as described in greater detail elsewhere,[94, 179-181] and used without further purification. The solvents used for the synthesis of the monomers and covalently attached polymer shell were all anhydrous and purchased in Aldrich Sure-Seal™ bottles. Water was supplied by a Barnstead Nanopure Water System (18 MΩ cm) equipped with spiral-wound ultrafilter (nominally 5 nm).

4.3 Methods

4.3.1 Synthesis of superparamagnetic cobalt coated with silica, Co@SiO2, and amino-functionalized silica-coated cobalt, Co@SiO2-NH2

The procedure to synthesize the superparamagnetic cores and functionalize their surfaces is based on a method developed by Kobayashi *et al.*,[182] with some modifications.[183] A solution consisting of 200 mL of 4.0×10^{-3} M $NaBH_4$ was prepared with 4.0×10^{-4} M citric acid. While sonicating and bubbling with nitrogen, 200 mL of $NaBH_4$ was mixed with 0.2 mL of 0.4 M $CoCl_2 \cdot 6H_2O$ for 1 min and 800 mL of absolute ethyl alcohol solution containing 14.4 µL 3-aminopropyltrimethoxysilane (APTMS) and 169 µL tetraethylorthosilicate (TEOS) was added rapidly. The reaction continued for 1 h under N_2 bubbling and probe sonication. After 1 h the particles were collected by centrifugation and washed 3× with anhydrous ethanol. The collected particles were

dispersed in 500 mL of absolute ethyl alcohol and mixed for 18 h with 0.1 mL of a mixture of 75% methyl trimethoxysilane (MTMS) and 25% N-[3-(Trimethoxysilyl)propyl]ethylenediamine] (AEAPTMS for the traditional, non-IUPAC name [(aminoethylamino)propy]ltrimethoxysilane). Afterwards, the mixture was concentrated to 1/3 of its original volume by a rotary evaporator. Then the particles were washed by centrifugation-redispersion with anhydrous ethanol until a ninhydrin test indicated proved the absence of free amine groups in the decanting liquid.

4.3.2 Preparation of Nε-carbobenzyloxy-L-lysine N-carboxyanhydride (CBL-NCA) monomer.

The general procedure of Daly and Poche'[61] was used, including the product purification method of Poché.[40] In a typical preparation, 5 grams of the amino acid Nε-carbobenzyloxy-L-lysine (CBL) was dissolved in 150 mL of anhydrous ethyl acetate in a 3-neck round bottom flask fitted with a reflux condenser and a nitrogen bubbler. The solution was heated to reflux and no more than 1/3 equivalent of triphosgene was added rapidly. The reaction continued to reflux under nitrogen for 4 h. As the reaction solution cleared, the flask containing the mixture was cooled to -5°C overnight. The cold solution was then washed quickly in a separatory funnel with 50 mL de-ionized water cooled to 0°C, followed by a wash with 50 mL of 0.5% $NaHCO_3$ chilled to 0°C. The organic layer was dried with anhydrous $MgSO_4$ as quickly as possible and gravity filtered. The solution was concentrated to 1/3 of its original volume under constant flow of nitrogen in a glove bag. Afterwards, 100 mL of anhydrous hexane was added to the solution causing the precipitation of the monomer. The concentrated slurry was kept overnight at -5°C, then collected by suction filtration in a glove bag under constant flow of nitrogen. The CBL-

NCA monomer was dried in a vacuum oven for 24 h. The typical yield is 70%. Additional details appear elsewhere.[184]

4.3.3 Polymerization of untethered poly(ε-carbobenzyloxy-L-lysine), PCBL

In nitrogen-filled glove bag, ~2.00 g of CBL-NCA was dissolved in 50 mL of anhydrous THF inside a 100 mL oven-dried round bottom flask. A magnetic stir bar was placed into the flask and capped with a rubber septum. The flask was placed into an aluminum bead bath (Lab Armor Beads) and sodium methoxide solution (0.3 mL) was injected. A bubbler containing silicon oil was connected to the flask and the reaction was heated to 35 °C and stirred until there was no bubble formation inside the oil in the bubbler (usually 2 days). The flask was then connected to a rotatory evaporator to reduce volume to 1/3 to obtain a viscous solution that was slowly poured into a beaker containing water. This caused the polypeptide to precipitate out of solution and the precipitate was suction filtered using a Whatman 90 mm filter paper and allowed to dry.

4.3.4 Synthesis of Co@SiO_2-PCBL particles by growing-from procedure

The amino-functionalized Co@SiO_2-NH_2 particles prepared as described above were dispersed in anhydrous dioxane by centrifugation-redispersion (2×). Then typically 20 mL of the dispersion was added to 5.0 g of the CBL-NCA, which was pre-dissolved in 200 mL of anhydrous dioxane in a round-bottom flask. The reaction vessel was connected to an Erlenmeyer flask filled with 50 mL 1N NaOH to capture the released CO_2. The reaction continued for 3 days at 35 °C in a nitrogen-inflated glove bag. The particles were collected by centrifugation and washed three times with dioxane and three times with dimethylformamide (DMF) to remove any untethered PCBL chains. In previous studies, it

was demonstrated that deliberately added polypeptide chains were removed by a similar procedure, while attached chains remain.[179] The XPS spectra confirm the desired chemistry at key steps (Figures S3 and S4). The particle batch was split and finally dispersed in DMF and *m*-cresol.

4.3.5 Removal of Co@SiO2 Core

Co@SiO_2–PCBL particles were precipitated out of DMF suspensions by adding water. The sample in a 4-mL vial was placed into a vacuum oven overnight at $T < 60$ °C to remove the water completely. The dried Co@SiO_2-PCBL particles had a mass of ~5–10 milligrams. About 2 mL of 5% HF solution was added to the dried particles (Caution: HF is toxic; double gloves, face shield, lab coat and apron are required, as well as calcium gluconate set aside from the immediate work space to apply to skin in case of contact. Teams of at least two were used for increased safety.) The vials sat undisturbed for 48 hours, allowing the HF to penetrate the particles and etch the silica cores. The 5% HF solution was then removed from the vial using a disposable

4.3.6 Dynamic Light Scattering

Samples were measured in dust-free 13 mm screw cap Pyrex test tubes. Each cell was precleaned using water from a Barnstead Nanopure water system equipped with spiral-wound, 5 nm ultrafilter, and tested for cleanliness by visual observation of the laser beam at ~40× magnification as it traversed the sample cell held in the scattering device. The cleaned and tested cells were wrapped in rinsed aluminum foil to prevent dust contamination, then dried in an oven prior to use. The solvents used for the scattering analysis of the cores were Nanopure water and ethyl alcohol, while the polypeptide-grafted

particles were analyzed in *m*-cresol. Organic solvents were purified from dust by a combination of centrifugation and filtration (0.1 μm Whatman PTFE), then transferred into the dust-free glass cells.

A custom-built multiangle apparatus equipped with 632.8 nm laser and ALV-5000 digital autocorrelator was used. To assess particle uniformity at three temperatures, measurements were made at multiple scattering angles from 30° to 90°. Subsequently, details of the expansion and contraction of Co@SiO_2-PCBL particle size in *m*-cresol were monitored with greater temperature resolution for several heating-cooling cycles at a single scattering angle of 75°. Cumulants and single-exponential analyses were used to fit the autocorrelation functions for these particles. Using the Stokes-Einstein relation, the apparent hydrodynamic radius, $R_{h,app}$ was calculated from the apparent diffusion, D_{app}, defined as the autocorrelation function decay rate Γ divided by the squared scattering vector magnitude, q^2. The required *m*-cresol viscosity (η) data as a function of Kelvin temperature (T) were taken from Tewari, Vesudevan and Ramakrishna.[185] Their results can be summarized by a linear Arrhenius fit:

$$\ln(\eta\,/\mathrm{cP}) = (-13.20 \pm 0.23) + (4709.7 \pm 67.3) \times (T\,/\mathrm{K})^{-1}$$

4.3.7 Transmission Electron Microscopy (TEM).

Samples were deposited onto carbon-coated copper specimen grids and dried in air. A Hitachi HD-2700 STEM working at an accelerating voltage of 200 kV was used to image the individual silica-coated cobalt particles. A JEOL 100 CX-II TEM working at an accelerating voltage of 100 kV was used to image the larger grouping of silica-coated cobalt particles and the silica coated cobalt snakes.

4.3.8 Scanning Electron Microscopy (SEM).

Samples were deposited onto silicon wafers and dried in air. A Hitachi SU8230 SEM working at an accelerating voltage of 1.5 kV was used to image the non-magnetic polypeptide-coated silica particles using the lower secondary electron detector. The SEM working at an accelerating voltage of 5 kV was used to image the polypeptide-coated cobalt-silica particles using both the upper and lower secondary electron detectors.

4.3.9 Gel Permeation Chromatography/Multiangle Light Scattering (GPC/MALS).

The molecular weight of PCBL was measured using a Tosoh EcoSEC HLC-8320GPC connected to a Wyatt Dawn EOS multi-angle-light scattering detector. The mobile phase was N,N-Dimethylformamide with 0.1M LiBr flowing at 0.35 mL/min. A TSK guard column SuperH-H (4.6mm ID × 3.5 cm L) was placed before two TSKgel SuperHM-H (mixed-bed) analytical columns (6.0 mm ID × 15 cm L), and the instrument temperature was set to 60 °C. Polymer samples of concentration 3–8 mg/mL were dissolved overnight prior to measurements. Solutions were filtered through Whatman PTFE 0.45 μm syringe filters into Agilent 2 mL GPC vials containing a 250 μL borosilicate glass conical insert to accommodate the small total volume. Three injections (20 μL) were performed for each sample. The specific refractive index increment, *dn/dc*, was 0.114 mL/g.

4.3.10 X-ray Photoelectron Spectroscopy (XPS)

The surface composition of the core and core-shell particles was investigated with a Kratos Analytical Axis 165 X-ray photoelectron spectrometer (XPS) with Al Kα-

radiation with an energy of 1.48 keV and a takeoff angle of 90°. For each sample, a survey spectrum was acquired using a pass energy of 80 eV, in addition to high-resolution spectra of all individual elements using a pass energy of 40 eV. The peak locations were calibrated based on the C1s signal at 284 eV.

4.3.11 Optical Rotation

Optical rotation measurements were carried out on a Jasco CD J-815 spectropolarimeter equipped with an ORDM-401 attachment featuring an optical null. Instrument performance was verified using sucrose in water and poly(γ-benzyl-α,L-glutamate) in dimethylformamide, DMF.[159, 161, 186-187] The optical rotation of PCBL-coated cobalt particles was measured in a temperature range of 10–50 °C with a precision of ± 0.1 °C. Each reported spectrum is a collection of 5 accumulations consisting of wavelength scans from 600–300 nm. Specific optical rotation at 436 nm was calculated from the raw optical rotation and subtracted manually from the blank (a cell containing *m*-cresol). An ORDM ZeroClear protocol was executed before each sample was analyzed. The raw optical rotation data was converted into specific optical rotation using the equation,

$$\alpha_{sp} = \frac{100 \cdot \alpha_{op}}{l \cdot c} \tag{9}$$

where α_{sp} is the specific optical rotation, α_{op} is optical rotation, l is the length of the cuvette in dm, and c is the concentration of the solution in g/100 mL.

4.3.12 Fourier Transform Infrared Spectroscopy (IR)

Infrared spectra were recorded with a Bruker Tensor 27 FT-IR spectrometer. A Spectra Tech high-pressure *in situ* reaction cell with a ZnSe ATR crystal was used to monitor the spectral changes of Co@SiO_2-PCBL in *m*-cresol as a function of temperature. Spectra were analyzed with OPUS 4.2 software. Each spectrum is a collection of 16 scans depending on the sample concentration (~ 50–60 ppm). Solvent (*m*-cresol) was measured as a background before the sample measurements.

4.3.13 Magnetization and Magnetic Susceptibility

Magnetic properties of the particles were measured in a Quantum Design Magnetic Property Measurement System (MPMS) SQUID magnetometer for temperatures between 10 and 50° C in fields of up to 50 kOe. Dried Co@SiO_2 samples were placed in gelatin capsules and measured inside quartz tubes. Liquid Co@SiO_2-PCBL dispersions were measured in custom-built quartz tubes with a seal made of poly(tetrafluoroethylene). Empty cell backgrounds were measured and subtracted from the raw data.

4.4 Results and Discussion

4.4.1 Particle Synthesis

Figure 43 illustrates the steps involved in the preparation of the Co@SiO_2-PCBL particles. After the cobalt–containing silica particles were synthesized, their surface was functionalized with a mixture of MTMS (75%) as spacer group and surface passivator and AEAPTMS (25%) as initiator for the ring-opening polymerization of CBL-NCA monomer.

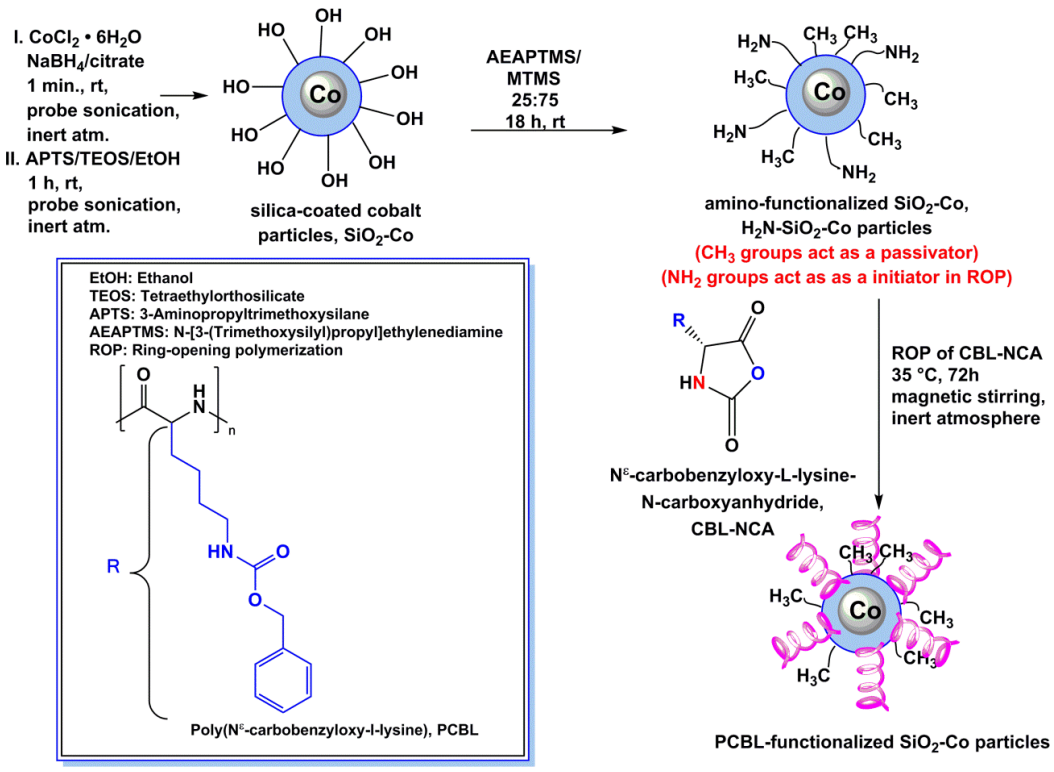

Figure 43. Schematic illustration of the steps involved in the preparation of PCBL-functionalized superparamagnetic silica particles (Co@SiO2-PCBL).

4.4.2 Particle Visualization

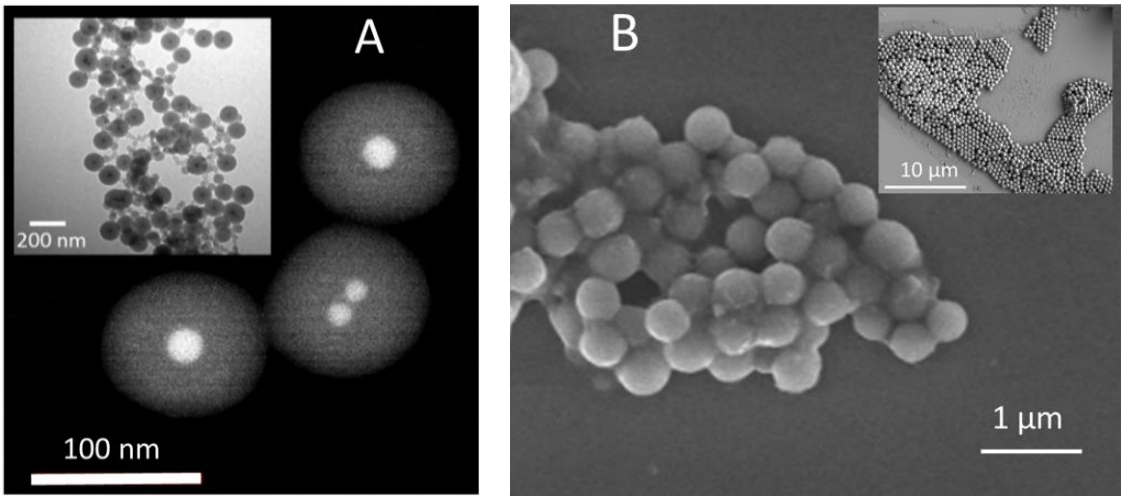

Figure 44. TEM negative image of unstained silica-coated cobalt particles; most have one central Co inclusion; inset shows positive image prior to isolation of Co-

containing particles by magnetic separation (A). SEM image of Co@SiO2-PCBL composite particles; inset: nonmagnetic PCBL-SiO_2 particles (B).

TEM images of typical cobalt-containing core particles are shown in Figure 44A. Most particles have a single cobalt inclusion, but imperfections do occur during the synthesis. Particles lacking a Co inclusion (a few are visible in the inset to Figure 44A) are easily separated from the Co-containing ones by attraction of the latter towards a magnet. A different issue can arise if the Co inclusion grows too large. If the diameter of the cobalt particles exceeds about 8 – 10 nm, permanent magnetic dipoles become stable and the particles chain together even without application of a magnetic field (Figure 45). Such particles were not used in this experiment but isolated and retained for other applications. Figure 44B shows a SEM image of the polypeptide-coated magnetic silica recovered after scattering measurements in *m*-cresol, followed by solvent exchange to DMF before deposition on the SEM stub. The inset shows a larger count of PCBL-coated silica particles, in this case without the magnetic nougat to demonstrate that magnetic and non-magnetic particles have the same spherical shape and size. Electron diffraction patterns were featureless, due to the amorphous nature of cobalt and silica, in agreement with Kobayashi *et al*.[188]

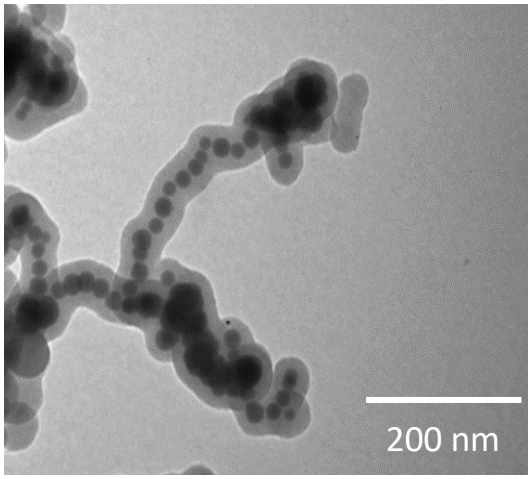

Figure 45. TEM images of unstained silica-coated cobalt particles, chained together because the Co cores grew too large to remain superparamagnetic.

4.4.3 Surface Group Characterization

XPS survey results obtained from the Co@SiO_2 core and Co@SiO_2-PCBL hybrid particles appear in Figure 46. The difference between the two Co@SiO_2-PCBL samples (Figure 46 C and D) is the way they were collected, which was either by attraction to a magnet or by sedimentation in water. Only particles collected by magnet were used for the studies in the main document. The collection of these two samples was to address the issue of whether the magnetically active particles differ from all particles, including any that may lack a Co inclusion and therefore cannot respond to the magnet. The experiment was motivated by early concerns that not all cobalt inclusions would be covered by a layer of silica—i.e., that some might be present on the surface to hinder initiation and growth of the polypeptide shell. Both Co@SiO_2-PCBL samples showed the presence of the polypeptide on the surface through the increase in the intensity of C and N peaks. Comparing Co@SiO_2 particles to amino-functionalized silica particles, the N 1s peak indicates the successful attachment of the amino silane group on the surface. The intensity of the N 1s peak

increases as the polymer is attached to the surface as well as that of the C 1s peak. Figure 47 compares high-resolution scans from individual elements detected on the surface. The decrease in the Si 2p for amino-functionalized silica particles compared to bare Co@SiO_2 particles indicates the attachment of the aminosilane group on the surface. As each layer is added to the particle, the signal intensity coming from the bottom layer diminishes.

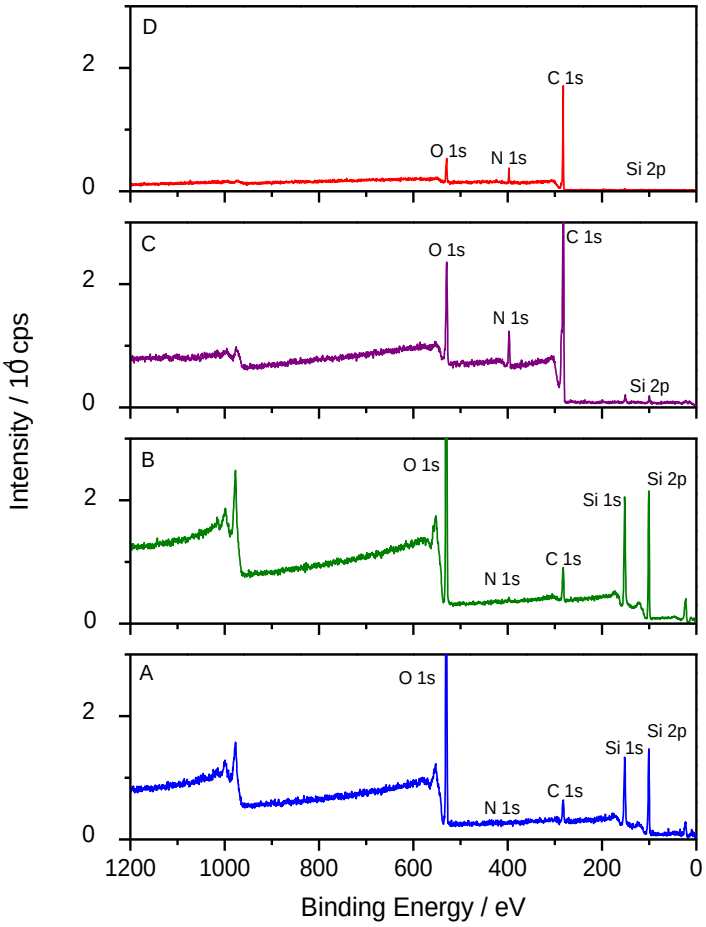

Figure 46. X-ray photoelectron survey spectra of (A) silica particles (B) amino functionalized silica particles (C) Co@SiO2-PCBL particles collected via magnet (D) Co@SiO2-PCBL particles collected via precipitation

The intensity further decreased with the addition of the polypeptide layer on the surface. Even though bare silica particles do not have carbon on the surface, some of the impurities or methoxy groups which stayed attached to the surface can contribute to the peak. As other layers are added to the particle the increase in the intensity of the carbon is consistent with the attachment of the polypeptide. N 1s is difficult to determine with these particles because the nitrogen concentration is very low compared to the other elements on the surface. The intensity of the nitrogen increases with the polypeptide attachment because they contain -NH2 groups on the top layer of the surface and –NH groups in the sidechain. Finally, the O1s intensity decreases and shifts slightly as the polypeptide is attached to the surface. For silica particles, the oxygen source is predominantly the Si-O-Si that forms the particles as well as the –OH groups on the surface. When the polypeptide grows, these groups are obscured. The new oxygen group closer to the surface is coming from the polypeptide and they are not as abundant as Si-O, so the intensity decreases. Also the peak shifts slightly because the oxygen sources are different.

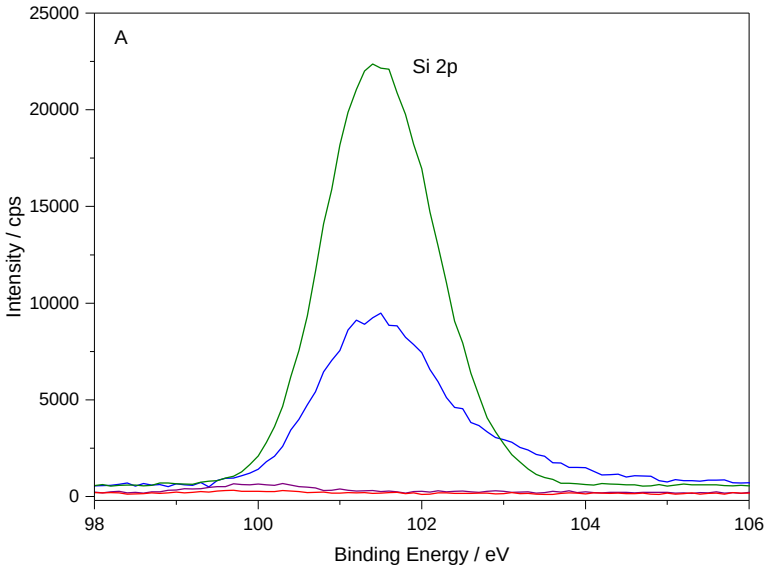

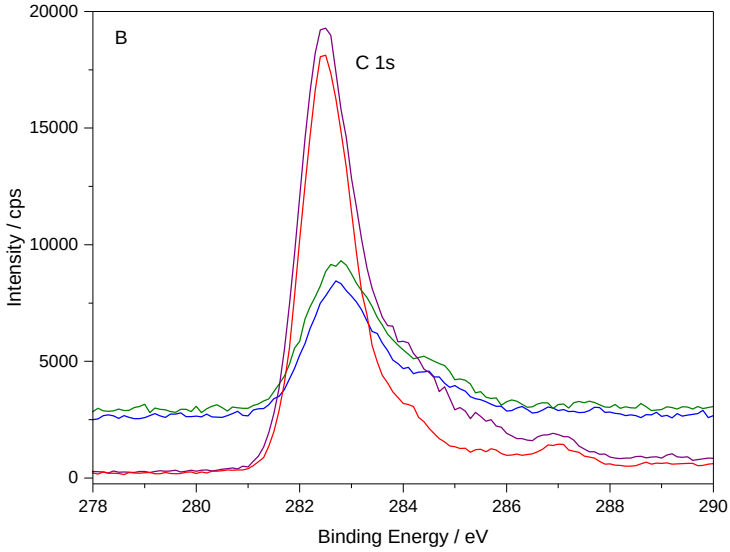
B
C 1s
Intensity / cps
Binding Energy / eV
20000
15000
10000
5000
0
278
280
282
284
286
288
290

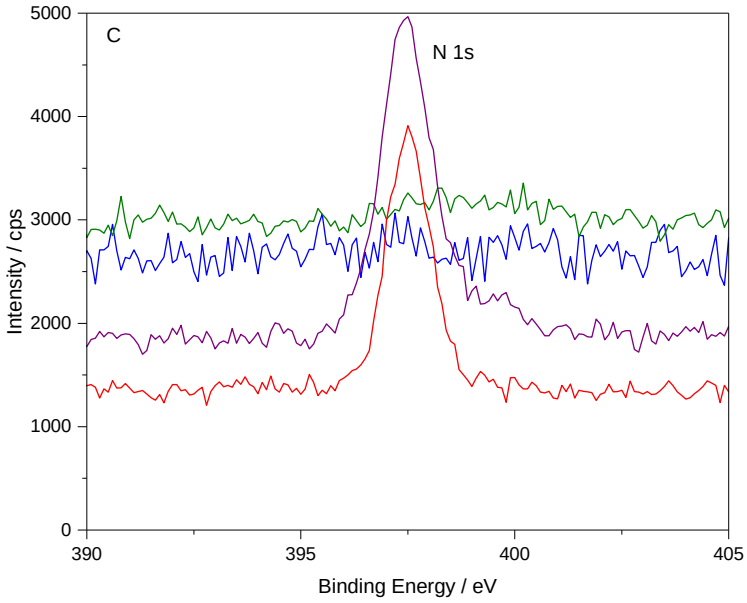
C
N 1s
Intensity / cps
Binding Energy / eV
5000
4000
3000
2000
1000
0
390
395
400
405

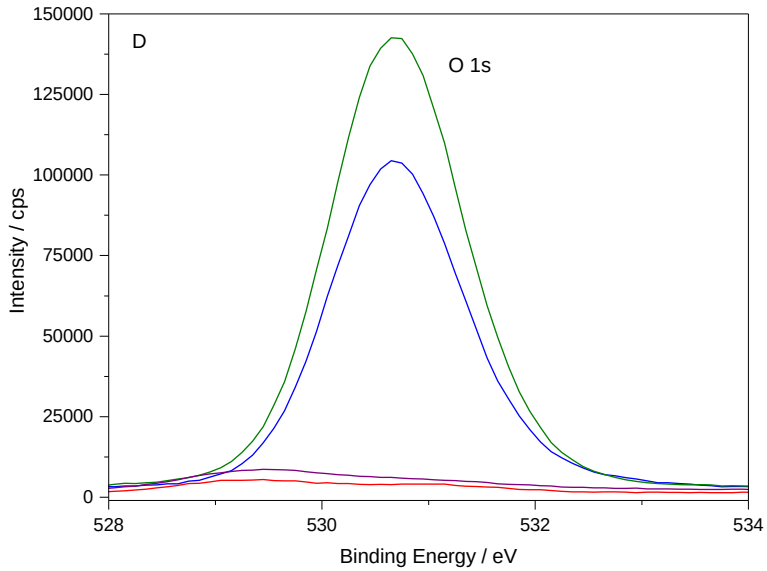

Figure 47. The XPS detail scans corresponding to (A) Si 2p (B) C 1s (C) N 1s (D) O 1s; (---) Silica particles, (---) Functionalized silica particles, (---) Co-PCBL collected via magnet, (---) Co-PCBL collected via sedimentation.

Table 7 shows the atomic compositions and mass percentages of the carbon, nitrogen, oxygen and silica present in the samples. There is a significant increase in carbon and nitrogen for the Co@SiO_2-PCBL hybrid particles when compared to the bare Co@SiO_2 cores. XPS can only detect within 10–20 nm of the surface of the samples; a layer of polymer weakens the signals from oxygen and silica in the core. The strong oxygen peak coming from the SiO_2 is replaced with the oxygen coming from the polymer shell. The calculated compositions are broadly consistent with the desired PCBL structure for the shell (expected atomic compositions for PCBL, neglecting hydrogen: 74% C, 10% N, 16% O). Not only are the compositions reasonably close to those expected for PCBL, the results do not depend on whether the samples were collected by magnet or by precipitation. This finding alleviates any residual concern that some Co inclusions would be located not at the

center of the silica spheres, but near the surface where they could influence the chemistry to functionalize the surface and initiate the growth of PCBL chains.

Table 7. Composition of Samples from XPS. [a]Collected via Magnet and [b]Collected by Sedimentation in Water.

	ATOMIC CONCENTRATIONS			MASS PERCENTAGE		
ELEMENTS	Silica	Co-PCBL[a]	Co-PCBL[b]	Silica	Co-PCBL[a]	Co-PCBL[b]
C-1s	10.74	80.02	80.29	6.67	74.79	75.91
N-1s	0.46	6.56	8.07	0.33	7.15	8.9
O-1s	57.48	11.98	11.08	47.53	14.92	13.95
Si-2p	31.32	1.44	0.56	45.47	3.14	1.24

4.4.4 Particle Characteristics

The batch chosen for this study had a Co@SiO_2 core radius of 88 nm and Co inclusion radius of ~9 nm. X-ray photoelectron spectra (Figure 46 and Figure 47) measured at various stages during the synthesis and subsequent thermogravimetric analysis of the final product demonstrated the progression of surface functionality expected for the reactions in Figure 43. Primary amines do normally initiate NCA monomers with attachment,[189] but absolute proof that the initiating amines have done so in this case is difficult for high-*M* shells. Previous studies have demonstrated the effectiveness of the

washing procedure, though. It completely removes unbound polypeptide even after its deliberate addition to bare silica.[179] Thermogravimetric analysis (Figure 48) quantified the amount of shell material present. The PCBL shell on the samples selected for further investigation accounted for ~39% of particle mass indicating well-solvated chains. The initial mass loss occurred around 300°C. The decomposition profile ended with a total mass of 60.8% of the original at 580°C, at which temperature a white-light gray solid residue remained.

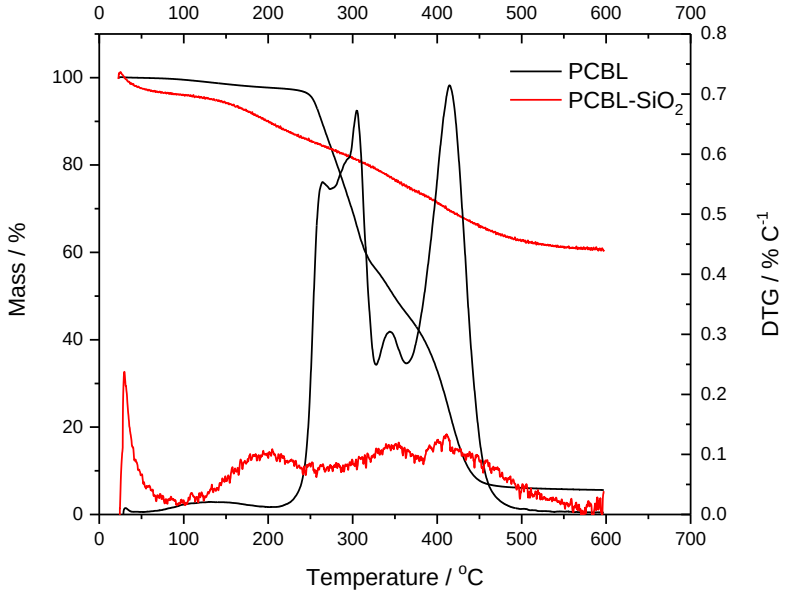

Figure 48. Thermogravimetric analysis of PCBL and Co@SiO2-PCBL magnetic cobalt-silica particles coated with PCBL. Also shown are the corresponding derivative plots.

Fong *et al.*[179] measured the particle core and the shell thickness to estimate the effective polypeptide density on the surface of PBLG-coated particles. By using a similar approach, the total mass of the PCBL-coated cobalt-silica samples can be estimated from

$$m_{tot} = \frac{4\pi}{3}[R_{Co}^3\rho_{Co} + (R_{Co-Si}^3 - R_{Co}^3)\rho_{SiO_2} + (R_{tot}^3 - R_{Co-Si}^3)\rho_{PCBL}] \quad (10)$$

where R_{Co} is the radius of the cobalt inclusion (9 nm; it is assumed there is one per composite particle), $R_{Co\text{-}Si}$ is the radius of silica-coated cobalt core particles (87.5 nm) and R_{tot} is the overall particle size after the grafting of the polypeptide (about 300 nm but it depends on temperature, as described in the main text). The density of cobalt, ρ_{Co}, is 8.9 g/cm^3, and the density of SiO_2, ρ_{SiO_2}, is 1.96 g/cm. Thus, the cobalt contributes 0.49% of the core mass, which is 60.8% of the total. The density of *solid* PCBL, ρ_{PCBL}, is about 1.26 g/cm^3 , but it is not safe to assume the shell is fully packed; instead, it is solvated. Adjustment of ρ_{PCBL} in Equation 10 to achieve a mass percent of 60.8% for the core, including Co nougat and SiO_2, leads to an effective density for PCBL in the shell of 0.049 g/cm^3. The Co mass is about 0.77% of the PCBL mass, or $m_{PCBL} = 130m_{Co}$. The percentage of mass attributed to the Co nougat is miniscule by comparison, about 0.3% of the total particle mass, about 130 times less than the PCBL mass.

These TGA results show much higher surface coverage than those previously published for PBLG-coated SiO_2 by Fong *et al.*[179] This is despite lower amino surface functionalization, thanks to the partial passivation scheme and extended AEAPTMS initiator used in the present work.

After digestion of the core by HF and collection of the PCBL shell and dissolution into the DMF-LiBr mobile phase, GPC/MALS revealed predominantly low-*M* polymer (2,700 g·mol^{-1}; $Đ$ = 1.1) but with substantial amounts of high-*M* polymer (M_w = 96,500

g·mol^{-1}; $Đ$ = 1.7). The weight average length of the larger polymer in helix form is L_w = 55 nm (i.e., $M_w \times h/M_o$ where h is the axial projection of the α-helix, 0.15 nm, and M_o is the monomer molar mass, 263 g·mol^{-1} for PCBL). Figure 49 reveals the presence of even larger polymers, up to at least M = 400,000 g·mol^{-1}, corresponding to L = 230 nm. When added to the Co@SiO_2 core (88 nm radius), the complete particle radius is expected to be about 318 nm at full helix extension. This estimation assumes possible extension of the helix near the particle surface is offset by partial draining near the particle periphery.

Figure 49B shows triplicate runs of the measured radius of gyration, R_g, of the PCBL chains clipped from the particles by HF, overlaid on triplicate runs of never-tethered PCBL prepared by initiation in free solution. The traces for the never-tethered PCBL are noisier because this sample was more uniform in length, meaning that high-M and low-M data lie in the wings of a GPC/MALS peak that is narrow compared to that shown in Figure 49A. Neither polymer approaches the sizes achieved by Fasman, Idelson and Blout[190] using methoxide as initiator, but they can be compared in the molecular weight range spanning 100,000 to 200,000 g·mol^{-1}. In this range, the HF-clipped PCBL and never-tethered PCBL have about the same R_g values, so the physical attributes, as seen by light scattering, are the same. Neither PCBL sample matches the expected size for a completely rigid α-helix ($R_{g,helix} = L/12^{1/2}$ where $L = M \times h/M_o$) but this is not surprising, as PCBL has long been known to lack the rigidity of, say, PBLG.[190] The data are consistent with a Flory exponent, ν_F in $R_g \propto M^{\nu_F}$, of about 0.8. This value should not be regarded as definitive for PCBL/DMF-0.1M LiBr because the range of measurement is too small, but it indicates an extended polymer.

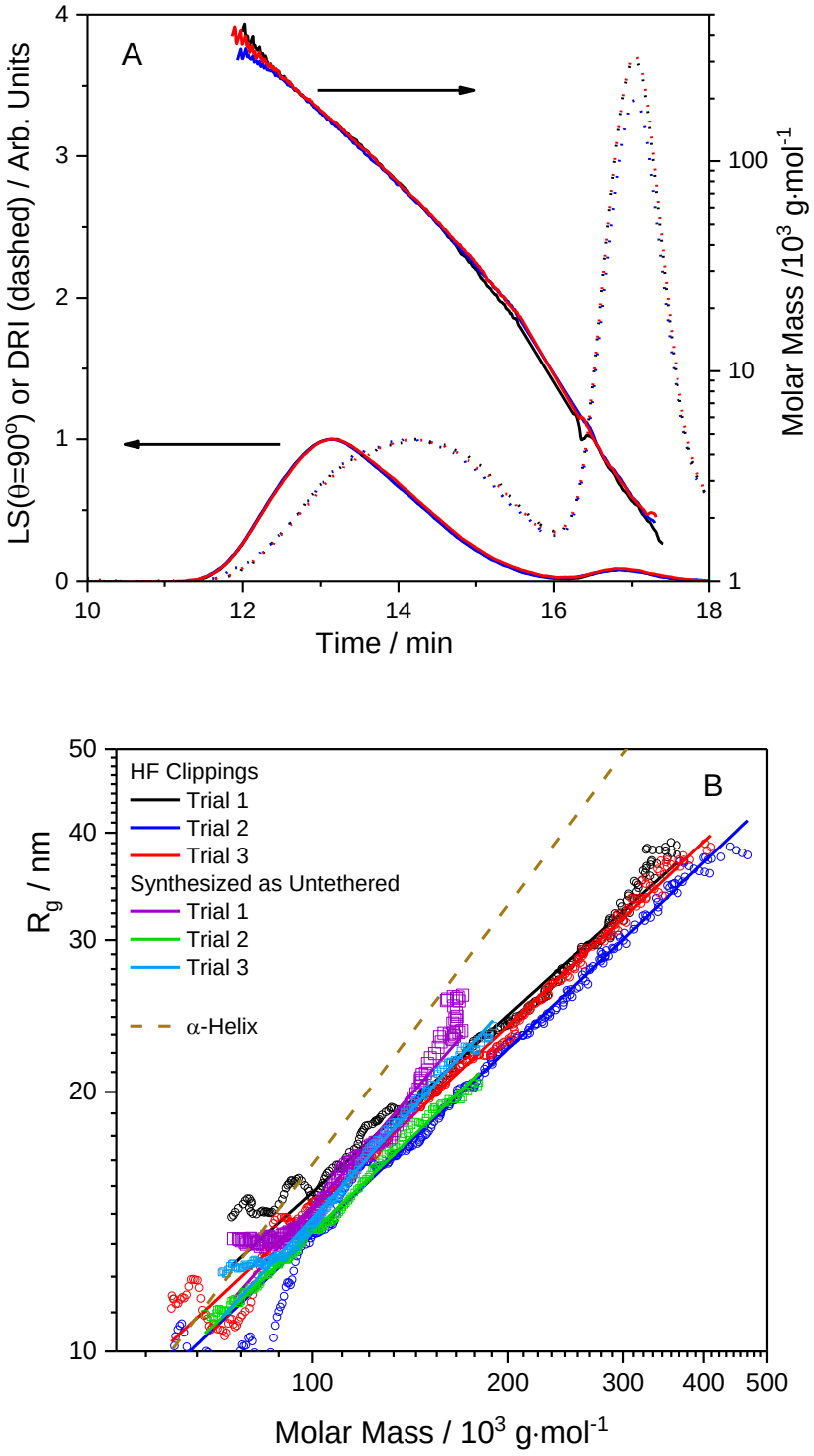

Figure 49. GPC/MALS molar mass chromatograms for PCBL clipped from Co@SiO2-PCBL particles by HF dissolution of the core, together with overlay of light scattering intensity (LS, θ = 90°) and differential refractive index (DRI) signals, triplicate runs (A); Conformation plots of radius of gyration vs molar mass for

polymer clipped from Co@SiO_2-PCBL particles, with overlay plots for never-tethered, methoxide-initiated PCBL, triplicate runs for each polymer (B).

4.4.5 Conformational Transition

4.4.5.1 DLS Evidence

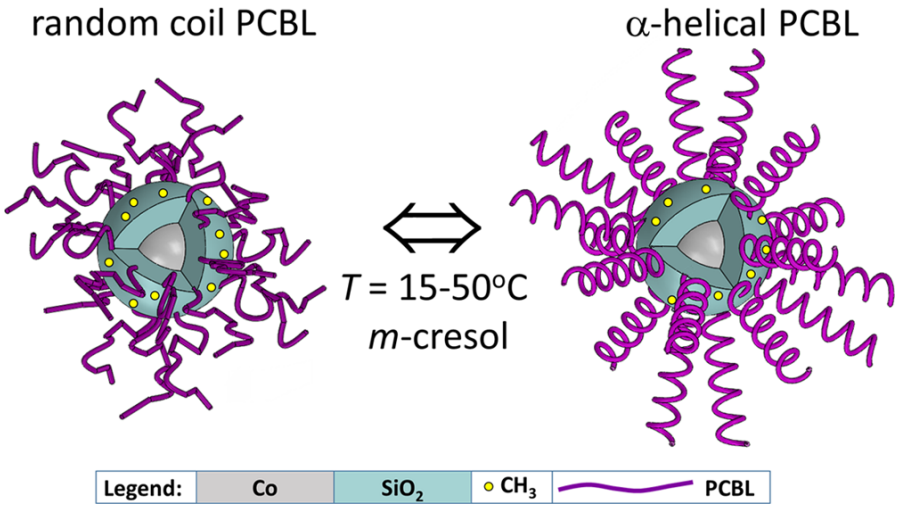

Figure 50. Schematic illustration of the conditions driving the inverse coil to helix transition of PCBL in m-cresol as a function of temperature. Not to scale.

DLS was used to follow the temperature-driven conformational change of Co@SiO_2-PCBL composite particles in *m*-cresol, illustrated in Figure 50. To bracket the response of the system, multiple-angle measurements were made at three temperatures, 15, 25, and 50 ºC, values that lie below, near and above the known transition of untethered PCBL (~27 ºC). The results (Figure 51) show an increase in apparent hydrodynamic radius, $R_{h,app}$, with temperature. The apparent radii meet the expectations of the above section and do not depend significantly on scattering angle, which for large particles is evidence that the suspensions are afflicted neither by aggregation nor by broad particle size distribution.

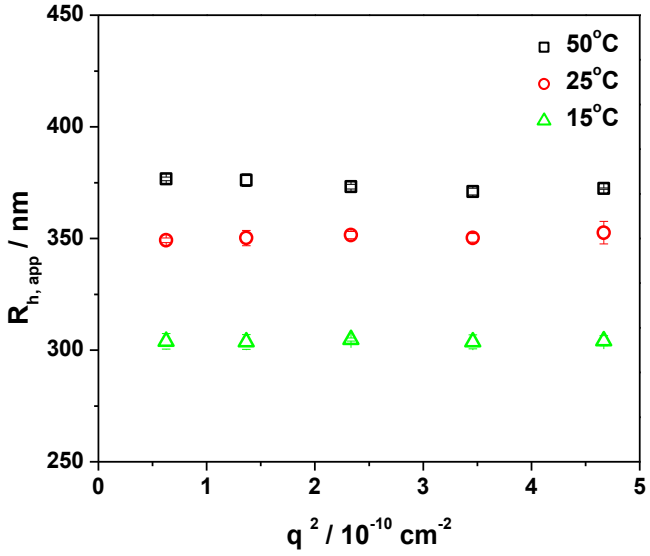

Figure 51. Apparent hydrodynamic radius of the Co@SiO2-PCBL particles measured at 15, 25, and 50°C in m-cresol plotted at different squared scattering vector magnitudes, corresponding to different scattering angles.

The independence of $R_{h,app}$ on scattering angle justifies the use of a single scattering angle for studies at additional temperatures. A Co@SiO_2-PCBL dispersion in *m*-cresol was measured at a scattering angle of 75° over three heating-cooling cycles in the 10–50°C temperature range. At each temperature step, the sample was equilibrated for 30 minutes before acquiring DLS data. This well exceeds instrument response time (< 10 min). As shown in Figure 52, the particle shells expand on heating. This response is attributed to the coil⇔helix transition of the PCBL shell, in consideration of the known behavior of untethered PCBL in *m*-cresol[158] and the knowledge that only small polypeptides fail to expand when the helix is formed.[191] The PCBL shell shrinks on cooling, corresponding to return to the random coil configuration. On the first heating cycle, the size is ~5% smaller than reported in Figure 51; such a difference is not cause for great concern, but it does suggest future studies might benefit from even longer equilibration times between

temperature steps. Also, the 20 nm downward drift between the end of the first heating cycle and start of the first cooling cycle suggests the particles may "overshoot" their size expansion at first. The behavior grew erratic (slightly different low- and high-temperature radii) after the third heating cycle, but transitions were still observed. Neither the "overshoot" nor the erratic behavior after three cycles is understood. The normalized variance from the cumulant fits,[192] μ_2/Γ^2, remained low (average value 0.05) and angle-invariant over the temperature range. This result, along with the above-noted independence of $R_{h,\,app}$ with scattering angle, argue against temperature induced aggregation as an explanation of the reversible transition seen in Figure 4.

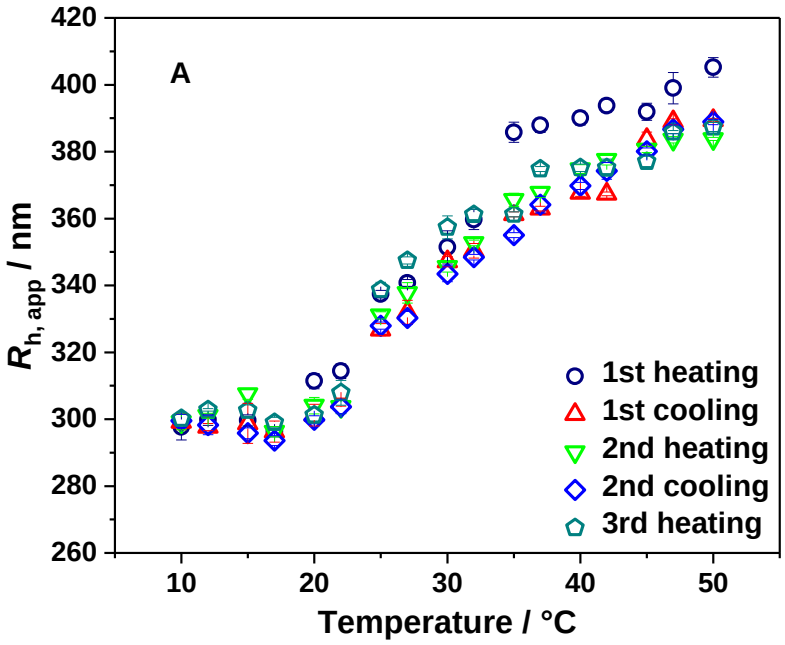

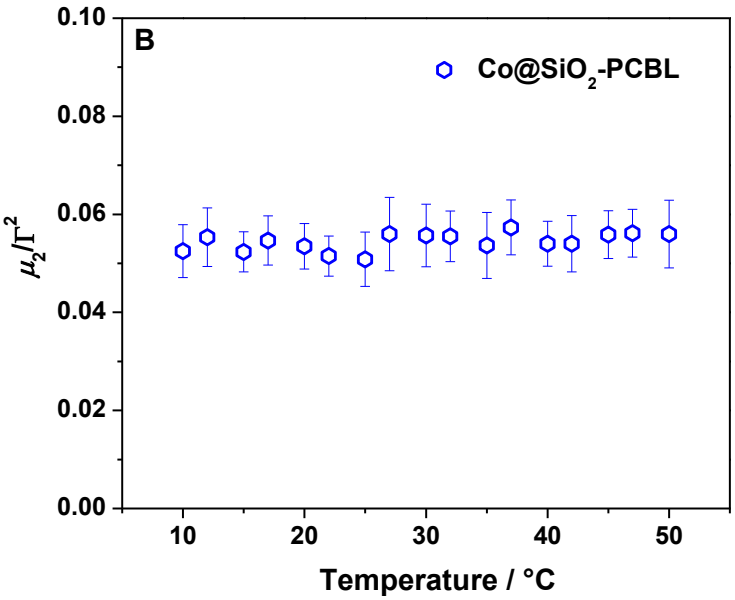

Figure 52. DLS results of PCBL-coated cobalt particles in m-cresol: (A) Temperature dependence of apparent hydrodynamic radius of PCBL particles (error bars represent triplicate runs at a single scattering angle, 75°) and (B) corresponding μ2/Γ^2 vs. temperature plot; each point is average of data collected during all heating and cooling cycles.

Neither did the intensity values from static light scattering reveal signs of aggregation. Therefore, aggregation was ruled out as an explanation for the transition or its minor peculiarities, such as overshoot and erratic behavior after three cycles. Investigation of those details would benefit from a method with greater resolution than DLS. Perhaps small-angle neutron scattering performed on particles with shells deuterated at selected sites could reveal more, though the limitations of neutron flux might prove a hardship for time-resolved studies. Meanwhile, the size transition appearing in Figure 52 is regarded as a quasi-equilibrium phenomenon. It is centered at a temperature close to the transitions reported by Matsuoka *et al*., who applied various methods to a range of molecular weights of untethered PCBL dissolved in *m*-cresol.[158] Our transition, which spans at least 20°C, is

broader than was reported at any molecular weight by these authors (their transition spans about 3°C for the sample closest in molecular weight to our M_w, to judge from Figure 7 of Ref. [158]). One possible cause for the broadening is the wide range of molecular weights present on the particle, as revealed by Figure 49B.

Before moving ahead to methods that probe chain conformation more directly than DLS, it needs to be noted that the possibility was considered that the transitions seen in Figure 52 could arise from the viscosity contribution of small amounts of residual untethered PCBL. Even if a large amount of untethered PCBL were present, it would remain almost invisible to DLS compared to the signal from the whole particles because scattering is proportional to the product of concentration, molecular weight and the differential refractive index contrast factor. Impossibly high concentrations and molecular weights of the low-contrast PCBL rods would be required to compete with the scattering from the whole particles, which have "molecular" weights in the billions. Nevertheless, one might question whether any untethered polymer could make its presence felt through alteration of the suspension viscosity. In principle, the suspension viscosity could rise as untethered polymer goes through its own coil→helix transition, causing the sigmoidal curve to sharpen.

To assess the importance of viscosity change as a possible cause of the different shapes in Figure 51 and Figure 57, the amount of untethered polymer is required. From TGA measurements, the total solids (hybrid particles plus untethered PCBL) concentration was about 0.15 mg/mL. The fractional increase in viscosity η above the solvent value η_o can be estimated from the lead terms of the usual Huggins equation:[193] $\frac{\eta - \eta_o}{\eta_o} = c[\eta]$ For

PCBL in *m*-cresol, the Mark-Houwink relation is $[\eta] = KM^{a}$ with $K = 1.99 \times 10^{-4}$ mL/g and $a = 1.08$ for helices at $T = 35^{o}$C, and $K = 118 \times 10^{-4}$ mL/g and $a = 0.74$ for coils at $T = 15^{o}$C.[158] Choosing a worst-case scenario of $M = 10^{6}$ g/mol (approaching the upper limit for the N-carboxyanhydride ring-opening polymerization[189] used to make the particle shells) and $c = 0.15$ mg/mL (the entire mass of the particles assigned to just the PCBL shell) leads to a 4% change in solution viscosity arising from the coil→helix transition. Thus, even with extreme assumptions the ~25% transition of the sigmoidal curves in Figure 51 of the main document cannot be ascribed to untethered PCBL.

4.4.5.2 Optical Rotation Evidence

The scattering experiments show a size change near the temperature at which untethered PCBL undergoes a coil-to-helix transition in *m*-cresol. In order to explore the nature of the transition, techniques sensitive to molecular conformations were applied. The magnetic character of the particles precludes the use of NMR, which is sometimes adept at following conformational transitions.[129] A nonmagnetic particle was prepared by omitting the nanoscale cobalt; these particles appeared in Figure 44B. The NMR behavior of such particles dispersed in *m*-cresol is best reserved for a separate report. Briefly, although certain peaks shifted by up to 1 ppm throughout the temperature range of interest, it was non-trivial to separate spectral changes due to polypeptide conformational transitions from general drift of the NMR peak positions due to temperature-induced changes in the overall H-bonding environment. NMR lifetime experiments are likely to prove revealing, but they are not necessary for the present purpose of determining whether the size transition in Figure 52 is caused by a change in polypeptide conformation.

In the polypeptide field, optical rotation and circular dichroism spectroscopy are often considered the most reliable indicators of chain conformation.[32–36] Although circular dichroism is ineffective in UV-opaque solvents including *m*-cresol, optical rotation works well. In our experiments, the spectrometer is set at a single wavelength and operates as a precise polarimeter with automated temperature control. Figure 53 shows optical rotation results for Co@SiO_2-PCBL particles from the same batch used for the DLS measurements, along with results from control experiments on untethered PCBL and PBLG. The response is normalized by the amount of polypeptide present, which must be maintained at a low value in the case of Co@SiO_2-PCBL particles in order to reduce interference from scattered light; these low concentrations account for the noise in the Co@SiO_2-PCBL signal. Early investigators of synthetic polypeptides established that the helical conformation gives rise to a less negative/more positive optical rotation versus the random coil conformation.[190] Thus, the increase from -200° to -50° for untethered PCBL indicates a change in the polypeptide structure to α-helix at higher temperatures. A noisier, yet still distinct, transition from -200° to +25° is observed for PCBL attached to Co@SiO_2. This again indicates structural change from random coil to helix, but the transition begins at a lower temperature and the change is larger. Indeed, the specific optical rotation approaches the nearly constant value seen for untethered PBLG, which remains in the helical conformation in *m*-cresol throughout the measured temperature range. The results confirm the temperature dependence reported long ago[158] for the optical rotation of untethered PCBL in *m*-cresol, and reveal that the same transition occurs when PCBL is attached to a particle, though broadened, in agreement with the DLS results.

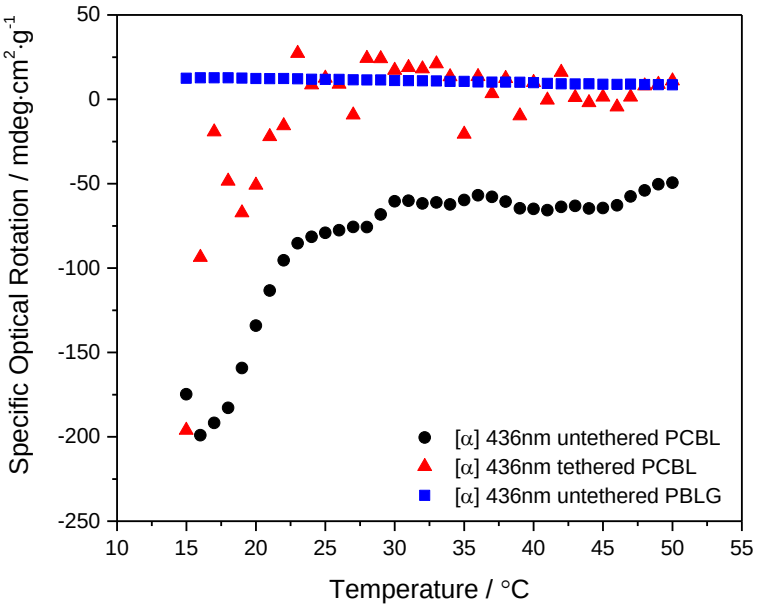

Figure 53. Temperature dependence of the specific optical rotation at 436 nm of PCBL in m-cresol (●), Co@SiO2-PCBL in m-cresol (▲), and PBLG in m-cresol (■). The data are normalized by the amount of polypeptide.

4.4.5.3 FTIR Evidence

FTIR measurements support the existence of a reversible, temperature-driven coil-to-helix transition for PCBL covalently attached to particles dispersed in *m*-cresol, but the signals are complicated (at least eight identifiable peaks) and the spectral changes due to conformational transition subtle. Several strong spectral signals arising from backbone vibrations characterize polypeptides and proteins:[194-195] the amide A band (mostly due to the N-H stretch but affected by overtones from the amide II); the amide I band (the backbone C=O stretch); the amide II band (C-N stretching and N-H bending); and, the Amide III band, which overlaps C-C, C-O and C-N linear stretches. The coupling of these transitions differs according to whether the polypeptide takes the form of an α-helix, β-

sheet or random coil. The Amide I C=O vibration is perhaps the most robust indicator of conformational transitions. Normally it is observed at 1650–1660 cm^{-1} for a random coil structure and at 1640–1650 cm^{-1} in the α-helical conformation.

Figure 54 shows FTIR spectra for Co@SiO_2-PCBL in *m*-cresol at several temperatures. The measured spectra reflect the complexities of the system, which contains amide groups in both the side chain and the main chain, dispersed in an organic, hydrogen-bonding solvent. Alignment of these results with the usual expectations for aqueous systems is not assured. To proceed, key features have been labelled (A, B, etc.). Feature A: In the Amide A region, a significant shift occurs from 3413 to about 3440 cm^{-1}. This reflects changes in the solvent-solvent and solvent-PCBL H-bonding as the solution is warmed. Feature B: the strong peak in the vicinity of 1700 cm^{-1} is assigned to the sidechain amide group C=O stretch. This peak exhibits a shift of about +4 cm^{-1} as the solution in *m*-cresol warms from 5°C to 30°C. Feature C: the observed frequency is near expectation for the amide I C=O stretch. There is no shift in the peak near 1651 cm^{-1}. One might expect a shift here reflecting the coil-to-helix transition, but instead a significant change occurs in the peak shape (compare the shoulder of the green curve at 30°C to the red or blue curves at 10°C and 5°C). The possibility for beta structures has not been considered yet. It seems not to be a significant factor for untethered PCBL,[158] but near-surface interactions for our particle-attached PCBL could in principle alter the energy landscape. This seems not to be the case because, had significant beta sheet structure been present, a convergence of peaks (1625 cm^{-1} + 1685 cm^{-1}) to a single peak at 1652 cm^{-1} for beta sheet → helix was be expected. Feature D: There is a +3 cm^{-1} shift in the peak near 1600 cm^{-1}. It is not clear what this peak represents, but *m*-cresol has a strong peak in this vicinity. Small errors in baseline

subtraction may have left that peak slightly exposed, or it could be part of the beta doublet (normally 1625 and 1685 cm^{-1}), in which case the 1700 cm^{-1} peak could be the other half of that doublet. Feature E: Not assigned. Feature F: This feature lies in the Amide II region, and mostly reflects NH bending. Features in this region include peak shifts of up to 10 cm^{-1}. At the feature F line all curves look similar, apart from differences in depth; a little to the right, at slightly lower frequencies, the blue curve for 5°C adopts a different shape from the green or red curves for 10°C and 30°C, respectively. Feature G. In this Amide III C-N or C-X (X=other atom) band, there is a dramatic change of shape with temperature. Feature H. This feature is difficult to assign, but there is a significant shape change with temperature.

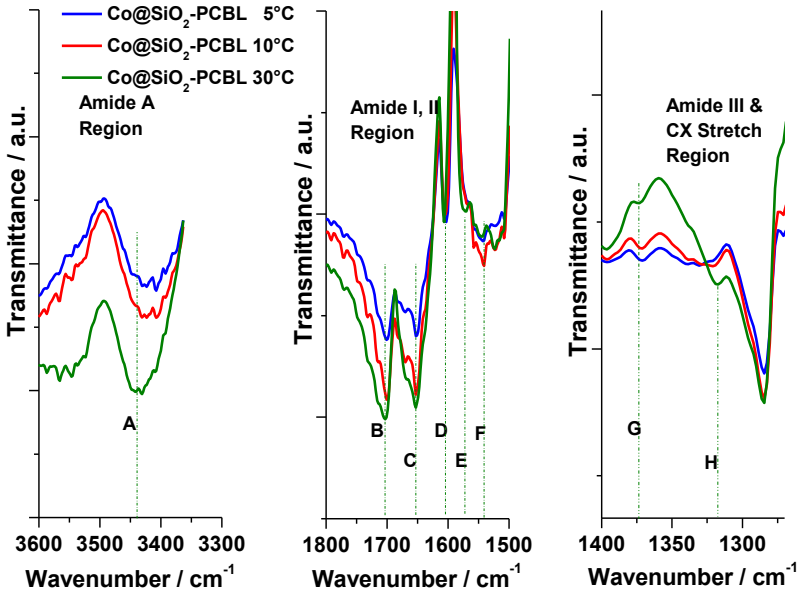

Figure 54. The infrared spectra of Co-PCBL particles in m-cresol at different temperatures. (left) Amide A region; (middle) Amide I-II region; (right) Amide III

and CX stretch region. Features associated with dashed vertical lines are discussed in the text.

To summarize the FTIR results, peaks known to be sensitive to the changes in H-bonding that accompany a coil→helix transition do change with temperature, whether in shape or central frequency. Several other peaks also shift or alter their shape. It would be difficult to explain these observations by nonspecific changes to polymer structure.

4.4.6 Magnetic Properties

4.4.6.1 Core Particle

The TEM images show that the cobalt particles are small enough to exhibit superparamagnetic behavior. This feature was confirmed by SQUID measurements, as seen in Figure 55. For comparison, the same figure also displays a magnetization curve for a commercially available superparamagnetic latex.

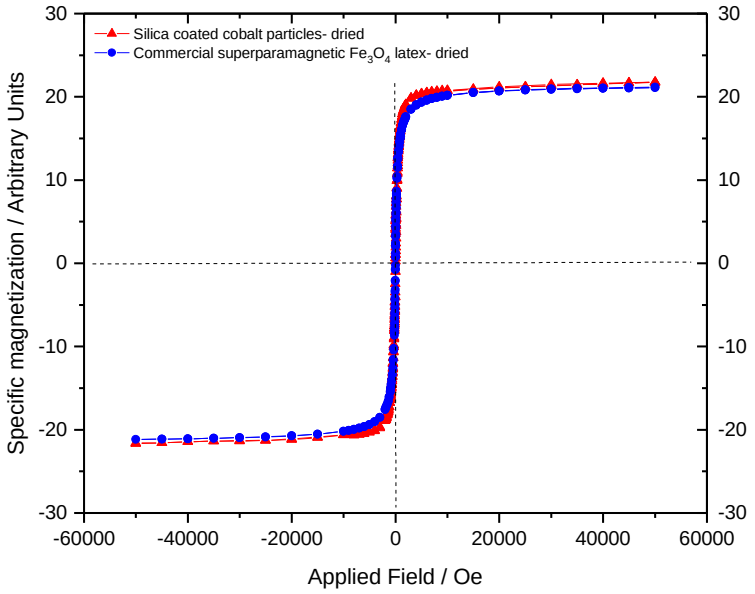

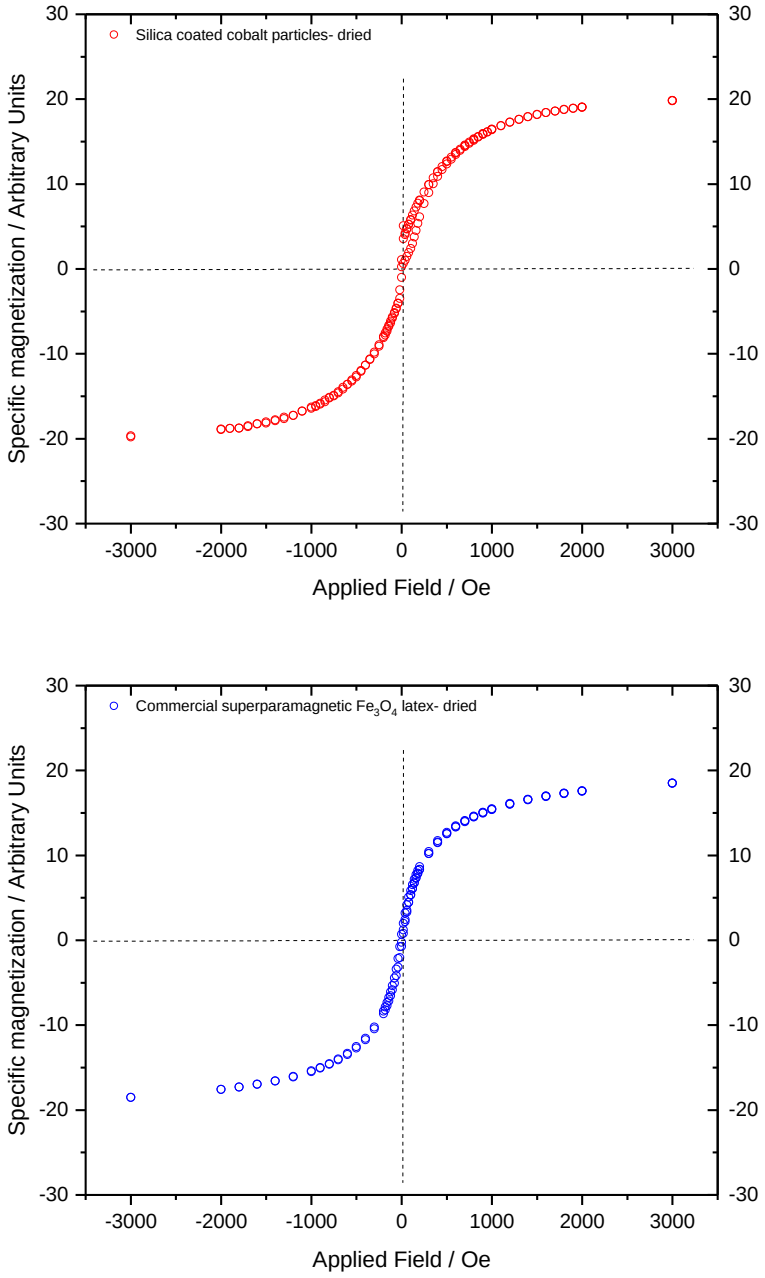

Figure 55. (A) Comparison of magnetic properties of silica-coated cobalt particles with commercial superparamagnetic latex. Both samples were dried in a vacuum oven for the measurements. (B) silica-coated cobalt particles, expanded scale. (C) commercial superparamagnetic latex, expanded scale.

4.4.6.2 Composite Polypeptide Particle

Measurements of dry Co@SiO_2-PCBL composite particles in a gelatin capsule were made at 27°C. As seen in Figure 56, the magnetization exhibits a small hysteresis suggestive of an exceedingly small coercive field similar in magnitude to that expected from the magnetic flux trapped in the superconducting magnet. Therefore, a claim about its magnitude is not made. The present experiments are also silent on specific magnetization of the cobalt nougat in these particles and how it changes due to the presence of a PCBL shell. Such a determination requires a difficult quantitative assessment of the small amount of cobalt in the Co@SiO_2 and Co@SiO_2-PCBL samples. Because the PCBL mass exceeds that of the Co by a factor of about 130 the possibility that the helix⇔coil transition might affect the magnetic properties of the particles was considered.

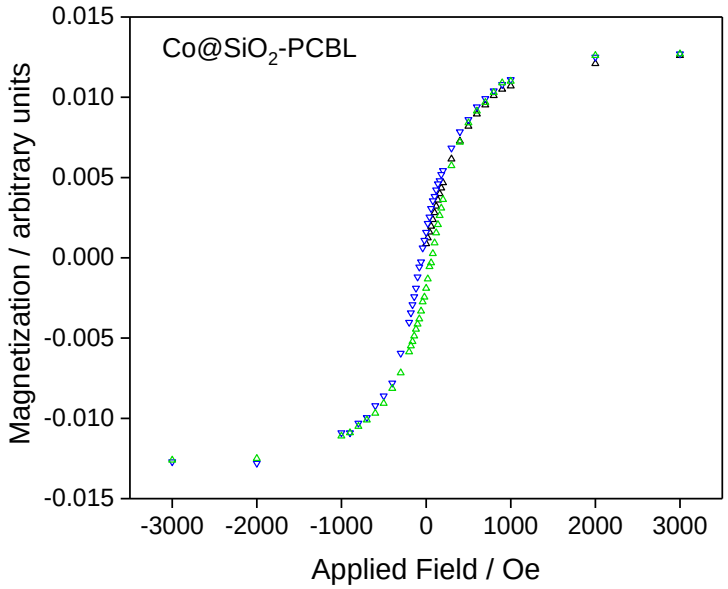

Figure 56. Magnetic hysteresis curve of dry Co@SiO2-PCBL particles in a gelatin capsule at 27ºC. Black points: initial positive field sweep from zero field; Blue points: Field sweep from 3 kOe to -3kOe; Green points: field sweep from -3kOe to 3kOe.

The magnetic susceptibility χ of PCBL-coated cobalt particles dispersed in *m*-cresol (10 mg/mL) and loaded into machined poly(tetrafluoroethylene) capsules was measured at various temperatures (Figure 56A). The particles exhibit a decreasing trend in susceptibility at ~27°C, which is the nominal PCBL coil⇔helix transition temperature. As a control, bare cobalt-silica spheres were also measured in similar fashion (Figure 56B). These control particles did not demonstrate a significant change in magnetic susceptibility. The results suggest the coil⇔helix transition slightly alters the magnetic response of the composite particles.

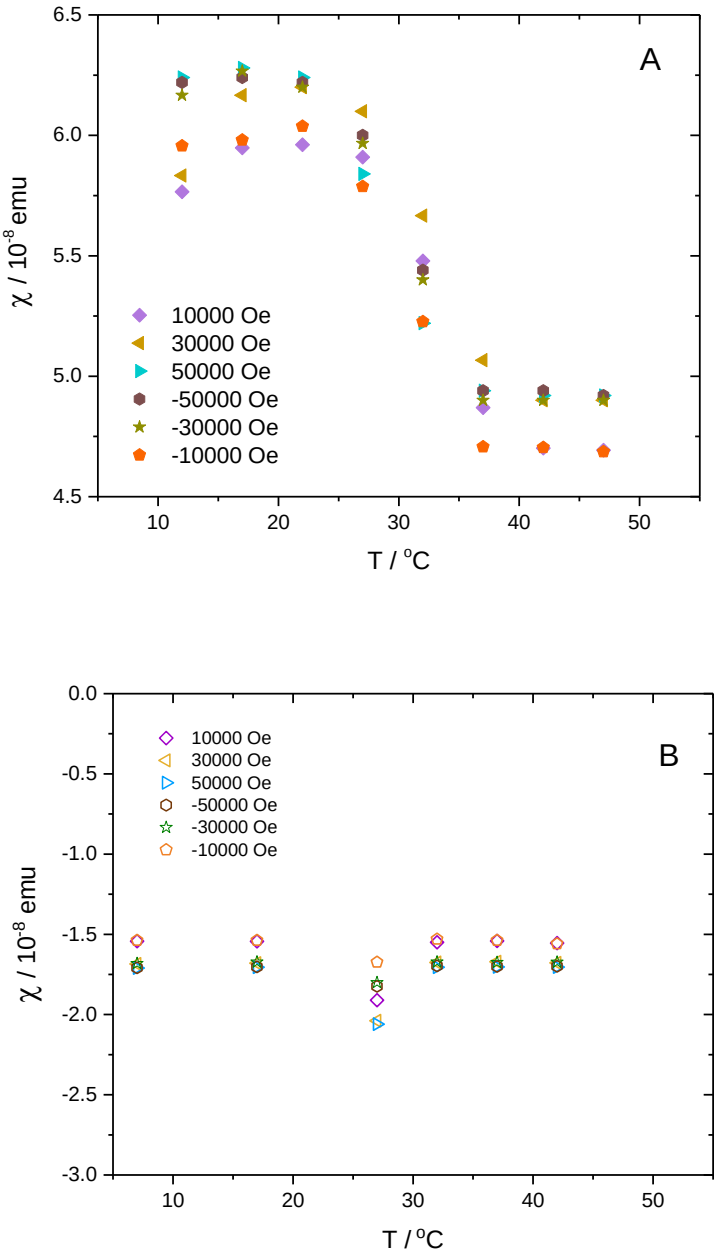

Figure 57. Magnetic susceptibility vs. temperature plots of (A) PCBL-grafted cobalt particles dispersed in m-cresol (for clarity, only selected fields are shown) and (B) silica-coated cobalt particles dispersed in m-cresol.

4.4.7 Aged Samples

Aging can deleteriously affect the particles in at least two ways. First, the cobalt center is susceptible to oxidation, with concomitant reduction of magnetic features such as the ability to be attracted, along with potential cargo, to a magnet. Many delivery applications are not imagined in *m*-cresol, but these particles should be easy to deprotect under mild conditions[75] to yield poly(L-lysine)-coated magnetic silica prior to use in aqueous media where they would be expected to bind negatively charged cargo. Second, if the particles are used for fundamental studies of the tethered coil⇔helix transition, it becomes important to know whether they must be made freshly or can be stored without loss of properties.

Both kinds of stability were assessed by re-investigating Co@SiO_2-PCBL particles that had been stored in PTFE-faced screw-capped glass vials for >5 years. SQUID measurements showed that ~50% of the initially available magnetic response remained. In contrast, Dobbrow and Schmidt,[196] who studied the stability of cobalt when stabilized with polystyrene and poly(caprolactone), found the magnetic properties faded in a matter of days. In addition to protection of the Co inclusion by the silica and PCBL layers, another probable reason the Co@SiO_2-PCBL particles retained more of their magnetic character is that they were suspended in *m*-cresol, which provides a sacrificial alternative target for oxygen. Visual observation supports the idea that *m*-cresol itself is not stable over such a long period; it turned a reddish color, presumably due to the formation of quinoid oxidation products. DLS studies were still possible on these reddish samples, the opportunity arose to assess whether the PCBL shell and its transition from random coil to α-helix when tethered to Co@SiO_2 is still active after long storage. The DLS measurements revealed some aggregation at ambient temperatures (falling $R_{h,app}$ vs q^2 plots) but this tendency

diminished as temperature increased. For improved measurements, the particles were separated from the reddish solvent by centrifugation. The supernatant was significantly less viscous than pure *m*-cresol, suggesting the cause of the particle coalescence was slow moisture uptake during the long storage. When the particles were re-suspended in fresh *m*-cresol, the $R_{h,app}$ vs q^2 plots flattened somewhat, but rising μ_2/Γ^2 trends with q^2 suggested dimerization or formation of higher aggregates (so-called internal modes, including rotation, can contribute to the overall decay of correlation functions [197]). The μ_2/Γ^2 values (typically 0.1–0.2) did not indicate wholesale aggregation, but they were higher than measured in the fresh samples (~0.055; see Figure 52B).

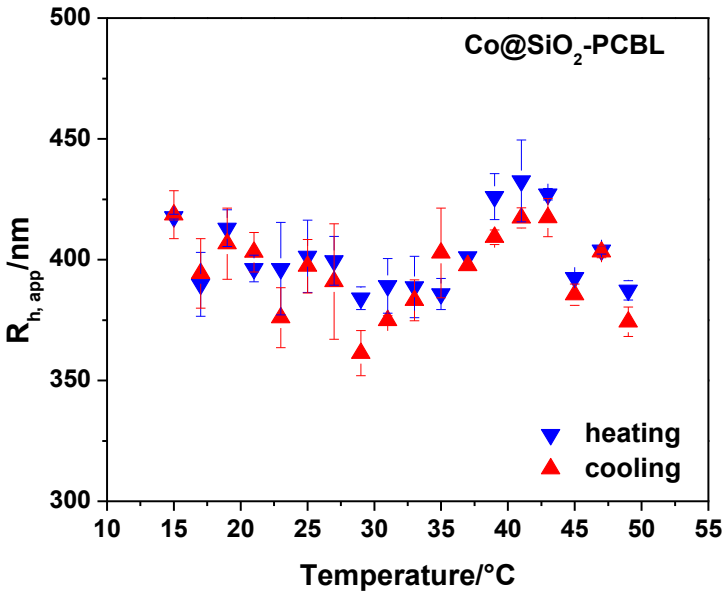

Figure 58. Apparent hydrodynamic radius vs. temperature in aged (>5 years) Co@SiO2-PCBL particles after redispersion in fresh m-cresol. Each point is an

average of four heating-cooling cycles and three repeat measurements within each cycle. Measurements were performed at one angle, 173° (external to the instrument).

What about the stability of the shell polymer, in particular the retention of a coil⇔helix transition over time? As shown in Figure 58, aged but freshly re-dispersed particles retained their ability to expand and contract with temperature changes in *m*-cresol, but the shape of the curve is as though Figure 52 were tilted slightly in the clockwise direction. The transition on heating still occurs (at slightly higher temperature, about 35ºC) but it follows a decline in size. After the transition, the size again decreases. This tilted curve is intriguing. Complex variations in size during helix-coil transitions have been simulated by Kemp and Chen[198] for untethered polypeptides. These authors join other investigators who argue that helix-coil transitions occur in stages. Samulski, Chen and Wade enumerated some of the early evidence for multistage transitions,[129] while Kastantin and Tirrell give a more recent account oriented towards transitions in polypeptide brushes.[199] The broad transition evidenced in Figure 52 for fresh samples can accommodate interpretation as a gradual transition from coil to helix, but there is no evidence of discrete steps. The broad molecular weight distribution of the PCBL can be a factor in the breadth and continuous nature of the transition. Also, the behavior of the aged samples cannot positively be identified as related to multiple-stage conformational transitions because it is also consistent with limited aggregation that would prevent the low-temperature plateau from reaching the smallest sizes associated with fully dispersed particles. In passing it is noted that Yan *et al*. observed a non-monotonic helix-to-coil transition in their study of hollow poly(glutamate) microgels stabilized by chitosan.[75] In this case, though, the transition is driven mostly by pH and is readily understood as the interplay of helical chain extension at low pH and charge-charge repulsion at high pH. Summarizing this section,

both functions of the Co@SiO_2-PCBL particles, magnetic response and a thermally induced size transition, remain even after >5 years of aging but subtle changes to the thermal response were noted.

4.5 Conclusion

Cobalt-containing silica particles with covalently attached PCBL homopolypeptide shells, when dispersed in *m*-cresol, exhibit a broad hydrodynamic size transition as the temperature increases past ~30°C. The size change is driven by the coil⇔helix transition of the PCBL shell polymer. PCBL was long ago was identified as a rare, thermally stimulated "shape-shifting" polypeptide that operates at a convenient temperature in a single organic solvent.[158] For PCBL tethered to silica particles, the transition is reversible for a limited number of times.

The Co@SiO_2-PCBL/*m*-cresol system can serve as a model for understanding the conformational transition of tethered polymer chains without the complication of pH or salt effects (which nevertheless prove useful in biomaterials applications; see for example Kar *et al.*[92] or Smith *et al.*[200]). It has long been thought that a two-state model for polypeptide transitions was oversimplified,[129] even when the polymer chains are not tethered to a surface. For chains that are attached to a flat surface, sharp "all-or-nothing" transitions have been suggested.[201] In contrast, the transitions described herein for PCBL covalently attached to a curved surface are broader than those seen by Matsuoka *et al.*[158] for untethered PCBL in *m*-cresol, regardless of polymer molecular weight. Some of the breadth may be due to molecular weight heterogeneity. Methods sensitive to molecular structural details will be required to understand the transitions of surface-bound PCBL.

Samples lacking the magnetic core of the present particles could be studied by NMR, for example. Such studies are relevant to the pH-driven expansion of influenza virus during the infection process that gains them access to a host cell.[202]

With regard to practical applications, few are envisioned in *m*-cresol. This viscous, pungent and oxidatively unstable solvent was chosen specifically for the simplicity of working in a single organic solvent. Yet the opportunity to chain the particles by application of a magnetic field, followed by covalent linking to yield poly(colloids), seems promising as a route to long, responsive fibers with potential for muscle-like contraction. The stability of the magnetic core and polypeptide shell polymer suggests a long shelf life for Co@SiO_2-PCBL particles and such poly(colloids) when dispersed in *m*-cresol. On an as-needed basis, it should be possible to deprotect the shell polymer to yield positively charged Co@SiO_2-poly(L-lysine) particles for magnetically directed antimicrobial formulations or delivery of negatively charged cargo such as DNA. Modulation of the magnetic response by the coil⇔helix transition, which is an unexpected finding of this work, suggests an intriguing mechanism to control such transport operations.

CHAPTER 5. SYNTHESIS AND CHARACTERIZATION OF POLYPEPTIDE-COATED JANUS PARTICLES

5.1 Introduction

Janus particles are interesting materials due to their inherent dual-face properties. They were named after the two-faced Roman God Janus and are colloidal particles that are anisotropic in shape and/or surface chemistry. These particles have the ability to self-assemble and can be made to have different amphiphilic, catalytic, optical, and magnetic properties.[35] Having such differing functionalization chemistries and properties on a single particle allows them to be used for drug delivery, interfacial chemistry, and reconfigurable materials.[33-35, 203] A commonly known use for Janus particles was developed in the 1970s with the creation of electronic ink technology, which uses polyethylene-coated Janus particles that align with a specific side facing toward the electronic screen when an electric field is applied to the system.[204] Anisotropic particles also have applications in microrheology and bio-imaging because with differing optical properties on each particle "face", the rotational and translational diffusion of these particles provides tracking information and more in-depth information of their surroundings.[37, 205-208]

There are many different approaches for synthesizing Janus particles. Most of the synthetic procedures can be classified into two main categories: surface modification or compartmentalization.[35] Surface modification refers to synthesizing or purchasing core particles that are isotropic, then altering the chemistry or functional groups on the surface post particle creation. Compartmentalization is when the entire core particle has an

anisotropic composition requiring the particles be synthesized from ground up.[35] Focus will be placed on using surface modification techniques to create Janus particles. The first type of surface modification method is modification at interfaces, which mainly involves some type of mask. This can be coating part of the particle to protect it from further modification or, using emulsions of wax or immiscible liquids to create a layer that will protect against chemical altering of the particle surface.[35, 203] Another type of surface modification method is physical deposition, which allows various compounds to be deposited onto the particle surface via an electron beam. This method provides more freedom for creating unusual geometries of Janus particles.[33-35]

All of these techniques are reliable and reproducible at the lab scale but depending on the chemistry and properties of the particles, industrial or large lab scale-up can still be a problem.[33, 203] In this work, an emphasis was placed on creating large, macro-sized Janus particles easily and inexpensively. The focus of the project was to use generic tape (Scotch brand), commercially available silica particles, and a custom-built sputter coating system to create the Janus core particles. An interesting area of Janus particles that is currently underexplored is the use of polypeptides. As shown in previous chapters, these responsive polymers yield unique characteristics to composite particles. Once the Janus core particle was synthesized, homopolypeptide was grafted to the surface to yield a responsive particle. These silica-polypeptide composite Janus particles are unique because they have an inorganic colloidal silica core, half of which is coated in chromium, and an organic polypeptide shell. Poly(ε-carbobenzyloxy-L-lysine) is the homopolypeptide that was polymerized from the Janus core and provides the responsive nature due to its inherent secondary conformational transition from coil-to-helix with temperature.

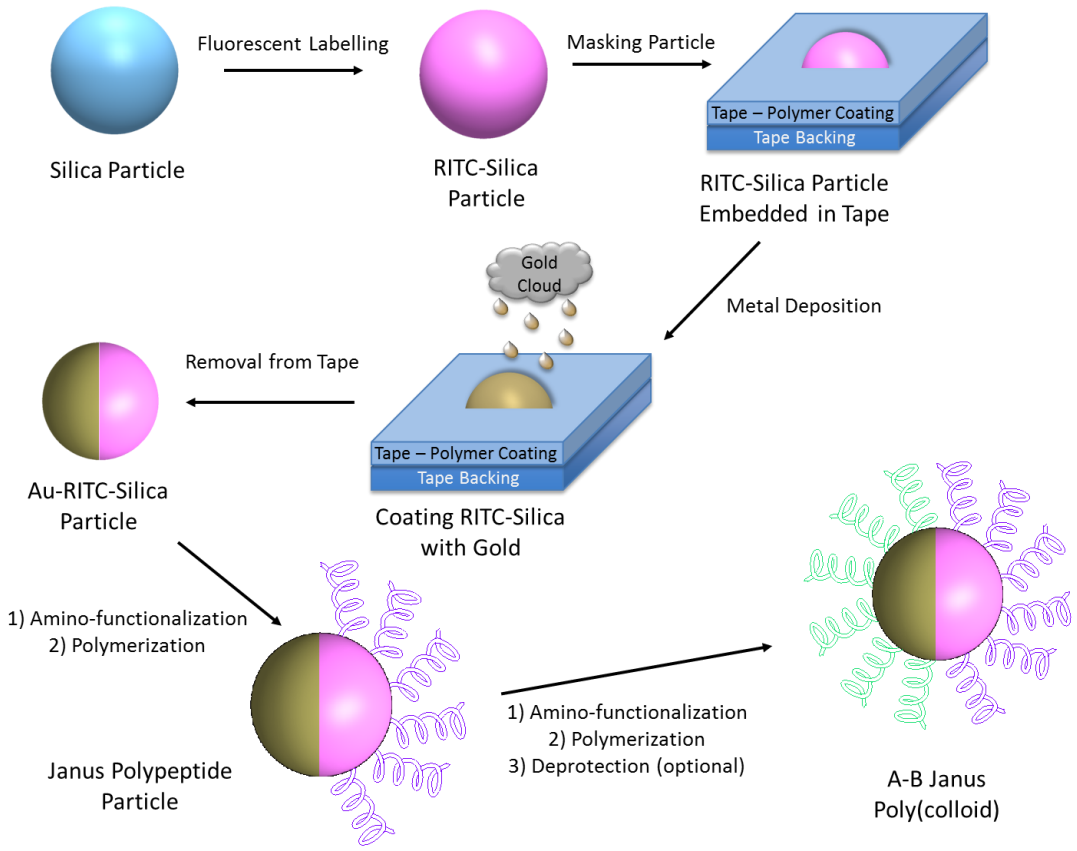

Figure 59. Schematic illustrating the long-term aim of the project to prepare colloidal AB monomers, leading to A-B Janus poly(colloid)s. The silica is fluorescently labelled and then sputter coated with gold to produce a biocompatible core particle. Once removed from the mask (tape) polypeptide-A (purple helices) can be polymerized from the silica side. Polypeptide-B (green helices) can be polymerized after additional functionalization of the gold side of the particle to result in the final poly(colloid).

Large, macromolecular-sized, responsive particles such as these polypeptide-coated Janus particles are interesting materials for making poly(colloids). Materials classified as poly(colloids) are polymeric chains whose monomeric repeat unit are colloidal particles.[209] These polypeptide-coated Janus particles would make up the monomer repeat unit. Ideally, different polypeptides or polymers can be placed on each half of the Janus core particle (silica half and metal half) to create a polypeptide-Janus monomer for the poly(colloid) formation. Figure 59 is an illustration of the poly(colloid) product and the

preceding steps that were imagined to create them. Having polypeptides attached to the surface would allow for these particles to be used in chiral separation due to the chirality of the polypeptide chains. Potential for enantiomer separation can be imparted on the particle if polypeptide enantiomers are attached to the different particle halves. Deprotection of the polypeptide side chains would result in the acid and base amino acid form of the polypeptide to produce zwitterionic particles. Etching of the Janus core particle can result in a vesicle structure that would allow further polypeptide conformational transition studies.

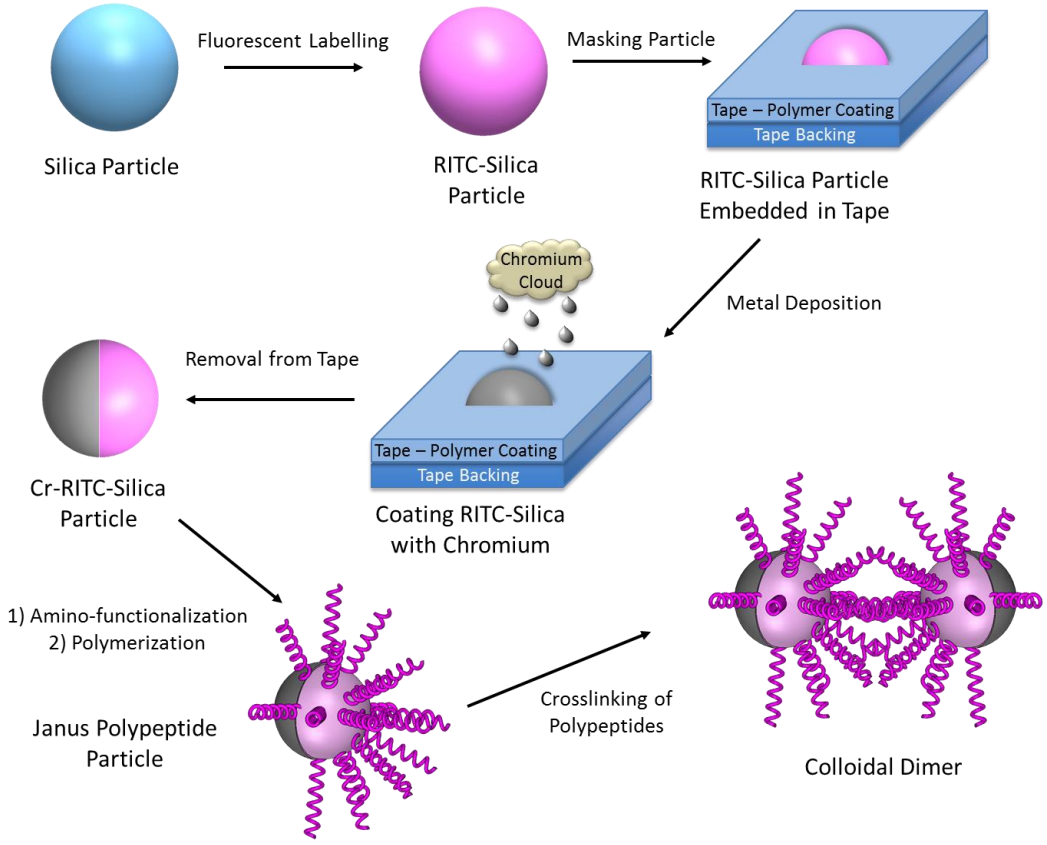

Figure 60. An illustration of the polypeptide Janus particles that will be synthesized as a proof of concept for Janus-polymer hybrid materials.

Focus in this work centered on providing a proof-of-concept that these larger Janus particles could be successfully synthesized with a method that can be scaled up in batch size using inexpensive materials. To provide a test system, chromium will be used instead of gold for the silica coating due to ease of attachment to silica particles. Polymerization of polypeptide on the non-metal half of the particle will be tested to ensure polypeptides can still be attached to the surface after metal deposition. Creation of half-metal, half-polypeptide coated Janus particles (shown in Figure 60) can find uses in chiral separations or as model systems to mimic magnetotatic bacteria.[208, 210]

5.2 Materials

Carbobenzyloxy-L-lysine (CBL), anhydrous hexane, anhydrous THF, sodium carbonate ($NaHCO_3$, anhydrous powder), RITC, ammonium hydroxide, APS, TEOS, triphosgene, magnesium sulfate ($MgSO_4$), pyridine, anhydrous DMF, toluene, xylene, acetone, and MTMS were purchased from Sigma-Aldrich and used as received. Silica particles (10 µm, GPC grade) were obtained from Alfa Aesar. Anhydrous ethyl acetate and glass microscope slides were purchased from VWR. Ethanol, 200 proof, was obtained from Koptec. Water (18 MΩ · cm) was withdrawn from a Millipore instrument. A Branson MH Series ultrasonic bath (Model 2800, M2800H) with a mechanical timer and heater outfitted with a solid tray for a 0.75-gallon tank as used as supplied from the manufacturer. Scotch tape (3M, Scotch Brand – Scotch Magic tape, product number – 810K) was purchased and used as received.

5.3 Methods

5.3.1 Synthesis of Dye Adduct

Approximately, 50 mg of RITC and 10 mL of ethanol were mixed together in a 100 mL round-bottom flask. The flask was capped with a septum and the contents were mixed by magnetic stirring for 30 min. A total of 0.5 mL of APS was injected into the stirring solution and the reaction was allowed to proceed for 18 h in the dark. The resultant material is rhodamine b isothiocyanate-3-aminopropyltriethoxy silane referred to as RITC-APS adduct.

5.3.2 Fluorescent Silica Cores

The three-neck flask containing ~250 mL of the purchased silica particles was attached to a separatory funnel. A combination of 10 mL of TEOS and 30 mL of ethanol were mixed and placed into the separatory funnel. The flow of the TEOS/ethanol solution was set to ~2 drops/min. A volume of 0.4 mL of RITC-APS adduct was injected into the silica suspension using a syringe. The reaction was allowed to proceed in the dark for 48 h under continuous stirring at room temperature. Once the reaction was complete, the fluorescently labelled core particles were washed with fresh ethanol by repeated centrifugation and dispersion (at least 5 times).

5.3.3 Making Silica Samples to be Coated with Chromium

The fluorescently labelled silica cores suspended in ethanol were sonicated in a bath sonicator to ensure proper dispersion of particles. The particles were pipetted onto a new, clean glass slide and allowed to air dry (~2 hours). The dried silica particles were

removed from the glass slide using tape and the tape was then placed onto a new, clean glass slide.

5.3.4 Chromium Coating of RITC-Silica Cores

Chromium films were deposited in a home-built DC magnetron sputter chamber at room temperature. The suspended particles to be coated were placed on a piece of Scotch tape on a glass slide. The glass slides were then loaded onto a 10 cm diameter rotating stage about 10 cm away from a circular, indirectly cooled magnetron cathode (Angstrom Sciences). The magnetron cathode is at a small (~10%) inclined angle relative to the axis of rotation of the stage. The rotation and target inclination promote uniform film deposition over a wide film area. The chromium target (99.95% purity, Kurt J. Lesker Co.) has a 1 inch diameter and 0.125 inch thickness. Pumpdown follows two stages: (1) a membrane roughing pump brings pressure below 7 Torr, then (2) a turbomolecular pump is used to reach 1 x 10^{-4} Torr. After pumpdown, argon (99.999%, Airgas) is introduced into the chamber and maintained at 40 mTorr using a gate valve. The magnetron is cooled by continuously running DI water at tap temperature. To initiate deposition, the magnetron power supply (Advanced Energy MDX-500) is activated under constant-power operation at a set point of 15 W, igniting a plasma. Deposition is controlled by maintaining a constant background pressure of 40 mTorr, and controlling the deposition time.

5.3.5 Removal of Chromium-coated RITC-Labelled Silica from Scotch Tape

Once the silica was coated with chromium, the tape was removed from the glass slide, placed into a scintillation vial containing xylene, and capped with a PTFE-lined cap. The vial was placed into the bath sonicator and was allowed to sonicate for ~1–2 hours

until all of the chromium-coated, RITC-labelled silica particles (Janus particles) were removed from the tape and resuspended in solution. Resuspended Janus particles were then washed 3× with toluene/DMF via centrifugation and redispersion to remove excess chromium. The Janus particles were then solvent exchange from toluene/DMF to ethanol via centrifugation and redispersion (~5×) and stored in a PTFE-capped vial.

5.3.6 Amino-functionalization of Silica Cores

A 10 mL aliquot of Janus particles was placed into a round-bottom flask, diluted with 90 mL of ethanol and then sonicated for 5 min. The round-bottom flask was wrapped in aluminum foil, and the solution was allowed to stir vigorously. A 1:3 ratio of APS to MTMS was injected into the suspension using a syringe and the reaction proceeded for 18 h at room temperature. Once the reaction was finished, the particles were washed by centrifugation and dispersion with clean ethanol. Washing continued until the ninhydrin test returned a negative result indicative of no free amino groups in the silica suspension. In order to perform the ninhydrin test, ~1 mL of the supernatant after centrifugation was placed into test tubes suspended in a water bath set to 50 °C. Approximately 2–5 drops of a 10% alcoholic ninhydrin solution were added to the tubes. Once the solution did not show any further change in color, the particles were washed by centrifugation and dispersion with anhydrous THF and stored in a dark vial to prevent photobleaching.

5.3.7 Synthesis of N-carboxyanhydride (NCA) monomer

In a medium glove bag (38 in x 51.5 in, deflated dimensions) under a nitrogen atmosphere, 150 mL of anhydrous ethyl acetate and ~5 g of the amino acid (dried overnight, at least 8 hours, *in vacuo*) were added to a 500 mL three-neck round bottom

flask. A stir bar was placed into the round bottom flask and the flask was capped with three rubber septa. The flask was removed from the glove bag, connected to a condenser capped with a rubber septum, and placed into an aluminum bead bath that was heated. Argon gas was bubbled through the reaction slurry to ensure an inert atmosphere, and the mixture was brought to reflux. In a small glove bag under a nitrogen atmosphere, ~2.06 g of triphosgene ([M]:[I] of ~3:1 with a slight excess added) was weighed out into an oven dried scintillation vial. The triphosgene was quickly added to the refluxing mixture and the reaction was allowed to proceed until the solution became clear. Once the solution cleared, the reflux was kept for one hour after which the reaction solution was cooled and placed into a -20 °C freezer to rest overnight. Removal of unreacted amino acid and side products was performed by washing the NCA according to the procedure developed by Poché and Daly.[211] The NCA solution was placed into a 500 mL separatory funnel with 100 mL of icy water, swirled to mix, and the organic phase of interest was retained. A 0.5% solution of NaHCO3, 100 mL, was added to the separatory funnel, swirled to mix, and the organic phase of interest was decanted into a clean 250 mL round-bottom flask. The flask was placed into the medium glove bag under an inert atmosphere where $MgSO_4$ was added quickly until no more clumping occurred, indicating that all water was removed from the NCA solution. The clear NCA solution was suction filtered through a Whatman 90 mm filter paper in a clean, dry vacuum flask to remove the $MgSO_4$. The filtered solution was placed into a new, clean, dry 250 mL round-bottom flask and the volume was reduced to 1/3 using a rotatory evaporator. Approximately 100 mL of cold anhydrous hexane was poured slowly into the NCA solution. White crystals of NCA started to form, and the flask was capped and placed into the freezer to allow precipitation to occur. The precipitated

NCA was suctioned filtered, inside a medium glove bag under an inert atmosphere, through Whatman 90 mm filter paper. The suction-dried NCA was placed into a new, clean, and dry 250 mL round bottom flask and dissolved in 15 mL of dry THF. Cold, dry hexane was again poured slowly into the flask while it was being swirled until white crystals began to form. The flask was capped and placed inside the freezer overnight for crystallization to occur. The recrystallization reaction was repeated at least once more for better purification of the NCA monomer.

5.3.8 Polymerization of Poly(ε-carbobenzyloxy-L-lysine) from the Silica Cores

In a flame-dried round-bottom flask inside a nitrogen-filled glove bag, ~1.93 g of CBL-NCA was dissolved in ~50 mL of anhydrous THF. A magnetic stir bar was placed into the flask and the flask was capped with a rubber septum. The flask is placed into an aluminum bead bath and 10 mL of amino-functionalized Janus cores suspended in THF are injected into the flask. A bubbler containing silicon oil was connected to the flask via tubing with a needle at the end. The reaction was heated to 35 °C and stirred until there was no bubble formation inside the oil in the bubbler (usually 2 days). The particles were then washed at least three times by repeated centrifugation and redispersion in THF. In the final step, half were resuspended in THF and the other half were resuspended in pyridine.

5.3.9 Scanning Electron Microscopy (SEM) with Energy Dispersive X-ray Spectroscopy (EDX).

A Hitachi SU8230 SEM working at an accelerating voltage of 1.0 kV was used to image the chromium-coated, RITC-labelled silica particles using the lower secondary electron detector. The same SEM working at an accelerating voltage of 10 kV was used to

perform EDX spectroscopy on the Janus particles to map the chromium and silica. Samples were deposited onto silicon wafers and dried in air.

5.3.10 Fluorescence Microscopy

A Motic AE31 inverted microscope with LED Epi-fluorescence option and outfitted with a TRITC (Rhodamine)/Dil/Cy3 filter cube set was used to image the fluorescently labelled silica particles. The light source is a CoolLED White Light Fluorescence Illuminator and the microscope stage is a universal attachable mechanical stage with well plate holders (128 X 86 mm). A Canon EOS 6D DSLR (digital single lens reflex) camera attached to the microscope using a C-mount was used to acquire the images. Samples were placed onto a glass microscope slide and allowed to air dry.

5.3.11 Fourier-Transform Infrared Spectroscopy (FTIR).

Spectra of untethered PCBL and PCBL tethered to the Janus particle core were obtained with a Thermo Scientific Nicolet iS50 FT-IR Spectrometer equipped with a Smart-iTR (ATR) accessory. Thermo Scientific Omnic 9 software was used to control the instrument and for data acquisition and analysis. Each sample was dried in the oven overnight (at least 12 h) prior to measurements. A total of 64 scans were taken for each sample with a resolution of one and a data spacing of 0.121 cm^{-1}. The final data format was absorbance, and an ATR correction was applied to the data. To ensure reproducibility a background scan was collect before every sample consisting of 16 scans.

5.3.12 Thermogravimetric Analysis (TGA).

Decomposition curves of the silica core particles, untethered polypeptides, and PCPs were obtained using a Mettler Toldeo TGA2 STAR System Thermogravimetric Analyzer. STARe Software version 16.00 was used to control the instrument and for data acquisition. The same software was used for data analysis via the evaluation window. A measurement in a nitrogen atmosphere was conducted for each of the silica cores, PCPs, and untethered polypeptide samples. The program was set to stabilize the temperature at 50 °C and hold for one min, then ramp the temperature from 50–600 °C at a rate of 10 °C/min, and finally return to room temperature at the end of the run. Approximately 0.5–3 mg of sample was added to a tared sample pan provided by Mettler Toledo.

5.4 Results

5.4.1 Synthesis and Characterization of the Silica Core Particles

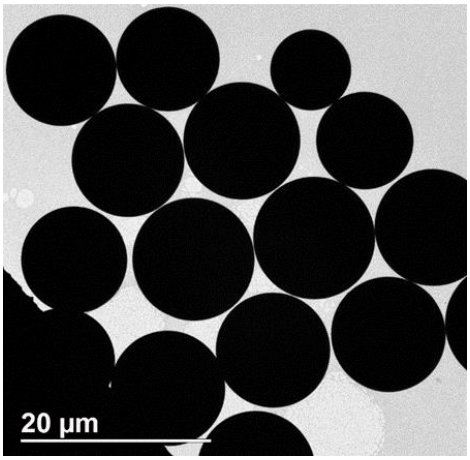

Figure 61. TEM of the commercially purchased silica particles before further functionalization. This confirms the particles are spherical in shape and their overall size 10 µm.

Instead of synthesizing the silica cores, commercially available silica particles were obtained and used. The average size of the silica particles is claimed by the vendor to be 10 µm. TEM was performed on the bare silica particles to determine their exact size and polydispersity. Figure 61 shows a TEM micrograph of relatively uniform spherical silica cores, confirming the particles purchased were 10 µm in size with a relatively low polydispersity.

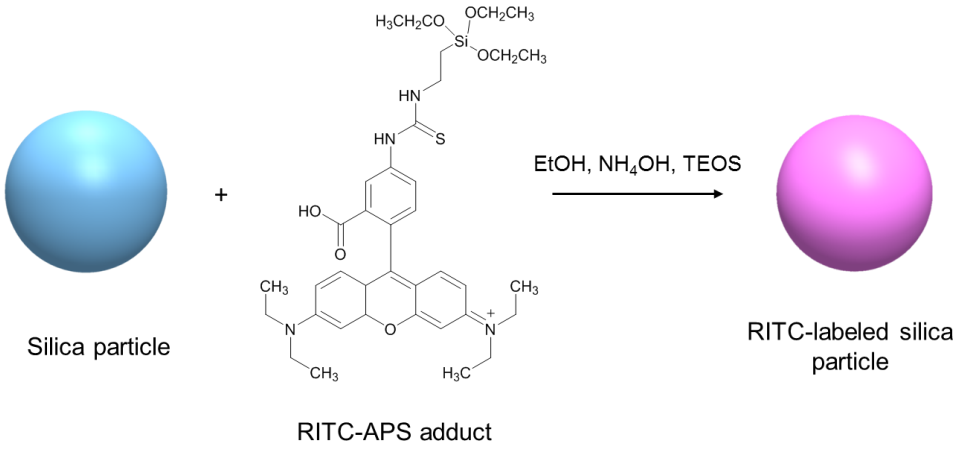

Figure 62. Schematic illustrating the fluorescent labelling of the bare silica core particles. The silica core particles are reacted with a dye adduct that allows for the covalent attachment and incorporation of the dye into the crosslinked silica particles.

To help aid in visualization of the silica core particles using different techniques, a fluorescent dye was covalently attached. A schematic of the fluorescent labelling reaction is shown in Figure 62. The particles were labelled with a rhodamine isothiocyanate dye, which allows for easier visualization using fluorescent microscopy techniques. Before the dye can be attached to the silica core, the dye molecule itself was reacted with a silane molecule to create a dye adduct which can react with the hydroxyl functional groups on the silica particle surface. The synthesis of the dye adduct and fluorescent labelling reaction was developed by previous group members.[87-88] Once the silica is fluorescently labelled,

the polypeptide-coated Janus particle will be created by coating half of the silica with chromium and the other half with polypeptide. Figure 63 shows a reaction schematic for the stepwise creation of the polypeptide-coated Janus particle.

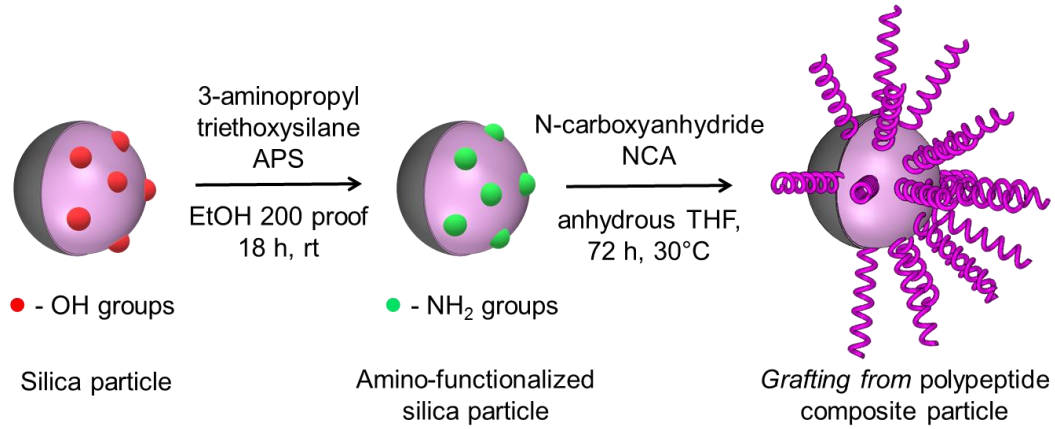

Figure 63. Reaction scheme illustrating the amino-functionalization and the hypothesized consequent polypeptide polymerization from the chromium-silica core surface via the *grafting from* method

After the fluorescent silica was synthesized, different microscopic techniques were used to characterize the particles. DLS was not used to determine the overall size because the particle size regime falls just outside of the limits for light scattering. Instead, SEM was used and Figure 64 shows two micrographs of the RITC-labelled silica. A fluorescence microscope was also used to confirm the fluorescent nature of the particles. Figure 65 shows an optical microscope image and its corresponding fluorescent microscope image of the RITC-labelled silica.

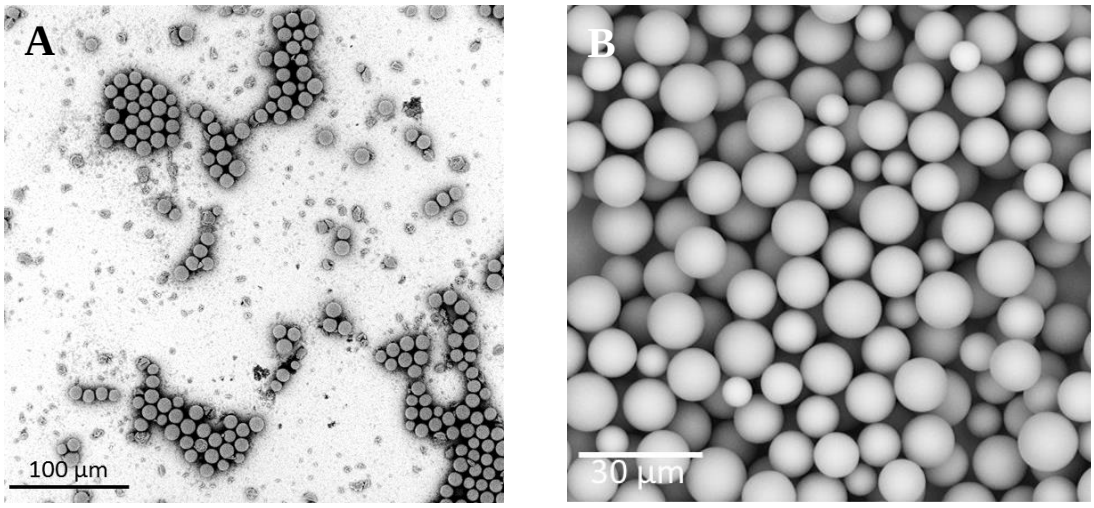

Figure 64. SEM images of the silica core particles after fluorescent labelling with RITC dye adduct showing the particles retained their spherical shape and overall size of 10 µm.

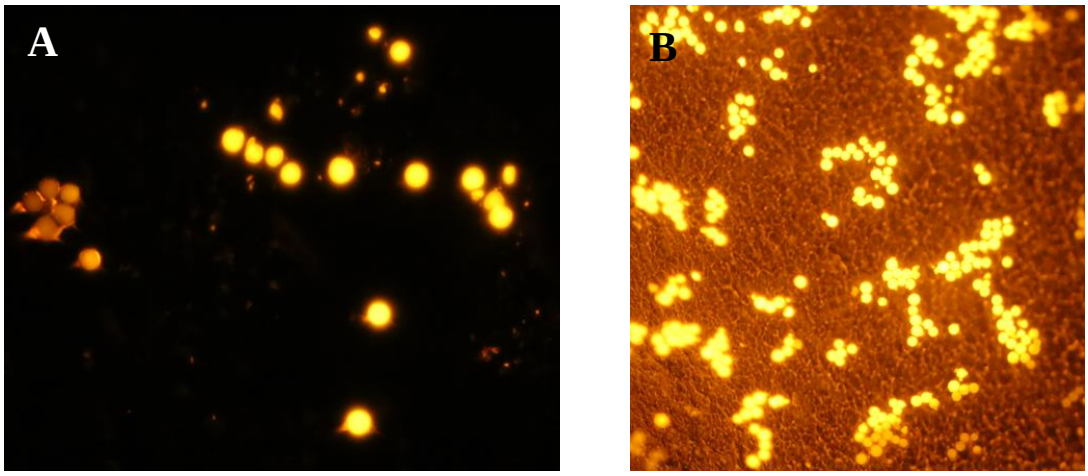

Figure 65. Epi-fluorescence microscope images of RITC-labelled silica core particles at 20× (A) and 10× (B) confirming fluorescent properties of particles. Silica particles are 10 µm in diameter.

5.4.2 Creating Janus Core Particles

When trying to determine a way to create Janus particles, a simple and easy procedure was desired. A common technique is the application of a mask to part of the particle surface so the uncovered part can be further functionalized or coated. An item readily available in labs, offices, homes, etc. is scotch tape. The idea to use Scotch tape as a low-cost mask arose from its accessibility and its industrial scalability. Realizing that the silica particles would need to be embedded into the tape while dried resulted in the use of sputter coating to apply a metallic coating to the unmasked part of the particle surface. In order to sputter-coat the silica particles a simple procedure was developed. Figure 66 illustrates the procedure for creating the sputter coated silica samples.

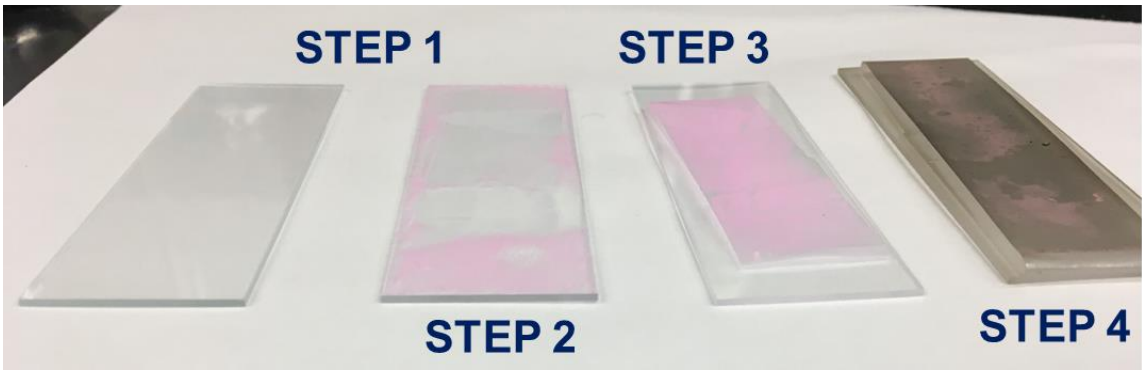

Figure 66. Images showing the procedure for sputter coating the fluorescently labelled silica particles with chromium. Step 1: take a clean glass slide and place the RITC-silica sample onto the slide. Step 2: once the sample is dry, roll a piece of tape over the dried silica sample. Step 3: transfer the tape sample with silica adhered to a new clean slide. Step 4: place the sample into the sputter coating chamber for set amount of time.

In determining the metal target that would be used for deposition, surface functionalization of the silica particles became a main deciding factor. Some metals require the silica surface to be modified from its inherent hydroxyl functional groups to various

other functional groups such as thiols. Due to its availability and strong interaction with silica without additional synthetic steps, chromium was chosen as the deposition metal. It also allows for further sputter coating with more biocompatible metals such as gold or silver. Using chromium provided an easy to work with metal that could be used for proof of concept studies and provide a pathway to more desirable surface covering materials.

Table 8. Solvents and Variables Tested for Removal of the Chromium Sputter-Coated Silica Particles from Different Types of Tape

Solvent	Variables Tested	Results
Acetone	Clear and Scotch Tape, Heat and No Heat	Plastic backing removed but silica stuck in adhesive (clear tape was worse than Scotch tape)
Toluene	Clear and Scotch Tape, Heat and No Heat	Nothing happened
THF	Clear and Scotch Tape, Heat and No Heat	Plastic backing removed but silica stuck in adhesive (clear tape was worse than Scotch tape)
DMF	Clear and Scotch Tape, Heat and No Heat	Tape shrivels up and everything is stuck together (clear tape was worse than Scotch tape)
Toluene/DMF	Clear and Scotch Tape, Heat and No Heat	Plastic backing removed and silica resuspended (clear tape was worse than Scotch tape)
Xylene	Scotch Tape, Heat and No Heat	Plastic backing removed and silica resuspended

Once the samples were sputter coated, a procedure for removal of the Janus cores needed to be developed. Difficulties were encountered when removing the sputter-coated samples from the tape. To determine the best method of removal from the tape a few variables were tested: solvent, type of tape, and sonication of samples with and without heat. Table 8 lists an overview of the variables tested and their corresponding results. The removal of the particles was tested by placing the tape, with sample sputter-coated and still embedded, into a vial with solvent. The vial was then placed into a bath sonicator and

sonicated until the solution turned gray in color and the tape was again clear, indicating that the particles were removed from the tape and resuspended in the solvent.

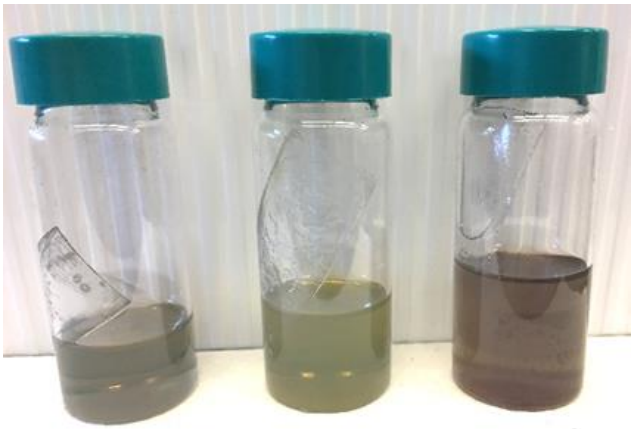

Figure 67. Different sputter coated samples in xylene after sonication and the particles were removed from the tape.

For the tape, only clear and regular Scotch tape was used. It was found that for removing particles from the tape, the Scotch tape worked better than the clear tape. Once it was determined that regular Scotch tape was the better substrate, sonication with and without heat was tested to determine the effect of temperature on the resuspension of the particles. Temperature did not seem to have a major effect on the number of particles removed from the tape and their subsequent resuspension. It did reduce the amount of time that the samples needed to sonicate to remove the particles without altering the chromium coating.

Lastly, different organic solvents were tested to determine which removed the samples from the tape and resulted in resuspension of the Janus cores. Of the six solvents tested, toluene was the worst solvent because nothing happened to the sample; the particles were still embedded into the pieces of tape. DMF, THF, and acetone were not useful

solvents either. DMF did have an effect on the plastic backing of the tape but it caused the tape itself to shrivel up and did not remove any particles from the tape. THF and acetone had the same results, the plastic backing of the tape was removed but the particles remained embedded in the polymer coating of the tape. This resulted in little to no particles being resuspended. The only solvents that removed the polymer coating from the plastic backing and resuspended the silica were xylene and a solvent mixture of toluene/DMF. The combination of removal variables chosen for future particle preparations was regular Scotch tape for embedding the samples, xylene as the removal solvent, and a bath sonicator operating under its heating setting. Figure 67 shows three different samples that were sputter coated and then removed from the tape using the final combination of variables.

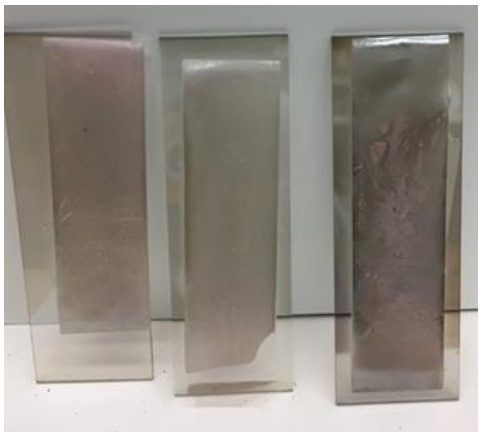

Figure 68. Images of RITC-silica that have been sputter coated for different periods of time (10, 15, and 20 minutes shown left to right).

The deposition time for sputter coating the samples was varied to determine its effect, and subsequently the metal-coating thickness, on the removal of the particles from the tape. Figure 68 shows three RITC-labelled silica samples that were sputter coated for 10, 15, and 20 minutes (left to right). Deposition time was varied from 5–20 minutes at 5 min intervals and the samples were then removed from the tape. A strong correlation

between deposition time and ease of removal from the tape was not apparent. Simply due to the larger number of samples made with a deposition time of 10 minutes, these samples were used to synthesize the polypeptide-coated Janus particles.

5.4.3 Characterization of Chromium-Silica Janus Particles

After sputter coating the RITC-silica particles, the samples were placed into an SEM to verify that they were in fact coated with chromium. Figure 69A shows an image of the chromium-coated RITC-silica core particles that are still embedded in the tape. The chromium can be seen on the silica particles because it produced a rough surface. It is apparent the rough surface is from deposited chromium when comparing to the previously shown SEM images of the RITC-labelled silica particles (see Figure 64). Additionally, to confirm the increase surface roughness is associated to the deposition of chromium, EDX was performed to help locate and map specific elements in the sample. Figure 69B shows the SEM-EDX image of the sputter-coated particles still embedded in the tape. EDX spectra were taking at multiple locations across the sample to ensure representative results. Because the particles are still embedded in the tape, the chromium should be located only on the exposed surface. Three main compounds identified using EDX were chromium (shown in pink), silica (shown in yellow), and the polymeric side of the tape (shown in green). This indicates that chromium was successfully deposited on the exposed silica particle surface and the side embedded in the tape will not be coated with chromium.

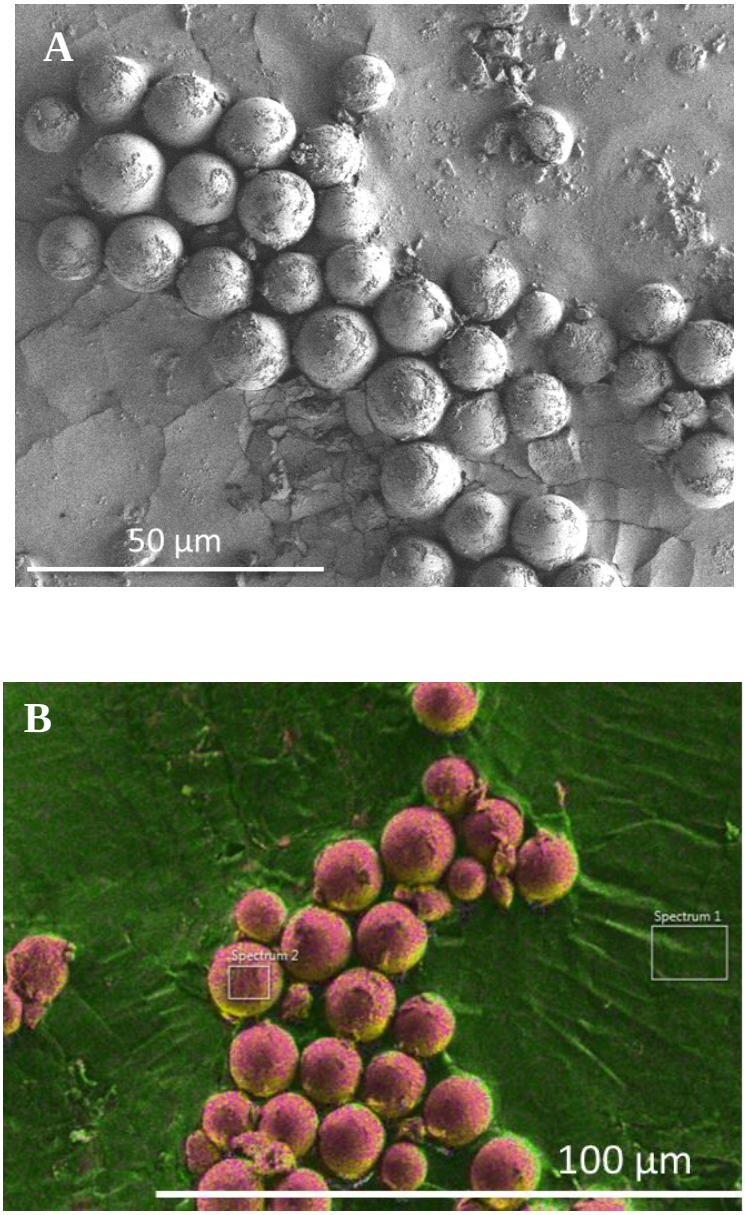

Figure 69. SEM image of Cr-RITC-Si Janus particles embedded in tape (A). EDX of Janus particles still embedded in the tape showing silica in yellow, chromium in pink, and the tape is shown in green.

Once their exposed surfaces were successfully coated with chromium, the particles were removed from the tape (placed in xylene and sonicated with heat) and resuspended in xylene. Figure 70A shows a SEM image of some Janus particles that were removed from

the tape and resuspended. It shows that the particles were successfully removed from the tape but there are still large chunks of debris present in the sample. To clean the sample and remove more of the debris, the particles were washed multiple times via centrifugation and redispersion (at least five times). During this washing process, the particles were solvent exchanged from xylene to 200 proof ethanol which is the solvent needed for further functionalization and polymerization reactions. Figure 70B shows a SEM image of a chromium-coated RITC-labelled silica Janus particle after washing and resuspension in ethanol. There is a significant decrease in debris surrounding the particle and the chromium coating is very apparent.

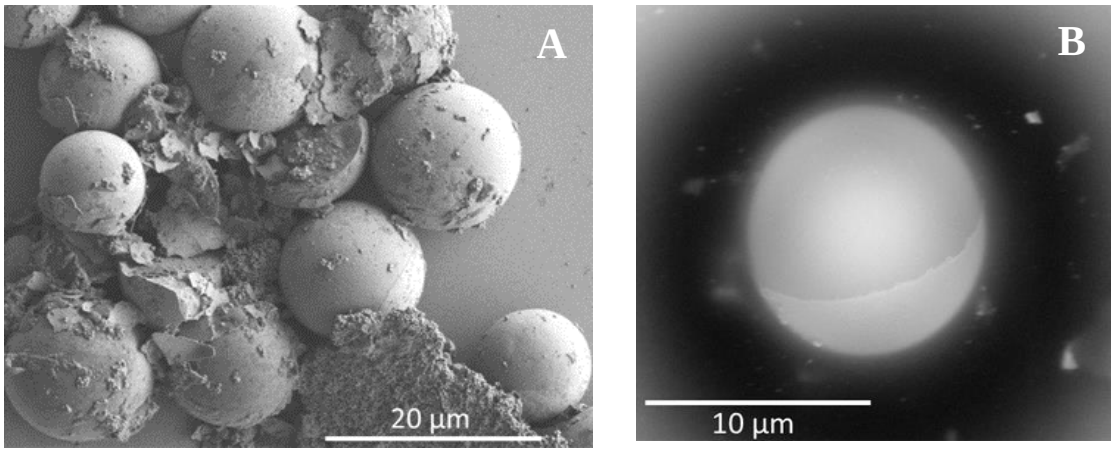

Figure 70. SEM of RITC-labelled silica that has been sputter coated with chromium and removed from the tape using xylene (A). An image of a Janus particle that was removed from the tape substrate and washed to remove excess debris (B).

Janus core particles were visualized using SEM coupled to EDX to ensure that the chromium coating was still present after the removal and washing process. Figure 71A shows a SEM image of a Janus core particle where a half-moon shaped coating can be seen on the particle surface. EDX was performed on the particle to ensure that the half-moon

shaped coating was chromium. Figure 71B shows the image of the particle with the EDX data coloring overlayed on the image. Confirmation that the coated surface was chromium is indicated in the image by the silica particle being colored blue and the chromium shown in purple.

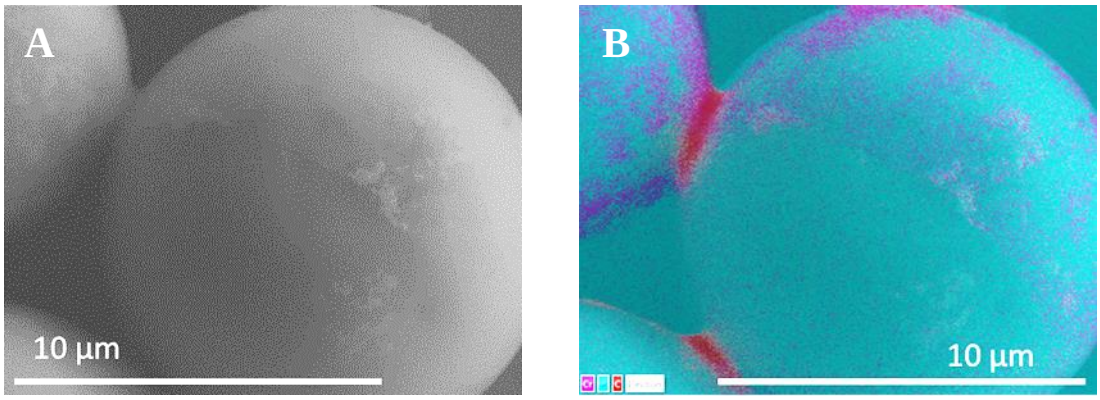

Figure 71. SEM of chromium-coated RITC-silica Janus particle showing two different surfaces on the particle (A). EDX of the same Janus particle confirming that the particle is chromium (purple) coated on the silica (blue) particle.

5.4.4 Polymerization and Characterization of Polypeptide-Coated Chromium-Silica Janus Particles

Ultimately, polypeptide-coated Janus particles with the chromium and polypeptide being on different halves of the particle were the desired material. To obtain these particles, the metal-coated cores still need to undergo a few more synthetic steps to create the final product. As a short overview, the Janus core particles are functionalized with a primary amine silane molecule on the silica half of the particle, which will initiate the ring-opening polymerization of the polypeptide monomer (an N-carboxyanhydride molecule). This will allow the polypeptide chains to polymerize from the particle surface via a *grafting from*

approach. The polypeptide-coated Janus particles were then washed multiple times (at least five times) via centrifugation and redispersion to remove any unreacted monomer and free polypeptide that may be in solution. Washed particles were resuspended in either THF or pyridine for further characterization studies.

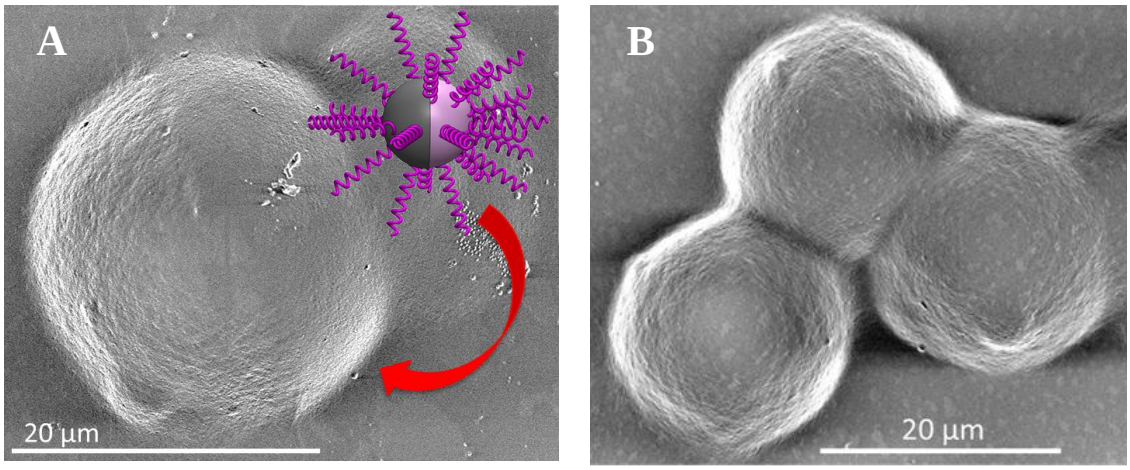

Figure 72. SEM of polypeptide-coated Janus particles with the chromium side visible (A), and multiple polypeptide-coated Janus particles (B). The inset in A is an illustration of the particle in the SEM image.

Initial characterization of the polypeptide-coated Janus particles was performed using an SEM to visualize any changes to the Janus core particles. Figure 72 shows two SEM images of the polypeptide-coated Janus particles. In Figure 72A, there is a distinct change to the surface of the particles indicating polypeptide was attached via the *grafting from* polymerization reaction. The chromium coating is still visible through the polypeptide coating on the particle in Figure 72A. Multiple particles are shown in Figure 72B with the same distortion to the particle surface to ensure that more than just a single core was coated with polypeptide.

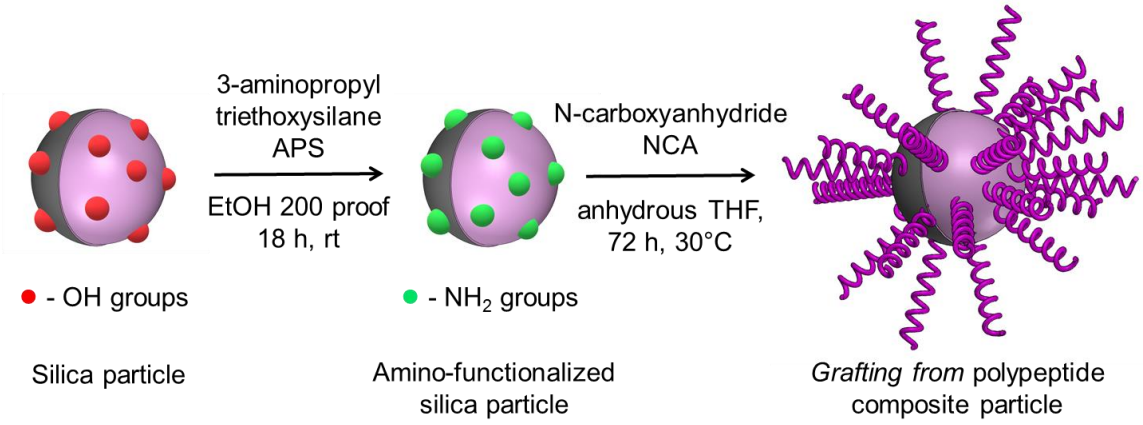

Figure 73. Reaction scheme illustrating the amino-functionalization and the consequent polypeptide polymerization from the chromium-silica core surface via the *grafting from* method. This resulted in a polypeptide-coated Janus core particle where polypeptide is grafted onto the entire Janus core particle surface.

The goal of this work was to create a polypeptide-coated Janus particle that has polypeptide on only the silica half of the core particle. It is apparent when looking at the particles with a SEM (Figure 72) that there is polypeptide on the entire Janus core surface and not just on the silica half. Figure 73 shows a reaction schematic that illustrates the actual outcome of the synthetic steps taken to try to create the hypothesized Janus particles. It was hypothesized that the chromium would prevent the coated half of the particles from functionalization with primary amine groups, but the affinity for the silane groups to interact with the chromium surface was not taken into account. Instead, the amino-silane molecule reacted with both the silica and chromium surfaces resulting in an amino-functionalized Janus particle with amine groups on the entire surface. This then allowed the polypeptide to be polymerized from both halves of the core particle and resulted in an entire polypeptide-coated Janus particle as shown in the reaction scheme in Figure 73.

Even though the final product obtained was not the desired product, it still resulted in a polypeptide-coated Janus particle based on SEM. Further characterization tehcniques

were used to confirm the presence of the polypeptide shell. FTIR was performed on the amino-functionalized Janus core particles and the polypeptide-coated Janus particles to confirm the addition of the polypeptide shell. The main spectral lines to identify in the polypeptide samples are the amide A band (N-H stretch), amide I band (backbone C=O stretch), amide II band (N-H bending), and the amide I C=O vibration.[49-50, 87] The amino-functionalized Janus core particles should have spectral lines associated with the primary amine groups (N-H stretch) and the crosslinked silica particle (Si-O stretch).

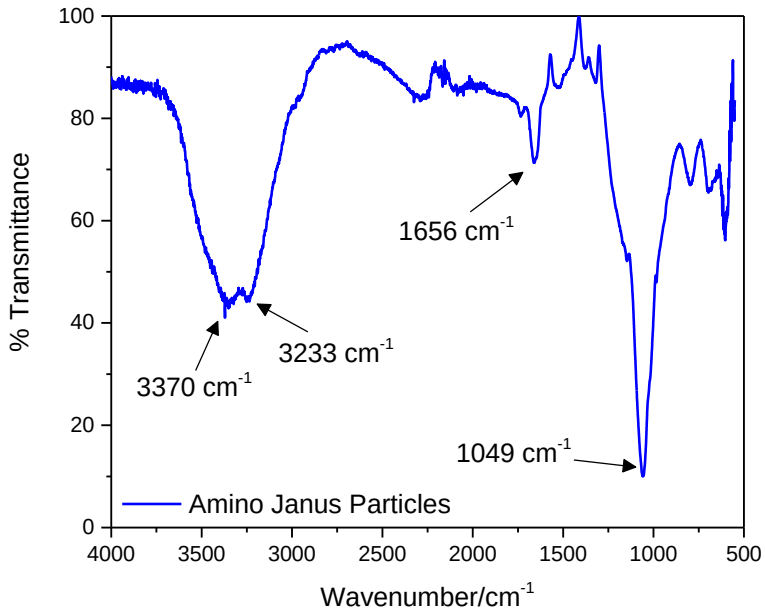

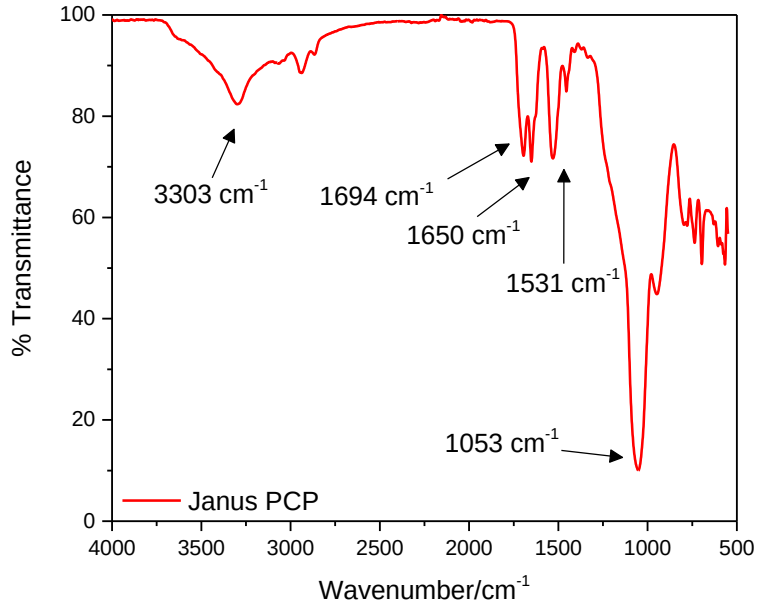

Figure 74. FTIR traces of (blue) Amino-functionalized Janus core particles and (red) Polypeptide-coated Janus particles. Peaks that are important in identifying the difference between amino-silica particles and polypeptide-coated particles are identified in each trace.

Figure 74 shows the FTIR spectra for the functionalized Janus core particle and the final polypeptide-coated particle. The amino-functionalized core, shown in blue, was identified by the characteristic primary amine peaks from the added functional groups to the original Cr-Si Janus core particle. These peaks are present at 3370 cm^{-1} and 3233 cm^{-1}. Another characteristic peak is found at 1049 cm^{-1} from the siloxane Si-O stretching in the core particle, made up predominately of silica, which produces a sharp spectral signal. The FTIR of the polypeptide-coated Janus particles is shown in red. The N-H amide stretch, resulting from the polypeptide backbone, is identified at 3303 cm^{-1}. There are important spectral signals in the polypeptide-coated particle spectrum at 1694 cm^{-1} and 1531 cm^{-1} showing the amide I band and the amide II band respectively. These peaks which are

usually stronger in signal appear more weak in these samples due to the abundance of silica present in the sample. The final peak that is highlighted in the polypeptide-coated particle sample is the strong spectral signal at 1053 cm^{-1} which indicates a siloxane stretch (Si-O) from the silica core particle.

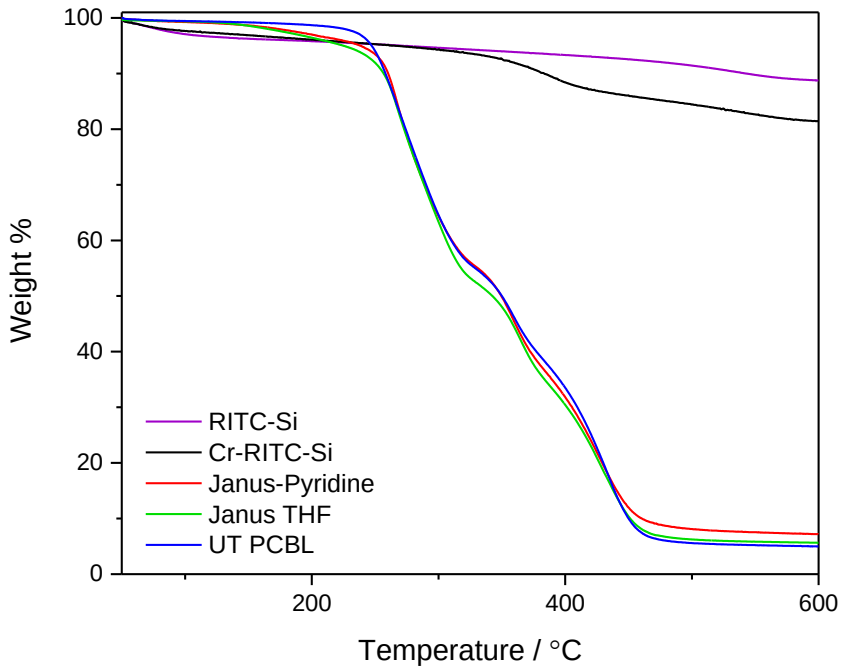

Figure 75. TGA traces for each step in the Janus particle synthesis: RITC-Si core particle (purple), Cr-RITC-Si Janus core particle (black), Polypeptide-coated Janus particle stored in pyridine (red), Polypeptide-coated Janus particle stored in THF (green), and untethered PCBL (blue).

Thermogravimetric analysis was also conducted on the polypeptide-coated Janus particles to confirm the attachment of the polypeptide shell to the core particle. Various stages of the polypeptide-coated Janus particle synthesis were analyzed using TGA to determine the effect each addition has on the overall degradation of the final product. Using the different degradation curves provided from TGA an estimation of the amount of

polypeptide grafted to the particle surface can be determined. Figure 75 shows the TGA traces for each of the samples analyzed. The RITC-labelled silica core and the chromium-coated RITC-labelled silica core particles were analyzed and characterized as control for the silica particle degradation and are shown in purple and black respectively. Untethered PCBL polypeptide was also used as a control for the polypeptide degradation and is shown in blue. The TGA for the polypeptide-coated Janus particles is shown in red and green. The polypeptide grafting density was estimated to be ~75%. The two different polypeptide-coated Janus particle samples are from the same polymerization reaction but after the final washing, the two samples were stored in either THF or pyridine. Both samples were run to make sure that the storage solvent did not affect the stability of the polypeptide-coated Janus particles.

5.5 Conclusion

Polypeptide-coated Janus particles were successfully synthesized using commercially available silica particles, scotch tape, and a homemade sputter coating system. Various characterization techniques aided in the analysis and visualization of the sequential steps of creating these Janus particles. PCBL was *grafted from* the Janus core surface to yield a stimuli responsive polypeptide-coated Janus particle.

The goal was to create a final product that had PCBL polymerized onto the silica half of the Janus core particle, leaving the chromium half open for further functionalization with other polypeptides such as PBLG. Large polypeptide-coated Janus particles having polypeptide A (PCBL) and polypeptide B (PBLG) on different halves of the particle would allow these materials to be used as pseudo di-block colloids for use as a monomer unit in

the creation of poly(colloids). The two polypeptides can also undergo a deprotection reaction to yield an AB monomer that is acid on half and base on the other half. Even though the final product consisted of PCBL tethered to the entire Janus core surface, these particles can find many uses in materials and polymer studies. Poly(colloids) can be created with these particles but instead of having a di-block colloid as the monomer, two separate polypeptide-coated Janus particle systems can be synthesized. The two systems would each be a monomer unit that can then be combined to create a poly(colloid) system.

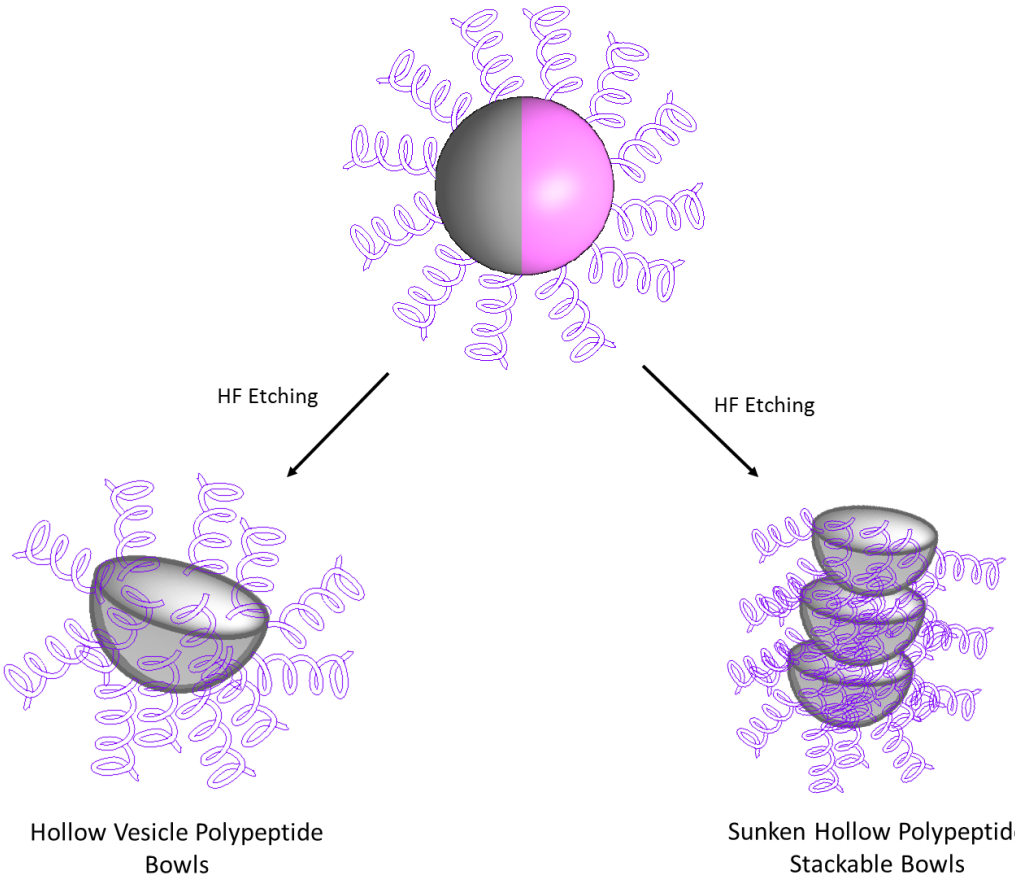

Figure 76. Illustration showing the removal of the silica core by HF etching of the polypeptide-coated Janus particles.

In addition to creating poly(colloids), these polypeptide-coated Janus particles can be used to create hollow vesicle structures. The silica core can be removed via etching with HF to leave a polypeptide vesicle with a small chromium side. An illustration of the removal of the silica core and the subsequent products is shown in Figure 76. Secondary conformational transition studies can be conducted on the polypeptide chains to determine if a hollow structure affects the transition. The hollow vesicle could also collapse on itself to create a half-moon shaped polypeptide-coated chromium structure. Interesting particle-particle interactions could be observed within this system and studies that probe the particle-particle stacking interactions could be conducted. Polymeric and materials studies would benefit from the development of these macromolecular-sized polypeptide-coated Janus particles.

CHAPTER 6. CONCLUSIONS AND FUTURE WORK

6.1 Conclusions

This work has presented detailed studies for increased understanding of the degradation and conformational transition of poly(carbobenzyloxy-L-lysine) (PCBL) and PCBL-PCPs. It has also presented composite materials synthesized with varying responsive and physical properties. Fundamental studies were performed on both untethered and tethered PCBL. Chapters 2 and 3 use untethered PCBL free in solution while chapters 4 and 5 rely on PCBL being tethered to a silica core particle.

The second and third chapter use ultrasonic energy (at either high or low powers) to study untethered PCBL. At higher power, ultrasonic energy was used to study the degradation of the polypeptide as a function of molecular weight, temperature, and concentration. It was found that molecular weight and concentration play a significant role in the overall degradation of the polymer chains. The higher the molecular weight, the more degradation of the polypeptide, whereas the higher the concentration of polypeptide in solution the less overall degradation. Temperature has a small effect on the breakdown of PCBL over long times. At lower power, ultrasonic energy was used to measure and follow the secondary conformational transition of PCBL. Optical rotation, the widely accepted technique for following conformational transitions, was used to compare the results and determine the validity of the sound velocity technique. It was found that both molecular weight and concentration shift the temperature at which the conformational transition occurs. Both techniques, optical rotation and sound velocity can follow the transitions and its subsequent shifts.

The fourth and fifth chapter center on studies where PCBL is tethered to a silica particle surface. Chapter 4 focuses on the synthesis and characterization of stimuli-responsive core-shell particles. The particles have a silica-coated cobalt core particle and a PCBL polypeptide shell. It was found that the polypeptide shell could still undergo its secondary conformational transition even after it is tethered for a core particle. In addition, the magnetic properties of the cobalt core are still active after coating with silica and polypeptide; however, the magnetic susceptibility is altered by the polypeptide conformation. It was demonstrated that the magnetic responsive of the cobalt is maintained after years of sitting in solution. The last chapter (Chapter 5) looks at the synthesis and characterization of polypeptide-coated Janus particles. A stimuli-responsive Janus particle was synthesized by sputter coating chromium on a silica core particle embedded in Scotch tape. After removal from the tape, PCBL was polymerized from the Janus particle core to create a polypeptide-coated Janus particle. Sequential characterization from the silica core to the final product was conducted to visualize the PCBL-coated Janus particles.

This dissertation provides a fundamental understanding of the breakdown and responsive nature of PCBL and PCBL composite particles. These findings provide understanding to continue expanding work with polypeptides and biomaterials for use in a variety of applications such as polycolloids, vesicles, and other responsive materials.

6.2 Future Works

The future works provided below will be aimed at extending the projects and use of materials found in this dissertation.

6.2.1 Jamming Phase Transition Studies

One area of research, the jamming phase transition, similarly linked to the glass transition of polymers, is still not well understood.[91, 212] Even less experimental evidence is available for polymeric and colloidal systems that are responsive in nature. Most of the studies conducted on the jamming of responsive materials use the stimuli responsive polymer, PNIPAM.[91, 212-213] Polypeptide composite particles can undergo similar changes by switching the polypeptide conformation while having the added benefits of chiroptical transitions and mesogenic surfaces. Additionally, the length and stiffness of the polypeptide when in helical form is expected to promote particle-particle interactions and interdigitation even at very low surface coverages, which to date has been difficult to probe experimentally. Preliminary jamming studies on silica cores using fluorescence photobleaching recovery (FPR) are shown in Figure 77.

A main issue with the jamming transition studies on the silica cores is the sedimentation of the cores after long acquisition times and large amounts of photobleaching of the samples from the laser source. In order to overcome the photobleaching issue, an image-based FPR system was developed. An inverted microscope was converted into an FPR instrument by inserting a Ronchi ruling in the image plane of the microscope. Image-based analysis software is currently being created in LabView to measure the return of fluorescence over time in the samples.

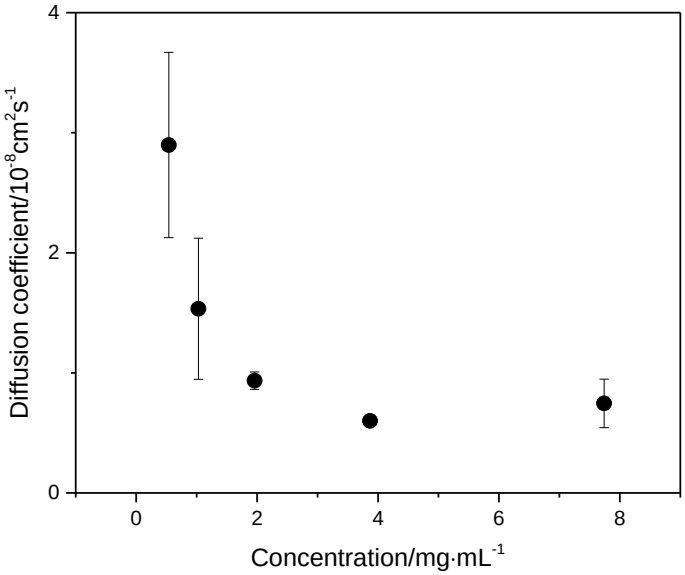

Figure 77. Calculated diffusion coefficients of FITC-labelled silica particles as a function of concentration for preliminary jamming phase transition studies.

6.2.2 Polypeptide-Janus Particles

Polypeptide-coated Janus particles were successfully synthesized and shown in Chapter 5 however, the product created was not the intended product. Future studies can be conducted on the particle obtained in Chapter 5 to etch away the silica and get a large hollow vesicle for uptake and release studies. In addition, the synthesis can be slightly altered to produce a Janus particle that is half coated in metal and the silica half is coated in polypeptide versus the entire particle being coated in polypeptide. An illustration of this Janus particle is shown in Figure 78. This will provide a particle that is stimuli-responsive on half of its surface, which can produce a self-propelling particle, micro motor, or a model system for mimicking magneotatic bacteria.[37, 205, 208]

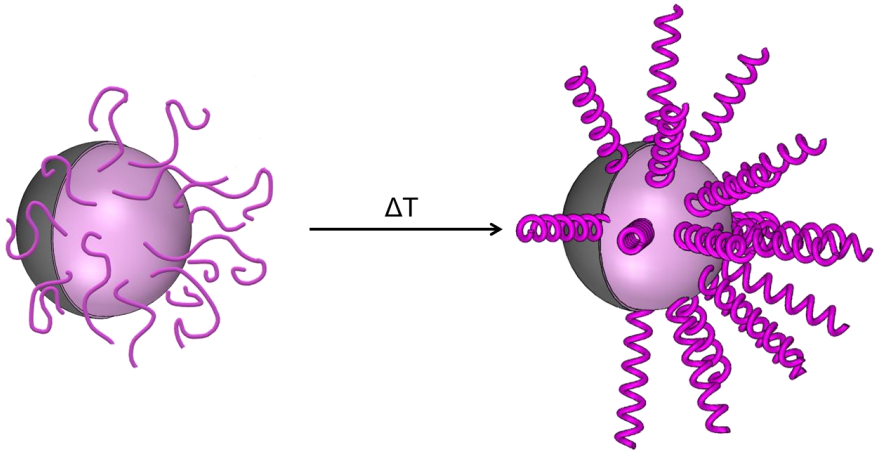

Figure 78. An illustration showing the reversible coil-helix transition of PCBL tethered to a Janus core particle. As temperature is changed, the polypeptide conformation changes which can induce self-propulsion in solution.

6.2.3 Crosslinking of Polypeptide Composite Particles

Polypeptide composite particles can find many uses in materials and biological applications. Future work can focus on the crosslinking of these particles which would result in a polycolloid structure.[209] These polycolloids can be used to study the conformational transition of the polypeptides when they are bound on both ends versus on a single end of the chain. The propagation of the conformational transition could also be studied using these systems. In addition, after the crosslinking of these particles, they can resemble long structures similar to muscle fibers.[70, 214] With the polypeptides ability to undergo a helix-coil transition, long crosslinked structures can be used to mimic artificial muscle fibers.[215-218]

CHAPTER 7. GENERAL SYNTHETIC METHODS AND CHARACTERIZATION TECHNIQUES

7.1 Introduction

The silica cores, polypeptides, and polypeptide composite particles used in this work were all synthesized from scratch in order to obtain specific core sizes, functionality, chemistry, and final characteristics.

7.2 Materials

All of the chemicals and solvents obtained were commercially available and were used without further purification. Chemicals used in the preparation of the materials described in the following sections are listed in the previous chapters after the Introduction section. The solvents used for the synthesis of the NCA monomers were all anhydrous and purchased in Sigma Aldrich Sure-Seal bottles. Unless otherwise stated the water used in all aqueous reactions was nanopure water. The nanopure water was supplied by a Millipore Nanopure Type 1 source (18 MΩ).

7.3 Preparation of non-magnetic colloidal silica core particles

7.3.1 Synthesis of silica core particles by the Stöber method.

The silica particles were synthesized using a modified Stöber procedure. In a three-neck round bottom flask 250 mL of ethanol was mixed with 50 mL of ammonium hydroxide to ensure a homogenous basic pH of ~9–10 (this was tested with litmus paper). The mixture was stirred vigorously for ~15 min. A solution consisting of 5 mL of TEOS

in 20 mL of ethanol was added quickly to the stirring mixture. The vigorous stirring was maintained and the reaction was allowed to continue for 2 hours. After the allotted time, the stirring was stopped and the reaction was left to rest while the fluorescent labelling reaction was set up.

* If the silica particles are not being fluorescently labelled then they are washed using centrifugation and dispersion in order to remove any leftover base in solution.

7.3.2 Synthesis of silica via reverse microemulsion

In a 500 mL three-neck round-bottom flask, 17.5 mL of Igepal CO-520 and 225 mL of cyclohexane were added. The flask was connected to an overhead mechanical stirrer and 5 mL of ammonium hydroxide was added to the flask. This mixture was allowed to stir at ~300 rpm for 10 minutes to create the microemulsion. After this time, 5 mL of TEOS was added quickly to the stirring solution and the reaction was allowed to proceed overnight. To break the microemulsion, methanol (~60 mL) was added to the solution and the solution was washed via centrifugation and redispersion. The particles were washed initially with methanol three times and then washed with ethanol for storage.

7.3.3 Preparation of the FITC-APS Adduct

In a 50 mL round bottom flask, 50 mg of FITC and 10 mL of ethanol were mixed together. The flask was capped with a septum and magnetic stirring for 30 min mixed the contents to produce a homogenous solution. A total of 0.5 mL of APS was injected into the stirring solution and the reaction was allowed to proceed for 18 h in the dark.

* The same procedure can be used to make RITC-APS adduct by substituting RITC for FITC.
* The FITC and APS should be in a 1:1 molar ratio.
* The reaction proceeds in the dark to prevent the dye from bleaching (aluminum foil is wrapped around the round bottom flask).

7.3.4 Synthesis of fluorescently labelled silica particles via Stöber method

After the silica seed particles were synthesized (Section 7.2.1), 10 mL of TEOS and 30 mL of ethanol were mixed in a 50 mL separatory funnel, which was attached to the three-neck round bottom flask. The flow of the solution was set at 2 drops/min. A volume of 0.4 mL of FITC-APS adduct was injected into the silica suspension using a syringe The reaction was allowed to proceed in the dark for 48 h under continuous vigorous stirring at room temperature. Once the reaction was complete the fluorescently labelled particles were washed with fresh ethanol by repeated centrifugation and dispersion.

* RTIC-labelled silica particles can be synthesized from the same protocol by switching FITC-APS adduct with the RTIC-APS adduct.
* The flask was wrapped in aluminum foil to produce a dark environment to prevent the dye from photobleaching.
* Washing of FITC-labelled silica was conducted until the supernatant no longer gave a fluorescence signal when illuminated with a 488 nm wavelength laser source.
* Washing of RITC-labelled silica was conducted until the supernatant no longer gave a fluorescence signal when illuminated with a 660 nm wavelength laser source.

7.3.5 Preparation of Fluorescently labelled silica via reverse microemulsion

The silica reaction is performed as described previously (Section 7.2.2) with the addition of the FITC-APS adduct (or RITC-APS adduct) added into the reaction vessel with the ammonium hydroxide. An example is described below:

In a 500 mL three-neck round-bottom flask, 17.5 mL of Igepal CO-520 and 225 mL of cyclohexane were added. The flask was connected to an overhead mechanical stirrer then 5 mL of ammonium hydroxide and 2 mL of the dye adduct (FITC-APS or RITC-APS) was added to the flask. This mixture was allowed to stir at ~300 rpm for 10 minutes to create the microemulsion and the flask was wrapped with aluminum foil to prevent photobleaching. After this time, 5 mL of TEOS was added quickly to the stirring solution and the reaction was allowed to proceed overnight. To break the microemulsion, methanol (~60 mL) was added to the solution and the solution was washed via centrifugation and redispersion. The particles were washed initially with methanol three times and then washed with ethanol for storage.

7.3.6 Protective silica coating on fluorescently labelled silica

In order to prevent dye leaking and bleaching a small silica coating can be synthesized on the fluorescently labelled silica particles from Section 10.2.3. The final size of the particles can be controlled using the calculations from Zhang *et al*.[12]

$$d = d_0(V/V_0)^{1/3} \quad (11)$$

In Equation 11, d is the final particle diameter, d_0 is the initial size of the silica particle, V_0 is the initial volume of TEOS used to prepare the silica particles, and V is the TEOS needed to obtain the particles finals diameter.

Example: From the fluorescently labelled silica suspension (Section 7.2.4), 100 mL of the suspension was taken and diluted with 100 mL of ethanol and placed into a 500 mL three-neck round bottom flask. The mixture was then sonicated in a sonicator bath for 10 min to ensure sufficient dispersion of the particles in the solution. An overhead mechanical stirrer was connected to the middle neck of the round bottom flask and then the flask was wrapped with aluminum foil to prevent photobleaching. A total of 43 mL of ammonium hydroxide was added to create a basic environment. The pH of the solution was tested with litmus paper (pH = 9–10). The mixture was stirred at 200 rpm for 15 min to form a homogenous solution. While stirring was taking place, 6 mL of TEOS was combined with 24 mL of ethanol and placed into a 125 mL separatory funnel which was then attached to one of the open necks on the three-neck round bottom flask. The flow of the solution was adjusted to be 2 drops/min and the silica suspension was stirred vigorously at 400 rpm. The reaction was allowed to continue at room temperature over the next 24 h. Once the reaction was completed the particles were washed with fresh, clean ethanol by centrifugation and dispersion to remove any leftover base in solution.

7.3.7 Silanization of the silica core particle

In order to obtain larger molecular weight polypeptides on the silica cores, the cores were functionalized using the amino precursor 3-aminopropyl triethoxysilane, APS mixed with a passivating agent, methylmethoxy silane, MTMS. The ratio of APS to MTMS can

be varied to alter desired surface coverage of amino groups on the silica particles. A 10 mL aliquot of the protected fluorescently labelled silica particles was placed into a 250 mL round bottom flask. It was diluted with 90 mL of 200 proof ethanol and then the suspension was sonicated for five min. The round bottom flask was wrapped in aluminum foil to prevent photobleaching of the particles and the solution was allowed to stir at a speed in which a vortex first occurs. A 1:3 ratio of APS to MTMS was injected into the suspension using a syringe and the reaction proceeded for 18 h at room temperature. Once the reaction was finished the particles were washed by centrifugation and dispersion with clean ethanol. Washing was continued until the ninhydrin test returned a negative result indicative of no free amino groups in the silica suspension. In order to perform the ninhydrin test, ~1 mL of the supernatant after centrifugation was placed into test tubes suspended in a water bath set to 50 °C. Approximately 2–5 drops of a 10% alcoholic ninhydrin solution was added to the tubes. If free amino groups are present in the supernatant, the solution will become purple or blue in color. Once the solution did not show any further change in color, the particles were washed by centrifugation and dispersion with anhydrous THF and stored in a dark vial to prevent photobleaching.

7.4 Synthesis of magnetic colloidal silica particles

7.4.1 Synthesis of silica coated cobalt core particles

A Qsonica probe ultrasonicator equipped with a ½" sonicating probe was attached to the middle neck of a 1 L three-neck round-bottom flask. The flask was capped with two septa and degassed with argon for 20 mins prior to use. While the flask degassed, in a separate glass container, a solution consisting of 800 mL of 200 proof ethanol, 14.4 μL of

APS, and 169 μL of TEOS was prepared. This solution will be referred to as the silica solution. In the degassed round-bottom flask, 200 mL of a freshly prepared and degassed solution of $4x10^{-4}$ M NaBH4 containing $4x10^{-3}$ M citric acid was quickly added. The argon was allowed to continue to bubble through the solution and the cobalt precursor solution (200 μL of a 0.4 M solution of $CoCl_2$, freshly prepared and degassed) was injected into the solution using a long needle. The probe sonicator was programmed to sonicate for 1 hour while operating at 40% amplitude. The formation of cobalt particles could be determined almost immediately when a grey coloration of the solution occurred (previously pink/red in color). After 1 min of sonicating, the silica solution (previously prepared) was added very quickly. The reaction was allowed to continue for the remaining programmed time and argon continued to bubble the entire time. After the entire hour was completed, the particles were washed either via a magnet or by centrifugation and redispersion. Either washing technique was performed at least three times to remove the reaction solution. The particles were redispersed in ethanol for storage.

7.4.2 Functionalization of the silica coated cobalt core particles

A 500 mL round-bottom flask was attached to an overhead mechanical stirrer. Approximately 70 mL of the silica coated cobalt particles were diluted with 200 mL of ethanol. A 1:3 ratio of amino-silane (APS or AEAPTMS) to MTMS was injected into the suspension using a syringe and the reaction proceeded for 18 h at room temperature. Once the reaction was finished the particles were washed by centrifugation and dispersion with clean ethanol. Washing was continued until the ninhydrin test returned a negative result indicative of no free amino groups in the silica suspension. In order to perform the ninhydrin test, ~1 mL of the supernatant after centrifugation was placed into test tubes

suspended in a water bath set to 50 °C. Approximately 2–5 drops of a 10% alcoholic ninhydrin solution was added to the tubes. If free amino groups are present in the supernatant, the solution will become purple or blue in color. Once the solution did not show any further change in color, the particles were washed by centrifugation and dispersion with anhydrous THF and stored in a dark vial to prevent photobleaching.

7.5 Synthesis of untethered polypeptides and polypeptide composite particles

7.5.1 Precursor molecule ε-carbobenzyloxy-L-lysine

The precursor molecule, CBL, can be purchased from Sigma Aldrich.

7.5.2 Precursor molecule γ-benzyl-α,L-glutamate

The precursor molecule, BLG, can be purchased from Sigma Aldrich. It can also be synthesized using a modified procedure from Blout and Karlson.[55]

In a 500 mL round bottom flask, 33 g of L-glutamic acid was added to 220 mL of benzyl alcohol. The mixture was heated to 90 °C for ~1 hour, after which 60 mL of 48% hydrobromic acid was added quickly to the solution. The reaction went clear quickly after the addition and was left to stir for another 30 minutes. Next, the reaction was cooled as quickly as possible to 35 °C. In a 2 L beaker, 440 mL of 200 proof ethanol and 66 mL of pyridine were added together and allowed to stir on a hot plate. The cooled reaction solution was added to the stirring mixture in the beaker. The new mixture was cooled to room temperature and then placed into an ice bath overnight to allow the product to precipitate.

The next day, the precipitated product was isolated via filtration. The product was recrystallized from a 1 L solution of 5% ethanol kept at pH ~7 with sodium bicarbonate. The recrystallization solution was heated but the temperature was kept < 70 °C for the shortest time possible to prevent the decomposition of the product back into the reactants. While the solution was hot, it was filtered, cooled rapidly to 3 °C, and then kept cold overnight for precipitation to occur.

The next day, the precipitate was isolated by filtration, washed with water (pH ~7 by adding sodium bicarbonate), washed with water, and then added to ethanol to create a slurry. The slurried solution was filtered, washed with ethyl ether, and air dried. Once dried, the product was placed into a vial and stored in the refrigerator until used.

* Aliquots were taken during each step of the reaction and filtration for further analysis and characterization.

7.5.3 Precursor molecule tyrosine

The precursor molecule, BTY, can be purchased from Sigma Aldrich.

7.5.4 Synthesis of NCA derivatives from amino acid precursors

In a medium glove bag under a nitrogen atmosphere, 150 mL of anhydrous ethyl acetate and 5 g of amino acid (previously dried overnight, at least 8 hours, *in vacuo*) were added to a 500 mL three-neck round bottom flask. A stir bar was placed into the round bottom flask and the flask was capped with 3 rubber septa. The flask was connected to a condenser, capped with a rubber septum, and placed into an aluminum bead bath that was

heated. Argon or nitrogen gas was bubbled through the reaction slurry to ensure an inert atmosphere and the mixture was brought to reflux.

In a small glove bag under a nitrogen atmosphere, 2.5 g of triphosgene was weighed out into a flame dried scintillation vial. The triphosgene was quickly added to the refluxing mixture and the reaction was allowed to proceed until the solution became clear. Once the solution cleared the reflux was kept for one hour after which the reaction solution was cooled and placed into a -20 °C freezer to rest overnight.

Washing the NCA according the procedure developed by Poché and Daly allowed for removal of unreacted NCA precursor and side products.[61] The NCA solution was placed into a 500 mL separatory funnel with 100 mL of icy water, swirled to mix, and the organic phase of interest was kept in the glassware. A 0.5% solution of $NaHCO_3$, 100 mL, was added to the separatory funnel, swirled to mix, and the organic phase of interest was decanted into a clean 250 mL round bottom flask. The flask was then placed into the medium glove bag under an inert atmosphere where $MgSO_4$ was added quickly until no more clumping occurred in the flask indicating that all water was removed from the NCA solution. The clear NCA solution was suction filtered through Whatman 90 mm filter paper in a clean, dry vacuum flask to remove the $MgSO_4$. The filtered solution was placed into a new, clean, dry 250 mL round bottom flask and the volume was reduced to 1/3 using a rotatory evaporator. Approximately 100 mL of cold anhydrous hexane was poured slowly into the NCA solution. White crystals of NCA started to form and the flask was capped and placed into the freezer to allow precipitation to occur.

The precipitated NCA was suctioned filtered, inside a medium glove bag under inert atmosphere, through Whatman 90 mm filter paper. If the NCA had a white and powdery appearance and it would be used within a couple of days, further purification was not necessary. The dried NCA was stored in an oven-dried scintillation vial with a PTFE-lined cap and placed into the freezer for storage. If the NCA needed to be purified further, it was placed into a new clean, dry 250 mL round bottom flask and dissolved in 15 mL of dry THF. Again cold dry hexane was poured slowly into the flask while it was being swirled until white crystals began to form. The flask was capped and placed inside the freezer overnight for crystallization to occur. The recrystallization reaction was repeated at least once more for better purification of the NCA monomer. Once purified, the NCA was placed into an oven-dried scintillation vial with PTFE-lined cap and placed into the freezer until used.

7.5.5 Synthesis of untethered polypeptides

In nitrogen-filled glove bag, ~2.00 g of CBL-NCA was dissolved in 50 mL of anhydrous THF inside a 100 mL oven-dried round bottom flask. A magnetic stir bar was placed into the flask and capped with a rubber septum. The flask was placed into an aluminum bead bath (Lab Armor Beads) and sodium methoxide solution (0.3 mL) was injected. A bubbler containing silicon oil was connected to the flask and the reaction was heated to 35 °C and stirred until there was no bubble formation inside the oil in the bubbler (usually 2 days). The flask was then connected to a rotatory evaporator to reduce volume to 1/3 to obtain a viscous solution that was slowly poured into a beaker containing water. This caused the polypeptide to precipitate out of solution and the precipitate was suction filtered using a Whatman 90 mm filter paper and allowed to dry.

* Example is shown for synthesizing untethered PCBL. To make other untethered polypeptides, use the NCA monomer made with the precursor molecule for the polypeptide being synthesized.

7.5.6 Synthesis of polypeptide composite particles

In a clean and dried 100 mL round bottom flask inside a nitrogen-filled glove bag, ~2.2 g of CBL-NCA was dissolved in ~50 mL of anhydrous THF. A magnetic stir bar was placed into the flask and the flask was capped with a rubber septum. The flask is placed into an aluminum bead bath and 10 mL of amino-functionalized Janus cores suspended in THF are injected into the flask. A bubbler containing silicon oil was connected to the flask via tubing with a needle at the end. The reaction was heated to 35 °C and stirred until there was no bubble formation inside the oil in the bubbler (usually 2 days). The particles are then washed at least three times by repeated centrifugation and redispersion in THF. In the final step, half are resuspended in THF and the other half are resuspended in pyridine.

7.6 Characterization Techniques

7.6.1 Light Scattering

7.6.1.1 Background

The light scattering technique has been used for many years to characterize particles, colloids and other systems.[219] It relies on thermodynamic methods to determine the mass, size, and shape of the particles. Additionally, dynamic light scattering can give the diffusion coefficient of the scattering particles, which is a second way to determine size. The molecular information about a given solute is obtained by measuring the intensity

of light scattered by the solution as a function of the polymer concentration, *c*, and the scattering angle, θ. The scattering intensity fluctuates because the particles in solution are undergoing Brownian motion, and so the distance between the scatterers in solution is constantly changing with time. The intensity fluctuations contain information about the rate of motion of the scatterers.[219]

The intensity fluctuations, although they seem random, are correlated on a short time scale and are followed with a correlation function.[219] In DLS, an autocorrelation function of the scattered light intensity is measured and after some amount of time the signal can be approximated by Equation 12.

$$G^{(2)}(t) = B(1 + f\left|g^{(1)}(t)\right|^2) \tag{12}$$

In this expression, *B* is the baseline and *f* is an instrumental parameter related to how many coherence areas the detector sees, strength of signal from solute molecules relative to that arising from solvent, and detector noise. The electric field autocorrelation function is $g^{(1)}(t)$, which in most cases is a simple exponential decay as shown in Equation 13.

$$g^{(1)}(t) = e^{-\Gamma t} \tag{13}$$

In Equation 13, Γ is the decay rate, which for simple translational diffusion is given by Equation 14.

$$\Gamma = \tau^{-1} = q^2 D_m \tag{14}$$

The mutual diffusion coefficient is represented by the term D_m, and the scattering vector magnitude, q, is defined in Equation 15.

$$q = 4\pi \cdot n \cdot \sin(\theta/2)/\lambda_o \tag{15}$$

The refractive index is represented by n, λ_o is the laser wavelength *in vacuo*, and θ, as mentioned previously, is the scattering angle. The resulting diffusion coefficient from Equation 14, D_m, when extrapolated to infinite dilution, becomes D_o. Once D_o is obtained, the hydrodynamic radius can be calculated using Equation 16 which is the Stokes-Einstein relation for determining size of a spherical scatterer.

$$R_h = \frac{kT}{6\pi\eta_o D_o} \tag{16}$$

In Equation 16, kT is the thermal energy where k is Boltzmann's constant and T is the temperature in Kelvin. The solvent viscosity is represented by η_o. The size, state of dispersion, and hydrodynamic radius can be calculated using these five equations.

DLS has been widely used in polymer and colloidal particle science.[220-223] Forster and Schmidt used this technique to determine how molecular weight, charge density, and salt affected the dynamic behavior of polyelectrolytes.[222] Pecora used DLS to study dynamics of macromolecules, more specifically DNA, in both dilute and nondilute solutions.[224] In this research, DLS will be used to determine the shape, size, and state of dispersion of the silica particles.

7.6.1.2 Sample Preparation and Measurements

A custom-built, multi-angle light scattering apparatus using an ALV-5000/E autocorrelator and a 660 nm laser or 488 nm laser source was used to measure the size of the silica cores and PCPs. Vials were cleaned thoroughly with soap and water before being wrapped in aluminum foil and placed into the oven to dry overnight. Solvent was filtered into the clean vials using a Whatman 0.02 μm PTFE filter (organic solvents). The samples were also filtered into the vials after the solvent using a Whatman 0.45 μm PTFE filter, or larger depending on particle and polypeptide size. Measurements were taken at multiple scattering angles ranging from θ = 15° to 120° and the size was calculated using the previously described theory.

7.6.2 Fluorescence Photobleaching Recovery

7.6.2.1 Background

Fluorescence Photobleaching Recovery (FPR) experiments have been used for decades to determine the mobility of objects through a system. These systems have ranged from proteins and lipids through biological matrices to polymer particles through a gel.[225-227] This technique has been used by Stricker et.al to determine assembly dynamics of E.coli and Sprague et.al to analyze binding interactions in live cells.[228-229] Groups have used it to determine lateral mobility and diffusion of molecules through membranes as shown by Wu et. al and Yguerabide et.al.[230-231] Our group has previously used FPR for various studies. Fong et.al used a patterned FPR experiment to determine the size distribution of colloidal particles.[232] Mustafa et.al used a temperature ramped FPR experiment to directly characterize thermoreversible gels.[225] In this work, FPR will be used to ascertain the

mobility, or lack thereof, of our polypeptide composite particles in amorphous and crystalline colloidal materials.

Biological studies of protein and molecule diffusion often use a technique they refer to as FRAP (fluorescence recovery after photobleaching). FRAP is similar to FPR in that the purpose of the experiments is to determine the mobility, diffusion coefficients, and other kinetic properties of fluorescently active biomolecules.[226] FPR is used when a sample is naturally fluorescent, or if a sample can be fluorescently labelled. The main purpose of this technique is to determine the diffusion coefficient of a fluorescent sample. The acronym itself describes the three-step experiment involved in obtaining results: fluorescing of the sample, photobleaching of the sample, and recovery of the fluorescent sample. An illustration of this process is shown in Figure 79. First, the fluorescence of a small, selected region of the sample is obtained using a dim (reading beam). A low intensity beam is used so as to not cause any sudden degradation of the fluorescent signal. Secondly, a bright pulse of light (usually from a laser) is used to permanently photobleach some of the fluorescent molecules attached to the sample. Lastly, the return of the fluorescent signal to the bleached region of the sample is measured. Fluorescence signal returns to the previously bleached region due to the exchange of bleached with unbleached molecules by diffusion.[226, 233]

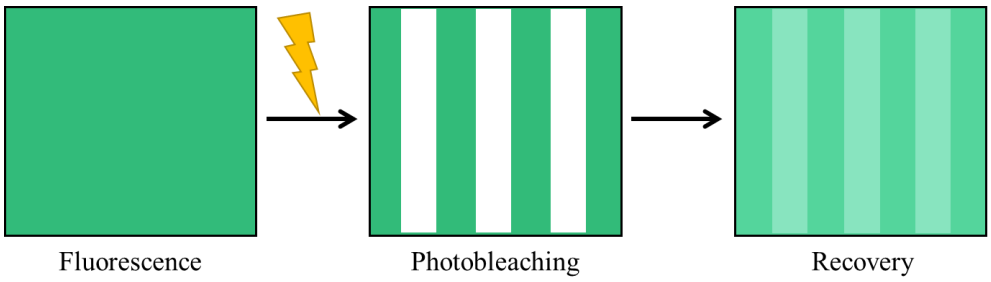

Figure 79. An illustration of the three-step process for an FPR experiment

One type of FPR experiment involves photobleaching a striped pattern into the fluorescent sample. A commonly used pattern is the Ronchi ruling, which is an optical grating that has black strips etched into the glass at equal distances from one another.[226] In order to produce this pattern the ruling is usually placed in the rear image plane of the microscope. The sample is photobleached with the pattern and then the Ronchi ruling is removed from the microscope so that the change in fluorescent intensity as a function of distance can be measured.[226] Using a striped pattern will result in a square wave shaped signal represented by Equation 17.

$$F(x,t=0) = F^{o} - \frac{C}{2} + \frac{C}{2}\left[\frac{4}{\pi}(\sin(K\chi) + \frac{1}{3}\sin(3K\chi) + \frac{1}{5}\sin(5K\chi) + \frac{1}{7}\sin(7K\chi) + \frac{1}{9}\sin(9K\chi) + \cdots)\right] \quad (17)$$

Currently modulation detection system similar to the system describe by Lanni and Ware is used.[233] In this system, instead of simply photobleaching the Ronchi ruling pattern into the sample and then removing the ruling, the modulation system will move the Ronchi ruling back and forth while the measurement takes place.[226] The modulation changes the resulting signal from a square wave shaped signal to a triangle wave shaped signal.

Equation 17 is then replaced with Equation 18 to represent the triangle wave signal because translational motion and ruling spacing need to be taken into account. Lanni and Ware's modulated stripped photobleaching method is beneficial because it not only lets the higher order harmonics in Equation 18 decay faster than those in Equation 17, but it also prevents photo degradation of the sample.[226]

$$V(t) \propto C_1(t)\sin(\omega t) - C_3(t)\sin(3\omega t) + C_5(t)\sin(5\omega t) - C_7(t)\sin(7\omega t) + \cdots \quad (18)$$

Initially, using the striped photobleaching method required experimentalists to perform deep bleaches in the sample.[226] These deep bleaches could potentially degrade the sample, which would cause inaccurate results and diffusion coefficients. The modulation of the system will lead to less degradation of the sample because even though the same amount of energy is being applied constantly, only half of the sample receives it at any given time. The black lines etched into the Ronchi ruling prevent further photobleaching of the region that is directly under the black lines at that time. The current modulated detection system set up in our lab will continue to be used for mobility studies, but a new, more appealing image based FPR system will be constructed in the future.

7.6.2.2 Sample Preparation and Analysis

A custom-built, fluorescence photobleaching recovery instrument with a 488 nm laser source was used to measure the diffusion of dextran, gelatin, and silica core particles. Samples were prepared in 4 mL scintillation vials. The solvent used for dextran and gelatin was nanopure water supplied by a Millipore Nanopure Type 1 source (18 MΩ). Silica core

particles were suspended in 200 proof ethanol (anhydrous) or THF. Samples were loaded into Vitracom capillary microscope slides. The cells were flame sealed using a propane torch and then dipped in wax to ensure a proper seal to prevent solvent and sample evaporation. The sealed cells were placed onto the microscope stage and secured with clay. At least three experiments were conducted at each of the three objectives (4, 7, and 10×) for reproducibility. A total of three ronchi ruling gratings were used (50, 100, and 150 lines/inch). A custom created software, FPRprogram, was used to control the instrument and acquire the experimental data. Another custom manufactured software, Anscan, is used for data analysis.

7.6.3 Gel Permeation Chromatography-Multi-angle Light Scattering

7.6.3.1 Background

Many different methods have been used to determine molecular weight such as intrinsic viscosity, light scattering, and osmometry.[234-235] A more recent and commonly used technique is gel permeation chromatography (GPC) also known as size exclusion chromatography (SEC). It is a commercially available technique that can be easily coupled with various other techniques in the form of detectors to provide characteristic information about polymers in solution such as absolute molecular weight and root-mean-square (RMS) radius of polymers in solution.

Initially the technique was used to characterize polymers but it evolved to handle larger macromolecules like proteins.[234] Chromatography is a two-phase separation technique having a fluid mobile phase that flows through a column packed with a solid immobile stationary phase. GPC relies on the permeation of polymers and macromolecules

through a packed column that contains different sizes of crosslinked particles with varying pore-sizes. Separation of the molecules occurs via the size exclusion principle.[235] Every molecule flowing through the instrument has a specific hydrodynamic volume, which allows it to interact in varying degrees with the pores in the crosslinked beads that make up the stationary phase of the column. Smaller molecules can diffuse in and out of the pores in the beads via Brownian motion due to their small hydrodynamic volume. This diffusion hinders the molecules progression through the column leading to a delay in the time it would take for the molecule to flow through the instrument. Larger molecules, due to their increased hydrodynamic volume, cannot penetrate the bead's pores so they instead pass by the beads and continue to flow with the mobile phase.[235] This phenomenon leads to the larger molecular weight molecules spending less time in the column compared to the smaller molecules. When looking at the retention time, the shorter the retention time the higher the molecular weight. A visual of this separation process is shown in Figure 80.

Various detectors can be attached to the GPC instrument and are separated into two main groups: concentration-sensitive detectors or molar mass sensitive detectors. The most common concentration-sensitive detector is the refractive index (RI) detector, which measures the change in refractive index as the concentration of the molecules in solution changes. A majority of the time there is pure solvent flowing through the RI detector so when the molecules arrive at the detector, the refractive index changes allowing the polymer concentration to be measured.

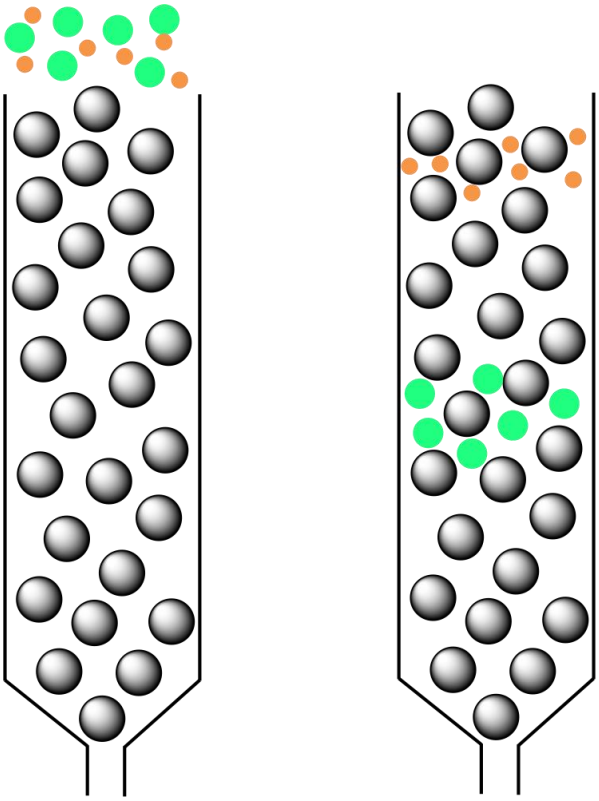

Figure 80. An illustration of the separation process for molecules in the GPC column. The molecules are separated based on size with the larger molecules eluding faster than the smaller molecules.

GPC tends to be a relative molecular weight method requiring calibration. Narrow molecular weight distribution (MWD) polymer standards, the most common being polystyrene, are used to create a calibration curve.[235] Molecular weights ranging between a few hundred g/mol up to 20,000,000 g/mol are commercially available. Calibration curves involve determining the elution volume or retention time for a series of polymer standards by determining its peak average. The method used most is a universal calibration that relies on the concept of polymer molecules hydrodynamic volume.[234] Einstein's viscosity law states that the product of the molar mass and intrinsic viscosity is directly proportional to the hydrodynamic volume. The relationship is shown in Equation 19. The GPC calibration curves for various different types of polymers can be merged into a single

plot if the data are plotted as log [η]M. The disadvantage of the universal calibration curve is that it is valid for a specific set of columns, solvent, and temperature and if any of those parameters are changed, a new calibration curve has to be performed.

$$[\eta] \propto \frac{V_h}{M} \tag{19}$$

Because the polymer chains are separated based on their size and not molecular weight, performing a calibration using polymers other than the one of interest has inherent error associated with it.[234-235] Another issue that needs to be accounted for is the conformation and shape of the polymer that is being used compared to the molecule of interest. A polymer standard that has a random coil conformation should not be used to create the calibration curve if the molecule of interest has a rigid rod conformation.

Due to the complexities that can arise from relying on a calibration curve, our GPC system is coupled to a multi-angle light scattering detector, which provide absolute molecular weights. Multi-angle light scattering detectors are capable of conducted static light scattering and dynamic light scattering measurements simultaneously.[234] The basic equation used in light scattering is known as the Rayleigh-Gans-Debye (RGD) approximation and is shown in Equation 20.

$$\frac{K * c}{R(\theta)} = \frac{1}{P(\theta)}\left(\frac{1}{M_w} + 2A_2c + 3A_3c^2 + \cdots\right) \tag{20}$$

In an experiment using GPC-MALS the scattered light is detected, at multiple angles (θ), for every fraction of polymer eluting from the instrument. A fundamental

parameter measured by light scattering for each fraction is M_w, which is an "absolute" measurement. Meaning that the M_w measurement is independent of experimental conditions such as solvent and temperature. One can see that $M_w \propto R(\theta)/c$, as shown in Equation 20. This means that each fraction of polymer eluted, the ratio of the signal from the SLS and concentration-sensitive detector (in this case an RI detector) is proportional to the weight-average molecular weight of the fraction, $M_{w,i}$. Because the fractions that elute from the column are narrow, they are assumed monodisperse. Combining a concentration-sensitive and SLS detector, the concentration and molecular weight of each elution fraction can be combined to give an overall MWD to produce an absolute molecular weight of the polymer independent of experimental conditions.

7.6.3.2 Sample Preparation and Analysis

Gel permeation chromatography with multi-angle light scattering, GPC-MALS, was used to measure the molecular weight of the synthesized PCBL. The instrument includes a Wyatt Dawn EOS multi-angle-light scattering detector connected to a Tosoh EcoSEC HLC-8320GPC. A TSK SuperH-H (4.6mm ID × 3.5 cm L) guard column was placed before two TSKgel SuperHM-H (mixed-bed) analytical columns (6.0 mm ID × 15 cm L) for the sample flow. A TSKgel SuperH-RC column (6.0 mm ID × 15 cm L) was used as the reference column for the dual flow type refractive index detector. The Tosoh EcoSEC HLC-8320GPC control module was used to operate the GPC, and data acquisition and analysis were controlled using the Wyatt Astra 5.0 software. The mobile phase was N,N-Dimethylformamide with 0.1M LiBr flowing at 0.35 mL/min, and the instrument temperature was set to 60 °C. Polymer samples of concentration 2–3 mg/mL were dissolved overnight (at least 12 h) prior to measurements to ensure homogeneity. Solutions

were then filtered through Whatman PTFE 0.45 μm syringe filters into Agilent 2 mL GPC vials. In order to obtain the absolute molecular weight of the polypeptide a dn/dc value of 0.123 mL/g was used for the data analysis. To establish reproducibility, multiple injections (20 μL) were performed for each sample measured by GPC/MALS.

7.6.4 Electron Microscopy

7.6.4.1 Scanning Electron Microscopy

Samples were deposited onto silicon wafers and dried in air. A Hitachi SU8230 SEM working at an accelerating voltage of 1.5 kV was used to image the non-magnetic polypeptide-coated silica particles using the lower secondary electron detector. The SEM working at an accelerating voltage of 5 kV was used to image the polypeptide-coated cobalt-silica particles using both the upper and lower secondary electron detectors. Energy Dispersive X-ray Spectroscopy (EDX) can be conducted on samples that are placed into the SEM. To do EDX, the SEM works at an accelerating voltage of 10 kV to map specific elements present in a sample.

7.6.4.2 Transmission Electron Microscopy

Samples were deposited onto carbon-coated copper specimen grids and dried in air. A Hitachi HD-2700 STEM working at an accelerating voltage of 200 kV was used to image the individual silica-coated cobalt particles. A JEOL 100 CX-II TEM working at an accelerating voltage of 100 kV was used to image other magnetic particles such as the larger grouping of silica-coated cobalt particles, the silica coated cobalt snakes, and the

silica-coated magnetite core particles. A Hitachi-HD 7700 TEM working at an accelerating voltage of 100 kV was used to image the non-magnetic silica particles.

7.6.5 Fourier-Transform Infrared Spectroscopy

Spectra of silica particles, polypeptides (monomers and product), and polypeptide composite particles were obtained with a Thermo Scientific Nicolet iS50 FT-IR Spectrometer equipped with a Smart-iTR (ATR) accessory. Thermo Scientific Omnic 9 software was used to control the instrument and for data acquisition and analysis. Each sample was dried in the oven overnight (at least 12h) prior to measurements. A total of 16 or 64 scans were taken for each sample with a resolution of one and a data spacing of 0.121 cm^{-1}. The final data format was transmittance and an ATR correction was applied to the data. To ensure reproducibility a background scan was collect before every sample consisting of 16 scans.

7.6.6 Thermogravimetric Analysis

TGA characterization of polypeptides and PCPs was conducted using two different TGA instruments. The two different instrument and methods used are detailed below. For each chapter the respective TGA analysis is outlined in the text.

TGA Analysis using Thermal Analysis (TA) Q600 TGA/DSC: TA Advantage v5.5.24 software was used to control the instrument and for data acquisition. TA Universal Analysis 2000 version 4.5A software was used for data analysis. A standard dual sample measurement in a nitrogen atmosphere was conducted for each of the tethered and untethered polypeptide samples. The program was set to stabilize the temperature at 50 °C

and hold for one min, then ramp the temperature from 50–600 °C at a rate of 10 °C/min, and finally return to room temperature at the end of the run. Approximately 2–3 mg of sample was added to a tared alumina sample pan purchased from TA instruments (Catalog # 960072.901 Alumina Sample Cups, 40 μL).

TGA Analysis using Mettler Toldeo TGA2 STAR System Thermogravimetric Analyzer: STARe Software version 16.00 was used to control the instrument and for data acquisition. The same software was used for data analysis via the evaluation window. A measurement in a nitrogen atmosphere was conducted for each of the silica cores, PCPs, and untethered polypeptide samples. The program was set to stabilize the temperature at 50 °C and hold for one min, then ramp the temperature from 50–600 °C at a rate of 10 °C/min, and finally return to room temperature at the end of the run. Approximately 0.5–3 mg of sample was added to a tared sample pan provided by Mettler Toledo.

7.6.7 Nuclear Magnetic Resonance

Proton NMR experiments and data analysis were conducted with a Bruker DRX 500 MHz instrument and the Bruker TopSpin 3.2 NMR program. ^{1}H NMR data collected were obtained with 500 MHz field strength, probe temperate of 297 K and with a residual internal standard TMS (δ 0.00). The solvent used for the measurements was deuterated THF (d_8-THF). Data analysis was performed using Mnova Lite CDE.

Examples of the monomer and polypeptide NMR spectra are shown below.

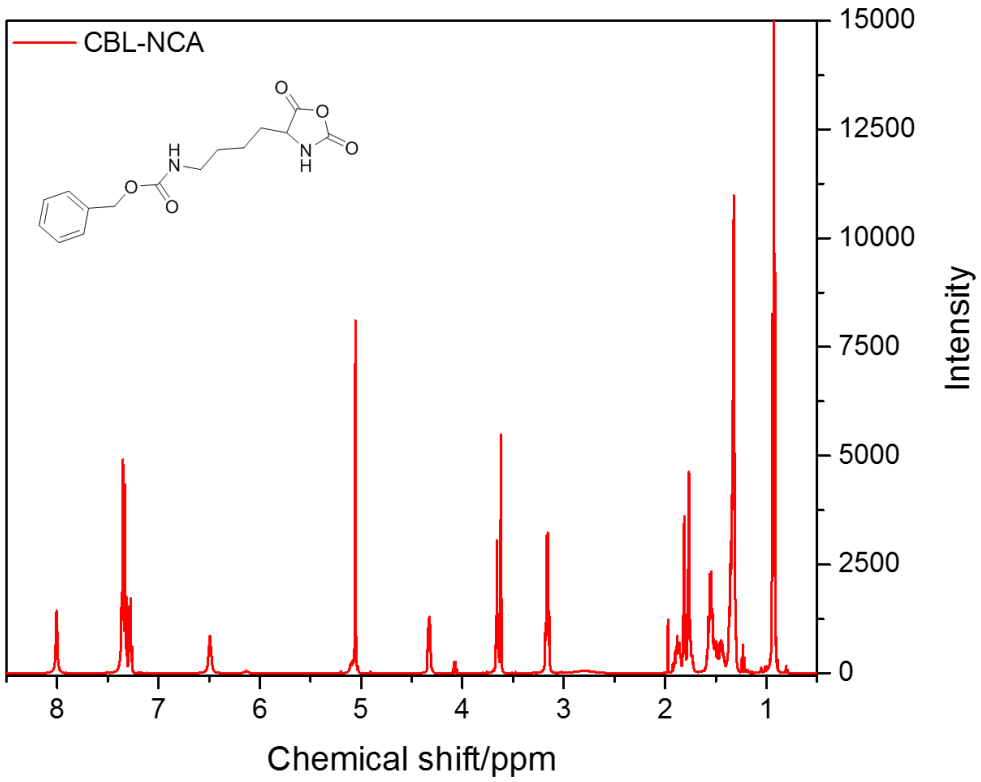

Figure 81. NMR spectrum for the polypeptide monomer CBL-NCA. The structure of the compound is shown in the upper right corner of the spectrum.

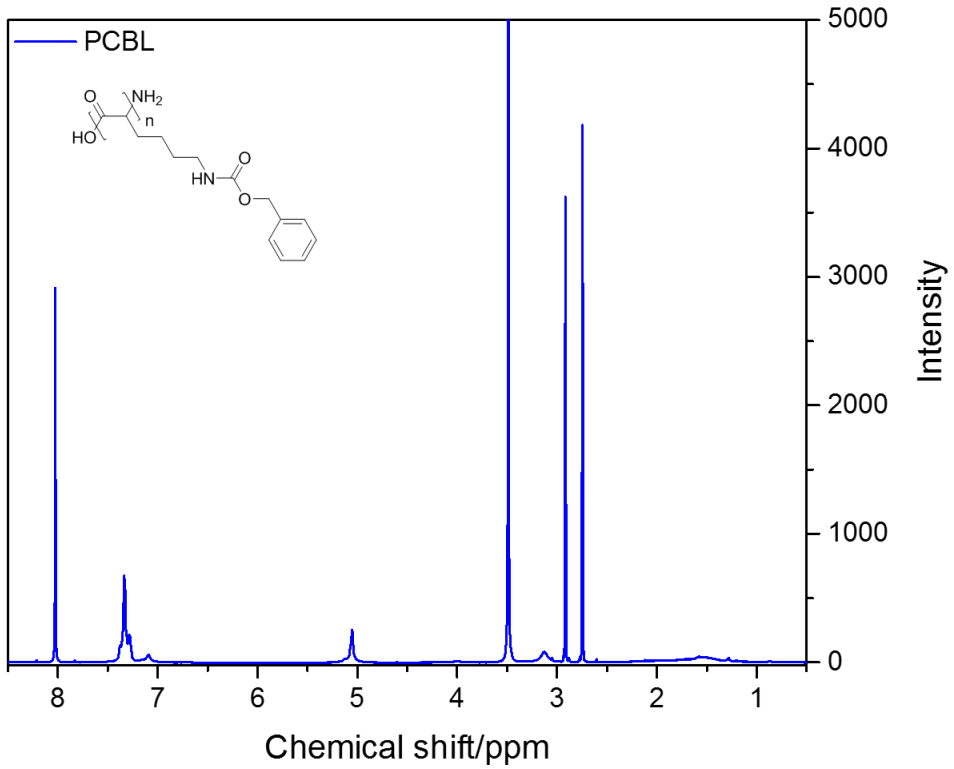

Figure 82. NMR spectrum for the polypeptide, PCBL. The structure of the compound is shown in the upper right corner of the spectrum

REFERENCES

1. Brinker, C. J.; Scherer, G. W., CHAPTER 3 - Hydrolysis and Condensation II: Silicates. In *Sol-Gel Science*, Brinker, C. J.; Scherer, G. W., Eds. Academic Press: San Diego, 1990; pp 96-233.

2. Iler, R. K., *The colloid chemistry of silica and silicates*. Cornell University Press: 1955.

3. Brinker, C. J.; Scherer, G. W., CHAPTER 1 - Introduction. In *Sol-Gel Science*, Brinker, C. J.; Scherer, G. W., Eds. Academic Press: San Diego, 1990; pp xvi-18.

4. *Colloidal silica : fundamentals and applications*. Boca Raton, FL: CRC Taylor & Francis, 2006.

5. Thanh, N. T. K.; Green, L. A. W., Functionalisation of nanoparticles for biomedical applications. *Nano Today* **2010,** *5* (3), 213-230.

6. Liberman, A.; Mendez, N.; Trogler, W. C.; Kummel, A. C., Synthesis and surface functionalization of silica nanoparticles for nanomedicine. *Surface Science Reports* **2014,** *69* (2), 132-158.

7. Hyde, E. D. E. R.; Seyfaee, A.; Neville, F.; Moreno-Atanasio, R., Colloidal Silica Particle Synthesis and Future Industrial Manufacturing Pathways: A Review. *Industrial & Engineering Chemistry Research* **2016,** *55* (33), 8891-8913.

8. Stöber, W.; Fink, A.; Bohn, E., Controlled growth of monodisperse silica spheres in the micron size range. *J Colloid Interf Sci* **1968,** *26* (1), 62-69.

9. Rosu, C.; Selcuk, S.; Soto-Cantu, E.; Russo, P. S., Progress in silica polypeptide composite colloidal hybrids: from silica cores to fuzzy shells. *Colloid Polym Sci* **2014,** *292* (5), 1009-1040.

10. Wang, L. L.; Asher, S. A., Fabrication of Silica Shell Photonic Crystals through Flexible Core Templates. *Chem Mater* **2009,** *21* (19), 4608-4613.

11. Bogush, G. H.; Tracy, M. A.; Zukoski, C. F., Preparation of Monodisperse Silica Particles - Control of Size and Mass Fraction. *J Non-Cryst Solids* **1988,** *104* (1), 95-106.

12. Zhang, J. H.; Zhan, P.; Wang, Z. L.; Zhang, W. Y.; Ming, N. B., Preparation of monodisperse silica particles with controllable size and shape. *Journal of Materials Research* **2011,** *18* (3), 649-653.

13. Osseo-Asare, K.; Arriagada, F. J., Preparation of SiO2 nanoparticles in a non-ionic reverse micellar system. *Colloids and Surfaces* **1990,** *50*, 321-339.

14. Zhao, L.; Zhao, Y.; Han, Y., Pore Fabrication in Various Silica-Based Nanoparticles by Controlled Etching. *Langmuir* **2010,** *26* (14), 11784-11789.

15. Giri, S.; Trewyn, B. G.; Stellmaker, M. P.; Lin, V. S.-Y., Stimuli-Responsive Controlled-Release Delivery System Based on Mesoporous Silica Nanorods Capped with Magnetic Nanoparticles. *Angewandte Chemie International Edition* **2005,** *44* (32), 5038-5044.

16. Mugica, L. C.; Rodríguez-Molina, B.; Ramos, S.; Kozina, A., Surface functionalization of silica particles for their efficient fluorescence and stereo selective modification. *Colloids and Surfaces A: Physicochemical and Engineering Aspects* **2016,** *500*, 79-87.

17. Liu, J.; Levine, A. L.; Mattoon, J. S.; Yamaguchi, M.; Lee, R. J.; Pan, X.; Rosol, T. J., Nanoparticles as image enhancing agents for ultrasonography. *Physics in Medicine and Biology* **2006,** *51* (9), 2179-2189.

18. Dirè, S.; Tagliazucca, V.; Callone, E.; Quaranta, A., Effect of functional groups on condensation and properties of sol–gel silica nanoparticles prepared by direct synthesis from organoalkoxysilanes. *Materials Chemistry and Physics* **2011,** *126* (3), 909-917.

19. Soto-Cantu, E.; Turksen-Selcuk, S.; Qiu, J. H.; Zhou, Z.; Russo, P. S.; Henk, M. C., Silica-Polypeptide Composite Particles: Controlling Shell Growth. *Langmuir* **2010,** *26* (19), 15604-15613.

20. Soto-Cantu, E.; Cueto, R.; Koch, J.; Russo, P. S., Synthesis and Rapid Characterization of Amine-Functionalized Silica. *Langmuir* **2012,** *28* (13), 5562-5569.

21. Santra, S., Fluorescent Silica Nanoparticles for Cancer Imaging. In *Cancer Nanotechnology: Methods and Protocols*, Grobmyer, S. R.; Moudgil, B. M., Eds. Humana Press: Totowa, NJ, 2010; pp 151-162.

22. Burns, A. A.; Vider, J.; Ow, H.; Herz, E.; Penate-Medina, O.; Baumgart, M.; Larson, S. M.; Wiesner, U.; Bradbury, M., Fluorescent Silica Nanoparticles with Efficient Urinary Excretion for Nanomedicine. *Nano Letters* **2009,** *9* (1), 442-448.

23. Bagwe, R. P.; Yang, C.; Hilliard, L. R.; Tan, W., Optimization of Dye-Doped Silica Nanoparticles Prepared Using a Reverse Microemulsion Method. *Langmuir* **2004,** *20* (19), 8336-8342.

24. Fuller, J. E.; Zugates, G. T.; Ferreira, L. S.; Ow, H. S.; Nguyen, N. N.; Wiesner, U. B.; Langer, R. S., Intracellular delivery of core–shell fluorescent silica nanoparticles. *Biomaterials* **2008,** *29* (10), 1526-1532.

25. Yu, A.; Gentle, I. R.; Lu, G. Q., Biocompatible polypeptide microcapsules via templating mesoporous silica spheres. *J Colloid Interf Sci* **2009,** *333* (1), 341-345.

26. Kar, M.; Tiwari, N.; Tiwari, M.; Lahiri, M.; Gupta, S. S., Poly-L-Arginine Grafted Silica Mesoporous Nanoparticles for Enhanced Cellular Uptake and their Application in DNA Delivery and Controlled Drug Release. *Particle & Particle Systems Characterization* **2013,** *30* (2), 166-179.

27. Thornton, P. D.; Heise, A., Highly Specific Dual Enzyme-Mediated Payload Release from Peptide-Coated Silica Particles. *J Am Chem Soc* **2010,** *132* (6), 2024-2028.

28. Chen, K.-J.; Chen, H.-L.; Tang, C.-C.; Wu, H.-H.; Jan, J.-S., Synthesis of silica/polypeptide hybrid nanomaterials and mesoporous silica by molecular replication of sheet-like polypeptide complexes through biomimetic mineralization. *Journal of Colloid and Interface Science* **2019,** *542*, 243-252.

29. Kuijk, A.; van Blaaderen, A.; Imhof, A., Synthesis of Monodisperse, Rodlike Silica Colloids with Tunable Aspect Ratio. *J Am Chem Soc* **2011,** *133* (8), 2346-2349.

30. Asher, S. A.; Holtz, J.; Weissman, J.; Pan, G. S., Mesoscopically periodic photonic-crystal materials for linear and nonlinear optics and chemical sensing. *Mrs Bull* **1998,** *23* (10), 44-50.

31. Datskos, P.; Sharma, J., Synthesis of Segmented Silica Rods by Regulation of the Growth Temperature. *Angew Chem Int Edit* **2014,** *53* (2), 451-454.

32. Yang, Y.; Chen, G. D.; Martinez-Miranda, L. J.; Yu, H.; Liu, K.; Nie, Z. H., Synthesis and Liquid-Crystal Behavior of Bent Colloidal Silica Rods. *J Am Chem Soc* **2016,** *138* (1), 68-71.

33. Hu, J.; Zhou, S. X.; Sun, Y. Y.; Fang, X. S.; Wu, L. M., Fabrication, properties and applications of Janus particles. *Chem Soc Rev* **2012,** *41* (11), 4356-4378.

34. Poggi, E.; Gohy, J.-F., Janus particles: from synthesis to application. *Colloid Polym Sci* **2017,** *295* (11), 2083-2108.

35. Zhang, J.; Grzybowski, B. A.; Granick, S., Janus Particle Synthesis, Assembly, and Application. *Langmuir* **2017,** *33* (28), 6964-6977.

36. Percebom, A. M.; Giner-Casares, J. J.; Claes, N.; Bals, S.; Loh, W.; Liz-Marzán, L. M., Janus gold nanoparticles obtained via spontaneous binary polymer shell segregation. *Chemical Communications* **2016,** *52* (23), 4278-4281.

37. Jurado-Sánchez, B.; Pacheco, M.; Maria-Hormigos, R.; Escarpa, A., Perspectives on Janus micromotors: Materials and applications. *Applied Materials Today* **2017,** *9*, 407-418.

38. Reguera, J.; Jiménez de Aberasturi, D.; Winckelmans, N.; Langer, J.; Bals, S.; Liz-Marzán, L. M., Synthesis of Janus plasmonic–magnetic, star–sphere nanoparticles, and their application in SERS detection. *Faraday Discussions* **2016,** *191* (0), 47-59.

39. Sun, C.; Lee, J. S. H.; Zhang, M., Magnetic nanoparticles in MR imaging and drug delivery. *Advanced Drug Delivery Reviews* **2008,** *60* (11), 1252-1265.

40. Tai, Y.; Wang, L.; Fan, G.; Gao, J. M.; Yu, H.; Zhang, L., Recent research progress on the preparation and application of magnetic nanospheres. *Polym. Int.* **2011,** *60*, 976.

41. Zhang, Y.; Kohler, N.; Zhang, M., Surface modification of superparamagnetic magnetite nanoparticles and their intracellular uptake. *Biomaterials* **2002,** *23* (7), 1553-1561.

42. Kobayashi, Y.; Horie, M.; Konno, M.; Rodriguez-Gonzalez, B.; Liz-Marzan, L. M., Preparation and properties of silica-coated cobalt nanoparticles. *J. Phys. Chem. B* **2003,** *107*, 7420.

43. Cao, Q. L.; Han, X. T.; Li, L., Two-Dimensional Manipulation of Magnetic Nanoparticles in Microfluidic Systems. *Appl Phys Express* **2013,** *6* (2).

44. Liu, D.; Li, Y.; Deng, J.; Yang, W., Synthesis and characterization of magnetic Fe3O4-silica-poly(γ-benzyl-l-glutamate) composite microspheres. *Reactive and Functional Polymers* **2011,** *71* (10), 1040-1044.

45. Odian, G., *Principles of Polymerization*. John Wiley & Sons Inc.: 2004.

46. Voet, D., *Fundamentals of biochemistry : life at the molecular level*. 4th ed. ed.; Hoboken, NJ: Wiley, 2013.

47. Cheng, J.; Deming, T. J., Synthesis of Polypeptides by Ring-Opening Polymerization of α-Amino Acid N-Carboxyanhydrides. In *Peptide-Based Materials*, Deming, T., Ed. Springer Berlin Heidelberg: Berlin, Heidelberg, 2012; pp 1-26.

48. Berg, J. M.; Tymoczko, J. L.; Stryer, L., *Biochemistry, Fifth Edition*. W.H. Freeman: 2002.

49. Block, H., *Poly([gamma]-benzyl-L-glutamate) and other glutamic acid containing polymers*. New York: Gordon and Breach Science Pub., 1983.

50. Fasman, G. D.; Idelson, M.; Blout, E. R., Synthesis and Conformation of High Molecular Weight Poly-Epsilon-Carbobenzyloxy-L-Lysine and Poly-L-Lysine.Hcl. *J Am Chem Soc* **1961,** *83* (3), 709-&.

51. Karasz, F. E.; O'Reilly, J. M.; Bair, H. E., Helix–coil transition in poly-ε-carbobenzoxy-L-lysine. *Biopolymers* **1965,** *3* (3), 241-247.

52. Karasz, F. E.; Oreilly, J. M., Deuteration and Solvent Composition Effects in Helix-Coil Transition of Poly-Gamma-Benzyl-L-Glutamate. *Biopolymers* **1966,** *4* (9), 1015-&.

53. Matsuoka, M.; Norisuye, T.; Teramoto, A.; Fujita, H., Solution properties of synthetic polypeptides. XV. Helix-coil transition in poly(epsilon-carbobenzyloxy L-lysine). *Biopolymers* **1973,** *12* (7), 1515-32.

54. Applequist, J., On Helix-Coil Equilibrium in Polypeptides. *J Chem Phys* **1963,** *38* (4), 934-&.

55. Blout, E. R.; Karlson, R. H., Polypeptides .3. The Synthesis of High Molecular Weight Poly-Gamma-Benzyl-L-Glutamates. *J Am Chem Soc* **1956,** *78* (5), 941-946.

56. Blout, E. R.; Karlson, R. H.; Doty, P.; Hargitay, B., Polypeptides .1. The Synthesis and the Molecular Weight of High Molecular Weight Polyglutamic Acids and Esters. *J Am Chem Soc* **1954,** *76* (17), 4492-4493.

57. Nakamoto, K.; Suga, H.; Seki, S.; Teramoto, A.; Norisuye, T.; Fujita, H., Solution Properties of Synthetic Polypeptides .19. Heat-Capacity Measurements on System of Poly(Epsilon-Carbobenzyloxy-L-Lysine) and Meta-Cresol in Helix-Coil Transition Region. *Macromolecules* **1974,** *7* (6), 784-789.

58. Nishioka, N.; Maekawa, A.; Teramoto, A., Solution Properties of Synthetic Polypeptides .21. Solvent Effect on Helix-Coil Transition of Poly(Epsilon-Carbobenzoxy L-Lysine). *Biopolymers* **1978,** *17* (3), 665-675.

59. Leuchs, H., Ueber die Glycin-carbonsäure. *Ber Dtsch Chem Ges* **1906,** *39* (1), 857-861.

60. Fuchs, F., On N-carbonic acid-anhydride. *Ber Dtsch Chem Ges* **1922,** *55*, 2943-2943.

61. Daly, W. H.; Poché, D., The preparation of N-carboxyanhydrides of α-amino acids using bis(trichloromethyl)carbonate. *Tetrahedron Lett* **1988,** *29* (46), 5859-5862.

62. Poche, D. S.; Moore, M. J.; Bowles, J. L., An unconventional method for purifying the N-carboxyanhydride derivatives of gamma-alkyl-L-glutamates. *Synthetic Commun* **1999,** *29* (5), 843-854.

63. Song, Z.; Han, Z.; Lv, S.; Chen, C.; Chen, L.; Yin, L.; Cheng, J., Synthetic polypeptides: from polymer design to supramolecular assembly and biomedical application. *Chem Soc Rev* **2017,** *46* (21), 6570-6599.

64. Idelson, M.; Blout, E. R., Polypeptides. XVIII.1 A Kinetic Study of the Polymerization of Amino Acid N-Carboxyanhydrides Initiated by Strong Bases. *J Am Chem Soc* **1958,** *80* (10), 2387-2393.

65. International Symposium on Poly--Amino, A., *Polyamino acids, polypeptides, and proteins*

proceedings of an international symposium held at the University of Wisconsin, 1961. Madison, University of Wisconsin Press: Madison, 1962.

66. Fasman, G. D., Poly---amino acids; protein models for conformational studies. **1967**.

67. Deming, T. J., Synthetic polypeptides for biomedical applications. *Prog Polym Sci* **2007,** *32* (8), 858-875.

68. Huang, J.; Heise, A., Stimuli responsive synthetic polypeptides derived from N-carboxyanhydride (NCA) polymerisation. *Chem Soc Rev* **2013,** *42* (17), 7373-7390.

69. Sela, M.; Katchalski, E., Biological Properties of Poly-α- Amino Acids. In *Adv Protein Chem*, Anfinsen, C. B.; Anson, M. L.; Bailey, K.; Edsall, J. T., Eds. Academic Press: 1959; Vol. 14, pp 391-478.

70. Pauling, L.; Corey, R. B., The Structure of Hair, Muscle, and Related Proteins. *Proc. Natl. Acad. Sci. U.S.A.* **1951,** *37*, 261.

71. Rodríguez-Hernández, J.; Lecommandoux, S., Reversible Inside−Out Micellization of pH-responsive and Water-Soluble Vesicles Based on Polypeptide Diblock Copolymers. *J Am Chem Soc* **2005,** *127* (7), 2026-2027.

72. Lu, H.; Wang, J.; Song, Z.; Yin, L.; Zhang, Y.; Tang, H.; Tu, C.; Lin, Y.; Cheng, J., Recent advances in amino acid N-carboxyanhydrides and synthetic polypeptides: chemistry, self-assembly and biological applications. *Chemical Communications* **2014,** *50* (2), 139-155.

73. Wang, Y. L.; Chang, Y. C., Synthesis and conformational transition of surface-tethered polypeptide: Poly(L-lysine). *Macromolecules* **2003,** *36*, 6511.

74. Wang, Y. L.; Chang, Y. C., Synthesis and conformational transition of surface-tethered polypeptide: Poly(L-glutamic acid). *Macromolecules* **2003,** *36* (17), 6503-6510.

75. Yan, S.; Sun, Y.; Chen, A.; Liu, L.; Zhang, K.; Li, G.; Duan, Y.; Yin, J., Templated fabrication of pH-responsive poly(l-glutamic acid) based nanogels via surface-grafting and macromolecular crosslinking. *RSC Adv.* **2017,** *7* (24), 14888-14901.

76. Worley, C. G.; Linton, R. W.; Samulski, E. T., Electric-Field-Enhanced Self-Assembly of .alpha.-helical polypeptides. *Langmuir* **1995,** *11* (10), 3805-3810.

77. Ramli, R. A.; Laftah, W. A.; Hashim, S., Core–shell polymers: a review. *RSC Adv.* **2013,** *3* (36), 15543-15565.

78. Hughes, L. J.; Brown, G. L., Heterogeneous polymer systems. I. Torsional modulus studies. *Journal of Applied Polymer Science* **1961,** *5* (17), 580-588.

79. Vlassopoulos, D.; Fytas, G., From Polymers to Colloids: Engineering the Dynamic Properties of Hairy Particles. In *High Solid Dispersions*, Cloitre, M., Ed. Springer Berlin Heidelberg: Berlin, Heidelberg, 2010; pp 1-54.

80. Wan, J.; Lv, D.; Cui, S.; Liang, F.; Yang, Z., Synthesis of hairy composite particles. *Polymer* **2019,** *172*, 247-252.

81. Kango, S.; Kalia, S.; Celli, A.; Njuguna, J.; Habibi, Y.; Kumar, R., Surface modification of inorganic nanoparticles for development of organic–inorganic nanocomposites—A review. *Prog Polym Sci* **2013,** *38* (8), 1232-1261.

82. Lv, D.; Sheng, L.; Wan, J.; Dong, J.; Ouyang, H.; Jiao, H.; Liu, J., Bioinspired hierarchically hairy particles for robust superhydrophobic coatings via a droplet dynamic template method. *Polym Chem-Uk* **2019,** *10* (3), 331-335.

83. Conde, J.; Doria, G.; Baptista, P., Noble metal nanoparticles applications in cancer. *J Drug Deliv* **2012,** *2012*, 751075-751075.

84. Balamurugan, S. S.; Soto-Cantu, E.; Cueto, R.; Russo, P. S., Preparation of Organosoluble Silica-Polypeptide Particles by "Click" Chemistry. *Macromolecules* **2010,** *43* (1), 62-70.

85. Fong, B.; Russo, P. S., Organophilic colloidal particles with a synthetic polypeptide coating. *Langmuir* **1999,** *15* (13), 4421-4426.

86. Kar, M.; Vijayakumar, P. S.; Prasad, B. L. V.; Gupta, S. S., Synthesis and Characterization of Poly-l-lysine-Grafted Silica Nanoparticles Synthesized via NCA Polymerization and Click Chemistry. *Langmuir* **2010,** *26* (8), 5772-5781.

87. Rosu, C. Silica Polypeptide-Based Colloids: Physical Properties and Novel Materials. Dissertation, Lousiana State Univerisity, Louisiana State University and Agricultural and Mechanical College, 2013.

88. Balamurugan, S.; Rosu, C.; Cueto, R.; Roy, A.; Rinaldi, C.; Russo, P., Synthesis, characterization and application of a fluorescent silica-polypeptide-composite particle. Lousiana State University, Georgia Institute of Technology, and University of Florida: 2015; pp 1-33.

89. Turksen-Selcuk, S.; Rosu, C.; Blake, A.; Soto-Cantu, E.; Qiu, J.; Wu, Y.; DiTusa, J. F.; Steffens, A.; Russo, P. S., Organophilic, Superparamagnetic, and Reversibly Thermoresponsive Silica-Polypeptide Core–Shell Particles. *Langmuir* **2019,** *35* (44), 14248-14257.

90. Liu, D.; Li, Y.; Deng, J. P.; Yang, W. T., Synthesis and characterization of magnetic Fe3O4-silica-poly(gamma-benzyl-L-glutamate) composite microspheres. *Reactive & Functional Polymers* **2011,** *71* (10), 1040-1044.

91. Siemens, A. O. N.; van Hecke, M., Jamming: A simple introduction. *Physica a-Statistical Mechanics and Its Applications* **2010,** *389* (20), 4255-4264.

92. Kar, M.; Pauline, M.; Sharma, K.; Kumaraswamy, G.; Sen Gupta, S., Synthesis of Poly-l-glutamic Acid Grafted Silica Nanoparticles and Their Assembly into Macroporous Structures. *Langmuir* **2011,** *27* (19), 12124-12133.

93. Borase, T.; Iacono, M.; Ali, S. I.; Thornton, P. D.; Heise, A., Polypeptide core–shell silica nanoparticles with high grafting density by N-carboxyanhydride (NCA) ring opening polymerization as responsive materials and for bioconjugation. *Polym Chem-Uk* **2012,** *3* (5), 1267-1275.

94. Fong, B.; Turksen, S.; Russo, P. S.; Stryjewski, W., Colloidal Crystals of Silica-Homopolypeptide Composite Particles. *Langmuir* **2004,** *20* (1), 266-269.

95. Soto-Cantu, E.; Russo, P. S., Silica-poly(benzyl-L-glutamate) core-shell particles of controlled shell content. *Abstr Pap Am Chem S* **2009,** *237*.

96. Ostlund, S. G.; Striegel, A. M., Ultrasonic degradation of poly(γ-benzyl-l-glutamate), an archetypal highly extended polymer. *Polymer Degradation and Stability* **2008,** *93* (8), 1510-1514.

97. Mohod, A. V.; Gogate, P. R., Ultrasonic degradation of polymers: Effect of operating parameters and intensification using additives for carboxymethyl cellulose (CMC) and polyvinyl alcohol (PVA). *Ultrasonics Sonochemistry* **2011,** *18* (3), 727-734.

98. Morris, M. J.; Striegel, A. M., The effect of styrene-methyl methacrylate monomeric arrangement on the ultrasonic degradation of copolymers. *Polymer Degradation and Stability* **2012,** *97* (11), 2185-2194.

99. Price, G. J.; Smith, P. F., Ultrasonic degradation of polymer solutions: 2. The effect of temperature, ultrasound intensity and dissolved gases on polystyrene in toluene. *Polymer* **1993,** *34* (19), 4111-4117.

100. Striegel, A. M., Influence of chain architecture on the mechanochemical degradation of macromolecules. *Journal of Biochemical and Biophysical Methods* **2003,** *56* (1), 117-139.

101. Basedow, A. M.; Ebert, K. H. In *Ultrasonic degradation of polymers in solution*, Berlin, Heidelberg, Springer Berlin Heidelberg: Berlin, Heidelberg, 1977; pp 83-148.

102. Bhuvaneswari. G, H., 3 - Degradability of Polymers. In *Recycling of Polyurethane Foams*, Thomas, S.; Rane, A. V.; Kanny, K.; V.K, A.; Thomas, M. G., Eds. William Andrew Publishing: 2018; pp 29-44.

103. Junior, J. A. J. ULTRASONIC DECROSSLINKING OF CROSSLINKED POLY (ETHYLENE). The University of Akron, 2007.

104. Grönroos, A.; Pirkonen, P.; Heikkinen, J.; Ihalainen, J.; Mursunen, H.; Sekki, H., Ultrasonic depolymerization of aqueous polyvinyl alcohol. *Ultrasonics Sonochemistry* **2001,** *8* (3), 259-264.

105. Grigore, M. E., Methods of Recycling, Properties and Applications of Recycled Thermoplastic Polymers. *Recycling* **2017,** *2* (4), 24.

106. Aldaye, F. A.; Palmer, A. L.; Sleiman, H. F., Assembling Materials with DNA as the Guide. *Science* **2008,** *321* (5897), 1795-1799.

107. Aldaye, F. A.; Sleiman, H. F., Sequential Self-Assembly of a DNA Hexagon as a Template for the Organization of Gold Nanoparticles. *Angewandte Chemie International Edition* **2006,** *45* (14), 2204-2209.

108. Bujold, K. E.; Lacroix, A.; Sleiman, H. F., DNA Nanostructures at the Interface with Biology. *Chem* **2018,** *4* (3), 495-521.

109. Conway, J. W.; McLaughlin, C. K.; Castor, K. J.; Sleiman, H., DNA nanostructure serum stability: greater than the sum of its parts. *Chemical Communications* **2013,** *49* (12), 1172-1174.

110. Ultrasonic Degradation of DNA. *DNA* **1989,** *8* (10), 697-701.

111. Sarker, S. R.; Ball, A. S.; Bhargava, S. K.; Soni, S. K., Evaluation of plasmid DNA stability against ultrasonic shear stress and its in vitro delivery efficiency using ionic liquid [Bmim][PF6]. *RSC Adv.* **2019,** *9* (50), 29225-29231.

112. Xu, Z. G.; Feng, Y. Y.; Liu, X. Y.; Guan, M.; Zhao, C. D.; Zhang, H. X., Synthesis and characterization of Fe3O4@SiO2@poly-L-alanine, peptide brush-magnetic microspheres through NCA chemistry for drug delivery and enrichment of BSA. *Colloid Surf. B-Biointerfaces* **2010,** *81* (2), 503-507.

113. Blout, E. R.; Idelson, M., Polypeptides .6. Poly-Alpha-L-Glutamic Acid - Preparation and Helix-Coil Conversions. *J Am Chem Soc* **1956,** *78* (2), 497-498.

114. Doty, P.; Holtzer, A. M.; Bradbury, J. H.; Blout, E. R., POLYPEPTIDES .2. THE CONFIGURATION OF POLYMERS OF GAMMA-BENZYL-L-GLUTAMATE IN SOLUTION. *J Am Chem Soc* **1954,** *76* (17), 4493-4494.

115. Blout, E. R.; Doty, P.; Yang, J. T., Polypeptides .12. The Optical Rotation and Configurational Stability of Alpha-Helices. *J Am Chem Soc* **1957,** *79* (3), 749-750.

116. Doty, P.; Lundberg, R. D., The Contribution of the Alpha-Helical Configuration to the Optical Rotation of Polypeptides and Proteins. *Proc. Natl. Acad. Sci. U. S. A.* **1957,** *43* (2), 213-222.

117. Urnes, P.; Doty, P., Optical Rotation and the Conformation of Polypeptides and Proteins. *Adv Protein Chem* **1961,** *16*, 401-544.

118. Semenyshyn, R.; Hentschel, M.; Stanglmair, C.; Teutsch, T.; Tarin, C.; Pacholski, C.; Giessen, H.; Neubrech, F., In Vitro Monitoring Conformational Changes of Polypeptide Monolayers Using Infrared Plasmonic Nanoantennas. *Nano Letters* **2019,** *19* (1), 1-7.

119. Lu, L.; Lahasky, S. H.; Zhang, D.; Garno, J. C., Directed Growth of Polymer Nanorods Using Surface-Initiated Ring-Opening Polymerization of N-Allyl N-Carboxyanhydride. *ACS Appl. Mater. Interfaces* **2016,** *8* (6), 4014-4022.

120. Lunn, J. D.; Shantz, D. F., Peptide Brush-Ordered Mesoporous Silica Nanocomposite Materials. *Chem Mater* **2009,** *21* (15), 3638-3648.

121. Yang, C.-T.; Wang, Y.; Chang, Y.-C., Effect of Solvents and Temperature on the Conformation of Poly(β-benzyl-l-aspartate) Brushes. *Biomacromolecules* **2010,** *11* (5), 1308-1313.

122. Barth, A., Infrared spectroscopy of proteins. *Biochimica et Biophysica Acta (BBA) - Bioenergetics* **2007,** *1767* (9), 1073-1101.

123. Bulheller, B. M.; Rodger, A.; Hirst, J. D., Circular and linear dichroism of proteins. *Phys. Chem. Chem. Phys.* **2007,** *9* (17), 2020-2035.

124. Chen, Y.-H.; Yang, J. T.; Martinez, H. M., Determination of the secondary structures of proteins by circular dichroism and optical rotatory dispersion. *Biochemistry-Us* **1972,** *11* (22), 4120-4131.

125. Amenabar, I.; Poly, S.; Nuansing, W.; Hubrich, E. H.; Govyadinov, A. A.; Huth, F.; Krutokhvostov, R.; Zhang, L.; Knez, M.; Heberle, J.; Bittner, A. M.; Hillenbrand, R., Structural analysis and mapping of individual protein complexes by infrared nanospectroscopy. *Nature Communications* **2013,** *4* (1), 2890.

126. Anand, N.; Murthy, N. S. R. K.; Naider, F.; Goodman, M., Conformational Aspects of Polypeptide Structure. XXXIV. Amino Acid Substituted Poly-L-Lysines. *Macromolecules* **1971,** *4* (5), 564-569.

127. Wüthrich, K., Protein structure determination in solution by NMR spectroscopy. *J Biol Chem* **1990,** *265* (36), 22059-62.

128. Bonduelle, C., Secondary structures of synthetic polypeptide polymers. *Polym Chem-Uk* **2018,** *9* (13), 1517-1529.

129. Samulski, E. T.; Chien, M.; Wade, C. G., Polypeptide sidechain secondary structure and the helix-coil transition: A NMR relaxation study. *Journal of Polymer Science: Polymer Symposia* **1974,** *46* (1), 335-340.

130. Turksen-Selcuk, S.; Rosu, C.; Blake, A.; Soto-Cantu, E.; Qiu, J.; Wu, Y.; DiTusa, J. F.; Steffens, A.; Russo, P. S., Organophilic, Superparamagnetic, and Reversibly Thermoresponsive Silica-Polypeptide Core–Shell Particles. *Langmuir* **2019**.

131. Noguchi, H.; Yang, J. T., Volume and sound velocity changes accompanying the α-helix to β-form and coil to α-helix transitions in aqueous solution. *Biopolymers* **1971,** *10* (12), 2569-2579.

132. Taulier, N.; Chalikian, T. V., Volumetric effects of ionization of amino and carboxyl termini of α,ω-aminocarboxylic acids. *Biophysical Chemistry* **2003,** *104* (1), 21-36.

133. Makino, S.; Noguchi, H., Volume and sound velocity changes associated with coil-β transition of poly (S-carboxymethyl L-cysteine) in aqueous solution. *Biopolymers* **1971,** *10* (7), 1253-1260.

134. Resa, P.; Elvira, L.; Montero de Espinosa, F., Concentration control in alcoholic fermentation processes from ultrasonic velocity measurements. *Food Research International* **2004,** *37* (6), 587-594.

135. Abdulagatov, I. M.; Akhmedova-Azizova, L. A.; Aliev, R. M.; Badavov, G. B., Measurements of the Density, Speed of Sound, Viscosity, and Derived Thermodynamic Properties of Geothermal Fluids. *Journal of Chemical & Engineering Data* **2016,** *61* (1), 234-246.

136. Hoche, S.; Hussein, M. A.; Becker, T., Critical process parameter of alcoholic yeast fermentation: speed of sound and density in the temperature range 5–30 °C. *International Journal of Food Science & Technology* **2014,** *49* (11), 2441-2448.

137. Outcalt, S.; Laesecke, A.; Freund, M. B., Density and Speed of Sound Measurements of Jet A and S-8 Aviation Turbine Fuels. *Energy & Fuels* **2009,** *23* (3), 1626-1633.

138. Rahiman, M. K.; Santhoshkumar, S., Comparative studies of oxygenated fuel synthesis with diesel from the measurements of density, speed of sound and refractive index. *J. Therm. Anal. Calorim.* **2019,** *136* (1), 295-304.

139. Tat, M. E.; Van Gerpen, J. H.; Soylu, S.; Canakci, M.; Monyem, A.; Wormley, S., The speed of sound and isentropic bulk modulus of biodiesel at 21°C from atmospheric pressure to 35 MPa. *Journal of the American Oil Chemists' Society* **2000,** *77* (3), 285-289.

140. Zhang, Y.; Chen, Y.; Zheng, Y.; He, X.; He, M., Measurements of the Speed of Sound in Liquid and Supercritical n-Octane and Isooctane. *Journal of Chemical & Engineering Data* **2018,** *63* (1), 102-112.

141. Zimm, B. H.; Bragg, J. K., Theory of the Phase Transition between Helix and Random Coil in Polypeptide Chains. *The Journal of Chemical Physics* **1959,** *31* (2), 526-535.

142. Doi, M.; Edwards, S. F., *The theory of polymer dynamics*. Clarendon Press: Oxford, 1986.

143. Pincus, P.; De Gennes, P. G., Nematic polymers. *Journal of Polymer Science: Polymer Symposia* **1978,** *65* (1), 85-90.

144. Lin, J.; Abe, A.; Furuya, H.; Okamoto, S., Liquid Crystal Formation Coupled with the Coil−Helix Transition in the Ternary System Poly(γ-benzyl l-glutamate)/Dichloroacetic Acid/Dichloroethane. *Macromolecules* **1996,** *29* (7), 2584-2589.

145. Leon, A. C., 3.12 - Descriptive and Inferential Statistics. In *Comprehensive Clinical Psychology*, Bellack, A. S.; Hersen, M., Eds. Pergamon: Oxford, 1998; pp 243-285.

146. Hoffman, J. I. E., Chapter 33 - Logistic Regression. In *Basic Biostatistics for Medical and Biomedical Practitioners (Second Edition)*, Hoffman, J. I. E., Ed. Academic Press: 2019; pp 581-589.

147. Urso, A.; Fiannaca, A.; La Rosa, M.; Ravì, V.; Rizzo, R., Data Mining: Prediction Methods. In *Encyclopedia of Bioinformatics and Computational Biology*, Ranganathan, S.; Gribskov, M.; Nakai, K.; Schönbach, C., Eds. Academic Press: Oxford, 2019; pp 413-430.

148. Zimm, B. H.; Bragg, J. K., Theory of the One-Dimensional Phase Transition in Polypeptide Chains. *Journal of Chemical Physics* **1958,** *28* (6), 1246-1247.

149. Schellman, J. A., The Factors Affecting the Stability of Hydrogen-bonded Polypeptide Structures in Solution. *The Journal of Physical Chemistry* **1958,** *62* (12), 1485-1494.

150. Bloomfield, V. A., Statistical thermodynamics of helix–coil transitions in biopolymers. *American Journal of Physics* **1999,** *67* (12), 1212-1215.

151. Scholtz, J. M.; Baldwin, R., The Mechanism of Alpha-Helix Formation by Peptides. *Annual review of biophysics and biomolecular structure* **1992,** *21*, 95-118.

152. Applequist, J., On the Helix-Coil Equilibrium in Polypeptides. *The Journal of Chemical Physics* **1963,** *38* (4), 934-941.

153. Hajime, N.; Tsi, Y. J., Volume and sound velocity changes accompanying the α-helix to β-form and coil to α-helix transitions in aqueous solution. *Biopolymers* **1971,** *10* (12), 2569-2579.

154. Ren, Y.; Baumgartner, R.; Fu, H.; van der Schoot, P.; Cheng, J.; Lin, Y., Revisiting the Helical Cooperativity of Synthetic Polypeptides in Solution. *Biomacromolecules* **2017,** *18* (8), 2324-2332.

155. Ye, L.; Liu, J.; Sheng, P.; Huang, J.; Weitz, D., Sound propagation in colloidal systems. *Journal de Physique IV Colloque* **1993,** *03* (C1), C1-183-C1-196.

156. Tai, Y.; Wang, L.; Fan, G.; Gao, J. m.; Yu, H.; Zhang, L., Recent research progress on the preparation and application of magnetic nanospheres. *Polymer International* **2011,** *60* (7), 976-994.

157. Brandenburg, B.; Koudstaal, W.; Goudsmit, J.; Klaren, V.; Tang, C.; Bujny, M. V.; Korse, H. J. W. M.; Kwaks, T.; Otterstrom, J. J.; Juraszek, J.; van Oijen, A. M.; Vogels, R.; Friesen, R. H. E., Mechanisms of Hemagglutinin Targeted Influenza Virus Neutralization. *PLoS ONE* **2013,** *8* (12), e80034.

158. Matsuoka, M.; Norisuye, T.; Teramoto, A.; Fujita, H., Solution Properties of Synthetic Polypeptides. XV. Helix-Coil Transition in Poly(epsilon-carbobenzoxy L-lysine). *Biopolymers* **1973,** *12*, 1515-1532.

159. Nishioka, N.; Maekawa, A.; Teramoto, A., Solution Properties of Synthetic Polypeptides. XXI. Solvent Effect on the Helix-Coil Transition of Poly(e-carbobenzoxy L-lysine). *Biopolymers* **1978,** *17*, 665-675.

160. Omura, I.; Teramoto, A.; Fujita, H., Dielectric-Dispersion of Polypeptide Solutions .2. Helix-Coil Transition of "Poly(Epsilon-Carbobenzoxy-L-Lysine) in M-Cresol. *Macromolecules* **1975,** *8* (3), 284-290.

161. Karasz, F. E.; Gajnos, G. E., Thermodynamics of the Helix-Coil Transition in Polypeptides in Binary Solvent Systems. *J.Phys.Chem.* **1973,** *77* (9), 1139-1145.

162. Poland, D.; Scheraga, H. A., *Theory of Helix-Coil Transitions in Biopolymers*. Academic Press: New York, 1970.

163. Wang, Y. L.; Chang, Y. C., Synthesis and conformational transition of surface-tethered polypeptide: Poly(L-lysine). *Macromolecules* **2003,** *36* (17), 6511-6518.

164. Wang, Y. L.; Chang, Y. C., Preparation of unidirectional end-grafted alpha-helical polypeptides by solvent quenching. *Journal of the American Chemical Society* **2003,** *125* (21), 6376-6377.

165. Wang, Y. L.; Chang, Y. C., Patterning of polypeptide thin films by the combination of surface-initiated vapor-deposition polymerization and photolithography. *Advanced Materials* **2003,** *15* (4), 290-293.

166. Wang, Y. L.; Chang, Y. C., Grafting of homo- and block co-polypeptides on solid substrates by an improved surface-initiated vapor deposition polymerization. *Langmuir* **2002,** *18* (25), 9859-9866.

167. Wang, Y.; Chang, Y. C., Synthesis and Conformational Transition of Surface-Tethered Polypeptide: Poly(L-glutamic acid). *Macromolecules* **2003,** *36* (17), 6503-6510.

168. Adiga, S. P.; Brenner, D. W., Toward designing smart nanovalves: Modeling of flow control through nanopores via the helix-coil transition of grafted polypeptide chains. *Macromolecules* **2007,** *40* (4), 1342-1348.

169. Rosu, C.; Selcuk, S.; Soto-Cantu, E.; Russo, P., Progress in silica polypeptide composite colloidal hybrids: from silica cores to fuzzy shells. *Colloid and Polymer Science* **2014**, 1-32.

170. Borase, T.; Heise, A., Hybrid Nanomaterials by Surface Grafting of Synthetic Polypeptides Using N-Carboxyanhydride (NCA) Polymerization. *Advanced Materials* **2016,** *28* (27), 5725-5731.

171. Hadjichristidis, N.; Iatrou, H.; Pitsikalis, M.; Sakellariou, G., Synthesis of well-defined polypeptide-based materials via the ring-opening polymerization of alpha-amino acid N-carboxyanhydrides. *Chem Rev* **2009,** *109* (11), 5528-78.

172. Xu, Z.; Feng, Y.; Liu, X.; Guan, M.; Zhao, C.; Zhang, H., Synthesis and characterization of Fe3O4@SiO2@poly-l-alanine, peptide brush–magnetic microspheres through NCA chemistry for drug delivery and enrichment of BSA. *Colloids and Surfaces B: Biointerfaces* **2010,** *81* (2), 503-507.

173. Pauling, L.; Corey, R. B., The Structure of Hair, Muscle, and Related Proteins. *Proceedings of the National Academy of Sciences* **1951,** *37* (5), 261-271.

174. Fong, B., unpublished results.

175. Soto-Cantu, E.; Turksen-Selcuk, S.; Qiu, J.; Zhou, Z.; Russo, P. S.; Henk, M. C., Silica-Polypeptide Composite Particles: Controlling Shell Growth. *Langmuir* **2010,** *26* (19), 15604-15613.

176. Turksen, S. Synthesis and Characterization of Superparamagnetic Silica-homopolypeptide Composite Particles. Chemistry, Louisiana State University, 2005.

177. Soto-Cantu, E. I. Synthesis and Surface Characterization of Silica-Polypeptide Composite Particles. 2008, Louisiana State University, 2008.

178. Rosu, C. Silica polypeptide-based colloids [electronic resource] : physical properties and novel materials. PhD, Louisiana State University, Baton Rouge, Louisiana USA, 2013.

179. Fong, B.; Russo, P. S., Organophilic Colloidal Particles with a Synthetic Polypeptide Coating. *Langmuir* **1999,** *15*, 4421-4426.

180. Fong, B.; Stryjewski, W.; Russo, P. S., On the Use of Pattern Fluorescence Photobleaching Recovery with Modulation Detection to Obtain Colloidal Size Distributions. *J.Coll.Int.Sci.* **2001,** *239* (2), 374-379.

181. Soto-Cantu, E. I.; Cueto, R.; Koch, J.; Russo, P. S., Synthesis and Rapid Characterization of Amine-Functionalized Silica. *Langmuir* **2012,** *28* (13), 5562-5569.

182. Kobayashi, Y.; Horie, M.; Konno, M.; Rodriguez-Gonzalez, B.; Liz-Marzan, L. M., Preparation and properties of silica-coated cobalt nanoparticles. *Journal of Physical Chemistry B* **2003,** *107* (30), 7420-7425.

183. Rosu, C.; Cueto, R.; Russo, P. S., Poly(colloid)s: "Polymerization" of Poly(l-tyrosine)-silica Composite Particles through the Photoinduced Cross-Linking of Unmodified Proteins Method. *Langmuir* **2016**.

184. Rosu, C.; Gorman, A. J.; Cueto, R.; Dooley, K. M.; Russo, P. S., Sculpting the internal architecture of fluorescent silica particles via a template-free approach. *Journal of Colloid and Interface Science* **2016,** *467*, 321-334.

185. Tewari, U. S.; Vesudevan, P.; Ramakrishna, V., Viscosity Behaviour of o-,m- & p-Cresol Melts. *Indian Journal of Chemistry* **1975,** *13*, 720-721.

186. Karasz, F. E.; Gajnos, G. E., Enthalpies of Helix-Coil Transitions in Polypeptides. *Biopolymers* **1974,** *13* (7), 725-734.

187. Karasz, F. E.; O'Reilly, J. M., Enthalpy Changes in the Helix-Coil Transition of Poly(g-benzyl L-glutamate). *Biopolymers* **1967,** *5*, 27-35.

188. Kobayashi, Y.; Horie, M.; Konno, M.; Rodríguez-González, B.; Liz-Marzán, L. M., Preparation and Properties of Silica-Coated Cobalt Nanoparticles. *The Journal of Physical Chemistry B* **2003,** *107* (30), 7420-7425.

189. Block, H., *Poly(g-benzyl-L-glutamate) and other Glutamic Acid Containing Polymers*. Gordon and Breach: New York, 1983.

190. Fasman, G. D.; Idelson, M.; Blout, E. R., The Synthesis and Conformation of High Molecular Weight Poly-epsilon-carbobenzyloxy-L-lysine and Poly-L-lysine-HCl. *J.Am.Chem.Soc.* **1961,** *83* (Feb. 5), 709-712.

191. Doty, P.; Bradbury, J. H.; Holtzer, A. M., Polypeptides. IV. The Molecular Weight, Configuration and Association of poly(gamma-benzyl L-glutamate) in Various Solvents. *J.Am.Chem.Soc.* **1956,** *78*, 947-954.

192. Koppel, D. E., Analysis of Macromolecular Polydispersity in Intensity Correlation Spectroscopy: The Method of Cumulants. *J.Chem.Phys.* **1972,** *57*, 4814-4820.

193. Yamakawa, H., *Modern Theory of Polymer Solutions*. Harper and Row: New York, 1971.

194. Jabs, A., Determination of Secondary Structure in Proteins by Fourier Transform Infrared Spectroscopy (FTIR). 2011.

195. Arrondo, J. L. R.; Muga, A.; Castresana, J.; Goni, F. M., Quantitative Studies of the Structure of Proteins in Solution by Fourier-Transform Infrared-Spectroscopy. *Progress in Biophysics & Molecular Biology* **1993,** *59* (1), 23-56.

196. Dobbrow, C.; Schmidt, A. M., Improvement of the oxidation stability of cobalt nanoparticles. *Beilstein Journal of Nanotechnology* **2012,** *3*, 75-81.

197. Berne, B.; Pecora, R., *Dynamic Light Scattering*. Wiley: New York, 1976.

198. Kemp, J. P.; Chen, J. Z. Y., Helical structures in proteins. *Biomacromolecules* **2001,** *2* (2), 389-401.

199. Kastantin, M.; Tirrell, M., Helix Formation in the Polymer Brush. *Macromolecules* **2011,** *44* (12), 4977-4987.

200. Smith, I. R.; Charlier, A. H. R.; Pritzlaff, A. M.; Shishlov, A.; Barnes, B.; Bentz, K. C.; Easterling, C. P.; Sumerlin, B. S.; Fanucci, G. E.; Savin, D. A., Probing Membrane Hydration at the Interface of Self-Assembled Peptide Amphiphiles Using Electron Paramagnetic Resonance. *ACS Macro Letters* **2018,** *7* (10), 1261-1266.

201. Buhot, A.; Halperin, A., Extension Behavior of helicogenic polypeptides. *Macromolecules* **2002,** *35* (8), 3238-3252.

202. Campbell, J. N.; Epand, R. M.; Russo, P. S., Structural Changes and Aggregation of Human Influenza Virus. *Biomacromolecules* **2004,** *5* (5), 1728-1735.

203. Pawar, A. B.; Kretzschmar, I., Fabrication, Assembly, and Application of Patchy Particles. *Macromol Rapid Comm* **2010,** *31* (2), 150-168.

204. Johal, P.; Chaudhary, S., Electronic paper technology. *Int. J. Adv. Res. Sci. Eng* **2013,** *2* (9), 106-110.

205. Pourrahimi, A. M.; Pumera, M., Multifunctional and self-propelled spherical Janus nano/micromotors: recent advances. *Nanoscale* **2018,** *10* (35), 16398-16415.

206. Reguera, J.; Jiménez de Aberasturi, D.; Henriksen-Lacey, M.; Langer, J.; Espinosa, A.; Szczupak, B.; Wilhelm, C.; Liz-Marzán, L. M., Janus plasmonic–magnetic gold–iron oxide nanoparticles as contrast agents for multimodal imaging. *Nanoscale* **2017,** *9* (27), 9467-9480.

207. Schick, I.; Lorenz, S.; Gehrig, D.; Schilmann, A.-M.; Bauer, H.; Panthöfer, M.; Fischer, K.; Strand, D.; Laquai, F.; Tremel, W., Multifunctional Two-Photon Active Silica-Coated Au@MnO Janus Particles for Selective Dual Functionalization and Imaging. *J Am Chem Soc* **2014,** *136* (6), 2473-2483.

208. Teo, B. M.; Young, D. J.; Loh, X. J., Magnetic Anisotropic Particles: Toward Remotely Actuated Applications. *Particle & Particle Systems Characterization* **2016,** *33* (10), 709-728.

209. Rosu, C.; Cueto, R.; Russo, P. S., Poly(colloid)s: “Polymerization” of Poly(L-tyrosine)-silica Composite Particles through the Photoinduced Cross-Linking of Unmodified Proteins Method. *Langmuir* **2016**, 8392.

210. Prozorov, T.; Bazylinski, D. A.; Mallapragada, S. K.; Prozorov, R., Novel magnetic nanomaterials inspired by magnetotactic bacteria: Topical review. *Materials Science and Engineering: R: Reports* **2013,** *74* (5), 133-172.

211. Poché, D. S.; Moore, M. J.; Bowles, J. L., An Unconventional Method for Purifying the N-carboxyanhydride Derivatives of γ-alkyl-L-glutamates. *Synthetic Commun* **1999,** *29* (5), 843-854.

212. Maccarrone, S.; Brambilla, G.; Pravaz, O.; Duri, A.; Ciccotti, M.; Fromental, J. M.; Pashkovski, E.; Lips, A.; Sessoms, D.; Trappe, V.; Cipelletti, L., Ultra-long range correlations of the dynamics of jammed soft matter. *Soft Matter* **2010,** *6* (21), 5514-5522.

213. Zhou, Z.; Hollingsworth, J. V.; Hong, S.; Cheng, H.; Han, C. C., Yielding Behavior in Colloidal Glasses: Comparison between "Hard Cage" and "Soft Cage". *Langmuir* **2014,** *30* (20), 5739-5746.

214. Osada, Y.; Okuzaki, H.; Hori, H., A Polymer Gel with Electrically Driven Motility. *Nature* **1992,** *355* (6357), 242-244.

215. Baughman, R. H., Conducting polymer artificial muscles. *Synthetic Met* **1996,** *78* (3), 339-353.

216. Brochu, P.; Pei, Q. B., Advances in Dielectric Elastomers for Actuators and Artificial Muscles. *Macromol Rapid Comm* **2010,** *31* (1), 10-36.

217. Mirfakhrai, T.; Madden, J. D. W.; Baughman, R. H., Polymer artificial muscles. *Mater Today* **2007,** *10* (4), 30-38.

218. Smela, E., Conjugated polymer actuators for biomedical applications. *Adv Mater* **2003,** *15* (6), 481-494.

219. Russo, P., A Practical Minicourse in Dynamic Light Scattering. Lousiana State University: 2012.

220. Asano, S.; Yamamoto, G., Light-Scattering by a Spheroidal Particle. *Appl Optics* **1975,** *14* (1), 29-49.

221. Debye, P., Molecular-Weight Determination by Light Scattering. *J Phys Colloid Chem* **1947,** *51* (1), 18-32.

222. Forster, S.; Schmidt, M.; Antonietti, M., Static and Dynamic Light-Scattering by Aqueous Polyelectrolyte Solutions - Effect of Molecular-Weight, Charge-Density and Added Salt. *Polymer* **1990,** *31* (5), 781-792.

223. Zimm, B. H., The Scattering of Light and the Radial Distribution Function of High Polymer Solutions. *J Chem Phys* **1948,** *16* (12), 1093-1099.

224. Pecora, R., Dynamic Light-Scattering from Macromolecules. *P Soc Photo-Opt Ins* **1993,** *1884*, 2-15.

225. Mustafa, M. B.; Tipton, D.; Russo, P. S., Temperature Ramped Fluorescence Photobleaching Recovery for the Direct Evaluation of Thermoreversible Gels. *Macromolecules* **1989,** *22* (3), 1500-1504.

226. Russo, P. S.; Qiu, J.; Edwin, N.; Choi, Y. W.; Doucet, G. J.; Sohn, D., Fluorescence Photobleaching Recovery. In *Soft Matter Characterization*, Borsali, R.; Pecora, R., Eds. Springer Netherlands: 2008; pp 605-636.

227. Yu, K.; Russo, P. S., Light scattering and fluorescence photobleaching recovery study of poly(amidoamine) cascade polymers in aqueous solution. *J Polym Sci Pol Phys* **1996,** *34* (8), 1467-1475.

228. Stricker, J.; Maddox, P.; Salmon, E. D.; Erickson, H. P., Rapid assembly dynamics of the Escherichia coli FtsZ-ring demonstrated by fluorescence recovery after photobleaching. *Proc. Natl. Acad. Sci. U. S. A.* **2002,** *99* (5), 3171-3175.

229. Sprague, B. L.; Pego, R. L.; Stavreva, D. A.; McNally, J. G., Analysis of binding reactions by fluorescence recovery after photobleaching. *Biophys J* **2004,** *86* (6), 3473-3495.

230. Wu, E. S.; Jacobson, K.; Papahadjopoulos, D., Lateral Diffusion in Phospholipid Multibilayers Measured by Fluorescence Recovery after Photobleaching. *Biochemistry-Us* **1977,** *16* (17), 3936-3941.

231. Yguerabide, J.; Schmidt, J. A.; Yguerabide, E. E., Lateral Mobility in Membranes as Detected by Fluorescence Recovery after Photobleaching. *Biophys J* **1982,** *40* (1), 69-75.

232. Fong, B.; Stryjewski, W.; Russo, P. S., On the use of pattern fluorescence photobleaching recovery with modulation detection to obtain colloidal size distributions. *J Colloid Interf Sci* **2001,** *239* (2), 374-379.

233. Lanni, F.; Ware, B. R., Modulation Detection of Fluorescence Photobleaching Recovery. *Rev Sci Instrum* **1982,** *53* (6), 905-908.

234. Striegel, A.; Yau, W. W.; Kirkland, J. J.; Bly, D. D., *Modern Size-Exclusion Liquid Chromatography: Practice of Gel Permeation and Gel Filtration Chromatography*. Wiley: 2009.

235. Sperling, L. H., *Introduction to physical polymer science*. 4th ed. ed.; Wiley: Hoboken, N.J., 2006.